Morphological Perspectives on Galaxy Evolution since z∼1.5

by

Michael Rutkowski

A Dissertation Presented in Partial Fulfillment
of the Requirements for the Degree
Doctor of Philosophy

Approved April 2013 by the
Graduate Supervisory Committee:

Rogier Windhorst, Chair
Judd Bowman
Nathaniel Butler
Steven Desch
Patrick Young

ARIZONA STATE UNIVERSITY

May 2013

ABSTRACT

Galaxies represent a fundamental catalyst in the "lifecycle" of matter in the Universe, and the study of galaxy assembly and evolution provides unique insight into the physical processes governing the transformation of matter from atoms to gas to stars. With the Hubble Space Telescope, the astrophysical community is able to study the formation and evolution of galaxies, at an unrivaled spatial resolution, over more than 90% of cosmic time. Here, I present results from two complementary studies of galaxy evolution in the local and intermediate redshift Universe which used new and archival HST images. First, I use archival broad-band HST WFPC2 optical images of local (d<63 Mpc) Seyfert-type galaxies to test the observed correlation between visually-classified host galaxy dust morphology and AGN class. Using quantitative parameters for classifying galaxy morphology, I do not measure a strong correlation between the galaxy morphology and AGN class. This result could imply that the Unified Model of AGN provides a sufficient model for the observed diversity of AGN, but this result could also indicate the quantitative techniques are insufficient for characterizing the dust morphology of local galaxies. To address the latter, I develop a new automated method using an inverse unsharp masking technique coupled to Source Extractor to detect and measure dust morphology. I measure no strong trends with dust-morphology and AGN class using this method, and conclude that the Unified Model remains sufficient to explain the diversity of AGN. Second, I use new UV-optical-near IR broad-band images obtained with the HST WFC3 in the Early Release Science (ERS) program to study the evolution of massive, early-type galaxies. These galaxies were once considered to be "red and dead", as a class uniformly devoid of recent star formation, but observations of these galaxies in the local Universe at UV wavelengths have revealed a significant fraction (30%) of ETGs to have recently formed a small fraction (5-10%) of their stellar mass in young stars. I extend the

study of recent star formation in ETGs to intermediate-redshift ($0.35< z <1.5$) with the ERS data. Comparing the mass fraction and age of young stellar populations identified in these ETGs from two-component SED analysis with the morphology of the ETG and the frequency of companions, I find that at this redshift many ETGs are likely to have experienced a minor burst of recent star formation. The mechanisms driving this recent star formation are varied, and evidence for both minor merger driven recent star formation as well as the evolution of transitioning ETGs is identified.

To my family, kin and not

ACKNOWLEDGEMENTS

I would like to acknowledge a number of grant and fellowship programs that have supported me financially during my graduate studies and the completion of this dissertation, including the US State Department Fulbright Fellowship Program, the NASA Space Grant Fellowship Program, the ASU Graduate College, and the Graduate and Professional Students Association. I thank the crew of STS-125 for refurbishing and repairing the Hubble Space Telescope; without their service, this dissertation could not have been completed. I thank the Director of the Space Telescope Science Institute for awarding Director's Discretionary time for the HST WFC3 Early Release Science program, and acknowledge the Hubble Legacy Archive, the online repository for HST data.

This dissertation could not have been completed without the support of my supervisor and colleagues at Arizona State University and abroad. Specifically, I thank Rogier Windhorst for allowing me to join the ERS team, helping me to refine the scope of this research, introducing me to many new collaborations and encouraging me to strike out on my own scientifically. I acknowledge my committee members for helpful conversations. I thank Seth Cohen and Russell Ryan for all of their help with errant codes and daunting tasks over these past six years. For their conversation and friendship, I thank Rolf Jansen, Hwihyun Kim, Kazuyuki Tamura, Duho Kim, Matt Mechtley, & Teresa Ashcraft; Sheen Yun-Kyeong, Jung Eun-Jung, Oh Kyuseok, Oh Sree, Lee Jaehyun and for his supervision and assistance abroad, Yi Sukyoung.

Finally, to my mother, who scrimped all year in order to buy her children the World Book Encyclopedia when what we thought we wanted was a Nintendo. To my father, who baffled me as a kid by knowing every question on Jeopardy, and who inspires me to wander by his stories of the same. To both of my parents, thank you

for the greatest gift: the desire to fall asleep each night knowing, experiencing, and appreciating more than I did the night before. To my sister, Kati, who is successful in life and love, and of whom I am quite jealous. To my sister, Grace, whom I have known since her first sunrise and watched grow up to be a power forward and a budding young scientist.

TABLE OF CONTENTS

LIST OF TABLES

LIST OF FIGURES

Chapter 1

INTRODUCTION

It has been said that observational astrophysics is akin to journalism. Unlike our colleagues in many other disciplines of physics, we observers can not build experiments—in the sense that we can not force galaxies to merge or stars to go supernova (only theorists have that awesome power). Instead, we can only observe the universe, take as good notes as is possible and then compile the data in such a way that, after applying our knowledge of the underlying physics, we can report the story of the universe in scientifically rigorous way. If we have done our jobs correctly and answered the "Four W's"—What, When, Where and Why—then with any luck, our reporting provides the scientific and general community new perspective on what the other 99.999999...% of the universe's mass, beyond our the Earth's local neighborhood—with its solitary star and few planet-sized dust bunnies—has been up to over the past $\sim$13 billion years.

Understanding the assembly and evolution of galaxies is fundamental to our understanding this story because of the unique role these objects serve. On sub-galactic scales, galaxies are "cosmic nurseries," host to the transformation of cold gas into stars, which will subsequently give rise to planetary systems, life, and apple pie. On supra-galactic scales, the super-massive black holes that galaxies foster, source the inter-galactic environment with hard, Ultraviolet photons, maintaining a fully-ionized universe at the current epoch.

Here I present the results of two unique investigations of galaxy evolution. By surveying "the scene" from multiple angles and "interviewing multiple witnesses," the developing story is best revealed. Though these studies have considered the properties of two disparate galaxy samples, they are linked by a similar methodology.

Specifically, in each study I have used galaxy morphology to constrain the formation and evolution of galaxies. In biology, it was once believed that "phylogeny recapitulates ontogeny", or in other words, that the morphology of organism in (embryonic) development was partially indicative of the species' evolutionary history. In observational astrophysics, such a mantra is often still assumed; i.e., galaxy morphology can indicate and be used to distinguish the evolutionary history of galaxies. For example, it is typically assumed that early-type galaxies formed their stars very early ($z > 4$) and now exist primarily as "red and dead" stellar systems, largely devoid of gas and young stars. In this dissertation, I intend to demonstrate that such a link between evolution history and the morphology of galaxies is not so clear.

In each study, I use new and archival data obtained with the Hubble Space Telescope. This telescope, a premier scientific instrument for the study of a wide range of astrophysical phenomena, is an astronomer's dream. For more than two decades, HST has been a "workhorse" instrument, able to reveal the universe at a superior spatial resolution from a unique perspective above the Earth's obscuring atmosphere.

1.1 Exploring the Nature of the Active Galactic Nuclei in Local Galaxies

It is now understood that most massive galaxies possess a super-massive black hole (SMBHs; $\sim 10^6 - 10^9 M_\odot$) in their cores. At their location at the bottom of their host galaxy's potential well, these SMBHs are in an ideal location to accrete baryonic matter in the form of stars and gas. But this consumption does not occur quietly nor is all material in the local potential well of the SMBH ultimately consumed. Though "black" themselves, the region immediately surrounding the black holes can emit significant radiation that can be detected by observers. The extreme physics of black holes and their accretion regions is not entirely understood, but we know that the coupling of the matter with strong magnetic fields can drive "jets" of radiation from

these objects, and the dynamical friction between baryons, which can energize gas and dust in the local environment causing it to emit strongly across the electromagnetic spectrum and produce an "Active Galactic Nuclei" (AGN). The emission from the gas in the local environment is configured in a "toroid"-shaped region immediately surrounding (r$\simeq 1-100$ pc) the SMBH. For decades, these objects were identified in both nearby and distant ($z \gg 1$) galaxies with a wide range of characteristics — some were identified with jets at radio, x-ray or even optical wavelengths, some outshined the stellar emission from their host galaxies, and others showed broad and narrow lines while others showed only narrow lines in their optical spectra. The Unified Model of AGN has provided a successful explanation for this observed diversity. In the Model, the diversity in spectral profiles in AGN can be attributed exclusively to the relative inclination angle of the dusty toroid in which the AGN is embedded, with respect to the observer. In "Type 1" AGN, the dusty toroid and intervening inter-stellar gas along the sight is oriented perpendicular to the observer, whereas in "Type 2" AGN, the SMBH is partially or fully obscured by the toroid. Thus, there is no fundamental physical distinction between the class of AGN. However, recent analysis of multi–wavelength spectral and image data suggests that the Unified Model is only a partial theory of AGN, and may need to be augmented to remain consistent with all observations. Studies using high spatial resolution ground– and space–based observations of local AGN show that Seyfert class and the "core" (r$\lesssim$1 kpc) host–galaxy morphology are correlated. Currently, this relationship has only been established qualitatively, by visual inspection of the core morphologies of low redshift ($z < 0.035$) Seyfert host galaxies (Malkan, Gorjian and Tam , 1998).

In Chapter 3, I re–establish this empirical relationship in Hubble Space Telescope (HST) optical imaging by visual inspection of a catalog of 85 local ($D < 63$Mpc) Seyfert galaxies. These data were obtained with the Wide-Field Planetary Camera

Figure 1.1: The WFPC2 onboard "SpaceShip Earth", its final destination. Photo Courtesy of Matt Mechtley.

2, an instrument that now resides in a museum, but due to the efforts of the HST Archive team is still, effectively, a "working instrument."

I also attempt to re–establish the core morphology–Seyfert class relationship using an automated, non-parametric technique that combines both existing classification parameters methods (the adapted CAS, G–M_{20}), and a new method which implements the `Source Extractor` (hereafter,`SE`) software for feature detection in unsharp–mask images. This new method is designed explicitly to detect dust features in the images. As all-sky surveys with large aperture telescopes become more common in astrophysics, such automated classification techniques are desirable as they provide a reproducible means for quickly assessing galaxy morphology. I use this automated approach to classify the morphology of the AGN cores and determine that Sy2 galaxies visually appear, on average, to have more dust features and are more concentrated in their stellar light profiles than Sy1. With the exception of this "dustiness" however, we do not measure a strong correlation between the dust morphology and the Seyfert class of the host galaxy using these quantitative techniques. We discuss the implications of these results in the context of the Unified Model. The

Figure 1.2: The launch of STS-125, SM4 from Cape Canaveral, Florida.

results of this research were published in 2013 in the Astronomical Journal.

1.2 The Evolution of ETGs over ∼6 Billion Years of Cosmic History

ETGs were once believed to have formed via a "monolithic collapse", forming the majority of their stars at high redshift. Recently, studies of the rest-frame UV-optical properties of these galaxies at low redshift have revealed that many ($> 30\%$) of these galaxies have recently formed a small, but a non-negligible fraction of their mass in young stars. Due to the technical limitations of previous generations of space-based observatories, it was impossible to extend an analysis of these galaxies recent star formation history to higher redshift, though. The successful installation of the HST WFC3 now makes such a study possible.

In Chapters 4 and 5, I present a panchromatic catalog of 102 visually-selected early-type galaxies (ETGs) using data from the Early Release Science (ERS) program with the Hubble Space Telescope (HST) Wide Field Camera 3 (WFC3) of the Great Observatories Origins Deep Survey-South (GOODS-S) field. The ETGs span a large redshift range, $0.35 \lesssim z \lesssim 1.5$, with the redshift of each spectroscopically-confirmed by previous published surveys of the ERS field. I combine our measured WFC3 ERS photometry and ACS GOODS-S archival data to gain continuous sensitivity to the rest-frame far-UV to near-IR emission of each ETG. The superior spatial resolution of the HST over this panchromatic baseline allows us to classify the ETGs by their small-scale internal structures, as well as their local environment. By fitting stellar population spectral templates to the broad-band photometry of the ETGs, I determine the mass, morphology, and star formation characteristics of these ETGs. This analysis confirms that a significant minority ($\sim$30-40%) of these ETGs have likely experienced a burst of low-level, recent star formation as they are identified with a minor fraction ($f_{YC} \sim 5-10\%$) of their total stellar mass in young stars ($t_{YC} \lesssim 1$ Gyr). I measure trends between the frequency of young stars and both the Sèrsic morphology and companion number of these ETGs. Though we are limited by the small number statistics associated with this sample, these results likely imply multiple physical mechanisms motivate the observed star formation in ETGs at intermediate redshift, in accordance with theory and observation of massive galaxies from both the local and high redshift universe. The work presented in Chapter 4 was published in 2012 in the Astrophysical Journal; Research presented in Chapter 5 is currently in preparation for submission to the Astrophysical Journal in 2013.

Chapter 2

LIST OF ACRONYMS

ACS - Advanced Camera for Surveys
AGN - Active Galactic Nuclei
BC03 - Bruzual & Charlot (2003)
CAS - "Concentration", "Asymmetry","Clumpiness"
CDF - Cumulative Distribution Function
CDF-S - Chandra Deep Field-South
EHB - Extreme Horizontal Branch
ERS - Early Release Science
ESO - European Southern Observatory
ETG - Early Type Galaxy
FUV - Far Ultraviolet
FWHM - Full-Width Half Maximum
GALEX - Galaxy Evolution Explorer
GOODS-S - Great Observatories Origins Deep Survey-South
HLA - Hubble Legacy Archive
HST - Hubble Space Telescope
IPAC - Infrared Processing and Analysis Center
IR - Infrared
IUM - Inverse Unsharp Mask
MARK - Markarian
MGT98 - Malkan, Gorjian & Tam (1998)
NASA - National Aeronautics and Space Administration
NED - NASA/IPAC Extragalactic Database
NGC - New General Catalog
NUV - Near Ultraviolet
PC - Planetary Camera
SE - Source Extractor
SED - Spectral Energy Distribution
ULIRG - Ultra Luminous Infrared Galaxy
UV - Ultraviolet
UVX - UV Upturn
WFC - Wide Field Camera
WFC3 - Wide Field Camera 3
WFPC2 - Wide Field Planetary Camera 2

Chapter 3

INVESTIGATING THE CORE MORPHOLOGY–SEYFERT CLASS RELATIONSHIP WITH HUBBLE SPACE TELESCOPE ARCHIVAL IMAGES OF LOCAL SEYFERT GALAXIES

This chapter is modified from Rutkowski et al. (2013), which has been accepted by the Astronomical Journal for publication.

Active Galactic Nuclei (AGN) are sustained by the accretion of material from their local environment onto a super–massive (M $\gtrsim 10^6$-$10^7 M_\odot$) black hole. In the Unified Model of AGN, the observed diversity in emission-line profiles of AGN is believed to be an observational bias introduced by the relative inclinations (with respect to the observer) of the central engine as it is nested within a toroid of dense molecular material (Barthel et al. , 1984; Antonucci et al. , 1993). Observations of the "zoo" of AGN (e.g., Seyferts, BL LAC objects, Radio galaxies) from X–ray to radio wavelengths have been remarkably well–explained by the Unified Model (for a review, see e.g., Urry & Padovani , 1995).

Despite the success of the model, numerous AGN in the local Universe are not well–explained within the paradigm of the Unified Model. Many tests of the Unified Model have concentrated on the observed diversity in the properties of Seyfert galaxies, which are broadly classified by their emission line profiles as: a) Sy1–1.9 (Sy1), observed with both broad (v$\gtrsim 10^3$km s^{-1}) and narrow line emission; and b) Seyfert 2 (Sy2), observed only with narrow line emission. For example, Tran (2001, 2003) identified Sy2 AGN that lack "hidden" Sy1 AGN as predicted by Unified Model, indicating that Sy2s may not be—as a class—identical to Sy1 AGN. Furthermore, Panessa & Bassani (2002) found that the column density of absorbers in Sy2 AGN implies the existence of dust absorbers on a larger physical scale (r$\gtrsim$1 kpc) than the

molecular toroid. Recently, Ricci et al. (2011) found "excess" X–ray emission from reflection in Sy2 AGN, that did not appear to a comparable extent in Sy1 AGN, indicating an environmental distinction between these two classes of AGN.

Malkan, Gorjian, & Tam (1998, hereafter MGT98) tested the Unified Model via a "snapshot" campaign (see §3.1 for details) conducted with HST Wide Field Planetary Camera 2 (WFPC2) using the F606W (λ_0=5907Å) filter, in which they observed the morphology of the inner core ($\sim$1 kpc) of 184 local ($z \lesssim 0.035$) Seyfert & HII (star-forming) galaxies. The authors visually inspected these images and determined that Sy1s are preferentially located in galaxies of "earlier–type" core morphology, and conversely that Sy2 AGN are more often hosted by galaxies with "later–type" cores where the definition of early- and late-type morphology is derived from a Hubble-type morphological classification of each galaxy. MGT98 also determined that the distribution of dust is more irregular and extends closer to the nucleus in Sy2 galaxies than it does in Sy1 AGN. Hereafter, I refer to these two empirical relationships as the "MGT98 relationship." These independent studies suggest that there may be a fundamental physical distinction between Sy1 and Sy2 galaxies, one that is not explained by the relative inclination with respect to the thick, gas-rich toroidal in which the AGN central engine is embedded. The contemporary debate on the nature of AGN is not framed exclusively by the Unified Model; other models of the central engine and the dusty accretion disk do exist (e.g., the "clumpy torus" model of Nenkova et al. , 2008), but I will discuss my analysis in the context of the Unified Model to provide an easier comparison with published results in the literature.

In this study, I test the Unified Model using images downloaded from the Hubble Legacy Archive (HLA)[1].. Specifically, I re–examine and extend the analysis first established in MGT98 using a catalog of 85 Seyfert galaxies selected using the criteria

[1] `http://hla.stsci.edu`

outlined in §3.1. In §3.2, I present the results of the visual inspection and classification of the catalog Seyfert galaxies. In §3.3, I present, apply and discuss an automated technique, which I use to quantify the distribution of any dust features (e.g., dust, stellar clusters, etc.) present in the cores of the catalog galaxies. This classification technique quantifies the distribution of the dust features that were used to qualify the degree of dust irregularity or morphological class of a galaxy in the original visual inspection (§3.2). In §3.4, I present a new automated technique developed to detect the dust features, which were identified in §3.2 and used in the visual classification of the galaxies' cores. I discuss the results, and implications, of the qualitative visual and quantitative automated analysis in Chapter 6. Throughout, I assume a ΛCDM cosmology with Ω_m=0.27, Ω_Λ=0.73, and H_0=70 km^{-1} s^{-1} Mpc^{-1} (Komatsu et al. , 2011).

3.1 Data and Image Processing

To test the MGT98 relationship, I require a sufficiently large sample of Sy1 and Sy2 AGN to ensure that any result can be interpreted in a statistically meaningful way. I therefore use the following selection criteria to identify this sample of AGN:

- Initial Catalog: I develop a large (N≃240) catalog from three large HST surveys of Seyfert galaxies (Ho et al. 1997; MGT98; Ho & Peng 2001) that were included in the NASA/IPAC Extragalactic Database (NED[2]). I refer the reader to the respective surveys for specific details associated with the sample selection of these AGN. Together, these surveys can be used to produce a catalog that is generally representative of the morphological diversity of Seyfert galaxies, although none of the samples is strictly volume complete.

[2]available online at `http://ned.ipac.caltech.edu`)

- HST WFPC2 F606W HLA Images: At optical wavelengths, the resolution of features with a linear spatial extent of $10 \lesssim \mathrm{r\ (pc)} \lesssim 100$ can only be achieved with large–aperture space–based observatories. Thus, I required galaxies to have HST WFPC2 F606W filter images in the HLA, prepared as mosaics of the WF1–3 and PC CCD images multidrizzled[3] to a uniform 0.10″ pixel scale. The mosaiced images were used to ensure that the intrinsically different pixel scales of the individual CCDs did not bias the identification and classification of sources. The HLA contains an image for more than 90% of the galaxies included in the initial catalog with this specific camera and filter combination. The fact that these images are available is partly a selection bias. Many of the observations I include in the catalog were observed by MGT98 in the snapshot campaign. Note that the F606W filter samples longward of the 4000Å break at all relevant redshifts in the catalog. This broad filter includes the rest-frame Hα and [NII] line emission which, in AGN, can be prominent. In §3.2, I discuss the effect of this emission on the qualitative analysis.

- "Face–On": I only included "face–on" galaxies to ensure that the dust features classified in §3.2 are physically confined to a region relatively close to the core (1 kpc) of the galaxy. I estimated the angle of inclination by eye, and excluded an additional 20% of AGN that appeared at inclinations approximately greater than $\sim$30°. I did not exclude those galaxies with inclination angles that could not be estimated (i.e., irregular galaxies), nor do I exclude elliptical galaxies.

- Distance less than 63 Mpc: I am interested in characterizing the structural properties of dust features with a linear size scale greater than 100 pc (for more details, see §3.4.1). I require at least 3.5 WFPC2 pixels (0.35″ in the HLA mosaic images) to span this physical scale. This sets the maximum allowable

[3]see http://stsdas.stsci.edu/multidrizzle/

distance to a catalog galaxy of 63 Mpc or, equivalently, a redshift $z \lesssim 0.015$. Sub–kiloparsec scale features (e.g., dust lanes, clump, or cloud formations such as bars, wisps, and tidal features like warps and tails) are easily discernible in galaxies nearer than this distance observed at the HST spatial resolution. I excluded an additional 50% of galaxies that were at distances greater than 63 Mpc. I model and discuss the dependence of the morphological classification parameters on spatial resolution (Addendum A1), and the galaxy distance (Addendum B1).

31 Sy1 and 54 Sy2 galaxies from the initial sample met all of these selection criteria, combined for a total of 85 Seyfert galaxies. This large sample ensures that the (Poisson) uncertainties from small number statistics are small. The catalog includes significantly fewer Sy1 than Sy2 galaxies, partly due to a bias towards Sy2 AGN in the initial sample. For example, only 44% of the galaxies in MGT98 are classified as Sy1 AGN. In the Unified Model, this represents a bias in the opening angle through which the AGN is viewed. Though this bias may be present, it will not significantly affect this study, because I am investigating the core morphological distinctions between the AGN sub-classes of the host galaxies (i.e., on scales of hundreds of parsecs, well beyond the ∼parsec scale of the thick, dusty torus). Where the data are available from NED, I plot the number of Seyfert galaxies by their host deVaucouleurs galaxy type and 60μm flux in Figures 3.1 & 3.2, respectively. These figures demonstrate that the catalog is not strongly dominated by a particular galaxy type or observed AGN luminosity.

I prepared the HLA mosaiced images for analysis by first visually identifying the (brightest) central pixel of each galaxy. I extracted a core region with physical dimensions of 2×2 kpc centered at this point. The HLA images that I used have

only been processed to the Level 2 standard, i.e., only images acquired during the same visit are drizzled and mosaiced in the HLA. Many of the galaxies were originally imaged as part of HST snapshot surveys (single exposures with $t_{exp} \simeq 500$s). As a result, cosmic rays can be a significant source of image noise in the mosaics. I used the routine, `l.a.cosmic` (van Dokkum , 2001) to clean the CCD images of cosmic rays[4]. Initially, we implemented `l.a.cosmic` using the author's suggested parameters, but found by iteration that a lower value for the object–detection contrast parameter, `sigclip`=2.5, produced cleaner images without significantly affecting the pixels of apparent scientific interest. Additional cleaning and preparation of the imaging was necessary for the following analyses, and I discuss those task–specific steps taken in §3.3.1.

3.2 Visual Classification of Core Morphology

The core morphologies of the AGN–host galaxies are diverse and early– and late–type morphologies, with varying degrees of complexity in dust and gas features, are represented in the catalog. In Figure 3.6, I provide images of a subset (4) of the galaxies for illustrations; each image has been scaled logarithmically. Images of all (85) galaxies are available in Appendix A. Here, I use this subset of galaxies specifically to discuss the various dust features and structures that I classify by eye.

Galaxies in the catalog display a wide variety of spiral arms–like features. In Appendix A, I provide images of two galaxies (MARK1330, NGC3081; Fig. p. & an., respectively) that show spiral arms that are easily distinguished from the stellar light. In some galaxies, these arms are reminiscent of galactic–scale spiral features, such as a stellar bar (NGC3081). Some spiral–arm like features are more unique. For example, MARK1330 has a single arm that appears to originate in the bright core of

[4]available online at `http://www.astro.yale.edu/dokkum/lacosmic/`

the galaxy. Furthermore, some galaxies appear to be relatively dusty with numerous features of various size scales, appearing in either organized or chaotic features (e.g. NGC1068, NGC1386, NGC1672, NGC3393; Figs. aa.,af.,ai.,& aq.).

In Appendix A, I also provide examples of galaxies whose cores are relatively sparsely populated with dust features. In some cases (e.g., NGC3608; Fig. at., Appendix A), these galaxies have few dust features. In other galaxies (e.g., NGC1058; Fig. z.) dust features appear most pronounced in the core of the galaxy ($r \lesssim$100-200 pc) and are less significant at larger radii.

I have visually inspected and classified each of the 85 galaxies in the catalog, first using the following criteria that were defined and used in MGT98. I divide these criteria into two general classes:

Class 1—Dust Classifiers:

- DI : Irregular dust;
- DC : Dust–disk/Dust–lane passing close or through center (i.e., bi–sected nucleus);
- D : Direction of dust lanes on one side of major axis, where direction is N, S, E, W, NW, NE, SW, or SE;
- F/W : Filaments/wisps, and;

Class 2—Ancillary Classifiers:

- R : Ring;
- E/S0: Elliptical or Lenticular;
- B : Bar;
- CL : Cluster, lumpy HII region, knots;

Four observers (P. Hegel, Hwihyun Kim, M. Rutkowski, & K. Tamura) inspected the 2×2 kpc postage stamp images in Appendix A and classified each of the Seyfert cores. I did not use the "normal" classifier, because its definition could not be independently inferred from MGT98. In practice, I note that galaxies that showed regular spiral and dust features in their core morphology were more often classified as F/W. Conversely those with more irregular spiral and dust features was classified as DI. These classifications are not mutually exclusive, i.e., galaxies could be classified as both DI and F/W. In Table 3.1 all unique visual classifications are provided.

The majority (91%) of galaxies were identified with dust features. Irregular dust features (DI) were observed in 42% (13/31) of Sy1 and 57% (31/54) of Sy2 AGN. In contrast, 68% (21/31) of Sy1, and (31/54) 57% of Sy2 host galaxies, showed regular filaments and wispy features (F/W).

Thus, by visual inspection, I find that Sy1 host galaxies are more regular in their dust morphologies than are Sy2 host galaxies, while Sy2 host galaxies are more chaotic or irregular in their dust morphologies than are Sy1 host galaxies.

To reduce ambiguity in the classification of regular and irregular dust features in the galaxies, and to provide a second confirmation of the MGT98 relationship, I developed an additional system specifically for the classification of the core dust morphology of Seyfert galaxies. This classification scheme is defined as follows:

- 1-"Nuclear spiral"—Distribution of features resembles a flocculent or "grand-design" spiral;
- 2-"Bar"—A bar–like feature in emission or absorption extends outward from the center of the galaxy;
- 3-"Dust-specific classification"—The previous designations considered all structure. The following classifications describe only the quality and spatial distribution of what we consider to be dust:
  - Group A:
    - s-"Late-type Spiral"—Dust appears distributed in a spiral pattern throughout more than 50% of the image. The "inner-arm" regions appear to be clear of any dust;
    - i-"Irregular"—No visually distinguishable pattern can be identified in the spatial distribution of dust, i.e., the dust is patchy and irregular in form;
  - Group B:
    - m-"High Extinction"—Dust features appear to be of high column density. The galaxy appears highly extincted. Dust lanes appear to "cut" through the ambient stellar light of the galaxy;
    - l-"Low Extinction"—Low contrast dust is present, but is barely discernible from the ambient stellar light.

In Table 3.2, I provide the classification using this scheme. If possible, galaxies were classified using Class 1 and 2, but all galaxies were classified according to their dust structure (Class 3). The sub-groups of Class 3 (A&B) were mutually exclusive;

e.g., no galaxy could be classified as '3is'. Galaxies could be classified by a single Group A and one Group B classification simultaneously (e.g., '3mi'). If there was a conflict in classifying dust structure amongst the four co-authors, the majority classification is listed in Table 3.2. If no majority was reached after first classification, the corresponding author made the final classification without knowledge of the Seyfert class in order to prevent any unintentional bias in the measurement of the Malkan relationship.

The WFPC2 F606W filter I used in this image classification is broad ($\lambda\lambda \simeq$4800-7200Å) and includes the Hα+[NII] line complex. In principle, this line emission could affect the visual classification. In practice, the contribution of line flux to the continuum is relatively minor —the contribution of the [NII] doublet to the total flux in this bandpass using the SDSS QSO composite spectrum (vanden Berk et al. , 2001) is $\ll$1%, and I estimate the ratio of the equivalent widths, $\mathrm{EW}_{\mathrm{H}\alpha}/\mathrm{EW}_{[NII]}$, of these lines to be $\simeq$ 3:2. Despite the minor contribution to the total observed flux in line emission, the photo–ionization of the gas-rich local medium by the central engine can produce significant "hotspots" at the wavelengths of these atomic lines, which appear as structure in the image. Cooke et al. (2000) has studied an example of this photo–ionization structure, the spiral-like "S" structure in one of the sample Seyferts hosts (NGC3393; Fig. aq. Appendix A). Though this emission contributes very little to the total flux in the core, the high contrast between these bright emitting sources and the local area could lead to "false positive" classifications of dust features. Fortunately, few AGN ($\sim$7-8 galaxies, see e.g., MARK3, MARK1066, NGC1068, NGC3393, NGC4939, & NGC7682 in Appendix A show evidence of these emitting structures and these highly localized structures were easy to visually distinguish in practice from the stellar and dust continuum.

In conclusion, I confirm that Sy2 host galaxies are significantly more likely to have irregular core morphologies: 58% of Sy2 host galaxies were classified as '3i'. In contrast, only 40% of Sy1 host galaxies were classified as '3i'. Furthermore, 39% Sy2 AGN were classified as '3s' in contrast to 53% of Sy1 host galaxies. The results of the visual classification agrees with the observations in MGT98.

Although visual inspection is effective for classifying the morphology of spatially resolved sub–structure in galaxies, it is time–consuming and it does not provide a quantifiable and independently reproducible measure of the irregularity of structures that can be directly compared with the results of similar studies. Though guidance was provided to the co-authors on how to classify varying degrees of dust structure using the Class 3, such classifications are highly subjective and conflicts in classification could arise between co-authors. For example, approximately 55% of the visual classifications of dust structure (Table 3.2) were not unanimous. This discrepancy can be largely attributed to the subjective definition of the Class 3 sub-classifications. In each galaxy, the co-authors implicitly emphasized the importance of dust features over when making their classification. In many galaxies, whether the authors chose to weight the significance of physically small or large-scale dust structure could change the structural classification significantly. Consider the case of NGC1365: this galaxy was classified with an irregular dust morphology due to the small-scale dust features that appear to dominate the visible sub-structure in the core. But, authors who (subconsciously or otherwise) emphasized the broad dust "lanes" in the north and (to a lesser extent) south may classify the core as having a "spiral" dust morphology. Neither classification is necessarily incorrect —the broad dust lanes are clearly associated with the prominent spiral arms in this galaxy when viewed in full scale. These complicating factors can weaken any conclusion drawn from the visual classification of galaxies.

In recent decades, as image analysis software and parametric classification techniques have become prevalent, the astrophysical community is beginning to implement automated methods for galaxy classification (e.g., Odewahn et al. , 1996; Conselice et al. , 2003; Lotz et al. , 2004). By relegating the task of object classification to automated software and algorithmic batch processing, these methods have gained popularity, because they can significantly reduce the time observers must spend inspecting each galaxy, and can provide a reproducible classification for each galaxy.

Therefore, I extend the original test of the Unified Model to include a quantitative assessment of the morphological differences between Seyfert galaxies. I present these techniques in §3.3 and §3.4. With these quantitative parameters I can reduce some of the biases implicit in visual inspection and test the MGT98 morphological distinctions in a new way.

3.3 Conventional Quantitative Morphological Parameters

A number of parameters have been defined to quantify galaxy morphology. These parameters are distinguished by their use of a pre-defined functional form—i.e., parametric or non-parametric—to express galaxy morphology. Some popular non-parametric morphological parameters are "CAS" (Conselice et al. , 2003, "Concentration", "Asymmetry", and "clumpinesS") and "Gini–M_{20}" (Abraham et al. , 2003; Lotz et al. , 2004, "Gini Coefficient" and M_{20}, the second–order moment of brightest 20% of the galaxy pixels). These methods are not without limitations (cf. Lisker , 2008), but each can be useful for assessing galaxy morphology. I chose to use these parameters in the subsequent analysis, because the distribution of dust features in the cores of Seyfert galaxies is unlikely to be well-described by a single functional form, e.g., the Sérsic function, broadly distinguishes between bulge- and disk-dominated light profiles.

Conselice et al. (2000) provide the following functional definitions of the CAS parameters.

The concentration index, C, is defined as:

$$\mathrm{C} = 5\ ln\ \left(\frac{r_{80}}{r_{20}}\right), \tag{3.1}$$

where r_{80} and r_{20} are the values of the circular radii enclosing 80% and 20% of the total flux. The typical range in concentration index values measured for galaxies on the Hubble sequence is $1 \lesssim \mathrm{C} \lesssim 5$ (Conselice , 2004; Hernández-Toledo et al. , 2008). Larger values of the concentration parameter are measured for galaxies that are more centrally peaked in their light profiles.

The asymmetry, A, is defined as:

$$\mathrm{A} = \frac{\sum_{a,b=0}^{x,y} |I_o(a,b) - I_\Phi(a,b)|}{2 \sum_{a,b=0}^{x,y} |I_o(a,b)|}, \tag{3.2}$$

where x and y correspond to the length (in pixels) of the image axes, I_o is the original image intensity, and I_Φ is intensity of pixels in an image with respect to the original orientation rotated through an angle of Φ (I set $\Phi = 180°$). Typically, A ranges from 0 (radially symmetric) to 1 (asymmetric), see e.g., Conselice et al. (2003).

Clumpiness, S, is defined as:

$$\mathrm{S} = 10 \times \sum_{a,b=0}^{x,y} \frac{(I_o(a,b) - I^\sigma(a,b)) - B(a,b)}{I_o(a,b)}, \tag{3.3}$$

where $I_o(a,b)$ is the image intensity in pixel (a,b), $I^\sigma(a,b)$ is the pixel intensity in the image convolved with a filter of Gaussian width σ, and B(a,b) is the estimated sky–background for a given pixel. Typically, $0 \lesssim \mathrm{S} \lesssim 1$ (see e.g., Conselice et al. , 2003), and galaxies that appear to be visually "clumpier" have higher values of S.

Abraham et al. (2003) and Lotz et al. (2004) provide the following functional definitions of the Gini–M_{20} parameters. The Gini parameter is defined as :

$$G = \frac{1}{\bar{f} n(n-1)} \sum_{j}^{n} (2j - n - 1) f_j, \tag{3.4}$$

where $\bar{f}$ is the mean over all pixel flux values (f_j), and n is the number of pixels. This parameter measures inequality in a distribution using the ratio of the area between the Lorentz curve, defined as:

$$L(p) = \frac{1}{\bar{f}} \int_0^p F^{-1}(u) du, \tag{3.5}$$

and the area under the curve of uniform equality ($= \frac{1}{2}$ of the total area). Although this parameter was originally developed by economists to study wealth distribution, this parameter can be applied to understand the distribution of light in galaxies. If the distribution of light in galaxies is sequestered in relatively few bright pixels, the Gini coefficient approximately equals unity. The Gini coefficient is approximately equal to zero in galaxies in which the flux associated with each pixel is nearly equal amongst all pixels. In other words, the Gini coefficient quantifies how sharply peaked, or "delta−function"− like the flux in galaxies is. Note that this parameter can be affected by the "sky" surface brightness estimate assumed by the user, which I discuss in Addendum C1.

The M_{20} parameter is calculated with respect to the total second–order moment, M_{tot}, flux per pixel, f_j, which is defined as:

$$M_{tot} = \sum_{j}^{n} M_j = \sum_{j}^{n} f_j [(x_j - x_c)^2 + (y_j - y_c)^2], \tag{3.6}$$

such that:

$$M_{20} = log \left(\frac{\sum_j^n M_j}{M_{tot}} \right), \text{while} \sum_{j}^{n} f_j < 0.2 f_{tot}, \tag{3.7}$$

where M_j is the second–order moment at a pixel j, and (x_c,y_c) are the coordinates of the central pixel. In general, $-3 \lesssim M_{20} \lesssim 0$ (Lotz et al. , 2004, 2008; Holwerda et al. ,

2011). If considered jointly with the Gini coefficient, Lotz et al. (2004) determined that larger values of M_{20} (with correspondingly smaller values of G) are associated with "multiple ULIRG" galaxies, and that M_{20} is a better discriminant of merger signatures in galaxies.

I measure these five parameters—CAS and Gini– M_{20}—to quantify distinctions between the distribution of light, which underpins the classifications I first made in (§3.2).

3.3.1 Case–specific Implementation of Conventional Morphological Parameters

The authors of CAS and G–M_{20} (Conselice et al. , 2003; Abraham et al. , 2003; Lotz et al. , 2004, respectively) each defined a method to prepare images for analysis that accounts for systematic issues (e.g., compensating for bright or saturated cores of the galaxies). This method of image preparation and analysis also ensures that the parameters are measured for the galaxy itself, and that the contributions from non-galactic emission are minimized. In this analysis, I calculate all morphological parameters applying a functional form that is consistent with—or identical to—the form presented in the literature. However, I caution that the images and specific science goals require us to use an algorithm for image preparation and parameter measurement that differs slightly from the published methods. In this section, I outline key differences between the data and methods I used and those presented in the literature.

First, I measured these conventional parameters in images of galaxies observed at fundamentally different spatial resolutions (see §3.3.2). All galaxies in the catalog have been observed with HST WFPC2 at a pixel scale of $0.10''$ pix^{-1}. In contrast, CAS and Gini-M_{20} are often measured from images obtained with ground–based telescopes that have relatively low spatial resolution in comparison with HST. For example,

Frei et al. (1996) present images obtained with the Lowell 1.1 and Palomar 1.5 meter telescopes at $\sim 2.0''$ resolution at full–width half maximum (FWHM). This data set has been used extensively to test the CAS and Gini-M_{20} parameters' ability to discriminate between the morphological classes and star–formation histories of nearby galaxies (e.g., Conselice et al. , 2003; Lotz et al. , 2004; Hernández-Toledo et al. , 2006, 2008). The different spatial resolutions between ground-based images and HST implies that the parameters will measures features of fundamentally different size–scales. In ground-based images, the small–scale structure is, in fact, undetected. Thus, parameters that are dependent on the pixel–specific flux values (e.g., M_{20}), rather than on the average light distribution (e.g., concentration index), may be more sensitive to these spatial–resolution differences because at lower resolution fine–scale structure are effectively smoothed out. In Addendum A1, I quantify the effect of spatial resolution on these five parameters I used to characterize the structure of dust features in the Seyfert galaxies.

Furthermore, in Conselice et al. (2003) and Lotz et al. (2004), the CAS and Gini-M_{20} parameters are measured in an image that is truncated at the Petrosian radius. The Petrosian radius is defined as the radius (r_p) at which the ratio of the surface brightness at r_p to the mean surface brightness of the galaxy interior to r_p equals to a fixed value, typically η=0.2. A Petrosian radius or similar constraint is applied to differentiate between galaxy and sky pixels so that the latter are not included in the calculation of CAS and G-M_{20}. The mean Petrosian radius measured in the r′–filter (λ_0=6166Å) of Sloan Digital Sky Survey (SDSS) Data Release 7 of these galaxies is ∼4.3 kpc[5]. Since I am did not classify dust features located at radii greater than 1 kpc, I do not use images truncated at r_p. Furthermore, at the mean

[5]Only 28 galaxies in the catalog were observed in SDSS DR7, available online at `http://www.sdss.org/dr7`, but those galaxies common to the survey and SDSS span a range of morphologies and distances, hence I consider the measured mean Petrosian radius to be representative for the catalog.

redshift of the catalog, the WFPC2 PC chip field of view is $\lesssim$2.8 kpc.

Finally, unlike with observations of the entire galaxy, I can make the reasonable assumption that most of the observed flux in the core arises from sources or features physically associated with the galaxy. Not all pixels are sensitive to the flux arising from the galaxy, though, and I use the following method to differentiate between the light arising from galaxy sources and other extraneous objects or noise.

- I set all pixels that occur at the edges and the chip gaps between the WFC and PC CCDs in the mosaiced images equal to zero. Furthermore, the center of the galaxy is often much (10–100×) brighter than the rest of the galaxy, likely due to the AGN emission. To avoid such extremely bright pixels from biasing the measurement of any of the automated classification parameters, I set a high threshold defined as the average of the inner–most 5×5 pixels for each galaxy. I set the pixel values above this threshold equal to zero in the CAS & G–M_{20} computations.

- If the functional form of a parameter explicitly required a background term, I set this term equal to zero. This analysis is focused on the cores of each galaxy ($\sim$1 kpc; or less than $0.5\times r_p$), which are significantly brighter, and have high enough surface brightness, that the contribution of background objects can be considered to be minimal. I assume that the images include only light from the galaxy itself and background emission from the zodiacal (foreground) light, which arises from sunlight scattered off of $\sim$100μm dust grains. From the generally dark HST on-orbit sky, the zodiacal sky surface brightness is a simple well–known function of ecliptic latitude and longitude ($\ell^{Eq.}, b^{Eq.}$). The average on–board HST F606W–band zodiacal sky brightness can be found in Table 6.3 of the WFPC2 Handbook McMaster et al. (2008), but I use measurements of

the zodiacal background from WFPC2 archival images presented by Windhorst et al. (in prep.) to estimate the emission from this dust in the F606W band. The latter (see Figure 3.3) give a more accurate mapping as a function of $\ell^{Eq.}$ & $b^{Eq.}$ of the zodiacal background which could not be directly calculated from the images, because the galaxy core typically over–filled the CCD. I correct for the zodiacal foreground emission prior to image analysis in §3.3.2 and §3.4.1. For more details, see Addendum C1.

- To measure clumpiness, I included an additional processing step motivated by the algorithm defined in Hambleton et al. (2011). Prior to calculating the clumpiness parameter as defined in Conselice et al. (2003), we first applied a 5×5 pixel boxcar smoothing to the input image with a one–dimensional size of kernel defined as: $2.0 \times \frac{1}{6} \times \ell$, where ℓ is the dimension of the galaxy image in pixels. By design (see §3.1), the linear size of the smoothing kernel is equivalent to $\frac{4}{6}$ or ∼0.67 kpc. If I assume that 4 kpc is approximately equal to the Petrosian radius for each galaxy in the sample, then this dimension is comparable to the smoothing kernel size applied in Conselice et al. (2003) and Hambleton et al. (2011). I tested this assumption of an average Petrosian radius, and found that using a larger or smaller value ($\Delta = \pm$2kpc) for the linear dimension of the kernel has less than ∼1% effect on the measurement of clumpiness.I produced the residual map by subtracting the smoothed galaxy image from the original input image. In this analysis, I also set all pixels within 1.0″ of the galaxy center equal to zero.

In the subsequent analysis, I removed all zero–valued pixels to prevent those pixels from affecting the calculation of any of the parameters.

Though I use identical—or nearly identical—functional definitions of each morphological parameter used in the literature, I am analyzing regions of the galaxies at physical size–scales that are significantly different than have been used in previous research. As a result, I cannot assume that the parameter measurements are directly comparable to the CAS and G$-$M$_{20}$ conventional measurements in the literature (e.g., Conselice et al. , 2003; Lotz et al. , 2004). I therefore refer to the parameters that I derived using the above criteria hereafter as $C^*A^*S^*$ and G^*–M^*_{20}, in order to distinguish these measurements from the conventional parameters.

3.3.2 Analytical Results and Discussion

Figure 3.4 provides three permutations of the measured G^*–M^*_{20}–C^* parameters. Sy1 and Sy2 (circle and square symbols) galaxies are represented in blue and red, respectively. I use this color scheme in all figures to distinguish the measurements for the two classes of Seyfert galaxies. It is noteworthy that the distribution of each of these parameters spans a range that is comparable to the range of the G, M$_{20}$, and C measured from ground-based images at the lower spatial resolution; $0.7 \lesssim G^* \lesssim 0.1$, $-2.5 \lesssim M^*_{20} \lesssim -0.5$, $2.5 \lesssim C^* \lesssim 5.5$.

In Figure 3.4(a) I overplot a dashed line which Lotz et al. (2004) determined differentiates "normal" galaxies (which reside below this line) from starburst galaxies or ULIRGs (i.e., Ultra Luminous Infrared Galaxies). Four of the Seyfert galaxies are measured to be on or above this line: NGC1672, NGC4303, NGC4395, NGC7469. The fact that these galaxies reside in this parameter space is appropriate, since these four galaxies are considered to be starburst or circum-nuclear starburst galaxies in the literature. However, approximately 32% of the Seyfert galaxies in the catalog are classified as starburst or circum–nuclear starburst galaxies. Hence, I conclude that G^* and M^*_{20} do not effectively discriminate between "normal" and starburst galaxies, as

these parameters are demonstrated to do in the literature. Note that G-M_{20} are used to distinguish starburst and "normal" galaxies when the complete galaxy morphology is considered, thus the morphology of the complete galaxy need not necessarily match with the core morphology of the galaxies measured using $C^*A^*S^*$ and G^*–M_{20}^*.

I can consider the relative distribution of the G^*–M_{20}^* values measured for the AGN. In Figure 3.4(a), I fit a Gaussian function to the G^* and M_{20}^* distribution and measure the shape, centroid, and peak of this function for both Sy1 and Sy2 AGN to be comparable. The parameters of the fitted Gaussian function are provided in Table 3.3.

I draw similar conclusions from the distribution of $M_{20}^* - C^*$ and $C^* - G^*$ presented in Figure 3.4(b) and (c), respectively. First, C^* is well–distributed in the same parameter space spanned by the conventional concentration index, calculated for the entire galaxy at lower spatial resolution. I fit a Gaussian to the C^* distribution measured for Sy1 and Sy2 AGN, and measured comparable values for the centroid and FWHM of each distribution (Table 3.3).

I perform a two–sample Kolmogorov–Smirnov (K–S) for the Sy1 and Sy2 distributions to test whether these distributions are self–similar. The two–sample K–S test can be used to measure the likelihood that two empirical distributions were drawn as independent samples from the same parent distribution. I use the K–S test here for two reasons, in contrast to more commonly measured statistical parameters (e.g., the χ^2 statistic): 1) the sample size for each distribution is small, which can lead to an incomplete distribution over the measured range; and 2) I do not know the parent distributions—a priori—from which the empirical distributions were drawn. I use the IDL routine `kstwo` to measure the K–S statistic, d, which equals to the supremum distance between the cumulative distribution functions (CDF) of the input distri-

butions. `kstwo` also reports the probability statistic, p, which is the likelihood of measuring the same supremum in a random re-sampling of the parent distributions expressed by the empirical distributions. The K–S test cannot provide any insight into the parent distribution(s) from which the empirical distributions are drawn, but it can be used to test the null hypothesis that the empirical distributions were drawn from the same parent distribution. When the K–S statistic is small or the probability is large (p>0.05), the null hypothesis cannot be rejected with confidence.

The results of the K-S test for the M_{20}^* and G^* parameter distributions are provided in Table 3.3. These distributions are indistinguishable for both Seyfert classes. However the K-S test measures a slightly larger values of d=0.38 for the distribution of C*, indicating that the CDFs are distinct. The associated probability statistic for C^* is small (p=0.01). I conclude that the C^* distributions measured for Sy1 and Sy2 are significantly different, and thus are likely to be drawn from unique independent parent distributions. This could support the morphological distinction between the cores of Sy1 and Sy2 galaxies that was identified by visual inspection in §3.2. In contrast, if G^*-M_{20}^* are indeed sufficiently robust metrics for distinguishing the distribution of light in the cores of these Seyfert galaxies, then the results of the K-S test suggest that these parameters do not quantitatively distinguish the galaxy morphologies of Sy1 and Sy2 AGN.

In comparison with C^*—which, in effect, measures the isophotal brightness (i.e., azimuthally averaged) of the host galaxy, the A^* (asymmetry) and S^* (clumpiness) parameters are relatively better-suited, in principle, to measure the effect of the presence of relatively small-scale, spatially stochastic dust absorbers on the observed stellar light profile of the galaxy's core. These parameters are not sensitive to "pixel-by-pixel" variations, but by design they are more sensitive to the smaller-scale variations in the light profile that occurd due to local absorbers. In the Figure

3.5(a)&(b), I consider the A^*&S^* distributions for the sub-classes of AGN, independently. I did not calculate asymmetry for NGC1058, NGC1386, NGC1672, NGC3486, NGC4051, NGC4303, NGC4395, and NGC4698, because the WFPC2 images of these galaxies included off-chip regions that were set to zero (see §3.3.1). These regions can seriously affect these measurements because asymmetry is calculated by differencing a rotated image with the original. The best-fit Gaussian function to each distribution are provided in Table 3.3. The Gaussians' parameters measured for Sy1 and Sy2 galaxies appear to be indistinguishable. I confirm this via a two-sample K-S test. The results of this test are presented in Table 3.3. I conclude from this test that both A^*&S^* distributions are likely drawn from the same parent distribution.

The uniformity in the C^*, A^*, S^*, & G*-M$^*_{20}$ distributions also suggests that the Hα+[NII] emission arising from the photo-ionization of gas (see §3.2) does not strongly affect the measurement of these parameters. Furthermore, if the A^* and S^* parameters are suitable metrics for quantifying the morphology of galaxies, then the results of this quantitative analysis do not support the correlation between core dust morphology and Seyfert class established by MGT98 and confirmed by the visual inspection in §3.2.

In conclusion, four of the five quantitative parameters (A^*, S^*, G^*, and M^*_{20}) measured for the galaxies do not support the qualitative conclusions developed from visual inspection. The distribution of C^* may be specific to the class of AGN, which could support the MGT98 relationship, but this parameter is the least- suited, in principle, for use in quantifying the morphological distinctions that supported the morphology-AGN class correlation. In Chapter 6, we extend the discussion of this parameter specfically, considering the results of Addendum A1, but here we conclude that, considerin in whole, these results do not support the MGT98 relationship.

3.4 Quantitative Morphology with Source Extractor

The results of the previous analysis could imply that $C^*A^*S^*$ & G^*-M^*_{20} parameters are insufficient as tools to distinguish the sub-kiloparsec scale features in AGN, rather than providing an effective test of the qualitative MGT98 relationship. To test this possibility, I develop additional non-parametric technique that uses Source Extractor (hereafter, SE Bertin & Arnouts , 1996) to measure the distribution of dust features in the cores of AGN host galaxies.

SE is an automated object detection software package that generates photometric object catalogs. This software is widely used for photometry and star/galaxy separation in UV-optical-IR images partly due to the software's speed when applied to large image mosaics. A review of the literature returns more than 3000 citations to Bertin & Arnouts (1996), with applications extending even beyond astrophysics (e.g., medical imaging of tissue cultures by Tamura et al. , 2010). The versatility of SE to detect and measure aperture photometry for galaxies motivated us to adapt SE for these purposes. In this study, I use SE only for object detection, because the algorithm I outline (§3.4.1) and apply (§3.4.2) may prevent accurate photometry.

SE has often been used in the study of nearby, dusty galaxies (see recent work by Kacprzak et al. , 2012; Holwerda et al. , 2012, for example). This research does not employ SE to directly detect and measure the properties of the absorbers. Rather, SE is used to derive the photometric properties of galaxies, and these data are coupled with the dust properties of the galaxy (e.g., covering fraction). In §3.4.1, I adapt SE to directly detect dust features that are visible to the eye. Thus, the use of SE to outline the characteristics of dust features that are fundamentally seen in absorption is a unique application of this software.

3.4.1 Technical Implementation to Identify Dust Features

In this Section, I outline the manner in which I used SE to identify dust features. To detect these objects, SE first calculates a local background, and determines whether each pixel contains flux is above a user-defined threshold, `detect_thresh`. All pixels exceeding this threshold are grouped with contiguous pixels that exceed this threshold. When a sufficient number (defined by the `detect_minarea` parameter) of contiguous pixels are found to meet the signal threshhold, the pixel group is recorded as an object in the object catalog. Finally, SE measures a variety of parameters (e.g., object center, total flux, size, orientation), and constructs a segmentation map of detected objects.

To detect objects corresponding to the visually detected dust features in the cores of the galaxies, it was necessary to first train SE using the WFPC2 images of the Seyfert host galaxies. Initially, I used the HLA image of each galaxy—appropriately cleaned of defects as detailed in §3.1—for object detection. After extensive testing, I could not determine a suitable combination of the parameters `detect_minarea` and `detect_thresh` that would force SE to identify a set of comparable objects to the set of dust features that I visually identified in §3.2. By setting `detect_thresh` low enough that nearly all visually identified dust features are recovered, too many of these features were broken into multiple unique objects. To alleviate this over-segmentation, I increased the `detect_minarea` parameter. In order to recover the majority of the visually identified dust features though, this parameter must be set unfavorably high; dust features were only detected when they were included as a component of a much larger, brighter object.

Direct detection of dust features with SE is difficult. This can be directly attributed to the manner by which SE detects objects. SE is designed to detect

peaks above the local background. In the images, the local background is bright, and not likely to be smooth because it arises from the ambient stellar background and not the astronomical/zodiacal sky. Furthermore, SE can not detect many of the dust features as they are observed in absorption with respect to the local background. These absorption features may be brighter than the true astrophysical background, but they are still fainter than the local background.

I therefore trained SE to identify objects that more closely matched with dust features identified (§3.2) by coupling object detection using SE with the "unsharp-mask" technique. The unsharp-mask is a common tool for image analysis, because it enhances features of specific spatial scales. In astronomical images, these features correspond to physical objects, such as stars, star clusters, and/or dust clouds. To apply this procedure, I first convolved the WFPC2 images with a Gaussian kernel to create a smoothed image. Next, I divided the convolved image by the original image to produce the inverse unsharp-mask image (hereafter, IUM)[6]. In principle, if we appropriately define the convolution kernel such that it enhances structures of specific size-scales corresponding to dust features and apply the IUM, those features should now be detected as a positive signal above the local background using SE with the appropriate detection parameters. In Figure 2.6, I provide an illustration of this technique. In Figure 2.6a&2.6b I show the core image of NGC3081 and a surface map of an inter-"arm" region. I convolved the image with a kernel (Figure 2.6c), and apply the IUM technique to produce Figure 2.6d. In this figure, it is apparent that the dust features in the region of interest have been enhanced by the IUM technique.

To produce the IUM image of each galaxy, I first assumed that giant molecular clouds (GMCs) are physically associated with dust features. To produce the appro-

[6]The unsharp-mask image is typically produced by either differencing or dividing the original image by the convolved image. When the contrast between the original and the convolved image is small, as it is in the WFPC2 images, these two different calculations yield similar results.

priate convolution kernel for each galaxy, I used the galaxy's redshift from NED to define a physical pixel scale (s_p; pixel kpc^{-1}) of the kernel. The linear size scale of GMCs is typically less than 100 pc (see Casoli, Combes, & Gerin , 1984; Fukui & Kawamura , 2010), so I defined the FWHM of the kernel equal to ℓ/s_p, initially with ℓ=100 pc. I tested a range of size scales, and determined that ℓ=80 pc optimally enhanced the sub-kiloparsec scale dust features that I visually identified in §3.2. I also determined the appropriate linear size of the kernel to be equal to X/10, where X is the length of each image axes in pixels.

I determined optimal SE parameters by an iterative process to find the segmentation map that most faithfully reproduced the dust features classified in §3.2. In this process, I fixed the SE parameter `detect_minarea` equal to $90.0/s_p$ for all objects. I required `detect_thresh` for each object pixel to be at least 1.5σ above the local sky-background in the IUM image. Additionally, I determined that the default values for the SE parameters `deblend_nthresh` and `deblend_mincont` equal to 32, and 0.03, respectively, were sufficient for dust feature detection in the IUM image.

I discuss the results of implementing this method using the optimized parameters in §3.4.2. The algorithm I have outlined above for the detection of dust features in absorption in images is generic. It is not applicable exclusively to these specific scientific interests. Thus, I have prepared all IDL procedures that I developed to implement this technique for the public. Readers who wish to apply this method to other science topics are encouraged to email the corresponding author.

3.4.2 Results and Discussion

In Figure 3.6, I presented a four-panel mosaic of 12 galaxies including the WFPC2 galaxy core image and its corresponding SE segmentation map. The first panel of these images was discussed in §3.2.

To produce the second image in Figure 3.6, I reproduced the segmentation images in DS9 using the built-in "SLS" color map[7]. This 256-bit "rainbow" color map (including black and white) allows the users' to better distinguish between different detected objects. However, when the total number of detected objects $N_t \gtrsim 40$, even this color map is insufficient to distinguish between all unique neighboring sources. As a result, many unique objects may appear as the same color, although these are not necessarily detected as the same physical object. This limitation of the color map does not affect the calculation of N_t. For most galaxies the segmentation maps show a number of objects near the edge of the image. Although some of these edge detections may be related to real dust features, I excluded these edge detections in the subsequent analysis and discussion.

A comparison of the segmentation map and the galaxy core images suggests that the general SE technique is remarkably successful in recovering only those dust features that I identified first by visual inspection. Specifically, the dust feature recovery rate using the IUM technique is very good for the majority (>95%) of the catalog. For example, bar and spiral arm-like features are well-recovered as unique objects (see, e.g., MARK1330). The fidelity of the object detection of the spiral arm features is often high enough in these galaxies (see, e.g., NGC3081) that the spiral arm features in the image are entirely reproduced in the corresponding segmentation map.

Galaxies with relatively many dust features—in both regular or chaotic spatial distributions—also appear to be faithfully reproduced in their associated segmentation maps. For example, the regular structures in NGC1068 and NGC1066 are detected with SE as are the more chaotic dust features, as seen in ES0137-634 and ESO323-G77. An interesting result of this IUM analysis is that the objects in some

[7] more details are available online at http://hea-www.harvard.edu/RD/ds9/

galaxies (e.g., NGC1386, NGC1672) are sometimes limited to particular quadrants of what appears to be a disk in the original image. The distribution of dust features suggests to the eye that this disk (in which the features are embedded) is moderately inclined towards the viewer. A discussion of the inclination effect of the molecular toroid are beyond the scope of this work, but I will consider this result in future work. I note that this possible disk inclination was identified first and only by using the SE technique. In images where the stellar light profile is exceptionally smooth and few dust features are identified by visual inspection, the IUM technique may detect objects that do not strongly correlate with the dust features visually identified in §3.2. This may represent a limitation of the IUM technique. In Figure 3, I included the images of two galaxies (NGC1058 and NGC3608)[8] that represent this small fraction ($< 5\%$) of the catalog galaxies. I do not remove these galaxies from the subsequent analysis for completeness and to illustrate to the reader instances when the SE technique may be limited in its ability to discern visually identified dust features. I caution that object detection in these few galaxies using the IUM technique may be more sensitive to local pixel-to-pixel noise variations than it is to signal variations arising from dust absorption.

In some galaxies, the possible photo-ionization structure appears to be the brightest structure visible in the image (see §3.2). Variations in the mean signal across these structures could affect the calculation of the local sky background with SE, and thus influence dust feature detection in those galaxies with possible photo-ionization emission structures. For example, such variations could explain the segmentation of what appears as one chaotic dusty region into two approximately equal area dust features along the outer edge of the northeastern "spiral-arm" photo-ionization structure

[8]Only four galaxies—MARK348, MARK352, NGC1058, NGC3608—showed any strong distinction between the number, size, and spatial distribution of objects detected with SE segmentation map and dust features noted by visual inspection in §3.2.

in NGC3393. But, in general, it does not appear that such structures have strongly affected the dust feature detection as the number and distribution of dust features still appears to be very well-correlated with the visually-identified dust features.

I also provided in Figure 3.6 two measurements of the characteristics of the dust structure quantified with the IUM technique. I plot the cumulative number of objects for each galaxy contained within circular annuli centered at each galaxy's core for a radius r_c, where $r_c = n \times \Delta r$ and Δr=2.0 pixels. Although I present square images of the galaxy, I only calculate the cumulative number for annuli with radii less than 1 kpc in the frame to remove edge detections. Using the cumulative object number distribution, I calculate a half-object radius (r_{half}) defined as the radius (in pixels units) of the annulus that contains the inner 50% of the total number of detected objects in each galaxy. This value is provided in physical units (parsecs) with measurement uncertainties in Table 3.2.

In Figure 3.7(a) I plot the distributions of r_{half}. I fit a Gaussian function to the distribution of r_{half} for Sy1 and Sy2 galaxies and provide the parameters of the best-fit functions in Table 3.4. There is no apparent distinction in the distribution of half-object radii between Sy1 and Sy2 galaxies. This is confirmed by a two-sample K-S test, the results of which indicate that the parent distributions from which the half-object radii distribution were drawn are not likely to be unique.

Figure 3.6 also includes the object surface density distribution (Σ) measured for the galaxies, which I defined as :

$$\Sigma = \log\left(\frac{N}{4\pi(\mathrm{r_2} - \mathrm{r_1})^2}\right) \tag{3.8}$$

where N is the number of objects contained within annuli of width equal to 10 pixels. I fit a linear function to the object surface density function versus radius and measure the best-fit slope (α). In Figure 3.7b, I provide the distribution of α measured. I

fit a Gaussian function to the distribution of α as measured for the two classes of AGN, and measure the Gaussian centroids and FWHM to be nearly equal (Table 3.4). The similarity in the distributions is confirmed by a two-sample K-S test. Thus, the distribution of the object surface density functions does not appear to be unique to the class of AGN.

In Figure 3.8a, I plot the number of objects (N_t) identified in each galaxy. I measure the centroid and half-width half maximum (HWHM) of both the Sy1 and Sy2 distributions (see Table 3.4). I fit a Lorentzian function, rather than a Gaussian function, to better account for the broad extension from the HWHM peak to large object numbers in the N_t distribution. The centroid of the best-fit Lorentzian function of objects equals to $\sim$18 for both classes of AGN, but the mean value of the Sy1 and Sy2 distributions equals to 47 and 35, respectively. Thus, these distributions appear to be significantly different. I confirm this result via a two-sample K-S test:I measure d=0.35 and p=0.01, and conclude the empirical distributions of N_t measured for the Sy1 and Sy2 galaxies are likely drawn from independent parent distributions. If the objects detected with SE physically correspond to dust features in the galaxies, then I conclude that Sy2 galaxies are, on average, dustier than Sy1 galaxies. If I remove the four galaxies discussed above for which the SE technique did not appear to detect objects that are closely associated with the dust features that I identified by visual inspection, though, I measure the K-S test probability statistic for the distributions of N_t equal to p=0.06. In this case, I can not reject the null hypothesis, and instead am forced to conclude that the distributions of N_t measured for Sy1 and Sy2 galaxies were likely drawn from the same parent population.

MGT98 did not consider the number of dust features explicitly, but the assignment of relative degrees of dustiness to galaxies implicitly reflects the number of dust features that were identified visually. In principle, it is easier to visually classify

the dust structure as "irregular" if it contains many dust features, because patterns and divergences are more readily identifie. Thus, the mean N_t measured for Sy1 and Sy2 (Figure 3.8a) may support, indirectly, the MGT98 relationship.

In Figure 3.8b and 3.8c, I also provide the covering fraction (f_c) and the average number of pixels (N_p) associated with objects detected by SE. I fit a Gaussian function to the distributions measured for each of these parameters, and observe no distinction between the centroid or FWHM measured for Sy1 and Sy2 (see Table 3.4). I confirm the similarity between the measured distributions by a K-S test, and conclude that these distributions are likely drawn from the same parent distribution. These results would not support the MGT98 relationship, or at least not demand it.

Throughout this work I have considered the results of this analysis only in the context of the Unified Model, as outlined in Antonucci et al. (1993). I restricted the discussion of these results to this context, in part, because I was motivated in this work to extend the analysis first presented in Malkan, Gorjian and Tam (1998), in which the authors make a similar assumption on the nature of AGN. The assumption of this model is still fair; despite extensive debate the Model provides a remarkably robust explanation for the observed diversity of AGN[9]. But this model is not without rivals. For example, the "clumpy torus" model reduces the thick, dusty torus—the inclination of which gives rise to the observed dichotomy of Seyfert-type AGN—to distinct individual dust clumps that are generally distributed about the central engine. In this model, the AGN type that one observes is not a "binary" function of perspective; rather, the probability of observing a Type 1 AGN decreases as the viewer moves towards an "edge-on" perspective but never reaches zero. I observe a core region that is hundreds of parsecs beyond the toroid, though. Thus, a full

[9]If only because many of the systematic considerations of the Unified Model are still, regrettably, limited by large measured uncertainties; cf. Guainazzi et al. 2011

interpretation of these results in the context of this model is beyond the scope of this project and I reserve that discussion for future work.

3.5 Addendum A1. Spatial Resolution: Ground vs. Space-based imaging

I have implicitly assumed throughout this paper that HST images are necessary to conduct the quantitative morphological analyses. If lower spatial resolution ground-based optical images could be used instead of the high spatial resolution HST images, I could significantly increase the number of galaxies reviewed. The SDSS archive, for example, would provide images of hundreds of local AGN.

I downloaded SDSS r′ images for 7 AGN that were in both the SDSS DR7 archive and the catalog presented in §3.1. I made thumbnails of the core (r <1 kpc) SDSS images of each galaxies and measured C^*, A^*, and S^* parameters using the same techniques outlined in §3.3.1 for each galaxy. In Figure 3.9, I compare these measurements with those presented in §3.3 which were measured in HST F606W images. It is apparent from this comparison that A^* and S^* cannot effectively discriminate between the morphologies of the SDSS galaxies. This result confirms that the quantitative morphological analysis I performed above requires the high spatial resolution HST images.

3.6 Addendum B1. Size-Scale Relation

Two galaxies that are identical (e.g., morphology), but at different distances from an observer, will appear different in images obtained with the same telescope, because each CCD pixel covers an intrinsically larger physical area in the more distant galaxy. As a result, the dust features in the more distant galaxy are less well-resolved spatially. The catalog includes galaxies in the range between $0.001 < z < 0.015$, or equivalently a factor of 10-15 in physical distance.

I selected six galaxies—NGC1068, NGC3185, NGC3227, NGC3608, NGC4725, NGC4941—with galaxy morphologies representative of those included in the catalog. These galaxies are all at distances $\simeq$ 15 Mpc, and I use these galaxies to quantify the extent to which I am able to identify or measure dust features in the catalog galaxies as a function of distance. I do not use the nearest galaxies ($D \lesssim 10$Mpc) in the catalog because these galaxies include large off-chip regions that significantly affect the measurement of asymmetry.

I rebinned each of these galaxies to a pixel scale, s, such that :

$$s = \ell_{GAL} \times \frac{D_{GAL}}{D_{z=0.015}}, \tag{3.9}$$

where ℓ is number of WFPC2 0.10″ pixels spanning 1000 pc at the physical distance, D, to the galaxy and $D_{z=0.015}$ corresponds to the distance to a galaxy at the upper redshift range of galaxies in the catalog (63 Mpc).

I measure C^*, A^*, S^* and G^*-M^*_{20} for these artificially-redshifted galaxies and compare the measured values with the original measurements (§3.3.2). This comparison is presented in Table 3.5 as $\delta = \frac{|X-Y|}{Y}$, where X and Y are the morphological parameters measured in galaxy images at D_{gal} and artificially redshifted to $D_{z=0.015}$.

In general, the measurement of these parameters does not seem to be strongly affected by the relative distance of the galaxy, at least over the relatively small redshift range that I consider in this project. For all parameters, δ is much smaller than the measured dispersion in the range of parameters measured in §3.3.2. I conclude that range of measured parameters (see Figures 3.4 and 3.5) are indicative of morphological distinctions between the cores of the sample galaxies, as I assumed in the discussion in §3.3.2.

3.7 Addendum C1. Sensitivity of measurements to the estimated sky-background

Windhorst et al. (in prep.) measured the surface brightness of the zodiacal background as function of $\ell^{Eq.}$ & $b^{Eq.}$ from 6600 archival WFPC2 F606W and F814W dark-time images. I reproduce these measurements for the F606W zodiacal background from Windhorst et al. (in prep.) in Figure 3.3. Originally, in §3.3.1, I estimated the surface brightness of the zodiacal background along the line-of-sight to each galaxy in the catalog, made the reasonable assumption that the only background emission present in the galaxy cores arises from the zodiacal background, and then corrected for this background alone in each image.

In this section, I measure the uncertainty in the measurements of $C^*A^*S^*$ and G^*-M^*_{20} and the object surface density distribution associated with the assumption of the surface brightness of the background in the images. In general, I determine that the brightness of the background has a minimal effect on the parameters' measurement, with the notable exception of G^*, and to a lesser extent the slope α parameters. In Figure 2.10, I compare the measurements of G^* for galaxies corrected for a zodiacal background equal to: a) zero (G^*_a); b) the Windhorst et al. background (G^*_b); and c) a hypothetical background 10 times larger than the measured in Windhorst et al. The latter estimate of the background emission is highly unlikely in any HST image (see Figure 3.3). I assume such a large background here only to provide an upper extremum to the measurement of the effect of the background surface brightness assumption.

The dispersion measured for most parameters, i.e., C^*, A^*, S^* and M^*_{20}, for different estimates of the zodiacal surface brightness was small (<1%). There is a large dispersion between G^*_a and G^*_c. I attribute this dispersion to the removal of relatively faint pixels from the measurement of G^* as increasingly larger values for

the sky surface brightnesses are subtracted from the images. This has the net effect of (artificially) enhancing the flux associated with relatively higher signal pixels, which increases G^*.

I measure a modest increase ($< 5\%$) in the measurement of α (the slope of the object surface density function), when comparing cases (a) and (c). Hence, adopting the most likely zodiacal sky-brightness as a function of $\ell^{Eq.}$ & $b^{Eq.}$—when this background is not directly measurable—is an acceptable and, in this case the only viable, approach.

3.8 Addendum D1. IUM Technique: Dust Feature Detection Threshold

The detection of dust features with SE is explicitly dependent on the detection parameters defined by the user in the configuration file. Here I discuss the typical contrast level of the dust features, relative to the "sky background" in the images, which SE detected for those parameters outlined in §3.4.1. I define the "contrast" as:

$$\text{Contrast} = \frac{f_{dust} - f_{meansky}}{f_{dust} + f_{meansky}} \times 100\%, \tag{3.10}$$

where f_{dust} is the flux associated with a detected object using the IUM technique and $f_{meansky}$ is the average sky value measured in a uniform "sky" region drawn from the core image.

I measured the contrast parameters for two representative galaxies in the sample, NGC3081 and NGC3608. The IUM technique appears to work very well in detecting the dust clumps in NGC3081, whereas NGC3608 was largely devoid of dust clumps according to the visual inspection. For each of these galaxies, I measured the contrast values for three detected dust clumps, using two relatively large but smooth "sky" regions (Area$\simeq$100-200 sq. pixels). The mean contrast, ($f_{dust} = \bar{f}$, the average

flux associated with the dust feature) measured for NGC3081 and NGC3608 equals 6 and 2%, respectively. Assuming f_{dust} equal to the flux of the brightest pixel in each of the dust features, the mean contrast is measured to 12% and 4% for the two galaxies. I measure the relative height of the mean flux associated with the dust features above the mean sky equal to 50-90$\times\sigma_{sky}$ for NGC3608 and NGC3081, respectively. I note the fainter sources could be detected if the SE detection parameters are revised, but this would introduce more "false positive" dust feature detections and fragment coherent visible structure.

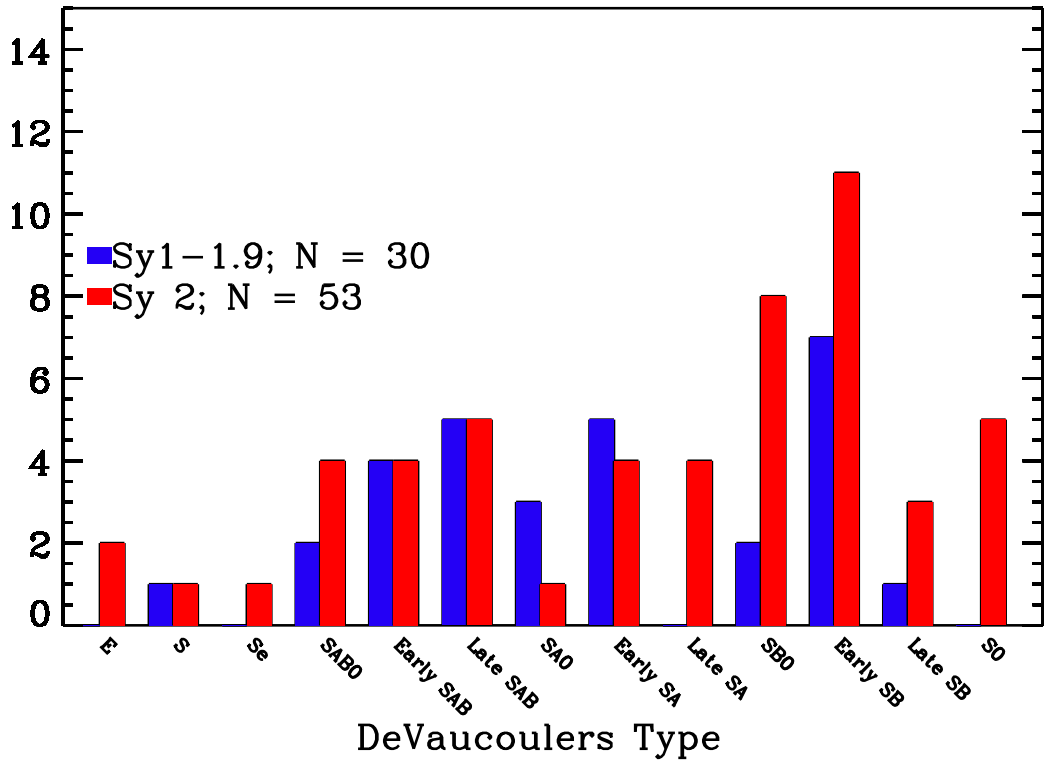

Figure 3.1: The distribution of galaxy morphologies compiled from NED. Two Sy1 AGN were not classified in NED. Though these galaxy morphologies are defined for the entire galaxy—not the core region which I am investigating —the similarity of these distributions confirms that that any distinction that we draw between these classes of AGN is not likely to be attributed to the galaxy morphology. Furthermore, neither class of AGN is biased to a particular class of galaxy, nor am I biased generally by the selection criteria towards fundamentally less-dusty galaxy types (i.e., early-type galaxies).

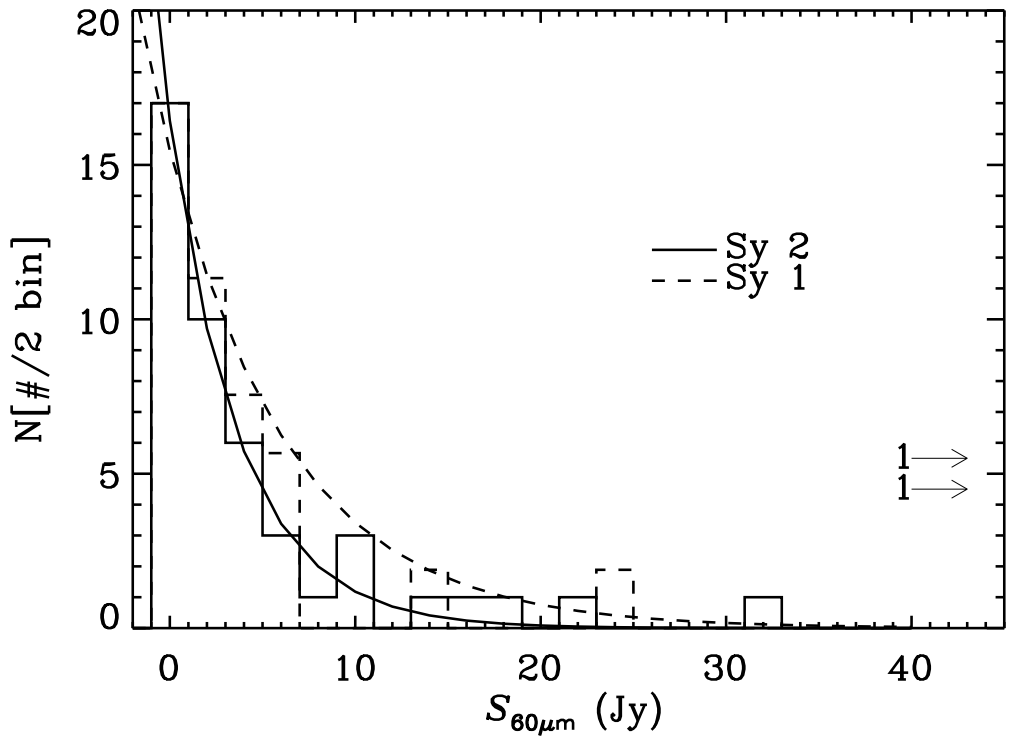

Figure 3.2: The FIR flux distribution of the catalog Seyfert galaxies from the IRAS Faint Source catalog (available via NED). The Sy1 distribution has been scaled to match the peak in the Sy2 distribution and both samples each had one AGN with measured FIR flux greater than 40 Jy (illustrated by arrows). I fitted an exponential function ($\propto exp[-f/\tau]$), where τ=3.8 & 6.7 for Sy1 and Sy2, respectively. I did not select Seyfert AGN on the basis of their FIR properties, but the samples appear to be generally similar, with the caveat that the sample has a known bias towards Sy2 AGN.

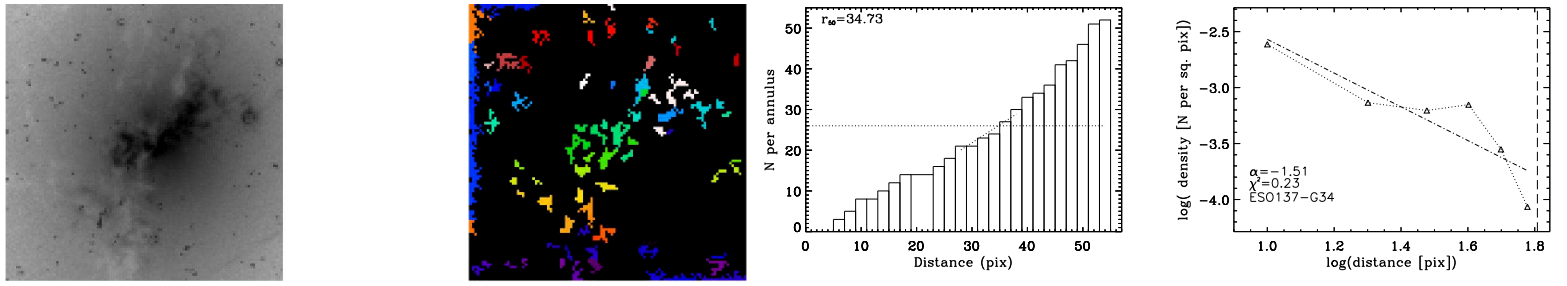

a.ESO137-G34

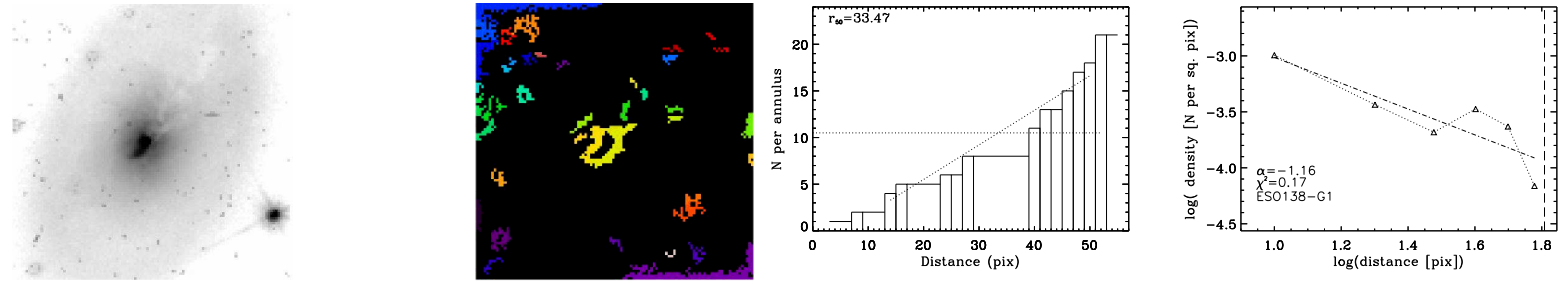

b.ESO138-G1

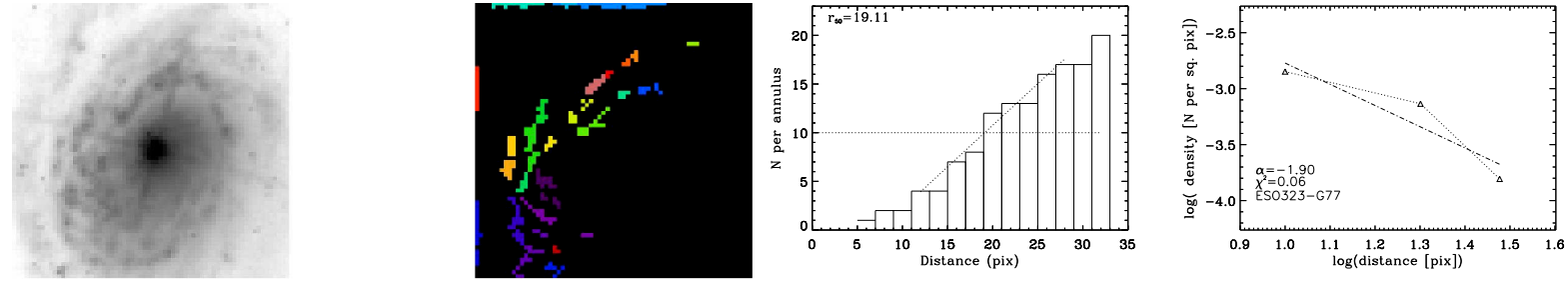

c.ESO323-G77

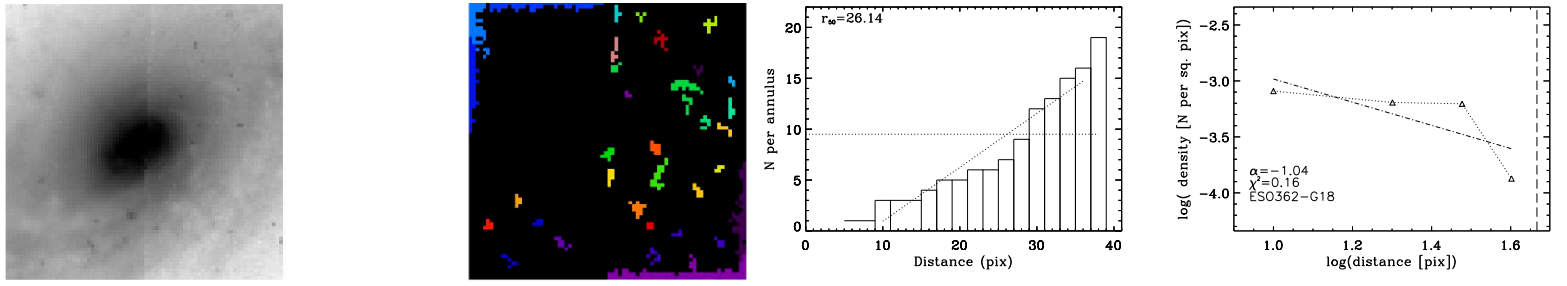

d.ESO362-G18

Fig 3(a.-d.): From left to right, I provide the WFPC2 F606W postage-stamp image of the catalog galaxy that was used to classify galaxy morphology qualitatively (§3.2) and quantitatively (§3.3 and §3.4). I have re-scaled the sizes of these images only for publication; full scale fits images are available on request. In the center-left panel, the segmentations maps that were generated using the inverse unsharp-mask method (§3.4.1) are provided. In the center-right panel, the cumulative number function of objects and the half-object radius as well as the object surface density (right panel), defined as the number of objects per annulus and the best-fit slope α. I discuss each of these data products at length in §3.4.2. Data for all galaxies is available in Appendix A.

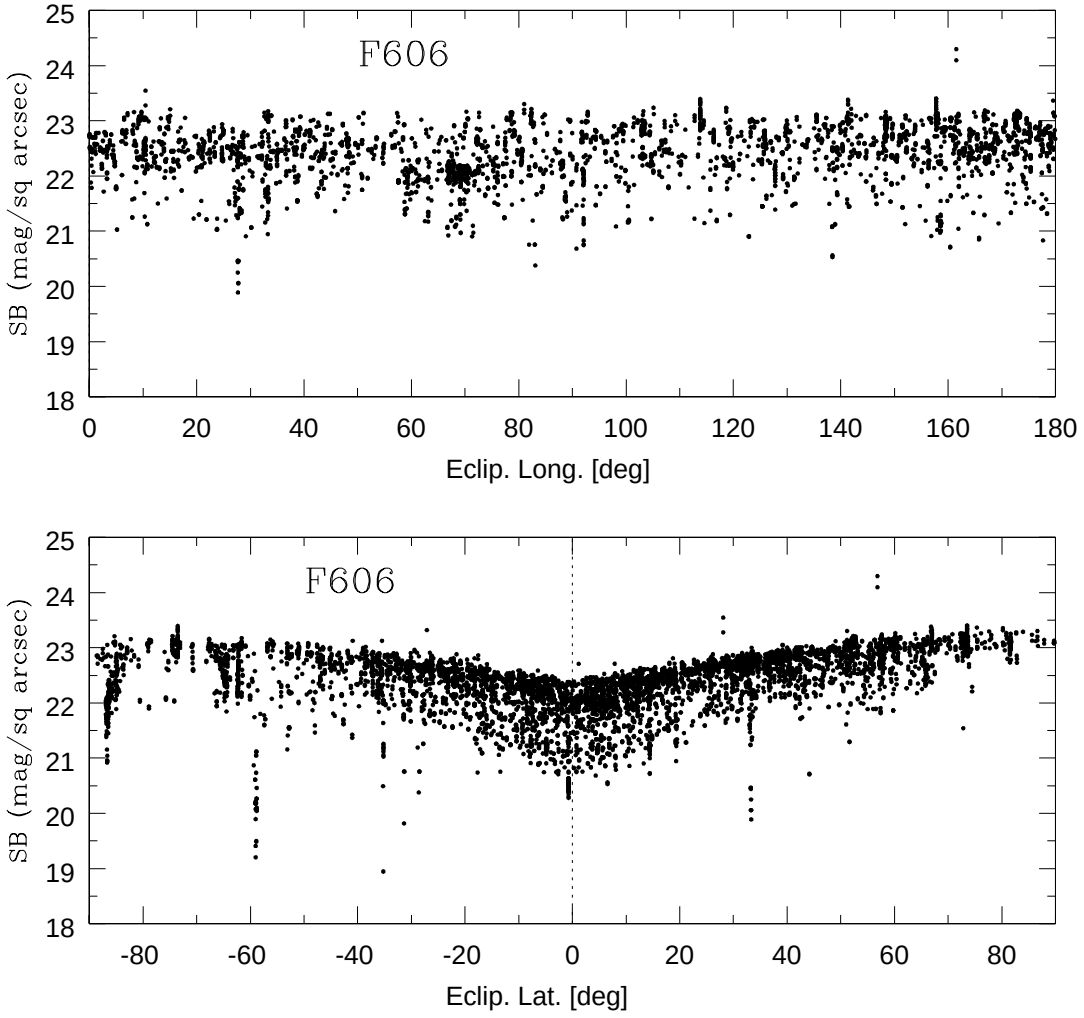

Figure 3.3: Windhorst et al. (in prep.) measured the surface brightness of the zodiacal background as a function of ecliptic latitude and longitude using ∼6600 dark-orbit, archival F606W WFPC2 images. I estimate the surface brightness of the zodiacal background along the line-of-sight to the catalog galaxies, and correct for this zodiacal emission by subtracting the background from the core image in §3.3.1.

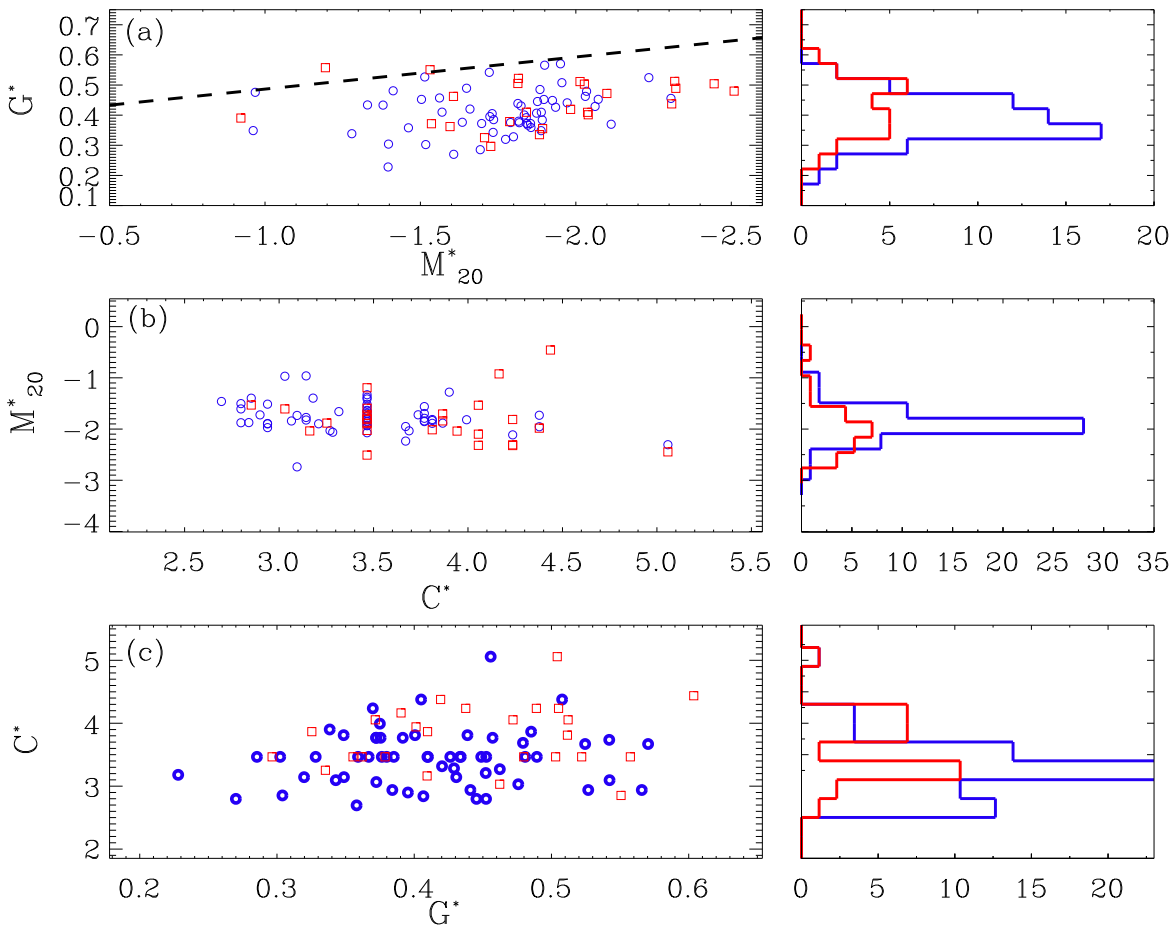

Figure 3.4: The C^*, G^*, & M^*_{20} parameters were defined in §3.3. Here, I plot the measured parameters for Sy1 and Sy2 AGN as blue circles and red squares, respectively. In (a), I overplot the empirically (Lotz et al. , 2004) defined that distinguished "normal" galaxies from Ultraluminous Infrared Galaxies (ULIRGs), but find that this line does not strongly differentiate starburst-type galaxies from "normal" galaxies. The distributions of each of these parameters appear indistinguishable for Sy1 and Sy2 (see §3.3.2 for more details). I confirm this with a two-sample Kolmogorov-Smirnov test. The measured K-S parameter is large for both the G^* and M^*_{20} distribution (d=0.28 and 0.29, respectively), but the associated probabilities are also both large (p=0.09 and 0.08). Therefore, I can not reject the null hypothesis that both distributions are drawn from unique parent distributions. However, the K-S test for the distribution of C^* does suggest that the measured distributions for Sy1 and Sy2 AGN are drawn from unique parent distributions (d=0.38 and p=0.01).

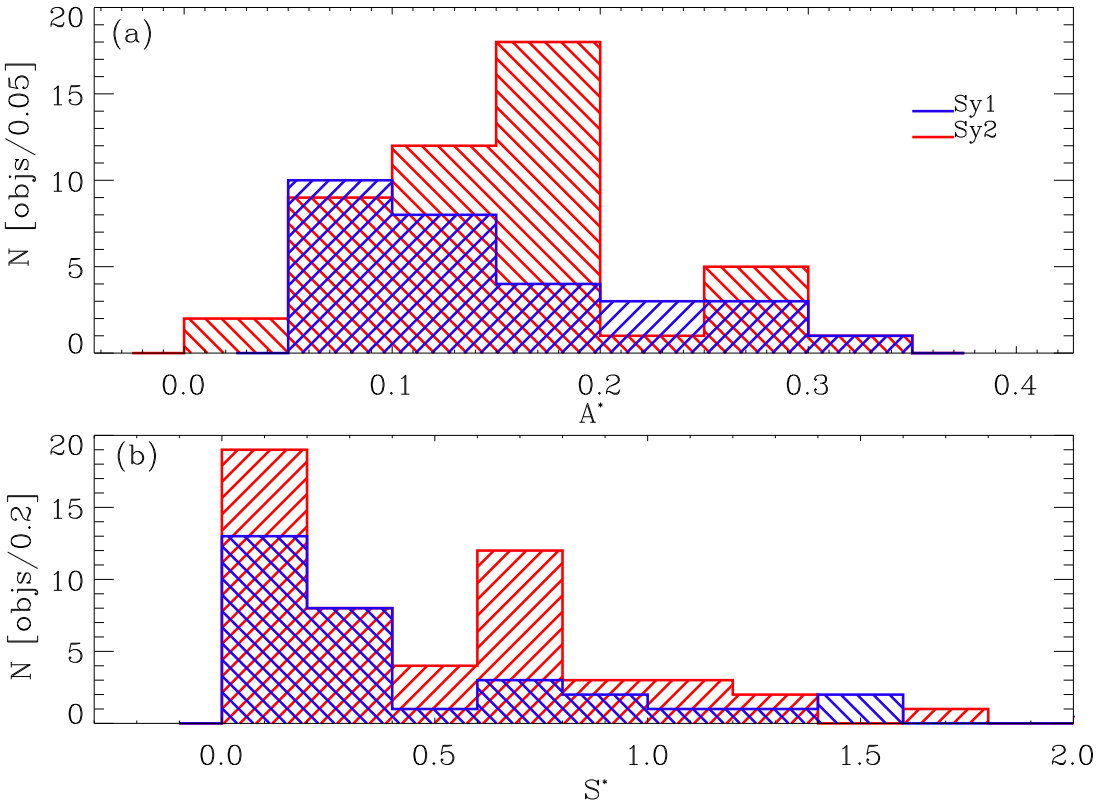

Figure 3.5: The distribution of A^* and S^*, the non- parametric measure of asymmetry and clumpiness (as defined in §3.3) measured for the AGN. I fit a Gaussian function to each distribution, and measure the centroids and FWHM of these distributions—the distributions appear indistinguishable. The results of a K-S test confirms that the two distributions are not independent.

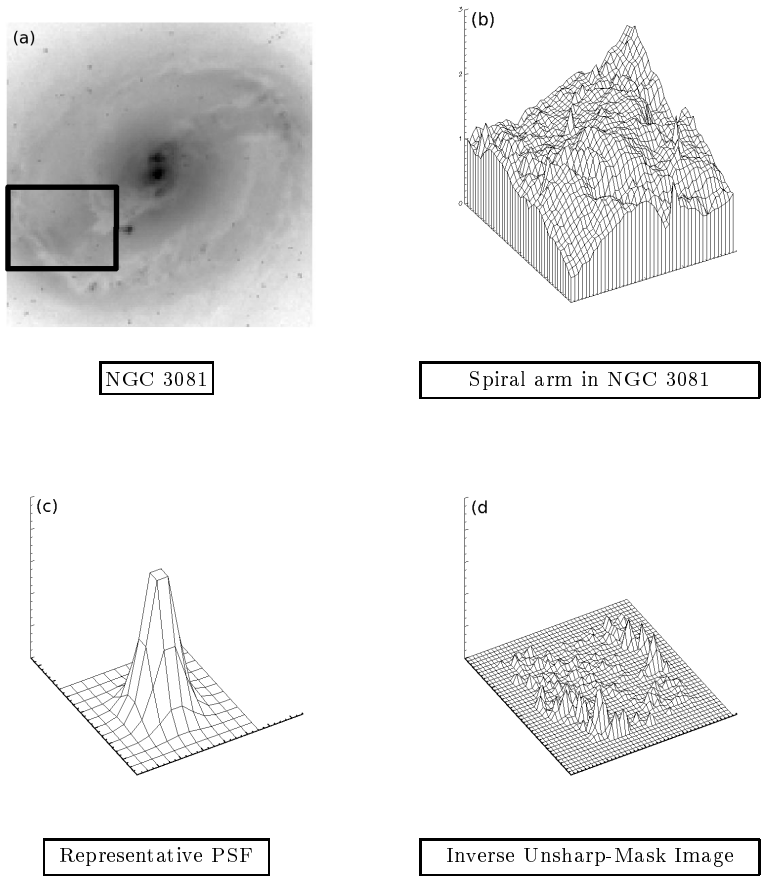

Figure 3.6: A cartoon representation of the inverse unsharp- mask technique (see §3.4.1) for detecting absorption of stellar light by dust and clumpy structures along the line- of- sight. In panel (a), the 2kpc × 2kpc postage stamp of NGC3081 is provided; here, gray indicates relatively high signal. The thick black square in this figure emphasizes a spiral arm and inter-arm region with interesting dust features and morphology. A surface map of this region is provided in panel (b); the arm is indicated by the deficit in signal (i.e., a "trough" extending in an arc from East to West). To produce the inverse unsharp-mask image, I smoothed image (a) with a representative kernel (panel c) and divided the convolved image by the original image. In panel (d), I provide the unsharp-mask surface map of the region in panel (b). It is apparent in panel (d) that the signal associated with the spiral arm region where dust absorption was most significant in panel (a) is now sufficiently high above the background to be detected using SE defined with an appropriate detection threshold.

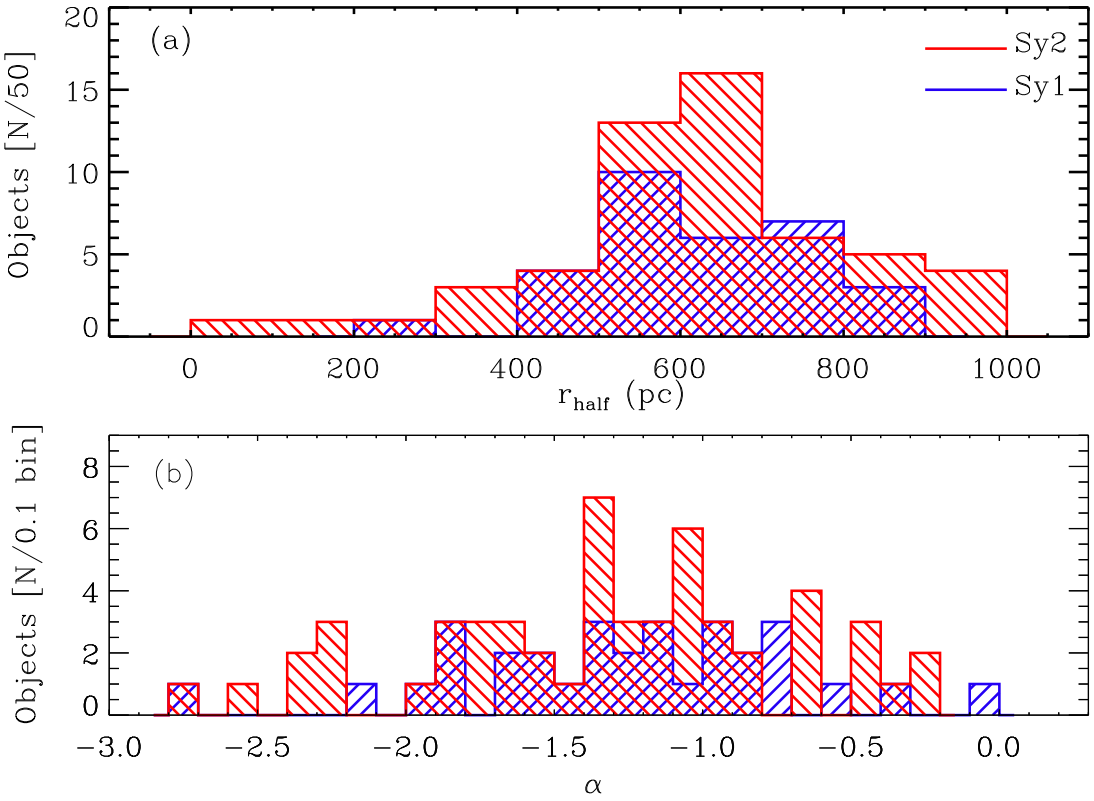

Figure 3.7: The distribution of the best-fitting exponential slopes, α, to the object surface density profile and the half object radii of objects or features measured for objects in all Sy1 and Sy2 galaxies detected by SE using the IUM technique (see §3.4.1). I fit Gaussian functions to each of the distributions, and the results of a K-S test confirms that the parents distribution from which the distributions were drawn are likely to be the same. This suggests that there is no significant difference between the azimuthally-averaged spatial distribution of objects, and thus the distribution of dust features for the Sy1 and Sy2 populations appears to be indistinguishable.

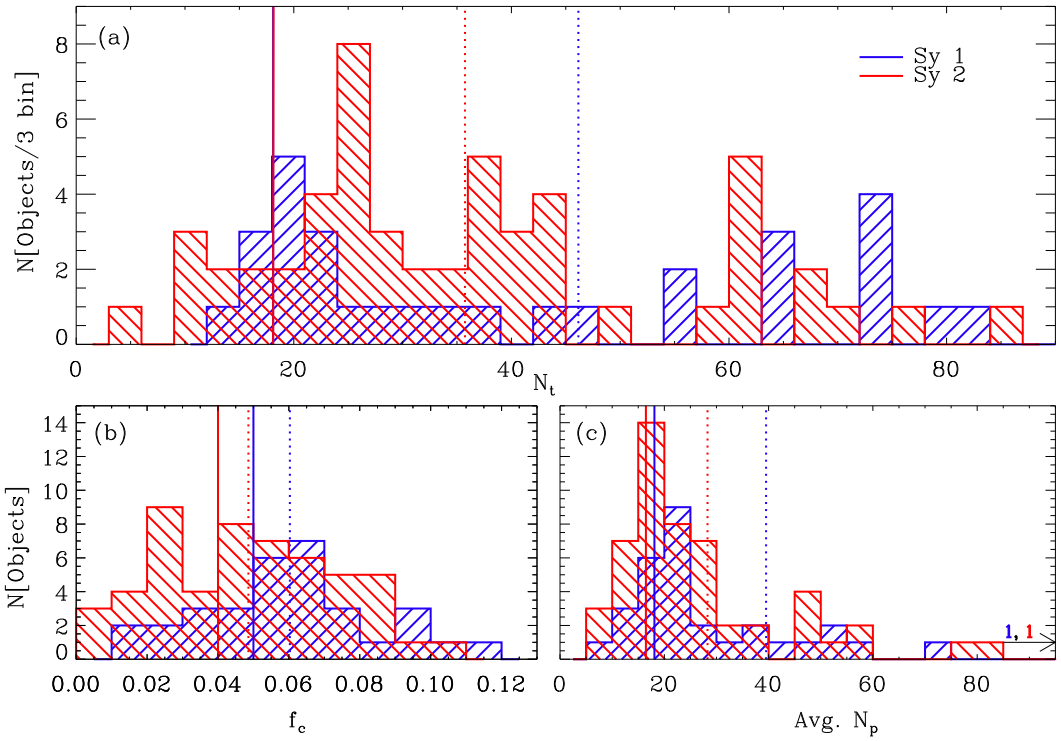

Figure 3.8: The relative distributions of three statistics derived from the quantitative morphological technique discussed in §3.4.1. Panel (a)[Top]: The number of dust features, N_t, detected in the core of each Seyfert galaxy. Panel (b): The distribution of covering fraction f_c of dust features in the sample as defined in §3.4.2. f_c equals to the fraction of the total core image area to the area associated with detected objects. In general, Sy1 and Sy2 host-galaxies cover similar fractions of area of the host galaxy core. Panel (c): The distribution of the average number of pixels N_p (i.e., object area= $N_p \times 0.1''^2$; see §3.4.2). Two galaxies (1 Sy1 and 1 Sy2) were detected with $N_p > 90$ objects, indicated by the arrow. In all panels, vertical dotted and solid lines indicate the mean and centroid (measured from the best-fitting Gaussian, or Lorentzian function to each distribution) of the distributions. The parameters of these fits, as well as the results of the two-sample Kolmogorov-Smirnov tests of these distributions, are provided in Table 3.4. Only for the distribution of total object number N_t does the K-S test suggest that the empirical distributions were not drawn from a common parent population.

Table 3.1: AGN-Host Galaxy, General Catalog

ID[a]	Alt. ID[b]	R.A. (J2000)	Decl.(J2000)	Distance[c]	Sy. Type	ϵ	NED Class
ESO103-G035	IR1833-654	18h38m20.3s	-65d25m39s	55.1	2.0	0.63	S0?
ESO137-G34	—	16h35m14.1s	-58d04m48s	37.8	2.0	0.21	SAB0/a?(s)
ESO138-G1	—	16h51m20.1s	-59d14m05s	37.8	2.0	0.50	E?
ESO323-G77	—	13h06m26.1s	-40d24m53s	62.3	1.0	0.33	(R)SAB0^0(rs)
ESO362-G008	—	05h11m09.0s	-34d23m35s	51.5	2.0	0.50	S0?
ESO362-G018	—	05h19m35.8s	-32d39m28s	65.4	1.0	0.33	SB0/a?(s) pec
ESO373-G29	—	09h47m43.5s	-32d50m15s	38.6	2.0	0.46	SB(rs)ab?
FRL312	IC3639	12h40m52.9s	-36d45m21s	45.2	2.0	0.00	SB(rs)bc?
FRL51	ESO140-G043	18h44m54.0s	-62d21m53s	58.8	1.0	0.43	(R')SB(s)b?
IR1249-131	NGC4748	12h52m12.5s	-13d24m53s	65.2	1.0	0.06	···
IR0450-032	PGC16226	04h52m44.5s	-03d12m57s	60.7	2.0	0.30	···
MARK352	—	00h59m53.3s	+31d49m37s	61.7	1.0	0.50	SA0
MARK1066	UGC02456	02h59m58.6s	+36d49m14s	49.8	2.0	0.41	(R)SB0^+(s)
MARK1126	NGC7450	23h00m47.8s	-12d55m07s	43.9	1.5	0.00	(R)SB(r)a
MARK1157	NGC0591	01h33m31.3s	+35d40m06s	63.0	2.0	0.23	(R')SB0/a
MARK1210	Phoenix	08h04m05.9s	+05d06m50s	56.0	1.0	0.00	S?
MARK1330	NGC4593	12h39m39.4s	-05d20m39s	37.2	1.0	0.25	(R)SB(rs)b
MARK270	NGC5283	13h41m05.8s	+67d40m20s	43.0	2.0	0.09	S0?
MARK3	UGC03426	06h15m36.4s	+71d02m15s	56.0	2.0	0.11	S0?
MARK313	NGC7465	23h02m01.0s	+15d57m53s	27.0	2.0	0.33	(R')SB0^0?(s)
MARK348	NGC0262	00h48m47.1s	+31d57m25s	62.4	2.0	0.00	SA0/a?(s)
MARK620	NGC2273	06h50m08.7s	+60d50m45s	25.3	2.0	0.21	SB(r)a?
MARK686	NGC5695	14h37m22.1s	+36d34m04s	58.5	2.0	0.28	S?
MARK744	NGC3786	11h39m42.6s	+31d54m33s	36.9	1.8	0.40	SAB(rs)a pec
MARK766	NGC4253	12h18m26.5s	+29d48m46s	53.6	1.5	0.20	(R')SB(s)a?
NGC1058	—	02h43m30.0s	+37d20m29s	7.10	2.0	0.06	SA(rs)c
NGC1068	MESSIER077	02h42m40.7s	-00d00m48s	15.6	2.0	0.15	(R)SA(rs)b
NGC1125	—	02h51m40.3s	-16d39m04s	45.2	2.0	0.50	(R')SB0/a?(r)
NGC1241	—	03h11m14.6s	-08d55m20s	56.0	2.0	0.39	SB(rs)b
NGC1358	—	03h33m39.7s	-05d05m22s	55.7	2.0	0.23	SAB0/a(r)
NGC1365	—	03h33m36.4s	-36d08m25s	22.5	1.5	0.44	SB(s)b
NGC1386	—	03h36m46.2s	-35d59m57s	11.9	2.0	0.61	SB0^+(s)
NGC1566	—	04h20m00.4s	-54d56m16s	20.6	1.0	0.20	SAB(s)bc
NGC1667	—	04h48m37.1s	-06d19m12s	63.0	2.0	0.22	SAB(r)c
NGC1672	—	04h45m42.5s	-59d14m50s	18.2	2.0	0.16	SB(r)bc
NGC2110	—	05h52m11.4s	-07d27m22s	32.1	2.0	0.23	SAB0^-
NGC2336	—	07h27m04.1s	+80d10m41s	30.3	2.0	0.45	SAB(r)bc
NGC2639	—	08h43m38.1s	+50d12m20s	46.0	1.9	0.35	(R)SA(r)a?
NGC2985	—	09h50m22.2s	+72d16m43s	18.1	1.9	0.21	(R')SA(rs)ab
NGC3081	—	09h59m29.5s	-22d49m35s	32.9	1.9	0.23	(R)SAB0/a(r)

AGN-host galaxies (Continued)

AGN-Host Galaxy, (Continued)

ID	Alt. ID	R.A.(J2000)	Decl.(J2000)	Distance	Sy. Type	ϵ	NED Class
NGC3185	—	10h17m38.6s	+21d41m18s	16.7	2.0	0.49	(R)SB(r)a
NGC3227	—	10h23m30.6s	+19d51m54s	15.8	1.5	0.33	SAB(s)a pec
NGC3393	—	10h48m23.5s	-25d09m43s	51.8	2.0	0.09	(R')SB(rs)a?
NGC3486	—	11h00m23.9s	+28d58m30s	9.34	2.0	0.26	SAB(r)c
NGC3516	—	11h06m47.5s	+72d34m07s	36.5	1.5	0.23	(R)SB0^0?(s)
NGC3608	—	11h16m59.0s	+18d08m55s	17.2	2.0	0.18	E2
NGC3718	—	11h32m34.9s	+53d04m05s	13.6	1.0	0.50	SB(s)a pec
NGC3783	—	11h39m01.8s	-37d44m19s	40.2	1.0	0.10	(R')SB(r)ab
NGC3982	—	11h56m28.1s	+55d07m31s	15.2	1.9	0.11	SAB(r)b?
NGC4051	—	12h03m09.6s	+44d31m53s	9.61	1.0	0.25	SAB(rs)bc
NGC4117	—	12h07m46.1s	+43d07m35s	12.8	2.0	0.63	$S0^0$?
NGC4303	MESSIER061	12h21m54.9s	+04d28m25s	21.5	2.0	0.10	SAB(rs)bc
NGC4378	—	12h25m18.1s	+04d55m31s	35.2	2.0	0.06	(R)SA(s)a
NGC4395	—	12h25m48.9s	+33d32m49s	4.37	1.8	0.16	SA(s)m?
NGC4477	—	12h30m02.2s	+13d38m12s	18.6	2.0	0.07	SB0(s)?
NGC4507	—	12h35m36.6s	-39d54m33s	48.9	2.0	0.23	(R')SAB(rs)b
NGC4639	—	12h42m52.4s	+13d15m27s	13.9	1.0	0.32	SAB(rs)bc
NGC4698	—	12h48m22.9s	+08d29m15s	13.8	2.0	0.37	SA(s)ab
NGC4725	—	12h50m26.6s	+25d30m03s	16.5	2.0	0.28	SAB(r)ab pec
NGC4939	—	13h04m14.4s	-10d20m23s	42.9	2.0	0.49	SA(s)bc
NGC4941	—	13h04m13.1s	-05d33m06s	15.2	2.0	0.47	(R)SAB(r)ab?
NGC4968	—	13h07m06.0s	-23d40m37s	40.8	2.0	0.52	(R')SAB0^0
NGC5135	—	13h25m44.1s	-29d50m01s	56.8	2.0	0.30	SB(s)ab
NGC5273	—	13h42m08.3s	+35d39m15s	14.6	1.5	0.06	$SA0^0$(s)
NGC5347	—	13h53m17.8s	+33d29m27s	32.1	2.0	0.23	(R')SB(rs)ab
NGC5427	—	14h03m26.1s	-06d01m51s	36.1	2.0	0.14	SA(s)c pec
NGC5643	—	14h32m40.7s	-44d10m28s	16.4	2.0	0.13	SAB(rs)c
NGC5929	—	15h26m06.2s	+41d40m14s	34.3	2.0	0.21	Sab? pec
NGC5953	—	15h34m32.4s	+15d11m38s	27.0	2.0	0.14	SAa? pec
NGC6221	—	16h52m46.1s	-59d13m07s	20.6	1.0	0.28	SB(s)c
NGC6217	—	16h32m39.2s	+78d11m53s	18.7	2.0	0.16	(R)SB(rs)bc
NGC6300	—	17h16m59.5s	-62d49m14s	15.2	2.0	0.33	SB(rs)b
NGC6814	—	19h42m40.6s	-10d19m25s	21.4	1.5	0.06	SAB(rs)bc
NGC6890	—	20h18m18.1s	-44d48m24s	33.3	1.9	0.20	SA(rs)b
NGC6951	—	20h37m14.1s	+66d06m20s	19.5	2.0	0.17	SAB(rs)bc
NGC7213	—	22h09m16.3s	-47d10m00s	24.0	1.0	0.09	SA(s)a?
NGC7314	—	22h35m46.2s	-26d03m02s	19.6	1.9	0.54	SAB(rs)bc
NGC7410	—	22h55m00.9s	-39d39m41s	24.0	2.0	0.69	SB(s)a
NGC7469	—	23h03m15.6s	+08d52m26s	67.8	1.0	0.26	(R')SAB(rs)a
NGC7496	—	23h09m47.3s	-43d25m41s	22.6	2.0	0.09	SB(s)b
NGC7590	—	23h18m54.8s	-42d14m21s	21.6	2.0	0.62	SA(rs)bc?
NGC7682	—	23h29m03.9s	+03d32m00s	71.3	2.0	0.08	SB(r)ab
NGC7743	—	23h44m21.1s	+09d56m03s	23.5	2.0	0.13	(R)SB0^+(s)

AGN-host galaxies (Continued)

AGN-Host Galaxy, (Continued)

ID	Alt. ID	R.A.(J2000)	Decl.(J2000)	Distance	Sy. Type	ϵ	NED Class
NGC788	—	02h01m06.4s	-06d48m56s	56.4	1.0	0.26	SA0/a?(s)
TOL0109-383	NGC0424	01h11m27.6s	-38d05m00s	48.7	2.0	0.55	(R)SB0/a?(r)

Notes- [a]: Object ID; [b]: NED preferred object ID; [c]: in Mpc using WMAP Year-7 cosmology (Komatsu et al. , 2011).

Table 3.2: AGN-Host Galaxy, Morphological Catalog

ID[a]	Morpho. Class A	Ancillary Class.	Morpho. Class B	α (χ^2)	Half Object Radius
IR1833-654	DI,F/W	B	2,3il	−0.45(0.21)	967.53±54.17
ESO137-G34	DI,DC	CL	3im	−1.51(0.23)	927.31±37.47
ESO138-G1	D-NW	—	3im	−1.16(0.17)	612.37±37.45
ESO323-G77	F/W	R,CL	1,3s	−1.90(0.06)	350.03±61.09
ESO362-G18	D-SW,DC,F/W	R	3sm	−1.04(0.16)	789.24±64.02
ESO362-G8	DC,DI	—	3il	−0.40(0.00)	···
ESO373-G29	DI,D-NE,F/W	B	3il	−0.69(0.22)	823.03±38.28
FRL312	DC,F/W	B	2,3im	−0.94(0.31)	562.27±44.66
FRL51	DI	CL	3il	−2.14(0.07)	392.60±57.75
IR1249-131	DC,F/W	R,CL	3sl	−0.93(0.06)	589.14±59.56
IR0450-032	DC	R	3im	−2.52(0.49)	604.99±63.79
MARK352	—	E/S0	—	−1.45(0.28)	296.90±60.49
MARK1066	F/W	B,CL	2,3sm	−2.25(0.19)	688.47±49.10
MARK1126	DI,F/W	B,R	2,3il	−1.14(0.32)	821.58±43.45
MARK1157	DI,F/W,D-NE	B,R	2,3sl	−1.09(0.00)	533.15±61.70
MARK1210	F/W	CL,R	3sl	−0.81(0.67)	919.57±55.01
MARK1330	F/W,DC	R	3sm	−1.53(0.24)	879.67±36.88
MARK270	F/W,D-S,DC	B	3sl	−1.38(0.19)	474.55±42.56
MARK3	DI,D-NE	B,CL	2,3im	−1.36(0.26)	817.55±55.07
MARK313	DI,DC,F/W	B,CL	3im	−1.54(0.73)	935.46±26.98
MARK348	F/W	—	3sl	−1.68(0.38)	646.81±61.17
MARK620	F/W,DI,D-N,	B,R,CL	3sm	−1.46(0.35)	551.32±25.24
MARK686	D-W,DC,F/W	—	3sm	−2.40(0.42)	485.03±57.41
MARK744	DI,DC	R,CL	3sl	−1.36(0.33)	528.30±36.61
MARK766	DI	—	3il	−1.97(0.54)	727.96±52.74
NGC1058	F/W,DI	CL	1,3s	−0.90(1.28)	699.35±7.144
NGC1068	F/W,DI	CL	1,3sm	−0.22(0.85)	855.87±15.64
NGC1125	DC,D-SW,DI	—	3im	−1.36(0.19)	592.58±44.69
NGC1241	DC,F/W	CL,R	3sm	−1.72(0.00)	535.62±55.09
NGC1358	DC,DI	—	3il	−1.62(0.24)	594.62±54.77
NGC1365	DC,F/W	CL	3im	−1.23(0.94)	620.82±22.46
NGC1386	D-NW,F/W,DC	—	1,3sm	−1.08(0.39)	543.61±11.95
NGC1566	F/W,DC	R	3sm	−1.00(0.22)	715.97±20.66
NGC1667	F/W,DC	—	3sl	−2.34(0.46)	641.56±61.70
NGC1672	F/W,DC	CL	1,3sm	−1.68(2.35)	558.84±18.29
NGC2110	F/W,DC,DI,D-N	—	1,3sm	−0.96(0.12)	566.33±31.96
NGC2336	DI	E/S0	3il	−0.83(0.31)	794.94±30.19
NGC2639	F/W,DC,D-NE	B	3im	−1.34(0.02)	513.96±45.49

AGN-host galaxies (Continued)

AGN-Host Galaxy, (Continued)

ID[a]	Morpho. Class A	Ancillary Class.	Morpho. Class B	α (χ^2)	Half Object Radius
NGC2985	F/W,DC	—	3s	−0.37(0.91)	718.04±18.17
NGC3081	DI,F/W	B,R,CL	1,2,3sm	−1.20(0.49)	738.19±32.72
NGC3185	DC,DI	R	3i	−1.99(0.08)	132.99±16.73
NGC3227	DI,DC	—	3il	−0.87(0.27)	549.46±15.91
NGC3393	F/W,DI,DC	B,CL	2,3sm	−2.27(0.04)	472.74±51.05
NGC3486	F/W,DI	R,CL	1,3sl	−0.65(2.00)	764.01±9.387
NGC3516	DI	—	3il	−1.55(0.04)	474.70±36.22
NGC3608	—	E/S0	—	−0.70(0.30)	851.63±17.23
NGC3718	DI,DC,D-SW	—	3im	−1.37(0.82)	492.53±13.66
NGC3783	DI	E/S0	3il	−1.70(0.21)	610.91±39.84
NGC3982	F/W,DI	R,CL	1,3sm	−0.02(0.69)	508.14±15.25
NGC4051	DC,DI	—	3im	−0.96(0.64)	800.02±9.650
NGC4117	DI,F/W,DC	R	3im	−0.25(1.14)	683.86±12.85
NGC4303	F/W	R	1,3sm	−1.77(1.28)	391.61±21.50
NGC4378	DI	—	3i	−1.70(0.17)	465.32±35.00
NGC4395	—	CL	—	−1.36(5.03)	526.02±4.402
NGC4477	DC,D-E	—	3il	−1.24(0.21)	540.95±18.62
NGC4507	D-S,DI	—	3im	−1.80(0.39)	592.75±48.20
NGC4639	F/W	B	2,3sl	−0.71(0.58)	793.61±14.00
NGC4698	DI	E/S0	3i	−1.02(0.48)	664.53±13.88
NGC4725	DI	E/S0	3il	−0.93(1.41)	743.22±16.58
NGC4939	D-W,F/W	B	2,3im	−1.15(0.16)	697.48±42.44
NGC4941	D-E,DI	—	3il	−0.49(1.08)	863.44±15.24
NGC4968	DC,F/W,D-NE	—	3im	−1.35(0.09)	609.44±40.38
NGC5135	DI	R,CL	3sm	−2.72(0.38)	578.57±55.80
NGC5273	F/W,DC,DI	—	3il	−1.87(0.79)	212.56±14.64
NGC5347	F/W,DI	R	3im	−0.44(0.35)	792.55±31.96
NGC5427	F/W	R,CL	1,3sm	−1.83(0.26)	789.46±35.80
NGC5643	F/W	CL	1,3sl	−1.18(1.25)	663.69±16.48
NGC5929	DC,DI	—	3il	−1.06(0.09)	667.89±34.09
NGC5953	F/W	CL	1,3sm	−1.32(1.63)	667.67±26.94
NGC6217	DI,DC	CL	3sm	−1.09(0.16)	694.41±20.58
NGC6221	DI,DC,D-SE	CL	3il	−0.78(0.21)	624.49±18.71
NGC6300	DI,D-SW	CL	3im	−1.08(0.20)	714.21±15.25
NGC6814	F/W,DC	B	2,3sl	−0.74(0.25)	585.77±21.46
NGC6890	F/W	CL	1,3sm	−1.11(0.37)	767.87±33.10
NGC6951	DI,F/W	R,B,CL	2,3sm	−1.38(0.67)	545.79±19.56
NGC7213	F/W	—	3sl	−1.22(0.26)	620.10±24.02
NGC7314	D-E,DC,F/W	—	3im	−0.58(0.29)	580.60±19.62
NGC7410	DC,F/W,D-NW	—	3im	−1.81(0.07)	450.93±24.03
NGC7469	F/W	R,B,CL	3sm	−2.75(0.07)	519.75±66.29
NGC7496	DC,DI,D-NW	CL	3im	−1.28(0.36)	641.13±22.63

AGN-host galaxies (Continued)

AGN-Host Galaxy, (Continued)

ID[a]	Morpho. Class A	Ancillary Class.	Morpho. Class B	α (χ^2)	Half Object Radius
NGC7590	F/W,D-NW	CL	3im	$-1.28(0.27)$	684.94 ± 21.63
NGC7682	DI	CL	3i	$-2.25(0.32)$	691.53 ± 69.57
NGC7743	F/W	—	3il	$-0.68(0.34)$	557.79 ± 23.47
NGC788	F/W,D-S	—	3sl	$-1.86(0.35)$	415.99 ± 55.44
TOL0109-383	D-SE,F/W	—	3im	$-1.87(0.46)$	668.87 ± 48.05

Notes- Combined results from qualitative and quantitative analyses are provided.
Cols.2-3:Morphological classifiers were adopted from Malkan, Gorjian and Tam (1998) and are defined as follows: Class A–F/W=Filaments/Wisps; DI=Irregular Dust; DC= dust lane passing close to, or bisecting, center; D-[direction]=dust lanes on one side of major axis. Ancillary–B=bar; CL=cluster, lumpy H II region, knots; E/S0=Elliptical; R=ring. I do not use the "Normal" classifier. For details, 3.2.
Col 4.: Class B–Classifiers defined to specifically characterize the dust morphology dust morphology in the cores of galaxies: 1:"Nuclear Spiral"; 2:"Bar"; and 3: "Dust Specific Notes" –s or i:"spiral" or "irregular" & m or l: "High" or "Low Extinction". The full description of the classifiers is provided in §3.2
Col. 5: Slope (α) of best–fit line to the object surface density profile defined in §3.4.2 Reduced χ^2 is provided in parantheses.
Col. 6: Half-Object Radius (pc) with uncertainty. Here "$\cdots$" indicates that a galaxy had an insufficiently few objects to measure the radius accurately.

Table 3.3: Morphology Comparison I: C^* A^* S^* & G^*–M_{20}^* Technique

Morpho.	Sy1		Sy2		K-S Test	
Param.	Centroid	FWHM	Centroid	FWHM	d	p
G^*	0.39	0.26	0.42	0.35	0.28	0.09
M_{20}^*	-1.89	0.74	-2.01	1.24	0.29	0.08
C^*	3.15	1.27	3.57	2.01	0.38	0.01
A^*	0.08	0.08	0.12	0.09	0.09	0.99
S^*	0.08	0.13	0.066	0.13	0.19	0.91

Notes- The parameters of the best–fit Gaussian function to the distribution of morphological parameters measured forSy1 and Sy2, respectively, are provided here. For more details and a discussion of the implications of these results in the test of the Unified Model, see §3.3.

Table 3.4: Morphology Comparison II: SE Technique

Morpho.	Sy1		Sy2		K-S Test	
Param.	Centroid	FWHM	Centroid	FWHM	d	p
α	-1.27	0.79	-1.30	0.88	0.14	0.69
r_{half}	570	226	572	195	0.33	0.43
N_t	18	4	18	15	0.35	0.01
f_c	0.05	0.04	0.04	0.05	0.37	0.16
N_p	18	7	16	11	0.12	0.98

Notes- The parameters of the best–fit Gaussian function to the distribution of morphological parameters measured forSy1 and Sy2, respectively, are provided here. The HWHM value is provided for N_t because a Lorentzian, Lorentzian, not a Gaussian, function was fit to the measured distribution of this parameter. For more details and a discussion of the implication of these results in the test of the Unified Model, see §3.4.1.

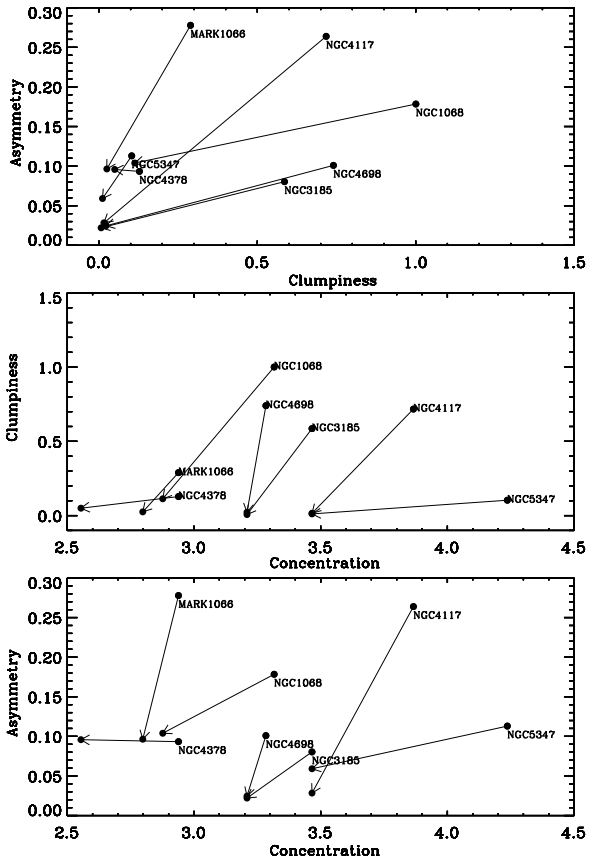

Figure 3.9: $C^*A^*S^*$ measured for the core (r<1kpc) of 7 AGN using HST F606W and SDSS r′ images. Line segments connect the measured values for each galaxy, and the vector points away from the parameter value measured from the HST image.

Table 3.5: Distance Dependence

Parameter	δ
G^*	1.5%
M^*_{20}	0.8%
C^*	10.9%
A^*	2.2%
S^*	14.1%

δ quantifies the dispersion of the parameter at native and artificially redshift spatial resolution. See Addendum B1 for details. The parameters of the best–fit Gaussian function to the distribution

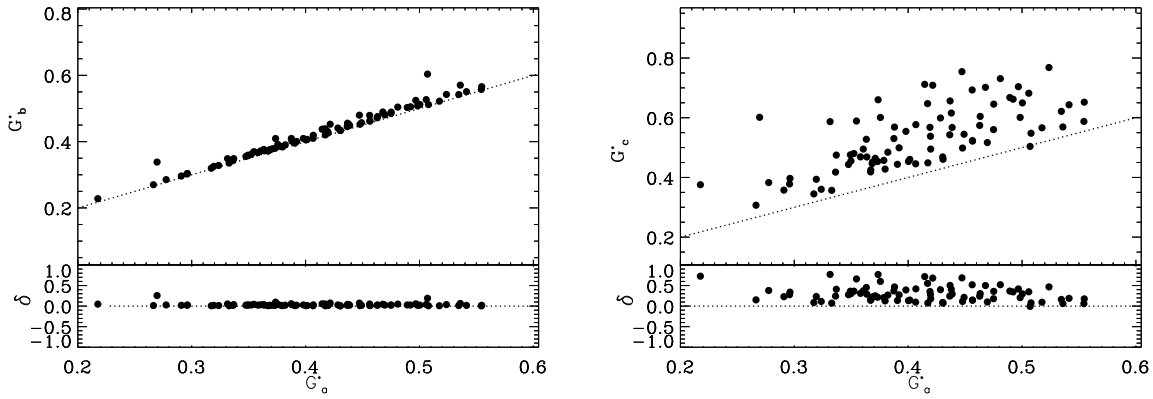

Figure 3.10: Parameter robustness to sky background (see Addendum C1). G^* was measured for the galaxies in images produced for three assumptions of the zodiacal background surface brightness equal to : (1) zero, G^*_a; (2) estimated from Windhorst et al. (in prep.), G^*_b, and (3) a (hypothetical) $10\times$ larger than Windhorst et al.,G^*_c. In the left (right) panel, I show the measured dispersion ($\delta = \frac{G^*_x - G^*_a}{G^*_a}$), where X indicates measurements in scenarios (2) and (3). I measure a significant difference ($> 20\%$) only for scenario (3).

Chapter 4

A PANCHROMATIC CATALOG OF EARLY-TYPE GALAXIES AT INTERMEDIATE REDSHIFT IN THE HUBBLE SPACE TELESCOPE WIDE FIELD CAMERA 3 EARLY RELEASE SCIENCE FIELD

The star-formation histories of early-type galaxies (ellipticals and S0s, hereafter denoted ETGs) are now known to be considerably more diverse than had been originally expected. Optical broad-band photometry initially suggested that ETGs in the local universe were largely composed of a homogeneous, old ($>$ 10 Gyr), and passively evolving stellar populations that were formed at a uniformly high redshift via the "monolithic collapse" scenario (e.g., Eggen, Lynden-Bell, and Sandage , 1962; Tinsley , 1980). However, high precision optical spectrophotometry (e.g., O'Connell , 1980; Rose , 1985; Worthey et al. , 1994; Trager et al. , 2000) shows that a significant fraction of nearby ETGs experienced prolonged episodes of star-formation, lasting until a few gigayears ago. Their inferred luminosity-weighted ages have recently been found to correlate with velocity dispersion as well as environment (Graves et al. , 2009; Clemens et al. , 2009; Scott et al. , 2009), so the mechanisms driving recent star-formation activity in ETGs are now coming into better focus. Cool interstellar material capable of fueling star-formation is also frequently present in ETGs (e.g. Morganti et al. , 2006; Lucero and Young , 2007, and references therein). These, and many other lines of evidence, including fine-structure (e.g., rings, shells, and ripples) in nearby ETGs (Schweizer et al. , 1990; Colbert et al. , 2001; Salim & Rich , 2010; Kaviraj , 2010), statistics of close pairs (Patton et al. , 2002), and the evolution of galaxy morphologies (van Dokkum , 2005; van Dokkum et al. , 2010), point toward a hierarchical, merger-dominated assembly of ETGs over an extended period (Toomre and Toomre , 1972; Barkana and Loeb , 2001; Kaviraj et al. , 2009, 2011,

and references therein).

Ultraviolet (UV) observations of large samples of ETGs, first enabled by the International Ultraviolet Explorer (IUE, see Kondo , 1987) and later by the Galaxy Evolution Explorer (GALEX, Martin et al. , 1997) and the Hubble Space Telescope (HST), confirmed the presence of late star-formation in many ETGs. The 1200-3000Å UV continuum is highly sensitive to small amounts of star-formation during the last ∼1 Gyr (see, Ferreras & Silk , 2000; Kaviraj et al. , 2009). With GALEX, Yi et al. (2005) found residual star-formation to be readily detectable in ETGs at low redshifts. Subsequently, a study of the UV-optical properties of ∼2100 ETGs by Kaviraj et al. (2007a) revealed that at least 30% of low-redshift ($z < 0.11$) field ETGs have UV-optical photometry consistent with active star-formation during the previous ∼1 Gyr. It is therefore of considerable interest to follow the incidence of rest-frame UV signatures of star-formation in ETGs to redshifts of z ∼1–2 at the HST diffraction limit.

The UV provides a valuable window on older, hot stellar populations as well. A UV upturn (UVX)—characterized by a sharp rise in the far-UV spectrum shortward of ∼2000 Å—has been detected in many low-redshift ETGs (e.g., Burstein et al. , 1988; Davis et al. , 2007; Jeong et al. , 2009, and references therein), but cannot be attributed to recent star-formation. The UVX is believed to arise predominantly from a small population of highly-evolved, hot, low-mass stars, especially extreme horizontal branch (EHB) stars (for a review, see O'Connell 1999). These stars have lost most of their hydrogen envelopes, thus exposing their hot (T≳20,000 K), helium-burning cores ($M < 0.52$ $M_{\odot}$, Dorman et al. , 1993). Various mechanisms are capable of reducing the envelopes, including giant branch mass-loss in metal-rich stars (Greggio & Renzini , 1990; Dorman et al. , 1995; Yi et al. , 1995, 1998), binary interactions (Han et al. , 2007), or extreme aging in a metal-poor population (Park & Lee , 1997). Most evidence favors a metal-rich UVX interpretation, but a much better

understanding of the underlying mechanisms could be obtained, if I could follow the evolution of the UVX with look-back time over the past 5–8 Gyr. A number of studies have attempted to determine lookback dependence up to $z \sim 0.5$ (Brown et al. , 2000, 2003; Yi & Yoon , 2004; Lee et al. , 2005; Ree et al. , 2007; Atlee et al. , 2009), but these were inconclusive, either because of small samples, or because of low signal-to-noise ratio.

The high spatial resolution and UV sensitivity of the HST WFC3 are well-suited to the study of low-level star-formation (see, e.g., Crockett et al. , 2011) and the UVX in intermediate redshift ETGs. In this paper, I describe the selection and photometric properties of a sample of intermediate redshift ($0.35 \lesssim z \lesssim 1.5$) ETGs obtained from observations of the GOODS-S field (Giavalisco et al. , 2004). This paper is the first in a series that will investigate the stellar population(s) extant in intermediate redshift ETGs in the ERS survey field.

This chapter is organized in the following manner. In §4.1, I briefly describe the ERS program, technical issues associated with WFC3 UV imaging relevant to this work, and the observations. In §4.2.1, I present the selection criteria used to produce the catalog, and in §4.2.2 I present and describe the photometric catalog. In §4.2.3, I discuss the fitting of model stellar populations defined by a single burst of star-formation to the broad-band spectral energy distribution (SED) of the ETGs, the results from which I used to measure the absolute photometry of the ETGs. In §4.2.4 and §4.2.5, I discuss the multi-wavelength morphological properties of the ETGs. In §4.3, I discuss the impact of the ETG selection criteria on catalog completeness. In §4.4 and §4.5, I present the rest-frame photometry transformation and discuss the rest-frame UV-optical photometry of the ETGs, respectively.

Throughout this chapter and the following, I assume a ΛCDM cosmology with

Ω_m=0.27, Ω_Λ=0.73, and H_0=70 km s^{-1} Mpc^{-1} (Komatsu et al. , 2011). I use the following designations : F225W, F275W, F336W, F435W, F606W, F775W, F850LP, F098M, F125W, and F160W represent the HST filters throughout; g' and r' represent the Sloan Digital Sky Survey (SDSS) filters (Fukugita et al. , 1996); FUV and NUV represent the GALEX 150 & 250 nm filters, respectively (Morrissey et al. , 2005). Throughout, I quote all fluxes on the AB-magnitude system (Oke and Gunn , 1983).

4.1 Observations

This sample of ETGs is drawn from the HST imaging with Advanced Camera for Surveys (ACS) and WFC3, which was obtained as part of the ERS program. Near-UV and near-IR observations were acquired as part of the WFC3 ERS program (HST Program ID #11359, PI: R. W. O'Connell), a 104 orbit medium-depth survey using the HST UVIS and IR cameras. A general introduction to the performance and calibration of the WFC3 is provided in Windhorst et al. (2011).

The ERS program observed approximately 50 square arcminutes in the GOODS-S field with the HST WFC3 UVIS in three filters: F225W and F275W for 2 orbits, and F336W for 1 orbit, per pointing, respectively. The program observed approximately 40 square arcminutes in the same field with the WFC3 IR in three filters: F098M, F125W, and F160W, each for 2 orbits per pointing. The 5σ 50% point-source completeness limits are: F225W=26.3, F275W=26.4, F336W=26.1, F098M=27.2, F125W=27.5, and F160W=27.2 mag (see Windhorst et al. , 2011). The analysis presented here was completed using mosaicked images produced for each of the UVIS and IR band tilings, and each image mosaic was drizzled to a pixel scale equal to 0.090″ $pixel^{-1}$. The UVIS filters have a small known red-leak (i.e., contamination by unwanted long-wavelength photons), which contributes no more than 3.0% of the total flux, even for ETGs at moderate redshift (see Addenum A2).

The WFC3 mosaics roughly cover the northern one-third of the GOODS-S field (Giavalisco et al. , 2004), and I incorporate the pre-existing ACS dataset (F435W, F606W, F775W, and F850LP) with the WFC3 observations. We produced mosaicked images of the GOODS-S ACS data, which were binned to match the pixel scale of the WFC3 UVIS/IR mosaics.

4.2 A UV-optical-IR Photometric Catalog of Early-Type Galaxies

4.2.1 Selection Criteria

I require the galaxies to have: (1) been imaged in all UV and IR bands, to uniform depth; (2) a spectroscopically-confirmed redshift in the range $0.35 \lesssim z \lesssim 1.5$; and (3) an ETG morphology.

There are many techniques for identifying ETGs at intermediate redshift. I am particularly motivated to include in the sample ETGs that encompass all possible star-formation histories, thus I do not select ETGs using traditional optical color-based methods, since these may be biased toward specific star-formation histories. For example, photometric selection techniques (e.g., optical color selection, see Bell et al. , 2004)— which assume a quiescent template SED—will exclude ETGs with on-going or recent star-formation. The quantitative morphological classification of galaxies is an alternative method of identifying a sample of ETGs (e.g., Conselice et al. , 2003; Abraham et al. , 2003; Lotz et al. , 2004). However, the robustness of each of these classifiers can be dramatically affected by a variety of systematics, such as the image signal-to-noise ratio (Conselice et al. , 2003; Lisker , 2008) and the bandpass in which the technique is applied (Taylor-Mager et al. , 2007; Conselice et al. , 2008). In lieu of these techniques, I select the sample by visual classification. This technique is subjective, but it has been successfully applied to the identification

of both low redshift (z $\sim$0.1; Schimonivich et al. , 2007) and intermediate redshift (z$\lesssim$1.3; Postman et al. , 2005; Ferreras et al. , 2009) ETGs. In §4.3 I show that the spectroscopic redshift requirement, and not the morphological selection technique, is the most significant source of bias.

Catalog ETGs were identified and then independently confirmed by co-authors (Sugata Kaviraj, Robert Mark Crockett) by visual inspection of the GOODS ACS F606W, F775W, and F850LP and ERS WFC3 IR F098M, F125W, and F160W image mosaics. The galaxies included in this sample exhibited the morphological characteristics of early-type galaxies—i.e. these galaxies exhibited a centrally peaked light profile, which declines sharply with radius, a high degree of rotational symmetry, and a lack of visible internal structure.

UV imaging can provide unique insight into the star-formation history of ETGs. Thus, I require the sample ETGs to be observed in each of the UV filter mosaics. To ensure that all galaxies were observed to a similar depth, I also require each ETG in the sample to be observed in the UV and IR image mosaics for at least the mean exposure time measured for each filter as given by Windhorst et al. (2011). Since I am interested in the star-formation histories of ETGs, and the WFC3 UVIS channel is only sensitive to UV emission at $\lambda \sim 1500$ Å for objects at redshift z$\gtrsim$0.35, I define this redshift as low-redshift cutoff of the sample. The high-redshift cutoff was selected to ensure that the visual inspection and classification of the ETG — in the filter set outlined above – considers the rest-frame V-band morphology. I am sensitive to at least the UV-optical SED of every ETG in the catalog.

The spectroscopic redshifts for these ETGs were derived from the analyses of spectra obtained with the Very Large Telescope (Le Fèvre et al. , 2004; Szokoly et al. , 2004; Mignoli et al. , 2005; Ravikumar et al. , 2007; Vanzella et al., 2008; Popesso

et al. , 2009) and Keck Telescopes (Strolger et al. , 2004; Daddi et al. , 2005) and the HST ACS Grism (G800L) (Daddi et al. , 2005; Pasquali et al. , 2006; Ferreras et al. , 2009). I find 102 ETGs that satisfy these selection criteria.

4.2.2 Photometry

I measured object fluxes using Source Extractor in dual-image mode (SE, Bertin & Arnouts , 1996), with the WFC3 F160W image as the detection band. For source detection, I required sources to be detected in minimally four connected pixels, each at $\geq 0.75\sigma$ above the local computed sky-background. For deblending, I adopted a contrast parameter of 10^{-3} with 32 sub-thresholds. Object photometry was determined with MAG_AUTO parameters Kron factor equal to 2.5 and minimum radius equal to 3.5 pixels.

I adopted gains for each filter using the mean exposure time calculated for each mosaic as follows: F225W and F275W equal to 5688 sec; F336W equal to 2778 sec and F098M, F125W, and F160W equal to 5017 sec (see Windhorst et al. , 2011). From Kalirai et al. (2009a,b) I assumed zeropoints for the filter set F225W, F275W, F336W, F098M, F125W, F160W equal to 24.06, 24.14, 24.64, 25.68, 26.25, 25.96 mag, respectively. I assumed zeropoints for the filter set F435W, F606W, F775W, and F850LP equal to 25.673, 26.486, 25.654, and 24.862 mag, respectively[1].

In Table 4.1 I present the measured photometry for the ETGs. SE non-detections are designated " $\cdots$ " (23 galaxies) and ETG fluxes with detections fainter than the recovery limits (discussed below) are designated "—" (52 galaxies), as explained in the footnotes of Table 4.1.

The combination of the stable WFC3 UV-optical-IR PSF and high spatial res-

[1]For more details, see http://archive.stsci.edu/pub/hlsp/goods/v2/h_goods_v2.0_rdm.html

olution allows many compact or low surface brightness (SB) ETG candidates to be detected and measured. These candidates may meet the morphological selection criteria in the "detection" image, but in dual-image mode SE returns flux measurements for these ETGs which are significantly below the formal completeness limits in the "measurement" image. Their formal flux uncertainties are larger than $\sim$1 mag (implying a signal-to-noise ratio $\lesssim$1). To ascertain the reliability of these faint flux measurements in the UV bandpasses, I inserted simulated galaxies into the images, and performed an object recovery test to measure the flux level where the signal-to-noise typically approaches $\sim$1. To derive 90% confidence limits, I inserted $\sim$60,000 simulated galaxy images representing a range of total magnitudes (24mag $<$ m $<$ 30mag) and half-light radii ($0.8'' <$ r_{hl} $< 2.25''$) into each of the UVIS mosaics, and measured the fraction of simulated galaxies which were recovered by SE, using the same SE configuration as discussed above. The simulated galaxies were defined with an $r^{1/4}$ ("bulge") or exponential SB profile ("disk"). From these simulations, I estimated the 90% recovery limits for simulated bulge profiles with half-light radius of $1.0''$ equal to F225W=26.5, F275W=26.6, F336W=26.4, and F435W=26.7 mag, respectively. I interpret ETGs with magnitudes fainter than these recovery limits as 1-σ upper limits.

In Figure 1, I provide ten-band postage stamp images of the ETGs. These images are converted to flux units (nJy), and displayed with the same linear gray-scale. Each postage stamp measures $11.2''$ on a side. In Table 4.1, the typical measured photometric uncertainties are small, and the typical uncertainties associated with an m=25 mag galaxy in the ERS and GOODS-S object catalog are: 0.26 (F225W), 0.24 (F275W), 0.34 (F336W), 0.06 (F435W), 0.05 (F606W), 0.07 (F775W), 0.07 (F850LP), 0.11 (F098M), 0.07 (F125W), and 0.12 mag (F160W), respectively. On average, the measured photometric uncertainties are larger for the UVIS bandpasses for this

catalog. This can be largely attributed to the lower telescope throughput, the lower intrinsic ETG flux, and the shorter effective exposure time per pixel in each UVIS bandpass, compared to the ACS and WFC3/IR instruments and image mosaics (see Fig. 1 in Windhorst et al. , 2011).

In Figure 4.2, the distribution of these galaxies is plotted as a solid histogram, and the distribution of all available spectroscopic redshifts in the CDF-S field is shown as a dashed histogram. The redshift peaks in this distribution at $z \approx 0.53$, 0.67, 0.73, 1.03, 1.09, 1.22, and 1.3 correspond to known large-scale structures in the Chandra Deep Field-South (CDF-S) (Gilli et al. , 2003; Popesso et al. , 2009).

4.2.3 Stellar Population Modeling

To measure absolute photometric properties of the ETGs, I first fit the population synthesis models of Bruzual and Charlot (2003) (hereafter, BC03) to the broad-band observed Optical-IR (F435W, F606W, F775W, F850LP, F098M, F125W, F160W) SED of each ETG, applying the standard techniques outlined in Papovich et al. (2001). The template library of models I used in this fitting routine was generated for BC03 single burst stellar templates defined by a Salpeter IMF, solar metallicity, no extinction from dust, and with the star-formation history of the single burst defined by an exponentially declining function, weighted by time constant, τ, i.e.,:

$$\psi(t) \propto e^{-t/\tau} \tag{4.1}$$

These models were defined for a grid of time constants[2] ($-2.0 < \log(\tau[\mathrm{Gyr}]) < 2.0$) and ages ($1\times10^8 < t(\mathrm{yr}) < 13.7\times10^9$).

I minimize the goodness-of-fit χ^2 statistic between this library of synthetic and observed fluxes to determine the optimal model[3]. For each galaxy, I required

[2]I calculate models for N=15 values of τ defined with a stepsize of $\frac{max(\log(\tau))-min(\log(\tau))}{(N-1)}$=0.28.

[3]I assume 7 degrees of freedom when determining the reduced χ^2 statistic.

the best-fitting age parameter to not be greater than the age of the Universe at the redshift of the ETG. From this best-fitting template the appropriate k-correction was then calculated, yielding an absolute magnitude for each ETG in the r', Johnson V, and F606W bandpasses (see Figure 4.3).

I fit the observed SEDs in this limited filter selection to ensure that the rest-frame optical and near-IR emission, which provides the best indication to the majority (old) stellar populations extant in the ETGs, is included in determining the best-fit spectral template. Fitting single burst models to the limited SED also ensures that rest-frame UV emission is largely excluded from the fitting. Emission at UV wavelengths that arises from multiply-aged young ($<$ 1 Gyr) and old ($\gg$ 1 Gyr) stellar populations or minority UV-bright old stellar populations not be well-fit with these single burst models. A detailed modeling of these complex stellar populations is beyond the intended scope of this work and I will present a more detailed analysis of the stellar populations extant in Chapter 5.

Typical reduced χ^2 determined from the SED-fitting were small ($\langle\chi^2_\nu\rangle = 1.1$) for ETGs at redshift z$\lesssim$0.6 (22 ETGs[4]). For this subset of ETGs, the mean mass, age and log(τ [Gyr]) were derived from the broad-band Optical-IR SED fitting, and measured to be equal to 1.1×10^{10}M$_\odot$, 2.8×10^9yr, and -0.3, respectively. At redshifts z$\gtrsim$0.6, the optical GOODS filter set is sensitive to significant rest-frame near-UV emission, the stellar source of which is not inherently well-described by the models in the single burst library used in this analysis. Nonetheless, the majority of ETGs at $z > 0.6$ are well-fitted by the single burst models. Only 13 ETGs were "failures" (which I define as ETGs with minimum $\chi^2_\nu > 5$); 11 of these ETGs had spectroscopic redshifts greater than 1. At this high redshift, the F435W ACS is sensitive to UV

[4]I excluded a single poorly-fitted faint (M$_V = -17$), compact ETG (J033244.97-274309.1) from this set when calculating these averages

emission ($\lambda > 1800$ Å) exclusively. Excluding these "failures", the mean mass, age and $\log(\tau[\mathrm{Gyr}])$ of this high redshift subset of the catalog are measured to be equal to: $9.2\times10^9 \mathrm{M}_\odot$, 2.8×10^9yr, and -0.3, respectively. This SED analysis demonstrates that I have identified a population of galaxies that are generally: 1) 'peaky" (i.e., low τ) in their star-formation history; 2) old (i.e., bulk stellar population formed >1 Gyr ago); and 3) have stellar masses comparable to the characteristic stellar mass of red galaxies ($\sim10^{11}\mathrm{M}_\odot$, see Marchesini et al. , 2009, cf. Figure 4.3) at these redshifts. Similar characteristics of the bulk stellar populations of galaxies are measured for low-redshift ETGs (see, e.g., Bell et al. , 2004). Thus, I initially conclude that I have selected galaxies representative of the class of intermediate to high mass ETGs.

4.2.4 Source Classification

In this section, I discuss the morphological properties and classification definitions for the ETGs. Although optical colors were not used to select or exclude ETGs, the color of the ETGs and/or neighboring galaxies may aid in understanding the star-formation history of the ETGs (see Peirani et al. , 2010). In the following comments, the definition of the ETG "companion(s)" is made strictly based on the close proximity—in projection—of any two or more galaxies. Furthermore, the classifications below are not mutually exclusive. When galaxies meet the qualifications for multiple classifications, we provide only the unique classifications and/or the most general classification. To qualitatively assess the primary ETG, its local environment, and any possible companions, I inspect the GOODS three-color, four panel $7.0''\times7.0''$cutouts prepared for four permutations[5] of the GOODS ACS F435W, F606W, F775W and F850LP images. In Figure 4.4, I provide the GOODS color cutouts of an ETG representative of

[5]The cutouts are available online at: http://archive.stsci.edu/eidol_v2.php. Specifically, the color cutouts are generated for BVi', BVz', $Bi'z'$, and $Vi'z'$ colors; where $BVi'z'$ refer to the ACS F435W, F606W, F775W and F850LP filters, respectively

each of the following classes:

- Comment "Comp." — ETG identified with companions. I note cases where the colors of galaxies in the color cutouts are similar to the ETG. This similarity could suggest that the galaxies are at a similar redshift, which would indicate that the ETG is a member of a small group. I define two sub-classes :
  - Comment "LSB-Comp." — Low surface brightness companions. ETGs with low SB companions are candidates for future work to study the role of minor mergers in moderating star-formation in intermediate redshift ETGs.
  - Comment "b-Comp" — ETG has blue companions(s). I note objects which have projected companions that are bluer than the primary ETG in all color cutouts. I speculate the enhanced emission in the F435W and/or F606W bands suggest that these possible companions have higher star-formation rates than the primary ETG.
- Comment "d" — ETG exhibits dust lane. The existence of a dust lane in an ETG has implications for the merger and star-formation history of the ETG.
- Comment "c" — Compact profile. These ETGs are notably more compact than the typical ETG in the sample, but were not identified as stars in Ravikumar et al. (2007) or Windhorst et al. (2011).
- Comment "DC" — ETG has double core. This designation applies to a single ETG (J033210.76-274234.6), which appears to be an ongoing major merger of two spheroidal galaxies both of which have prominent central cores.

- Comment "S0" — S0 candidate. These ETGs show evidence for a bright core-bulge component, continuous light distribution, and an extended disk-like profile.

- Comment "VGM" — Visual group member. These ETGs exist in a region of probable local overdensity of both early- and late-type galaxies, as well as low SB companions.

In Table 4.2 (Column 4), I comment on the morphology, light-profile, and the environment of the ETGs.

4.2.5 Active Galactic Nuclei

While weak active galactic nuclei (AGN) do not dominate the optical SED of their host ETG (Kron, Koo, & Windhorst , 1985), these may contribute emission in the UV spectrum of galaxies (vanden Berk et al. , 2001, and references therein). Therefore, to understand the stellar sources of UV flux in the ETGs, I must identify and account for weak AGN contamination. AGN were flagged in the catalog by matching the positions of the ETGs to the X-ray (Giacconi et al. , 2002; Luo et al. , 2010) and radio (Miller et al. , 2008) source catalogs. In Table 4.2, I denote X-ray and/or radio sources as "X*" "R*", respectively (or "XR*" if the ETG was identified in both catalogs). I give the AGN classifications (Table 4.2, Column 3) from Szokoly et al. (2004), which are based on the X-ray luminosity, hardness ratios, and optical line-widths. Nine ETGs in the catalog were matched with sources in the X-ray and/or radio.

4.3 Catalog Completeness

While the morphological selection criteria ensure the galaxies are generally representative of the class of ETGs, the high spatial resolution HST ACS and WFC3 imaging

allows us to identify sub-structure (e.g., dust lanes, which would be unresolved in ground-based imaging) which ensures the catalog better captures the morphological diversity of ETGs. I also conclude that the ETG masses are approximately equal to the characteristic stellar mass parameter, $10^{10} \leq M_*[M_\odot] \leq 10^{12}$ (see §4.2.3 and Figure 4.3). Thus, the catalog is representative of the class of intermediate to high mass ETGs. Yet, the selection criteria must necessarily imply that the catalog is an incomplete assessment of the ETGs in the ERS survey volume. In this section, I discuss the extent to which selection criteria affects catalog completeness.

To quantify the number of ETGs I exclude from the catalog by enforcing the selection criteria, I inspected a randomly-selected region in the F160W mosaic with an area equal to ∼10% of the total area of the ERS field. Therein, I identified ∼180 galaxies which have sufficiently high signal-to-noise ratio, surface brightness, and spatial extent to be morphologically-classified. I visually classified 45 of these galaxies as ETGs. Approximately 35% (17 ETGs) of these galaxies were included in the catalog. If I extrapolate this observed fraction to the full ERS field, I estimate that there are ∼1800 visually-classifiable galaxies in the field, of which ∼280 galaxies could have been morphologically classified as ETGs, but were not included in the catalog because they lacked spectroscopically-confirmed redshifts[6]. Thus, I can assume that as a result of the spectroscopic redshift incompleteness, I am likely excluding a population of ETGs approximately 2–3 times larger than the catalog in §4.2.2. I conclude that the requirement that each ETG have a spectroscopically-confirmed redshift most strongly prevents the definition of a complete sample of ETGs in the ERS field.

At low to intermediate redshift ($z \gtrsim 0.6$), this incompleteness disproportionately affects fainter galaxies. Large (greater than a few square degrees) spectroscopic sur-

[6]This sample likely includes morphological ETGs at $z \gtrsim 1.5$, but I can reasonably assume (cf. Bezanson et al. , 2009; Ryan et al. , 2012) that the number of ETGs at high redshift is a small fraction of the lower redshift ($z < 1.5$) ETG population

veys of thousands of galaxies have noted the paucity of low-luminosity ($M_B > -18$) red galaxies (Weiner et al. , 2005; Willmer et al. , 2006). This paucity can be partly attributed to the difficulty associated with the measurement of spectroscopic redshifts for galaxies with largely featureless spectra, with few (or no) weak lines, that are common to quiescent faint galaxies. At high redshift ($z \gtrsim 1$), the measurement of spectroscopic redshifts is increasingly more difficult because ground-based optical-near IR spectrometers can not adequately constrain the 3648Å Balmer complex. Furthermore, color-based candidate galaxy selection at optical wavelengths (e.g., F775W$-$F850LP $>$ 0.6 mag; Vanzella et al., 2008) will intrinsically select high redshift ($z > 1$) ETGs with bluer rest-frame UV-optical colors. As a result, these technical limitations and color selections promote spectroscopic redshift incompleteness in surveys of red galaxies at high redshift across the mass spectrum.

I can not rule out the effect of cosmic variance in the ERS field as an additional source of incompleteness in the catalog. Willmer et al. (2006) measured the best-fit Schechter luminosity function parameters from 11,000 galaxies at $z \lesssim 1$ in the DEEP2 Survey (Davis et al. , 2007), and provide these results for two sub-populations, "red" and "blue" galaxies[7]. Assuming the best-fit Schechter parameters for the "red" sample measured at $z = 0.5$, we estimate that the ERS survey volume defined for $0.4 < z < 0.7$ contains only $\sim$1 luminous ($M_V < -22$ mag) ETG.

4.4 Conversion to Rest-Frame UV-Optical Photometry

The measured rest-frame FUV–optical photometry provides a uniform basis for studying the star-formation histories of the ETGs. Here we describe and apply an interpolation method to transform the observed photometry to a "standard" set of FUV, NUV, g', r', and Johnson V bandpasses. I select this filter set for this analysis because

[7]"Red" and "blue" galaxies are distinguished using the color criterion U$-$ B$=-0.032(M_B + 21.52)+0.204$

there are now extensive references in the literature which use the same filter set in the study of nearby and low-redshift ETGs (e.g. Kaviraj et al. , 2007a; Schawinski et al. , 2007; Ree et al. , 2007; Kaviraj , 2010, and references therein).

First, I generated a library of hybrid spectral templates defined by two instantaneous bursts of star-formation. The first burst occurred at a fixed redshift ($z = 3$) with a fixed solar metallicity ($Z_1 = Z_{\odot}$). The second burst was modeled assuming a variable stellar mass fraction (f_2), age of burst (t_2), dust content characterized by E (B$-$V), and metallicity (Z_2). The full parameter space represented in the library of hybrid spectral templates is provided in Table 4.3. Next, I identified a set (Table 4.4) of WFC3 and ACS "proxy" filters that most closely trace the bandpasses corresponding to the desired filters (FUV, NUV, Johnson V, g', and r') at the relevant redshift. Finally, I folded the library of spectral templates with this filter set to determine the proxy and desired rest-frame colors. To define a general transformation function for each redshift, I fit a second-order polynomial to the desired colors as a function of proxy color. These transformations can be considered as a generalized k-correction.

The BC03 models are known to be an incomplete representation of the UV spectrum of ETGs with ages >3 Gyr (see Kaviraj et al. , 2007a, 2008) due to their treatment of the UV upturn. The UV energy distribution in the BC03 models does not include the effects of extreme HB stars which are expected to dominate this region of the spectrum of old stellar populations. Therefore, I use a set of templates which are a hybrid of BC03 models and Yi et al. (1999, 2003) for stellar populations of ages $\gtrsim$3 Gyr. This hybrid library has been demonstrated (Kaviraj et al. , 2007a, 2008) to fit observed ETGs across a large redshift range ($0 < z < 1$) with both young and old UV-bright stellar populations.

The rest-frame UV-optical colors are given for the sample in Table 4.5. Following the convention of Table 4.1, I designate SE non-detections in the blue proxy band as " $\cdots$ ". ETGs not detected at or above the 1σ completeness limits (§4.2.2) in the bandpasses used to determine the rest-frame UV–optical colors are designated "—".

The $(g'–r')_{rest}$ and rest-frame Johnson V and r' apparent magnitudes are also provided in Table 4.5. The $(g'–r')_{rest}$ colors were calculated using a method similar to the one outlined above for converting the observed photometry to rest-frame UV-optical colors, though the $(g'–r')_{rest}$ transformation function was calculated for a different proxy filter set (see Table 4.4). To calculate the Johnson V and r' apparent magnitudes presented in Table 4.5, the F606W filter was fixed as the proxy filter and a linear transformation function was fit to the proxy and desired apparent magnitudes measured from the hybrid template library. Typically, I measure the difference for any proxy-desired bandpass pair to be small (less than 0.1 mag), but at higher redshifts, the redshifting of the Balmer break in the spectrum through the bandpass can produce larger offsets. Particularly, between the F606W and Johnson V bandpasses, these offsets can be as large as $\sim$1.1 mag

4.5 Discussion of Rest-Frame Panchromatic Photometry

In the upper panel of Figures 4.5 and 4.6, the apparent colors and associated photometric uncertainties bars are plotted for reference. I calculate these colors by simply differencing the apparent magnitudes in the proxy bandpasses for each redshift bin (see Table 4.4). I show in the lower panel of Figures 4.5 and 4.6 the $(NUV–V)_{rest}$ and $(FUV–V)_{rest}$ colors, which are calculated using the best-fit transformation function from §4.4. Each ETG is plotted with its measured photometric and systematic (i.e., associated with the transformation) uncertainties. An asterisk indicates that

the ETG was identified by the radio or X-ray surveys of the CDF-S (see §4.2.5). I show the integrated $(\mathrm{NUV–V})_{rest}$ and $(\mathrm{FUV–V})_{rest}$ colors from the GALEX UV Atlas of Nearby Galaxies (Gil de Paz et al. , 2007) for NGC 221 (M32), 1399, and 1404 (triangles). I select these specific ETGs, since they well-represent the evolved red sequence of ETGs in the local Universe.

I also show the rest-frame colors of three model galaxies, generated using the BC03 single burst templates (see §4.2.3) for three star-formation histories defined by Equation 5.1 for $\log(\tau[\mathrm{Gyr}])\simeq$ 1.1 (blue),−0.3 (green), and −2.0 (red). For each model, I assume solar metallicity, a Salpeter IMF, no dust, and formation redshift $z_f = 4.0$. The time since z_f is plotted as the upper abcissa in each Figure. This formation redshift can be considered to represent the effective start of star-formation in ETGs, because it is approximately halfway in cosmic time between the start of cosmic star-formation at $z \simeq 10$ (Komatsu et al. , 2011) and the (broad) peak of the cosmic star-formation history at $z \simeq 2$ (Madau et al. , 1998).

Over the surveyed redshift range, Figures 4.5 and 4.6 show that the majority of ETGs have UV–optical colors no bluer than the $\log(\tau[\mathrm{Gyr}]) \simeq 1.1$ single burst model, suggesting that these ETGs have not undergone a significant, recent star-formation event which would be identified by $(\mathrm{NUV–V})_{rest} \gtrsim -1.0$ mag. Secondly, only a minority of ETGs can be well-described by a quiescent, instantaneous star-formation history that assumes a high formation redshift ($z_f = 4.0$). Finally, I note that the "red envelope" of the $(\mathrm{FUV–V})_{rest}$ and $(\mathrm{NUV–V})_{rest}$ colors, the latter is most sensitive to recent star-formation, remains constant across the intermediate redshift $z < 0.5$.

Furthermore, few (1-2) ETGs at intermediate redshift ($z \lesssim 0.6$) have measured rest-frame colors as red as those observed for the strongest UV upturn galaxy in the

local Universe, NGC 1399. In §4.2.3 and §4.3 I showed that the selection criteria (unavoidably) defined a catalog that is deficient in bright ($M < -22$ mag) ETGs. Assuming a stellar mass-to-light ratio of these bright ETGs approximately equal to unity, the masses of these ETGs are greater than $\sim 10^{11}$ $M_{\odot}$, e.g., early-type brightest cluster galaxies (BCGs, with stellar masses $10^{10.5} < M_{*}\,[M_{\odot}] < 10^{11.5}$; see von den Linden 2007) and cD-type galaxies ($M_{*}[M_{\odot}] \gtrsim 10^{12}$), which is consistent with the results presented with Figure 4.3. From theory and observations of the UVX in low-redshift ETGs, I expect that an optimal sample for the study of the UVX at intermediate redshift would include the oldest ($\gtrsim$6 Gyr, Tantalo et al. , 1996) and brightest ETGs. The latter is due to the observation that the strength of the UVX is positively correlated with host galaxy luminosity (Burstein et al. , 1988). Thus, the analysis in §4.2.3 and §4.3 suggested, and Figures 4.5 and 4.6 confirm, that the catalog is deficient in these ETGs best-suited for the analysis of the UVX.

Some ETGs may contain UVX stellar populations, but these ETGs are likely to be dominated in the UV by emission from young, not old, stellar populations. Any future work that seeks to model the UVX evolution over cosmic time using the catalog must do so with caution, and take care to include multiple stellar populations in the SED analysis.

At higher redshift ($z \gtrsim 0.5$), the rest-frame UV-optical colors are uniquely sensitive to recent star-formation, because the older evolved stellar populations do not contribute significantly to the UV SED of the host ETGs (Ferreras & Silk , 2000; Yi et al. , 2005; Kaviraj et al. , 2007b, 2009). If the measured rest-frame colors of the ETGs are compared with the results from Yi et al. (2005) and Kaviraj et al. (2007a), these colors indicate a wide range of star-formation histories ranging from continuous star-formation ($\log(\tau[\mathrm{Gyr}]) = 1.1$) to nearly-quiescent ($\log(\tau[\mathrm{Gyr}]) = -0.3$), assuming a uniform formation redshift of the majority stellar population.

In Figure 4.7, I show the rest-frame UV-optical color-color diagram for the ETGs that are brighter than the simulated 1σ 90% recovery limits (see §4.2.2), with photometric and systematic uncertainties included. Furthermore, I color-code the data to correspond with the redshift of the ETG; the color scheme is defined in Figure 4.7. In Figure 4.7, the $(g'–r')_{rest}$ colors of ETGs span $\lesssim$1 mag. The $(g'–r')_{rest}$ colors of the ETGs are also well-distributed as a function of redshift and color, which indicates that UV-optical transformation function defined in §4.4 is not affected by any large systematic uncertainties. In Figure 4.8, I show the $(g'–r')_{rest}$ colors of the ETGs with respect to the absolute r' magnitudes. Since the color distribution is bounded by reasonable population synthesis models (Figures 4.5 and 4.6) and the the rest-frame optical photometry is unaffected by large amplitude systematic or photometric uncertainties (Figure 4.7), the bimodality in the $(g'–r')_{rest}$ colors which distinguishes luminous red ETGs from lower luminosity blue ETGs present in the Figure is not an artifact. Though the optical colors of ETGs are a poor discriminator of recent star-formation history of ETGs, the distribution of rest-frame optical colors supports the previous conclusion that there exists a diversity in the star-formation histories of these ETGs.

Finally, in Figures 4.5 and 4.6, we note a transition from peaky star-formation histories for the highest redshift ($z\gtrsim1$) ETGs to a more gradual and sustained star-formation in ETGs at low to intermediate redshifts ($z\lesssim1$) across the entire surveyed redshift range. Specifically, at high redshift ($z\gtrsim$) 1), many ETGs appear to cluster near to the $\log(\tau[\mathrm{Gyr}])= -0.3$ curve, whereas no low to intermediate redshift ($z\lesssim1$) ETGs exist on this curve and few have $(FUV-V)_{rest}\lesssim6$. But I do not make an interpretation of this trend as it may not represent a physical transition. In §4.3, I outlined a number of biases implicit in optical-near IR spectroscopic redshift surveys that specifically select against red ETGs, both at intermediate and high redshift. The

paucity of red ETGs at low to intermediate redshift may be partially attributed to the spectroscopic redshift incompleteness, and as a result, this transition would not indicate a physical evolution in the star-formation histories of these ETGs. To determine the significance of this apparent transition I require a catalog of ETGs selected in such a way that the biases introduced by spectroscopic redshift incompleteness are minimized. To produce this catalog, future selection and spectroscopic observations of intermediate and high redshift ETGs in the ERS field must be made in the near-IR.

4.6 Addendum A2. Red-Leak

Ultraviolet observations of objects with weak UV emission and red SEDs may be prone to significant red-leaks, where long-wavelength photons can be incorrectly counted as UV photons. Despite significant efforts by the WFC3 instrument team to minimize red-leaks, it is important to understand this effect on the photometry of a typical ETG.

I measure the red-leak associated with each of the WFC3 UVIS filter response curves (see Figure 4.9) for model SEDs defined over a range of redshift $0.35 \lesssim z \lesssim 1.5$ by measuring the ratio of flux at $\lambda > 4000$Å to the total:

$$\mathcal{R} = \frac{\left\langle F_{\lambda > 4000\ \text{Å}} \right\rangle}{\langle F_\lambda \rangle} = \frac{\int_0^{\nu_0} F_\nu T_\nu d\nu/\nu}{\int_0^{\infty} F_\nu T_\nu d\nu/\nu} \tag{4.2}$$

where $\nu_0 = c/4000$ Å, F_ν represents the flux per unit frequency associated with the model spectrum, and T_ν is the filter response[8].

Because the UV emission profile of an homogeneously old ETG model can vary significantly with the models of the UVX stellar populations (see §4.3), I measured the effect of filter red-leak for two template spectra. I used the Coleman, Wu

[8]The response curves are provided by the synthetic photometry IRAF package synphot, which was prepared by STSCI for the HST instrument suite; more details are available online at www.stsci.edu/resources/software_hardware/stsdas/synphot

and Weedman (1980) Elliptical and a BC03 exponentially-declining star-formation template with $\log(\tau[\mathrm{Gyr}]) = -2.0$ and an absolute age of $\sim$12 Gyr (even when current cosmology dictates that such an old model is infeasible) to define the model SEDs. I consider the grid of model spectra for the redshift range, $0.35 \lesssim z \lesssim 1.5$, and provide the maximum red-leak measured for this grid in Table 4.6. I conclude that the filter red-leak in this redshift range is never larger than 3.5%, even for the bluest F225W filter.

Table 4.1: Early-Type Galaxies Catalog, Measured Photometry

GOODS ID	α(J2000)	δ(J2000)	F225W	F275W	F336W	F435W	F606W	F775W	F850LP	F098M	F125W	F160W	z
			Δm	Δm	Δm	Δm	Δm	Δm	Δm	Δm	Δm	Δm	
J033202.71	03:32:02.71	-27:43:10.87	23.07	23.30	21.62	20.24	18.82	18.28	18.01	17.91	17.69	17.50	0.493
-274310.8			0.17	0.20	0.06	0.00	0.00	0.00	0.00	0.00	0.00	0.00	
J033203.29	03:32:03.29	-27:45:11.47	26.00	25.89	25.50	25.13	24.42	23.78	23.61	23.44	23.37	23.18	0.542
-274511.4			0.35	0.29	0.27	0.06	0.02	0.02	0.02	0.02	0.02	0.02	
J033205.09	03:32:05.09	-27:45:14.03	24.88	24.92	24.80	24.51	23.94	23.23	22.99	22.98	22.74	22.59	0.763
-274514.0			0.18	0.17	0.21	0.03	0.02	0.02	0.01	0.02	0.01	0.01	
J033205.13	03:32:05.13	-27:43:51.05	24.28	24.04	24.06	23.84	23.36	22.63	22.45	22.41	22.26	22.18	0.806
-274351.0			0.09	0.06	0.09	0.02	0.01	0.01	0.01	0.01	0.01	0.01	
J033206.27	03:32:06.27	-27:45:36.68	—	—	25.62	25.67	23.00	21.54	21.04	20.85	20.44	20.06	0.669
-274536.7			—	—	0.72	0.20	0.01	0.01	0.01	0.00	0.00	0.00	
J033206.48	03:32:06.48	-27:44:03.68	—	25.78	26.07	—	24.43	23.03	22.11	21.85	21.41	21.03	0.958
-274403.6			—	0.46	0.83	—	0.04	0.02	0.01	0.01	0.00	0.00	
J033206.81	03:32:06.81	-27:45:24.37	25.61	—	26.37	26.12	25.42	23.91	23.18	22.75	22.03	21.65	1.373
-274524.3			0.38	—	0.94	0.20	0.09	0.04	0.02	0.02	0.01	0.01	
J033207.55	03:32:07.55	-27:43:56.68	—	—	—	—	25.13	23.76	22.81	22.40	21.88	21.50	1.370
-274356.6			—	—	—	—	0.14	0.06	0.03	0.02	0.01	0.01	
J033207.95	03:32:07.95	-27:42:12.18	26.47	—	—	26.46	24.96	23.64	23.17	23.01	22.68	22.39	0.740
-274212.1			0.66	—	—	0.23	0.05	0.02	0.02	0.01	0.01	0.01	
J033208.41	03:32:08.41	-27:42:31.37	26.31	···	25.99	24.83	22.87	21.74	21.34	21.19	20.85	20.53	0.540
-274231.3			0.94	···	0.85	0.09	0.01	0.01	0.01	0.00	0.00	0.00	
J033208.45	03:32:08.44	-27:41:45.95	25.06	25.20	24.57	25.15	23.55	22.00	21.44	21.22	20.81	20.42	0.730
-274145.9			0.41	0.43	0.25	0.14	0.03	0.01	0.01	0.01	0.00	0.00	
J033208.53	03:32:08.53	-27:42:17.78	24.10	25.02	24.60	24.35	22.70	21.27	20.76	20.57	20.16	19.80	0.730
-274217.7			0.22	0.46	0.43	0.10	0.02	0.01	0.01	0.00	0.00	0.00	
J033208.55	03:32:08.55	-27:42:31.14	26.31	26.23	25.93	26.55	25.10	23.79	23.52	23.31	23.08	22.83	0.509
-274231.1			0.76	0.65	0.67	0.34	0.07	0.04	0.04	0.02	0.01	0.01	
J033208.65	03:32:08.65	-27:45:01.84	—	—	26.32	25.31	23.11	21.62	20.98	20.84	20.50	20.20	0.873
-274501.8			—	—	1.01	0.10	0.01	0.01	0.00	0.00	0.00	0.00	
J033208.90	03:32:08.90	-27:43:44.36	25.39	25.51	25.23	24.60	23.35	22.77	22.59	22.52	22.38	22.23	0.580
-274344.3			0.29	0.30	0.32	0.05	0.01	0.01	0.01	0.01	0.01	0.01	
J033209.09	03:32:09.09	-27:45:10.85	25.83	25.57	25.27	25.38	24.54	24.24	23.97	24.00	24.01	23.92	0.401
-274510.8			0.27	0.20	0.21	0.06	0.02	0.03	0.03	0.03	0.02	0.02	
J033209.19	03:32:09.19	-27:42:25.66	—	—	—	25.80	23.57	22.10	21.61	21.38	21.00	20.64	0.720
-274225.6			—	—	—	0.22	0.02	0.01	0.01	0.01	0.00	0.00	
J033210.04	03:32:10.04	-27:43:33.15	26.06	25.23	25.55	25.30	23.74	22.15	21.14	20.87	20.34	19.95	1.009
-274333.1			1.11	0.48	0.86	0.19	0.03	0.01	0.01	0.00	0.00	0.00	
J033210.12	03:32:10.12	-27:43:33.37	—	···	···	26.46	24.69	23.20	22.23	21.91	21.44	21.06	1.009
-274333.3			—	···	···	0.26	0.04	0.02	0.01	0.01	0.00	0.00	

Continued on Next Page...

Table 1:ETG Catalog, Measured Phot. (Continued)

GOODS ID	α(J2000)	δ(J2000)	F225W	F275W	F336W	F435W	F606W	F775W	F850LP	F098M	F125W	F160W	z
			Δm	Δm	Δm	Δm	Δm	Δm	Δm	Δm	Δm	Δm	
J033210.16	03:32:10.16	-27:43:34.38	···	···	···	25.84	24.25	22.61	21.65	21.45	20.91	20.53	0.990
-274334.3			···	···	···	0.34	0.06	0.02	0.01	0.01	0.00	0.00	
J033210.76	03:32:10.76	-27:42:34.65	23.46	23.33	23.05	21.73	19.89	19.00	18.64	18.50	18.17	17.85	0.419
-274234.6			0.15	0.12	0.13	0.01	0.00	0.00	0.00	0.00	0.00	0.00	
J033210.86	03:32:10.86	-27:44:41.24	26.45	26.17	—	—	24.69	23.43	22.98	22.88	22.55	22.23	0.676
-274441.2			0.66	0.47	—	—	0.03	0.02	0.01	0.01	0.01	0.01	
J033211.21	03:32:11.21	-27:45:33.44	26.31	—	—	26.07	24.62	23.18	22.16	21.79	21.32	20.99	1.215
-274533.4			0.72	—	—	0.20	0.04	0.02	0.01	0.01	0.00	0.00	
J033211.61	03:32:11.61	-27:45:54.13	—	25.50	25.71	25.80	24.15	22.73	21.75	21.38	20.93	20.55	1.039
-274554.1			—	0.41	0.67	0.21	0.03	0.01	0.01	0.01	0.00	0.00	
J033212.20	03:32:12.19	-27:45:30.04	25.04	24.93	24.44	24.28	22.32	21.06	20.64	20.50	20.17	19.86	0.676
-274530.1			0.48	0.41	0.34	0.09	0.01	0.01	0.00	0.00	0.00	0.00	
J033212.31	03:32:12.31	-27:45:27.43	···	25.53	25.03	25.57	23.46	22.17	21.77	21.61	21.29	21.01	0.680
-274527.4			···	0.45	0.40	0.18	0.02	0.01	0.01	0.01	0.00	0.00	
J033212.47	03:32:12.47	-27:42:24.24	—	—	25.50	24.87	23.04	22.19	21.92	21.78	21.55	21.30	0.417
-274224.2			—	—	0.41	0.06	0.01	0.01	0.01	0.01	0.00	0.00	
J033214.26	03:32:14.26	-27:42:54.28	—	···	26.19	26.38	24.96	23.90	23.48	23.34	22.94	22.68	0.814
-274254.2			—	···	0.62	0.18	0.05	0.03	0.03	0.02	0.01	0.01	
J033214.45	03:32:14.45	-27:44:56.58	—	—	25.39	—	24.81	23.37	22.95	22.80	22.43	22.14	0.737
-274456.6			—	—	0.37	—	0.05	0.02	0.02	0.02	0.01	0.01	
J033214.65	03:32:14.65	-27:41:36.56	25.75	25.67	—	26.12	25.42	23.84	23.00	22.51	21.77	21.33	1.338
-274136.6			0.63	0.55	—	0.29	0.13	0.05	0.03	0.02	0.01	0.01	
J033214.68	03:32:14.69	-27:43:37.10	26.49	25.42	25.28	25.08	24.31	23.44	22.95	22.88	22.58	22.42	0.910
-274337.1			0.70	0.24	0.28	0.05	0.02	0.02	0.01	0.02	0.01	0.01	
J033214.73	03:32:14.73	-27:41:53.32	···	26.07	—	25.07	23.40	22.56	22.22	22.09	21.85	21.60	0.490
-274153.3			···	0.51	—	0.07	0.01	0.01	0.01	0.01	0.01	0.01	
J033214.78	03:32:14.78	-27:44:33.11	—	—	—	—	24.52	23.11	22.63	22.41	21.93	21.57	0.736
-274433.1			—	—	—	—	0.04	0.02	0.01	0.01	0.01	0.00	
J033214.83	03:32:14.83	-27:41:57.13	—	—	—	25.18	23.54	22.34	21.96	21.84	21.53	21.25	0.680
-274157.1			—	—	—	0.09	0.02	0.01	0.01	0.01	0.00	0.00	
J033215.98	03:32:15.99	-27:44:22.96	25.60	25.80	25.63	24.48	22.96	21.78	21.41	21.28	21.00	20.75	0.735
-274422.9			0.68	0.75	0.84	0.06	0.01	0.01	0.01	0.01	0.00	0.00	
J033216.19	03:32:16.20	-27:44:23.14	25.48	25.86	25.63	24.82	23.25	22.45	22.15	22.08	21.81	21.63	0.419
-274423.1			0.50	0.65	0.70	0.06	0.01	0.01	0.01	0.01	0.01	0.01	
J033217.11	03:32:17.11	-27:42:20.90	26.31	26.17	24.69	24.99	25.15	25.11	25.26	25.09	24.32	25.25	1.240
-274220.9			0.37	0.32	0.11	0.04	0.04	0.06	0.09	0.06	0.02	0.06	
J033217.12	03:32:17.12	-27:44:07.73	···	—	—	26.51	24.59	23.14	22.66	22.53	22.15	21.83	0.730
-274407.7			···	—	—	0.25	0.03	0.01	0.01	0.01	0.01	0.01	
J033217.14	03:32:17.14	-27:43:03.30	24.16	23.92	23.37	23.07	21.69	20.81	20.53	20.37	20.15	19.81	0.556
-274303.3			0.13	0.10	0.08	0.02	0.00	0.00	0.00	0.00	0.00	0.00	
J033217.49	03:32:17.49	-27:44:36.73	25.43	25.08	24.78	24.68	23.01	21.80	21.36	21.23	20.89	20.60	0.734
-274436.7			0.67	0.45	0.45	0.11	0.02	0.01	0.01	0.01	0.00	0.00	

Continued on Next Page...

Table 1:ETG Catalog, Measured Phot. (Continued)

GOODS ID	α(J2000)	δ(J2000)	F225W	F275W	F336W	F435W	F606W	F775W	F850LP	F098M	F125W	F160W	z
			Δm	Δm	Δm	Δm	Δm	Δm	Δm	Δm	Δm	Δm	
J033217.91	03:32:17.91	-27:41:22.70	25.77	26.44	···	26.65	24.48	22.96	22.04	21.73	21.24	20.87	1.039
-274122.7			0.62	1.08	···	0.48	0.05	0.02	0.01	0.01	0.00	0.00	
J033218.31	03:32:18.31	-27:42:33.52	23.96	23.80	24.72	23.51	21.44	20.37	19.99	19.88	19.54	19.24	0.519
-274233.5			0.20	0.16	0.47	0.04	0.00	0.00	0.00	0.00	0.00	0.00	
J033218.64	03:32:18.64	-27:41:44.43	—	26.23	···	—	27.29	25.56	24.66	24.11	23.38	23.01	1.325
-274144.4			—	0.46	···	—	0.35	0.12	0.07	0.03	0.01	0.01	
J033218.74	03:32:18.73	-27:44:15.90	25.15	25.03	24.90	24.20	22.28	21.21	20.86	20.76	20.45	20.14	0.509
-274415.8			0.41	0.34	0.40	0.06	0.01	0.01	0.00	0.00	0.00	0.00	
J033219.02	03:32:19.02	-27:42:42.73	26.25	—	26.33	25.70	24.75	23.38	22.61	22.15	21.72	21.41	1.019
-274242.7			0.95	—	1.25	0.19	0.07	0.03	0.02	0.01	0.01	0.00	
J033219.48	03:32:19.48	-27:42:16.81	24.37	25.08	24.08	23.01	21.31	20.49	20.19	20.05	19.76	19.50	0.382
-274216.8			0.28	0.50	0.29	0.03	0.00	0.00	0.00	0.00	0.00	0.00	
J033219.59	03:32:19.59	-27:43:03.80	—	24.98	25.02	24.62	22.79	21.42	21.02	20.86	20.58	20.27	0.735
-274303.8			—	0.33	0.44	0.09	0.01	0.01	0.01	0.00	0.00	0.00	
J033219.77	03:32:19.77	-27:42:04.00	—	···	—	26.70	25.70	24.17	23.29	23.02	22.59	22.32	1.044
-274204.0			—	···	—	0.42	0.10	0.04	0.02	0.02	0.01	0.01	
J033220.02	03:32:20.02	-27:41:04.25	25.34	25.63	25.06	25.59	23.41	21.89	21.43	21.23	20.81	20.46	0.681
-274104.2			0.50	0.60	0.41	0.19	0.02	0.01	0.01	0.01	0.00	0.00	
J033220.09	03:32:20.09	-27:41:06.75	—	26.54	25.57	—	25.19	23.20	22.25	21.74	20.97	20.56	1.309
-274106.7			—	1.41	0.67	—	0.11	0.03	0.02	0.01	0.00	0.00	
J033220.67	03:32:20.67	-27:44:46.42	24.54	24.82	26.26	25.21	23.28	21.95	21.47	21.26	20.82	20.45	0.726
-274446.4			0.25	0.31	1.45	0.14	0.02	0.01	0.01	0.01	0.00	0.00	
J033221.28	03:32:21.28	-27:44:35.60	25.62	25.34	24.82	23.76	21.55	20.34	19.89	19.70	19.31	18.96	0.620
-274435.6			0.55	0.40	0.32	0.03	0.00	0.00	0.00	0.00	0.00	0.00	
J033222.33	03:32:22.33	-27:42:26.54	···	···	···	···	25.31	23.55	22.63	22.34	21.82	21.41	1.018
-274226.5			···	···	···	···	0.09	0.03	0.02	0.01	0.01	0.01	
J033222.58	03:32:22.58	-27:41:41.18	—	···	25.19	24.31	22.36	21.32	20.96	20.85	20.53	20.24	0.509
-274141.2			—	···	0.48	0.06	0.01	0.00	0.00	0.00	0.00	0.00	
J033222.58	03:32:22.58	-27:41:52.04	—	—	—	26.38	25.28	24.71	24.55	24.78	24.65	24.59	0.529
-274152.1			—	—	—	0.15	0.04	0.04	0.04	0.06	0.03	0.04	
J033223.01	03:32:23.02	-27:43:31.49	—	—	26.27	26.49	23.89	22.45	21.97	21.78	21.43	21.10	0.740
-274331.5			—	—	0.87	0.35	0.03	0.01	0.01	0.01	0.00	0.00	
J033224.36	03:32:24.37	-27:43:15.18	—	26.26	25.62	24.44	24.47	24.64	24.60	24.46	24.07	24.75	1.271
-274315.2			—	0.29	0.22	0.02	0.02	0.04	0.04	0.04	0.02	0.05	
J033224.98	03:32:24.98	-27:41:01.52	24.79	24.20	23.56	23.45	22.43	21.38	20.99	20.85	20.48	20.20	0.569
-274101.5			0.29	0.15	0.11	0.03	0.01	0.01	0.01	0.00	0.00	0.00	
J033225.11	03:32:25.11	-27:44:25.59	25.60	25.04	25.48	25.38	25.20	24.82	24.35	24.32	24.12	23.88	1.220
-274425.6			0.29	0.16	0.29	0.07	0.05	0.05	0.04	0.04	0.02	0.03	
J033225.29	03:32:25.29	-27:42:24.20	—	—	26.05	24.59	23.09	22.41	22.21	22.14	22.05	21.92	0.612
-274224.2			—	—	0.43	0.03	0.01	0.01	0.01	0.01	0.00	0.00	
J033225.47	03:32:25.47	-27:43:27.55	···	25.35	23.87	24.55	21.98	20.52	20.04	19.87	19.47	19.10	0.690
-274327.6			···	0.70	0.26	0.11	0.01	0.00	0.00	0.00	0.00	0.00	

Continued on Next Page...

Table 1:ETG Catalog, Measured Phot. (Continued)

GOODS ID	α(J2000)	δ(J2000)	F225W	F275W	F336W	F435W	F606W	F775W	F850LP	F098M	F125W	F160W	z
			Δm	Δm	Δm	Δm	Δm	Δm	Δm	Δm	Δm	Δm	
J033225.85	03:32:25.85	-27:42:46.12	25.74	25.31	—	26.11	25.20	23.94	23.12	23.02	22.40	22.05	1.182
-274246.1			0.60	0.38	—	0.30	0.11	0.06	0.03	0.03	0.01	0.01	
J033225.97	03:32:25.97	-27:43:12.56	—	—	—	—	26.46	24.80	24.00	23.84	23.27	22.87	0.972
-274312.5			—	—	—	—	0.17	0.06	0.03	0.03	0.01	0.01	
J033225.98	03:32:25.98	-27:43:18.93	26.31	—	···	26.65	25.42	23.89	22.87	22.52	22.02	21.66	1.215
-274318.9			0.67	—	···	0.32	0.08	0.03	0.02	0.01	0.01	0.01	
J033226.05	03:32:26.05	-27:42:36.54	···	—	—	—	27.09	24.93	23.92	23.31	22.16	21.65	1.125
-274236.5			···	—	—	—	0.41	0.10	0.05	0.03	0.01	0.01	
J033226.71	03:32:26.71	-27:43:40.15	26.05	···	—	25.00	23.10	21.91	21.51	21.41	21.07	20.77	0.550
-274340.2			0.71	···	—	0.10	0.01	0.01	0.01	0.01	0.00	0.00	
J033227.18	03:32:27.18	-27:44:16.46	24.49	23.73	23.76	22.51	20.57	19.63	19.28	19.15	18.82	18.51	0.610
-274416.5			0.40	0.18	0.25	0.02	0.00	0.00	0.00	0.00	0.00	0.00	
J033227.62	03:32:27.62	-27:41:44.91	24.39	25.25	24.85	24.02	22.74	21.59	21.27	21.20	20.83	20.49	0.667
-274144.9			0.14	0.28	0.26	0.03	0.01	0.00	0.00	0.00	0.00	0.00	
J033227.70	03:32:27.70	-27:40:43.69	—	···	—	25.94	23.90	22.43	21.56	21.32	20.90	20.57	0.967
-274043.7			—	···	—	0.21	0.03	0.01	0.01	0.01	0.00	0.00	
J033227.84	03:32:27.84	-27:41:36.82	25.95	24.91	—	25.47	24.06	22.72	21.89	21.54	21.07	20.71	1.042
-274136.8			1.22	0.45	—	0.23	0.06	0.03	0.02	0.01	0.01	0.00	
J033227.86	03:32:27.86	-27:43:13.58	···	···	—	25.97	25.73	25.00	24.36	24.01	23.13	22.80	1.338
-274313.6			···	···	—	0.11	0.08	0.07	0.05	0.03	0.01	0.01	
J033228.88	03:32:28.87	-27:41:29.32	25.70	25.96	24.92	24.32	22.61	21.07	20.58	20.38	19.97	19.61	0.732
-274129.3			0.92	1.08	0.56	0.09	0.02	0.01	0.01	0.00	0.00	0.00	
J033229.04	03:32:29.04	-27:44:32.21	···	···	—	—	27.36	25.16	24.45	23.93	22.86	22.38	1.202
-274432.2			···	···	—	—	0.45	0.10	0.06	0.04	0.01	0.01	
J033229.30	03:32:29.30	-27:42:44.85	—	25.89	···	25.72	25.00	23.91	23.28	23.03	22.50	22.25	0.880
-274244.8			—	0.40	···	0.11	0.05	0.03	0.02	0.02	0.01	0.01	
J033229.64	03:32:29.64	-27:40:30.25	26.31	26.24	25.34	25.72	25.02	24.01	23.31	23.17	22.79	22.46	1.136
-274030.3			0.64	0.55	0.32	0.12	0.06	0.04	0.03	0.02	0.01	0.01	
J033230.56	03:32:30.56	-27:41:45.69	24.94	24.73	24.14	24.29	23.55	22.64	22.32	22.22	21.86	21.66	0.837
-274145.7			0.22	0.16	0.13	0.04	0.02	0.01	0.01	0.01	0.01	0.01	
J033231.84	03:32:31.84	-27:43:29.41	···	—	25.64	—	25.35	24.14	23.25	22.92	22.43	22.04	1.024
-274329.4			···	—	0.65	—	0.11	0.06	0.03	0.03	0.01	0.01	
J033232.34	03:32:32.33	-27:43:45.83	26.12	26.09	25.89	25.58	25.10	24.37	23.94	23.82	23.54	23.38	1.026
-274345.8			0.40	0.36	0.40	0.08	0.04	0.03	0.03	0.03	0.02	0.02	
J033232.57	03:32:32.57	-27:41:33.79	26.12	—	23.88	26.37	25.95	25.45	25.26	25.43	25.21	25.33	0.736
-274133.8			0.35	—	0.05	0.12	0.07	0.08	0.08	0.09	0.05	0.07	
J033232.96	03:32:32.96	-27:41:06.77	23.88s	23.76	23.63	23.27	22.40	21.90	21.67	21.59	21.51	21.31	0.472
-274106.8			0.07	0.06	0.07	0.01	0.01	0.01	0.01	0.01	0.00	0.00	
J033233.28	03:32:33.29	-27:42:35.97	—	—	—	—	27.60	25.74	24.67	24.32	23.62	23.11	1.215
-274236.0			—	—	—	—	0.44	0.14	0.06	0.05	0.02	0.01	
J033233.40	03:32:33.40	-27:41:38.92	26.01	24.97	24.66	24.52	23.59	22.39	21.62	21.43	21.02	20.74	1.045
-274138.9			0.76	0.27	0.27	0.06	0.02	0.01	0.01	0.01	0.00	0.00	

Continued on Next Page...

Table 1:ETG Catalog, Measured Phot. (Continued)

GOODS ID	α(J2000)	δ(J2000)	F225W	F275W	F336W	F435W	F606W	F775W	F850LP	F098M	F125W	F160W	z
			Δm	Δm	Δm	Δm	Δm	Δm	Δm	Δm	Δm	Δm	
J033233.87	03:32:33.87	-27:43:57.55	—	25.85	26.19	26.42	25.00	23.46	22.64	22.41	21.98	21.64	0.978
-274357.6			—	0.41	0.77	0.25	0.06	0.02	0.01	0.01	0.01	0.01	
J033234.34	03:32:34.35	-27:43:50.10	24.18	24.11	23.37	24.24	22.47	21.24	20.86	20.71	20.39	20.09	0.660
-274350.1			0.29	0.25	0.17	0.09	0.01	0.01	0.01	0.01	0.00	0.00	
J033235.10	03:32:35.10	-27:44:10.61	24.80	25.27	24.92	24.44	23.91	23.36	23.03	22.86	22.12	21.71	0.838
-274410.7			0.23	0.33	0.31	0.06	0.03	0.03	0.03	0.03	0.01	0.01	
J033235.63	03:32:35.63	-27:43:10.03	25.21	25.82	25.88	25.27	24.54	22.96	21.93	21.54	20.97	20.59	1.190
-274310.2			0.51	0.81	1.18	0.18	0.08	0.03	0.01	0.01	0.00	0.00	
J033236.72	03:32:36.72	-27:44:06.41	24.56	24.88	24.74	24.37	23.12	21.99	21.58	21.43	21.04	20.73	0.665
-274406.4			0.24	0.30	0.35	0.07	0.02	0.01	0.01	0.01	0.01	0.01	
J033237.32	03:32:37.32	-27:43:34.30	25.79	—	24.14	24.56	23.09	21.79	21.37	21.17	20.81	20.49	0.660
-274334.3			0.99	—	0.25	0.11	0.02	0.01	0.01	0.01	0.00	0.00	
J033237.38	03:32:37.38	-27:41:26.21	25.63	24.66	24.26	23.78	21.35	19.93	19.47	19.29	18.91	18.54	0.671
-274126.2			0.82	0.31	0.29	0.05	0.01	0.00	0.00	0.00	0.00	0.00	
J033238.06	03:32:38.05	-27:41:28.35	25.99	···	24.43	25.39	22.84	21.36	20.87	20.69	20.28	19.93	0.665
-274128.4			1.06	···	0.32	0.21	0.02	0.01	0.01	0.01	0.00	0.00	
J033238.36	03:32:38.36	-27:41:28.38	···	26.36	25.92	25.85	23.85	22.60	22.17	22.00	21.67	21.36	0.869
-274128.4			···	0.80	0.71	0.18	0.03	0.02	0.01	0.01	0.01	0.00	
J033238.44	03:32:38.44	-27:40:19.55	25.76	—	···	26.08	24.45	23.00	22.09	21.82	21.30	20.90	1.033
-274019.6			0.78	—	···	0.36	0.06	0.03	0.02	0.01	0.01	0.00	
J033238.48	03:32:38.48	-27:43:13.76	25.22	24.71	24.28	23.24	22.20	21.79	21.65	21.58	21.48	21.36	0.430
-274313.8			0.60	0.35	0.31	0.03	0.01	0.01	0.01	0.01	0.01	0.01	
J033239.17	03:32:39.16	-27:40:26.54	25.76	24.73	24.60	24.52	22.94	21.57	21.16	21.04	20.69	20.42	0.768
-274026.5			0.72	0.26	0.31	0.08	0.02	0.01	0.01	0.01	0.00	0.00	
J033239.17	03:32:39.17	-27:42:57.75	24.59	25.39	23.65	22.22	20.35	19.47	19.16	19.06	18.75	18.45	0.419
-274257.7			0.49	0.94	0.26	0.02	0.00	0.00	0.00	0.00	0.00	0.00	
J033239.18	03:32:39.18	-27:43:29.00	—	26.53	25.99	—	25.75	24.46	23.45	23.09	22.49	22.05	1.178
-274329.0			—	1.01	0.84	—	0.15	0.08	0.04	0.03	0.01	0.01	
J033239.52	03:32:39.52	-27:41:17.42	26.46	—	···	26.60	24.53	23.06	22.10	21.82	21.34	20.98	1.039
-274117.4			0.97	—	···	0.38	0.06	0.03	0.01	0.01	0.00	0.00	
J033240.38	03:32:40.38	-27:43:38.27	25.14	24.85	24.93	24.72	24.29	23.26	22.28	21.94	21.46	21.07	1.179
-274338.3			0.51	0.36	0.52	0.12	0.07	0.05	0.02	0.02	0.01	0.01	
J033241.63	03:32:41.63	-27:41:51.41	25.77	—	—	25.28	24.44	23.32	22.60	22.07	21.34	20.97	1.427
-274151.5			0.62	—	—	0.14	0.07	0.04	0.03	0.01	0.00	0.00	
J033242.36	03:32:42.35	-27:42:37.96	25.27	—	25.26	23.82	21.56	20.34	19.94	19.81	19.47	19.12	0.566
-274238.0			0.64	—	0.78	0.06	0.01	0.00	0.00	0.00	0.00	0.00	
J033243.93	03:32:43.93	-27:42:32.32	—	26.09	25.75	26.01	25.14	23.56	22.62	22.03	21.12	20.63	1.193
-274232.4			—	0.88	0.87	0.32	0.12	0.05	0.02	0.01	0.00	0.00	
J033244.97	03:32:44.97	-27:43:09.02	—	···	—	26.68	24.87	24.32	24.01	23.69	22.59	21.78	0.444
-274309.1			—	···	—	0.34	0.05	0.05	0.05	0.04	0.01	0.01	

Continued on Next Page...

Table 1:ETG Catalog, Measured Phot. (Continued)

GOODS ID	α(J2000)	δ(J2000)	F225W	F275W	F336W	F435W	F606W	F775W	F850LP	F098M	F125W	F160W	z
			Δm	Δm	Δm	Δm	Δm	Δm	Δm	Δm	Δm	Δm	

Notes- Objects detected in the ERS F160W mosaic but not measured by SE in the ERS or GOODS mosaics are designated " $\cdots$ ". 1σ 90% recovery limits were calculated in §4.2.2 to be equal to F225W=26.5, F275W=26.6, F336W=26.4, & F435W=26.7 mag. Detections fainter than these recovery limits are designated "—". Measured photometric uncertainties, Δm, are provided for each ETG.

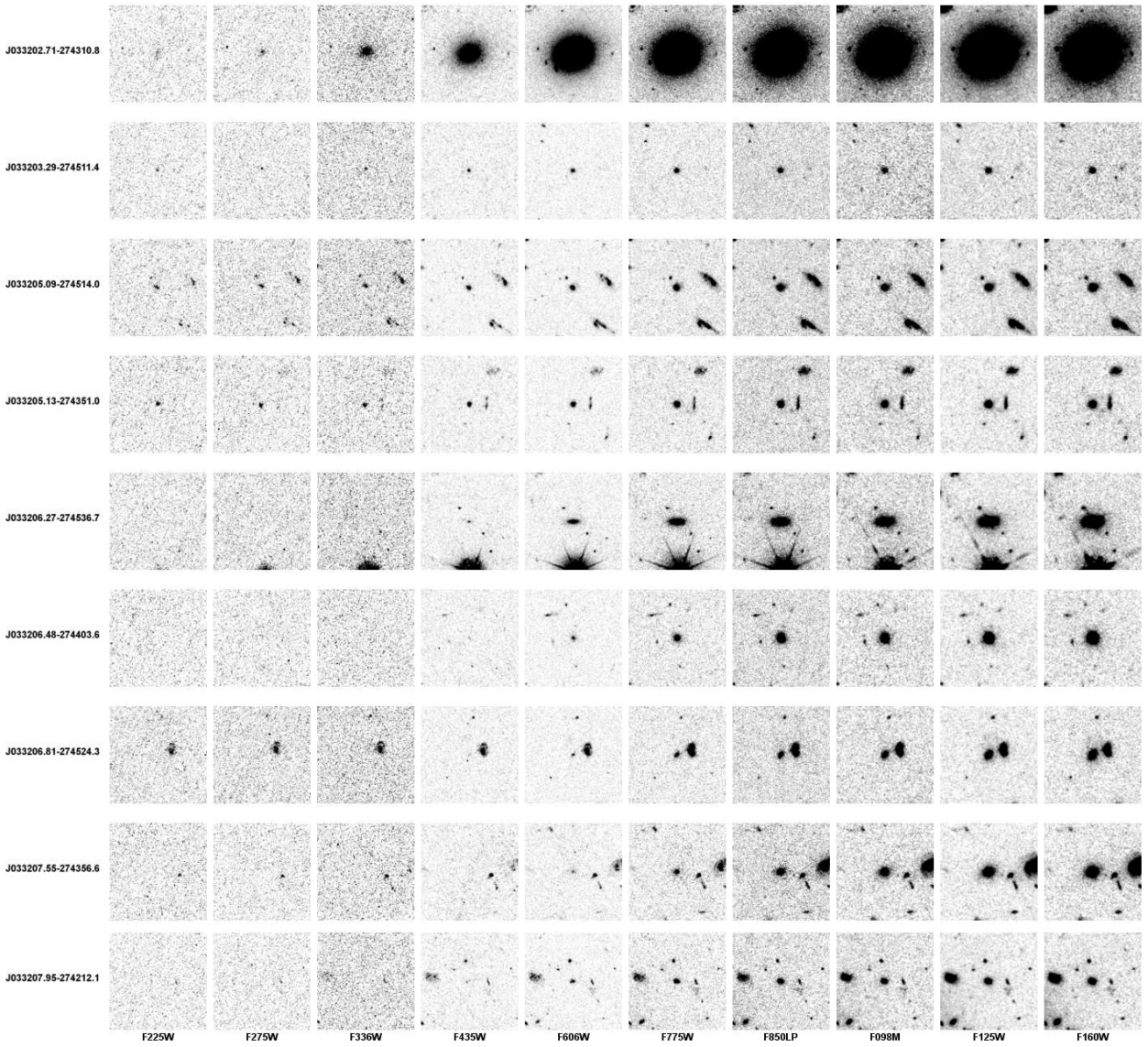

Figure 4.1: Ten-band thumbnails of the first 9 catalog ETGs ordered, from left to right, by increasing wavelength with the GOODS Object ID. Each image has been converted into flux units (nJy), and all are displayed with the same scale. All postage stamps are 11.2 arcseconds (128 pixels) on a side. Images of all ETGs are provided in Appendix B.

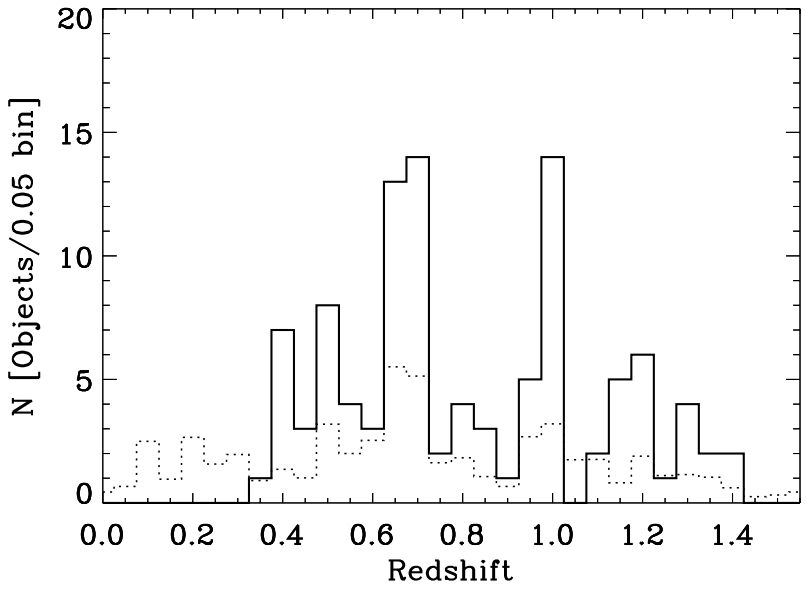

Figure 4.2: The spectroscopic redshift distribution of ETGs is plotted as a solid histogram; the distribution of spectroscopic redshifts for the entire CDF-S is plotted as a dot-dashed histogram. The CDF-S distribution has been scaled by a factor of $\frac{1}{75}$, such that both redshift distributions can be plotted on the same axis for comparison. The peaks in this distribution indicate known large-scale structure in the CDF-S. The selection of ETGs amplifies these peaks because ETGs are known to be more strongly clustered than field galaxies.

Table 4.2: Early-Type Galaxies Catalog, Additional Parameters

GOODS ID	X-ray/Radio Source?	AGN Note	Comments
J033202.71-274310.8	–	–	LSB-Comp
J033203.29-274511.4	–	–	–
J033205.09-274514.0	–	–	Comp
J033205.13-274351.0	–	–	Comp
J033206.27-274536.7	X*	ABS	S0
J033206.48-274403.6	–	–	LSB-Comp
J033206.81-274524.3	–	–	–
J033207.55-274356.6	–	–	–
J033207.95-274212.1	–	–	–
J033208.41-274231.3	–	–	Comp
J033208.45-274145.9	–	–	Comp
J033208.53-274217.7	X*	ABS	b-Comp
J033208.55-274231.1	–	–	Comp
J033208.65-274501.8	–	–	b-Comp
J033208.90-274344.3	–	–	–
J033209.09-274510.8	–	–	–
J033209.19-274225.6	X*	ABS	S0
J033210.04-274333.1	–	–	VGM
J033210.12-274333.3	–	–	VGM
J033210.16-274334.3	–	–	VGM
J033210.76-274234.6	–	–	DC
J033210.86-274441.2	–	–	–
J033211.21-274533.4	–	–	LSB-Comp
J033211.61-274554.1	–	–	S0
J033212.20-274530.1	XR*	AGN-2,LEX	VGM
J033212.31-274527.4	–	–	VGM
J033212.47-274224.2	–	–	–
J033214.26-274254.2	–	–	Comp
J033214.45-274456.6	–	–	Comp
J033214.65-274136.6	–	–	–
J033214.68-274337.1	–	–	S0,Comp
J033214.73-274153.3	–	–	–
J033214.78-274433.1	–	–	–
J033214.83-274157.1	–	–	m
J033215.98-274422.9	–	–	Comp
J033216.19-274423.1	–	–	Comp
J033217.11-274220.9	–	–	c,b-Comp
J033217.12-274407.7	–	–	–
J033217.14-274303.3	XR*	AGN-1,BLAGN	LSB-Comp
J033217.49-274436.7	–	–	–
J033217.91-274122.7	–	–	–
J033218.31-274233.5	–	–	S0,VGM
J033218.64-274144.4	–	–	c
J033218.74-274415.8	–	–	VGM
J033219.02-274242.7	–	–	VGM
J033219.48-274216.8	–	–	–
J033219.59-274303.8	–	–	VGM
J033219.77-274204.0	–	–	c,LSB-Comp
J033220.02-274104.2	–	–	LSB-Comp
J033220.09-274106.7	–	–	Comp.
J033220.67-274446.4	–	–	S0,Comp
J033221.28-274435.6	XR*	–	m,VGM
J033222.33-274226.5	–	–	S0
J033222.58-274141.2	–	–	Comp
J033222.58-274152.1	–	–	c
J033223.01-274331.5	–	–	Comp
J033224.36-274315.2	–	–	c
J033224.98-274101.5	X*	AGN-2,LEX	Comp
J033225.11-274425.6	–	–	c
J033225.29-274224.2	–	–	LSB-Comp
J033225.47-274327.6	–	–	Comp

Continued on next page ...

Table 2:ETG Catalog, Additional Parameters (Continued)

GOODS ID	X-ray/Radio Source?	AGN Note	Comments
J033225.85-274246.1	–	–	c,VGM
J033225.97-274312.5	–	–	c
J033225.98-274318.9	–	–	S0,VGM
J033226.05-274236.5	–	–	b-Comp
J033226.71-274340.2	–	–	Comp
J033227.18-274416.5	–	–	S0,m
J033227.62-274144.9	X*	AGN-2,HEX	S0
J033227.70-274043.7	–	–	S0
J033227.84-274136.8	–	–	Comp
J033227.86-274313.6	–	–	c
J033228.88-274129.3	–	–	d,Comp
J033229.04-274432.2	–	–	c
J033229.30-274244.8	–	–	–
J033229.64-274030.3	–	–	–
J033230.56-274145.7	–	–	m,b-Comp
J033231.84-274329.4	–	–	c
J033232.34-274345.8	–	–	c
J033232.57-274133.8	–	–	c
J033232.96-274106.8	–	–	LSB-Comp
J033233.28-274236.0	–	–	c
J033233.40-274138.9	–	–	–
J033233.87-274357.6	–	–	–
J033234.34-274350.1	X*	AGN-2,LEX	b-Comp
J033235.10-274410.7	–	–	c,VGM
J033235.63-274310.2	–	–	S0,Comp
J033236.72-274406.4	–	–	S0
J033237.32-274334.3	–	–	LSB-Comp
J033237.38-274126.2	–	–	Comp.
J033238.06-274128.4	–	–	b-Comp.
J033238.36-274128.4	–	–	LSB-Comp
J033238.44-274019.6	–	–	–
J033238.48-274313.8	–	–	–
J033239.17-274026.5	–	–	m
J033239.17-274257.7	–	–	–
J033239.18-274329.0	–	–	–
J033239.52-274117.4	–	–	–
J033240.38-274338.3	–	–	–
J033241.63-274151.5	–	–	–
J033242.36-274238.0	–	–	Comp
J033243.93-274232.4	–	–	c
J033244.97-274309.1	–	–	c

Notes-

Col. 1 : GOODS Identifier String

Col. 2 : Galaxies identified in X-ray, Radio, or both surveys are denoted here by "X*", "R*" or "XR*", respectively.

Col. 3 : X-ray and optical spectral classification of ETGs are from Szokoly et al. (2004). For X-ray classifications, objects are primarily distinguished by the hardness ratio (HR) of the X-ray spectrum: ≤ 0.2 for AGN-1 ($>$-0.2 for AGN-2). For Optical classification, "BLAGN" denotes a broad-line AGN source; "HEX" ("LEX") indicates "high" ("low") degree of excitation; "ABS" denotes a typical galaxy absorption line system; for more details on these designations see Szokoly et al. (2004).

Col. 4 : Comments flags: Comp –potential satellites or companion; b-Comp. – blue companions; LSB-Comp. – low surface brightness companions; c – compact; DC – Double Core; d – potential dust lane; S0 – S0 candidate; VGM – visual group member. For details regarding each of these designations, see §4.2.4.

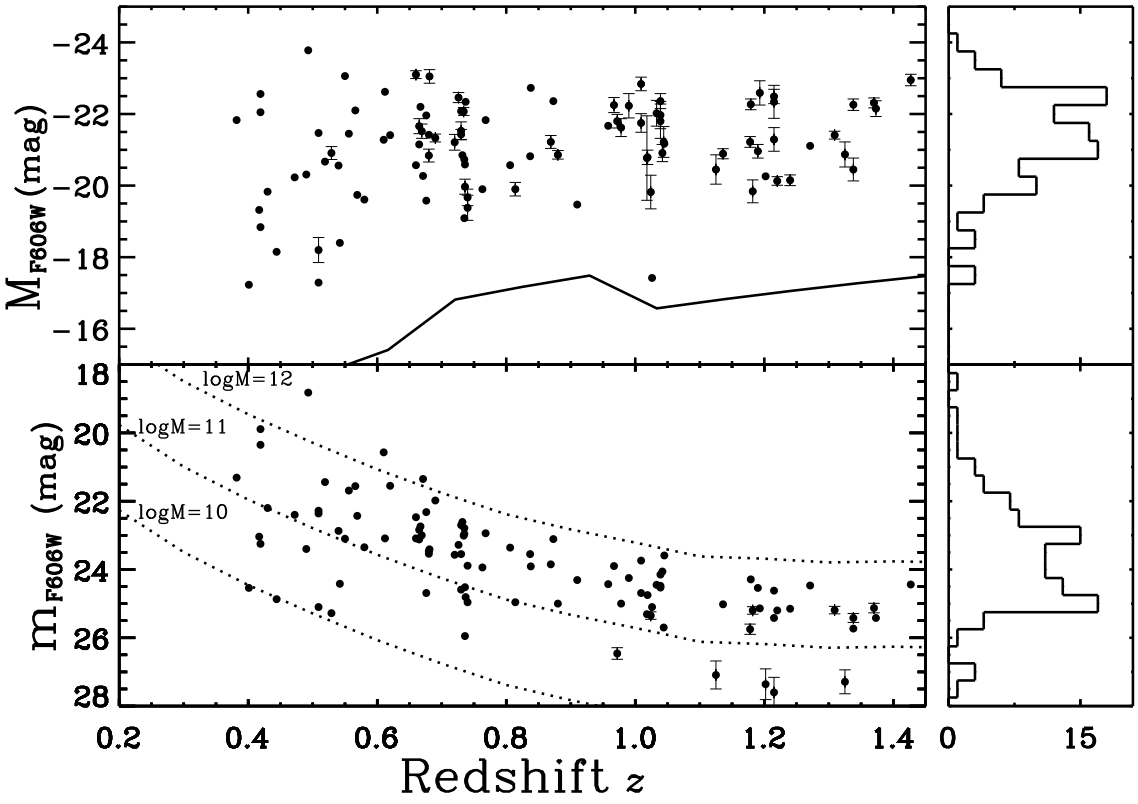

Figure 4.3: Absolute and apparent magnitudes are plotted versus the spectroscopic redshift of each ETG. For clarity, photometric uncertainties are only overplotted if the $\Delta m > 0.1$ AB mag. Upper Panel: The absolute F606W magnitudes were measured for the ETGs using the best-fit single burst stellar population model to the SED of each ETG as outlined in §4.2.3. I overplot the photometric completeness limits (solid curve), which I derived from the recovery limits (see §4.2.2). Lower Panel: In addition to the apparent F606W magnitudes measured for the ETGs, I overplot the apparent F606W magnitudes of a maximally old BC03 model galaxy with a star-formation history defined by Equation 5.1, with $\log(\tau[\mathrm{Gyr}])=-0.3$ and $z_f=4.0$. For each model, we assume no dust, solar metallicity and a Salpeter IMF. The only free parameter was the stellar mass of the template galaxy, which we overplot for each curve. The majority of ETGs are bounded by the $10 < \log(\mathrm{M}\ [\mathrm{M}_\odot]) < 12$ curves; in comparison to published mass functions of massive galaxies (e.g., Marchesini et al. , 2009) this suggests that these ETGs are near or above the characteristic stellar mass. I provide for both panels, at right, a number histogram, corresponding to the plotted absolute (apparent) magnitudes.

Table 4.3: Model Galaxy Template Parameters

Parameter	Range
t_2	0.001 - 12 Gyr
f_2	0.001 - 1
Z_2	0.1 - 2.5 $Z_\odot$
E(B–V)	0 - 0.5

The parameter space represented in the grid of spectral model templates used to determine the (NUV–V), (FUV–V), (g′–r′) colors is provided here. The variable parameters outlined here are as follows : t_2 = time of second star-formation burst; f_2 = fraction of stars generated in second burst; Z_2 = stellar metallicity of second burst; E(B–V) = dust extinction parameter. For complete details of the model templates and their star-formation histories, see §4.4

Table 4.4: Proxy Filter List for (UV–V) Rest-Frame Color Conversions

Redshift	GALEX FUV Proxy	GALEX NUV Proxy	Sloan g′ Proxy	Sloan r′ Proxy	Johnson V Proxy
0.30	F225W	F275W	F606W	F775W	F775W
0.35	F225W	F336W	F606W	F850LP	F775W
0.40	F225W	F336W	F606W	F850LP	F775W
0.45	F225W	F336W	F606W	F850LP	F775W
0.50	F225W	F336W	F775W	F098M	F850LP
0.55	F225W	F336W	F775W	F098M	F850LP
0.60	F225W	F336W	F775W	F098M	F850LP
0.65	F225W	F336W	F775W	F098M	F850LP
0.70	F275W	F435W	F775W	F098M	F098M
0.75	F275W	F435W	F850LP	F098M	F098M
0.80	F275W	F435W	F850LP	F098M	F098M
0.85	F275W	F435W	F850LP	F098M	F098M
0.90	F275W	F435W	F850LP	F098M	F098M
1.00	F275W	F435W	F098M	F125W	F098M
1.10	F336W	F435W	F098M	F125W	F125W
1.20	F336W	F435W	F098M	F125W	F125W
1.30	F336W	F606W	F098M	F125W	F125W
1.40	F336W	F606W	F098M	F125W	F125W

Notes: The development and application of these color transformations is discussed in §4.4.

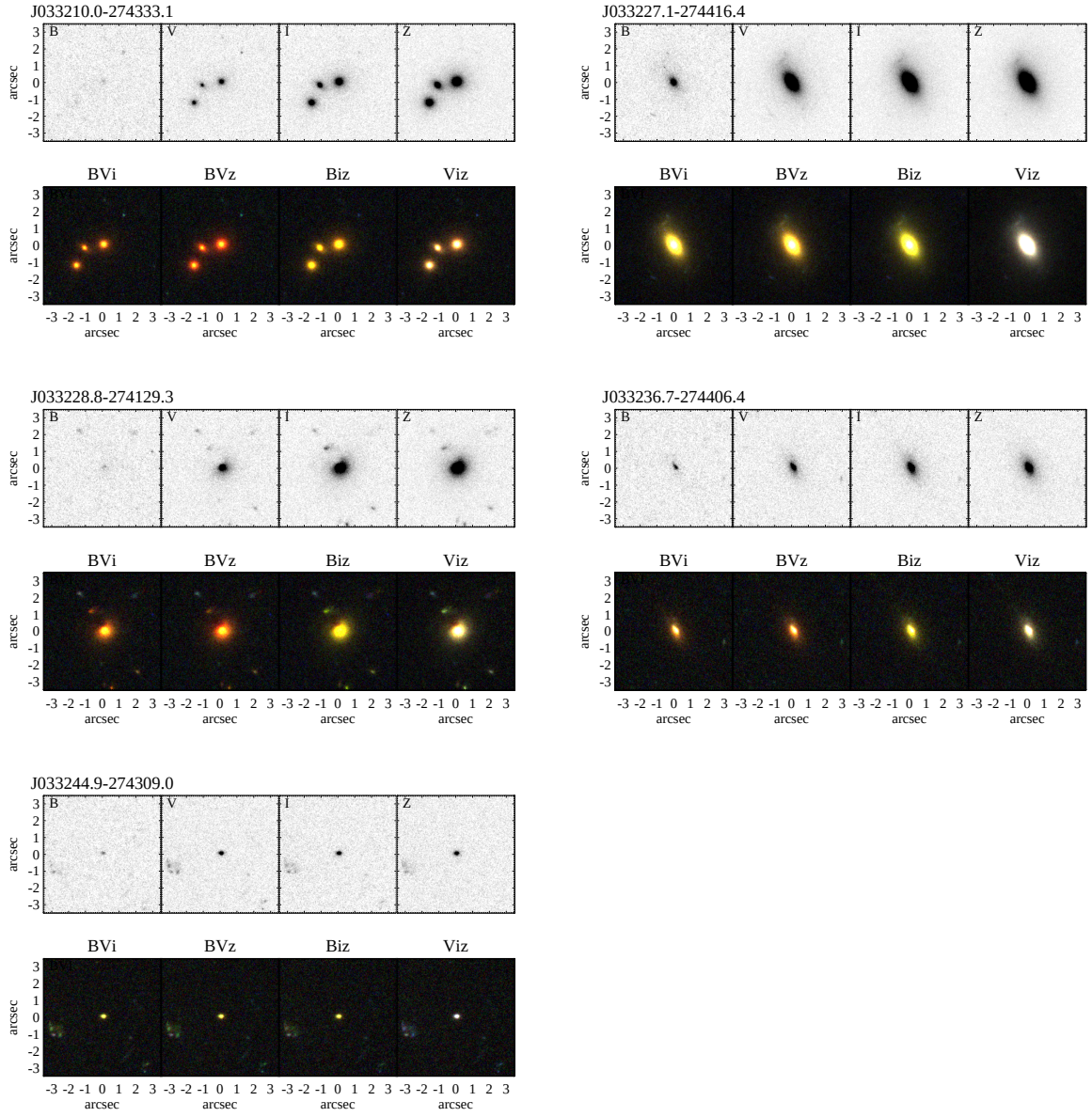

Figure 4.4: Cutouts of six ETGs selected to represent one of each of the classes defined in §4.2.4. The galaxy cutouts, and the comment class it represents, is defined as follows : J033210.0-274333.1 — Visual Group Member; J033227.1-274416.4 — Low Surface Brightness Companion (North-east, roughly parallel to minor axis); J033228.8-274129.3 — dust; J033236.7-274406.4 — S0; J033244.9-274309.0 — compact. These images were generated using the GOODS ACS Cutout Tool, available at http: // archive. stsci.edu/eidol_v2.php

Table 4.5: Early-Type Galaxies Catalog, Converted Photometry

GOODS ID	$(FUV–V)_p$	$(FUV–V)_r$	$(NUV–V)_p$	$(NUV–V)_r$	$(g'–r')_p$	$(g'–r')_r$	M_{F606W}	M_V	$M_{r'}$	m_V	$m_{r'}$
	Δm		Δm		Δm						
J033202.71	4.78	5.08	3.34	3.38	0.81	0.43	-23.87	-23.78	-23.93	19.39	18.57
-274310.8		0.17		0.05		0.00	0.00				
J033203.29	2.38	2.29	1.88	1.76	0.34	0.41	-18.47	-18.40	-18.53	25.04	24.28
-274511.4		0.33		0.24		0.03	0.07				
J033205.09	1.94	1.90	1.53	1.50	0.01	0.01	-19.96	-19.90	-20.01	24.42	23.85
-274514.0		0.16		0.03		0.06	0.04				
J033205.13	1.63	1.61	1.43	1.44	0.04	0.14	-20.59	-20.57	-20.62	23.85	23.10
-274351.0		0.06		0.02		0.04	0.03				
J033206.27	—	—	4.77	4.16	0.69	0.75	-21.68	-21.52	-21.80	23.54	22.85
-274536.7		—		0.58		0.01	0.20				
J033206.48	3.93	3.90	—	—	0.25	0.81	-21.81	-21.67	-21.92	25.13	24.18
-274403.6		0.45		—		0.03	0.05				
J033206.81	4.34	3.85	3.38	3.36	0.72	0.44	-22.26	-22.15	-22.35	26.56	25.41
-274524.3		0.86		0.10		0.01	0.22				
J033207.55	—	—	3.25	3.20	0.51	0.32	-22.38	-22.31	-22.45	26.27	25.12
-274356.6		—		0.16		0.01	2.23				
J033207.95	—	—	3.44	3.48	0.63	0.65	-19.80	-19.67	-19.90	25.44	24.87
-274212.1		—		0.25		0.02	0.23				
J033208.41	4.96	4.80	4.64	4.23	0.55	0.68	-20.71	-20.56	-20.82	23.49	22.73
-274231.3		0.92		0.74		0.01	0.09				
J033208.45	3.98	3.92	3.93	4.01	0.77	0.80	-21.59	-21.43	-21.71	24.03	23.46
-274145.9		0.42		0.15		0.01	0.14				
J033208.53	4.45	4.39	3.78	3.84	0.69	0.72	-22.23	-22.08	-22.35	23.18	22.61
-274217.7		0.45		0.11		0.00	0.10				
J033208.55	2.78	2.67	2.40	2.23	0.47	0.59	-18.33	-18.20	-18.44	25.72	24.96
-274231.1		0.73		0.60		0.05	0.35				
J033208.65	—	—	4.46	4.48	0.14	0.49	-22.48	-22.36	-22.57	23.60	22.85
-274501.8		—		0.09		0.00	0.10				
J033208.90	2.79	2.67	2.63	2.49	0.25	0.29	-19.67	-19.61	-19.71	23.97	23.21
-274344.3		0.28		0.29		0.01	0.05				
J033209.09	1.59	1.72	1.03	1.03	0.56	0.31	-17.26	-17.23	-17.28	25.11	24.29
-274510.8		0.29		0.21		0.02	0.08				
J033209.19	—	—	4.42	4.55	0.72	0.74	-21.36	-21.21	-21.47	24.05	23.48
-274225.6		—		0.24		0.01	0.22				
J033210.04	4.35	4.30	4.42	4.48	0.52	0.36	-23.00	-22.84	-23.12	24.65	23.49
-274333.1		0.47		0.16		0.00	0.19				
J033210.12	···	···	4.54	4.58	0.47	0.31	-21.91	-21.75	-22.02	25.60	24.44
-274333.3		···		0.23		0.00	0.26				

Continued on Next Page...

Table 5: ETG Catalog, Converted Phot. (Continued)

GOODS ID	$(FUV–V)_p$	$(FUV–V)_r$ (Unc.)	$(NUV–V)_p$	$(NUV–V)_r$ (Unc.)	$(g'–r')_p$	$(g'–r')_r$ (Unc.)	M_{F606W}	M_V	$M_{r'}$	m_V	$m_{r'}$
J033210.16	···	···	4.38	4.42	0.20	0.65	-22.38	-22.23	-22.50	24.95	24.00
-274334.3		···		0.31		0.03	0.34				
J033210.76	4.45	4.74	4.04	4.01	1.25	0.74	-22.71	-22.56	-22.82	20.46	19.64
-274234.6		0.15		0.12		0.00	0.01				
J033210.86	3.47	3.33	—	—	0.55	0.60	-19.71	-19.58	-19.80	25.23	24.54
-274441.2		0.64		—		0.02	0.04				
J033211.21	—	—	4.75	3.80	0.47	0.31	-22.60	-22.49	-22.68	25.81	24.47
-274533.4		—		0.15		0.00	0.20				
J033211.61	4.12	4.07	4.42	4.47	0.44	0.29	-22.51	-22.36	-22.62	25.06	23.90
-274554.1		0.40		0.18		0.00	0.21				
J033212.20	4.40	4.24	3.94	3.49	0.56	0.61	-22.08	-21.96	-22.18	22.86	22.17
-274530.1		0.47		0.28		0.01	0.09				
J033212.31	···	···	3.42	3.06	0.56	0.61	-20.97	-20.84	-21.06	24.00	23.31
-274527.4		···		0.33		0.01	0.18				
J033212.47	—	—	3.30	3.30	1.12	0.65	-19.45	-19.32	-19.55	23.61	22.79
-274224.2		—		0.39		0.00	0.06				
J033214.26	···	···	3.03	3.07	0.14	0.46	-19.82	-19.71	-19.91	25.45	24.70
-274254.2		···		0.18		0.11	0.19				
J033214.45	—	—	4.65	4.82	0.56	0.59	-20.03	-19.90	-20.13	25.29	24.72
-274456.6		—		0.79		0.02	0.06				
J033214.65	—	—	3.64	3.68	0.74	0.45	-22.48	-22.34	-22.59	26.56	25.41
-274136.6		—		0.15		0.01	0.32				
J033214.68	2.54	2.53	2.20	2.30	0.07	0.27	-20.53	-20.45	-20.60	25.01	24.06
-274337.1		0.23		0.05		0.06	0.06				
J033214.73	···	···	—	—	1.17	0.65	-19.58	-19.47	-19.67	23.97	23.15
-274337.1		···		—		0.00	0.07				
J033214.78	—	—	4.65	4.82	0.69	0.72	-20.46	-20.31	-20.58	25.00	24.43
-274433.1		—		0.56		0.02	0.05				
J033214.83	—	—	—	—	0.50	0.55	-20.71	-20.59	-20.81	24.08	23.39
-274157.1		—		—		0.01	0.09				
J033215.98	4.51	4.46	3.19	3.21	0.50	0.53	-21.52	-21.42	-21.61	23.44	22.87
-274422.9		0.74		0.06		0.01	0.06				
J033216.19	3.02	3.25	3.17	3.17	1.10	0.64	-19.21	-19.09	-19.30	23.82	23.00
-274423.1		0.52		0.68		0.00	0.06				
J033217.11	0.37	0.28	0.67	0.58	0.76	0.51	-18.85	-18.84	-18.84	26.34	25.00
-274220.9		0.09		0.03		0.04	0.15				
J033217.12	···	···	3.97	4.06	0.61	0.63	-20.29	-20.15	-20.39	25.07	24.50
-274407.7		···		0.27		0.01	0.25				
J033217.14	3.62	3.47	2.84	2.67	0.44	0.52	-21.64	-21.53	-21.73	22.31	21.55
-274303.3		0.12		0.07		0.00	0.02				
J033217.49	3.85	3.79	3.45	3.48	0.56	0.59	-21.57	-21.45	-21.67	23.49	22.92
-274436.7		0.44		0.12		0.01	0.11				

Continued on Next Page...

Table 5: ETG Catalog, Converted Phot. (Continued)

GOODS ID	$(FUV–V)_p$	$(FUV–V)_r$ (Unc.)	$(NUV–V)_p$	$(NUV–V)_r$ (Unc.)	$(g'–r')_p$	$(g'–r')_r$ (Unc.)	M_{F606W}	M_V	$M_{r'}$	m_V	$m_{r'}$
J033217.91	4.71	4.65	4.92	4.91	0.49	0.32	-22.21	-22.07	-22.32	25.39	24.23
-274122.7		1.07		0.41		0.00	0.48				
J033218.31	3.96	3.82	4.72	4.30	0.49	0.60	-21.94	-21.80	-22.05	22.06	21.30
-274233.5		0.19		0.41		0.00	0.04				
J033218.64	···	···	3.91	4.00	0.73	0.45	-20.80	-20.67	-20.91	28.43	27.28
-274144.4		···		0.44		0.01	0.37				
J033218.74	4.28	4.14	4.03	3.69	0.44	0.55	-21.00	-20.87	-21.11	22.90	22.14
-274415.8		0.40		0.35		0.01	0.06				
J033219.02	—	—	3.55	3.67	0.43	0.28	-21.62	-21.47	-21.73	25.66	24.50
-274242.7		—		0.17		0.01	0.20				
J033219.48	3.88	4.16	3.59	3.58	1.12	0.70	-20.93	-20.79	-21.03	21.68	21.08
-274216.8		0.28		0.30		0.00	0.03				
J033219.59	4.11	4.06	3.76	3.82	0.56	0.58	-21.94	-21.83	-22.03	23.27	22.70
-274303.8		0.32		0.09		0.00	0.09				
J033219.77	···	···	3.68	3.79	0.43	0.28	-20.85	-20.73	-20.95	26.61	25.45
-274204.0		···		0.38		0.01	0.43				
J033220.02	3.90	3.76	3.82	3.40	0.66	0.71	-21.37	-21.22	-21.49	23.95	23.26
-274104.2		0.48		0.34		0.01	0.19				
J033220.09	4.60	4.09	4.22	4.39	0.76	0.47	-23.20	-23.05	-23.31	26.33	25.18
-274106.7		0.61		0.14		0.00	1.67				
J033220.67	3.55	3.50	3.94	4.03	0.69	0.71	-21.56	-21.41	-21.68	23.76	23.19
-274446.4		0.30		0.15		0.01	0.14				
J033221.28	5.73	5.54	4.93	4.51	0.63	0.73	-22.61	-22.46	-22.72	22.09	21.40
-274435.6		0.54		0.26		0.00	0.03				
J033222.33	···	···	···	···	0.51	0.35	-21.56	-21.41	-21.68	26.22	25.06
-274226.5		···		···		0.01	0.09				
J033222.58	—	—	4.23	3.86	0.47	0.58	-20.90	-20.77	-21.01	22.98	22.22
-274141.2		—		0.42		0.00	0.06				
J033222.58	—	—	—	—	0.07	0.08	-17.31	-17.29	-17.32	25.90	25.14
-274152.1		—		—		0.08	0.18				
J033223.01	—	—	4.70	4.88	0.67	0.69	-21.04	-20.91	-21.15	24.37	23.80
-274331.5		—		0.39		0.01	0.35				
J033224.36	1.55	1.31	0.37	0.33	0.38	0.25	-19.37	-19.38	-19.35	25.66	24.32
-274315.2		0.19		0.02		0.02	0.09				
J033224.98	3.80	3.64	2.56	2.42	0.52	0.63	-21.24	-21.11	-21.33	23.05	22.29
-274101.5		0.28		0.10		0.01	0.03				
J033225.11	1.35	1.14	1.25	1.06	0.20	0.13	-19.79	-19.74	-19.82	26.39	25.05
-274425.6		0.25		0.05		0.02	0.12				
J033225.29	—	—	3.84	3.59	0.27	0.31	-20.16	-20.13	-20.20	23.63	22.94
-274224.2		—		0.37		0.01	0.03				
J033225.47	···	···	4.00	3.54	0.64	0.70	-22.77	-22.62	-22.89	22.52	21.83
-274327.6		···		0.21		0.00	0.11				

Continued on Next Page...

Table 5: ETG Catalog, Converted Phot. (Continued)

GOODS ID	$(FUV–V)_p$	$(FUV–V)_r$ (Unc.)	$(NUV–V)_p$	$(NUV–V)_r$ (Unc.)	$(g'–r')_p$	$(g'–r')_r$ (Unc.)	M_{F606W}	M_V	$M_{r'}$	m_V	$m_{r'}$
J033225.85	—	—	3.71	3.00	0.62	0.42	-21.43	-21.33	-21.52	26.27	25.00
-274246.1		—		0.24		0.02	0.32				
J033225.97	—	—	—	—	0.16	0.54	-19.98	-19.84	-20.09	27.16	26.21
-274312.5		—		—	0.12	0.19					
J033225.98	···	···	4.62	3.71	0.50	0.33	-21.92	-21.80	-22.02	26.61	25.27
-274318.9		···		0.24		0.00	0.33				
J033226.05	—	—	—	—	1.14	0.82	-21.47	-21.29	-21.60	28.16	26.89
-274236.5		—		—		0.02	0.42				
J033226.71	4.53	4.36	—	—	0.50	0.59	-20.58	-20.45	-20.69	23.72	22.96
-274340.2		0.69		—		0.01	0.10				
J033227.18	5.20	5.02	4.47	4.14	0.47	0.55	-23.18	-23.06	-23.27	21.11	20.42
-274416.5		0.39		0.21		0.00	0.02				
J033227.62	3.11	2.99	3.64	3.25	0.38	0.43	-21.40	-21.28	-21.49	23.28	22.59
-274144.9		0.13		0.21		0.00	0.03				
J033227.70	···	···	4.62	4.63	0.23	0.76	-22.34	-22.20	-22.44	24.60	23.65
-274043.7		···		0.19		0.03	0.21				
J033227.84	3.36	3.32	3.92	4.03	0.47	0.31	-22.40	-22.25	-22.50	24.97	23.81
-274136.8		0.44		0.21		0.01	0.24				
J033227.86	—	—	2.60	2.46	0.88	0.54	-21.05	-20.91	-21.16	26.87	25.72
-274313.6		—		0.08		0.01	0.16				
J033228.88	5.57	5.51	3.94	4.02	0.69	0.71	-22.41	-22.26	-22.53	23.09	22.52
-274129.3		1.07		0.09		0.00	0.09				
J033229.04	—	—	—	—	1.07	0.71	-21.03	-20.85	-21.16	28.55	27.21
-274432.2		—		—		0.02	0.10				
J033229.30	2.85	2.84	2.68	2.75	0.25	0.82	-20.39	-20.26	-20.49	25.49	24.74
-274244.8		0.39		0.11		0.08	0.12				
J033229.64	2.54	2.19	2.92	2.37	0.38	0.25	-20.95	-20.86	-21.02	26.09	24.82
-274030.3		0.28		0.09		0.01	0.14				
J033230.56	2.51	2.48	2.07	2.09	0.10	0.33	-20.97	-20.89	-21.04	24.04	23.29
-274145.7		0.15		0.04		0.04	0.05				
J033231.84	—	—	—	—	0.49	0.32	-20.97	-20.82	-21.08	26.26	25.10
-274329.4		—		—		0.02	0.12				
J033232.34	2.27	2.24	1.76	1.91	0.28	0.17	-19.88	-19.82	-19.94	26.01	24.85
-274345.8		0.35		0.08		0.02	0.10				
J033232.57	—	—	0.94	0.87	0.02	0.03	-17.42	-17.42	-17.42	26.43	25.86
-274133.8		—		0.14		0.13	0.21				
J033232.96	1.97	2.14	1.72	1.79	0.73	0.38	-20.03	-19.97	-20.08	22.97	22.15
-274106.8		0.07		0.07		0.00	0.02				
J033233.28	—	—	4.19	3.38	0.69	0.46	-20.39	-20.23	-20.51	28.79	27.45
-274236.0		—		0.55		0.03	0.85				
J033233.40	3.53	3.49	3.09	3.24	0.41	0.26	-22.45	-22.34	-22.53	24.50	23.34
-274138.9		0.26		0.05		0.00	0.06				

Continued on Next Page...

Table 5: ETG Catalog, Converted Phot. (Continued)

GOODS ID	$(FUV–V)_p$	$(FUV–V)_r$ (Unc.)	$(NUV–V)_p$	$(NUV–V)_r$ (Unc.)	$(g'–r')_p$	$(g'–r')_r$ (Unc.)	M_{F606W}	M_V	$M_{r'}$	m_V	$m_{r'}$
J033233.87	3.44	3.42	4.01	4.06	0.23	0.73	-21.31	-21.17	-21.42	25.70	24.75
-274357.6		0.40		0.23		0.03	0.25				
J033234.34	3.31	3.19	2.66	2.42	0.52	0.58	-21.75	-21.62	-21.85	23.01	22.32
-274350.1		0.28		0.14		0.01	0.09				
J033235.10	2.40	2.38	1.57	1.59	0.17	0.55	-20.69	-20.57	-20.79	24.40	23.65
-274410.7		0.32		0.06		0.13	0.08				
J033235.63	4.90	4.37	4.30	3.47	0.56	0.39	-22.88	-22.73	-22.99	25.61	24.34
-274310.2		1.10		0.14		0.00	0.19				
J033236.72	2.97	2.86	3.30	2.97	0.56	0.61	-21.09	-20.96	-21.19	23.66	22.97
-274406.4		0.23		0.29		0.01	0.07				
J033237.32	4.42	4.26	2.96	2.68	0.62	0.67	-21.29	-21.15	-21.40	23.63	22.94
-274334.3		0.96		0.21		0.01	0.11				
J033237.38	6.15	5.98	4.96	4.32	0.63	0.69	-23.26	-23.10	-23.37	21.89	21.20
-274126.2		0.81		0.23		0.00	0.05				
J033238.06	5.11	4.95	3.73	3.33	0.67	0.72	-21.82	-21.66	-21.94	23.38	22.69
-274128.4		1.04		0.26		0.01	0.21				
J033238.36	4.36	4.33	3.85	3.88	0.17	0.58	-21.33	-21.22	-21.42	24.34	23.59
-274128.4		0.79		0.17		0.04	0.18				
J033238.44	—	—	4.26	4.33	0.51	0.35	-22.17	-22.02	-22.28	25.36	24.20
-274019.6		—		0.32		0.01	0.36				
J033238.48	3.42	3.67	2.48	2.49	0.55	0.29	-19.88	-19.83	-19.91	22.77	21.95
-274313.8		0.62		0.30		0.00	0.03				
J033239.17	3.68	3.63	3.47	3.53	0.12	0.35	-21.94	-21.83	-22.03	23.42	22.85
-274026.5		0.25		0.08		0.04	0.08				
J033239.17	5.12	5.41	4.18	4.14	1.19	0.70	-22.19	-22.05	-22.30	20.92	20.10
-274257.7		0.49		0.24		0.00	0.02				
J033239.18	3.50	3.06	—	—	0.60	0.41	-21.36	-21.22	-21.46	26.82	25.55
-274329.0		0.76		—		0.02	0.17				
J033239.52	—	—	4.78	4.79	0.47	0.32	-22.11	-21.97	-22.21	25.44	24.28
-274117.4		—		0.33		0.00	0.38				
J033240.38	3.47	3.03	3.26	2.64	0.47	0.32	-22.39	-22.27	-22.48	25.36	24.09
-274338.3		0.47		0.09		0.01	0.15				
J033241.63	—	—	3.10	2.94	0.73	0.41	-23.05	-22.95	-23.14	25.37	24.48
-274151.5		—		0.07		0.00	0.16				
J033242.36	5.32	5.14	5.31	4.83	0.52	0.63	-22.24	-22.10	-22.36	22.18	21.42
-274238.0		0.62		0.66		0.00	0.06				
J033243.93	4.62	4.11	4.88	3.94	0.91	0.64	-22.77	-22.59	-22.90	26.21	24.94
-274232.4		0.80		0.25		0.00	0.34				
J033244.97	—	—	—	—	0.86	0.49	-18.31	-18.15	-18.43	25.44	24.62
-274309.1		—		—		0.04	0.35				

Continued on Next Page...

Table 5: ETG Catalog, Converted Phot. (Continued)

GOODS ID	$(FUV–V)_p$	$(FUV–V)_r$ (Unc.)	$(NUV–V)_p$	$(NUV–V)_r$ (Unc.)	$(g'–r')_p$	$(g'–r')_r$ (Unc.)	M_{F606W}	M_V	$M_{r'}$	m_V	$m_{r'}$

Notes: Subscripts on column headings designate whether the colors are observed ("p"– proxy) or rest-frame ("r"). Galaxies that were SE detections but fell below the 90%1-σ completeness limits (see §4.2.2) in one or more filters used in the transformation are denoted "—". ETGs which were SE non-detections in the blue proxy band are denoted " $\cdots$ "(see §4.1). The uncertainties, Δm, reported for rest-frame quantities include measured photometeric and systematic uncertainties (see §4.2.2 and 4.4).

Table 4.6: WFC3 UVIS Estimated Red-Leak† for Model ETGs

Filter	BC03	CWW
F336W	0.2%	2.9×10^{-2}%
F275W	1.2%	0.15%
F225W	3.5%	0.26%

Notes-†—The red-leak is defined in §4.6

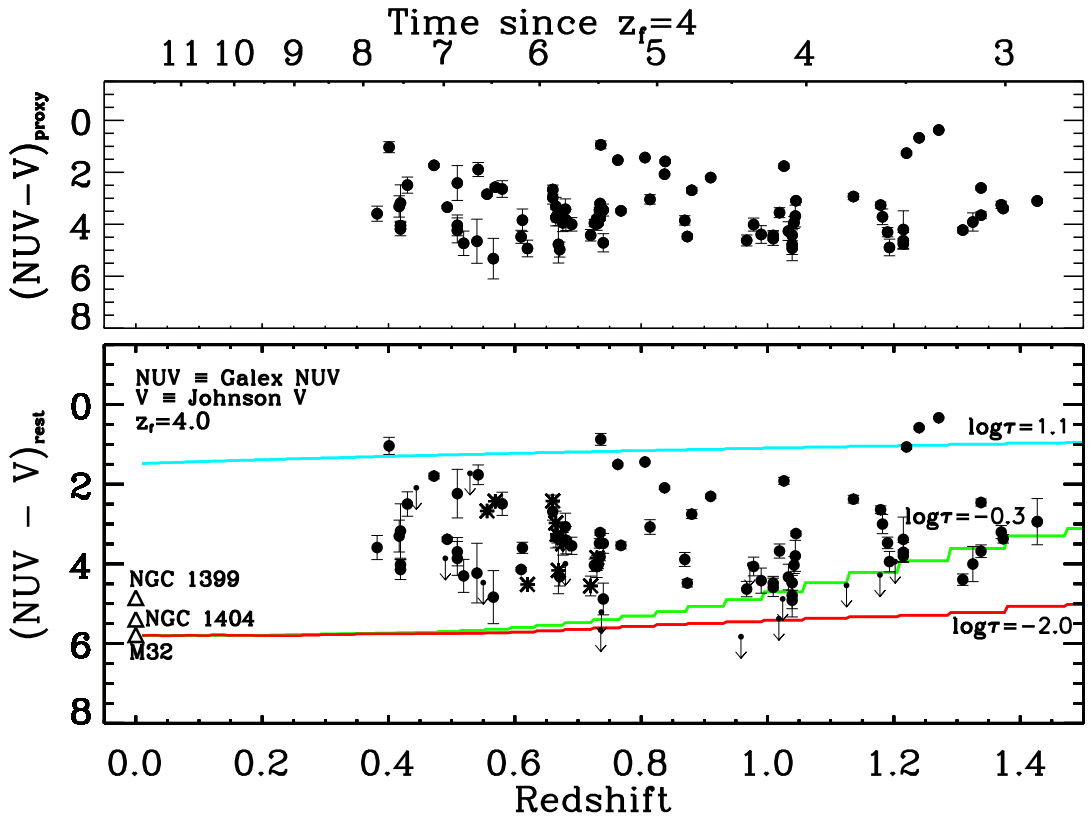

Figure 4.5: Upper Panel : The observed (NUV–V) colors of the catalog of ETGs in the ERS field. I calculate the observed colors by differencing the observed photometry for the combination of WFC/ACS filters that most closely matches that region of spectrum assessed by the NUV and Johnson V filters, respectively (see Table 4.4). On the upper abscissa, I provide the time (Gyr) since z_f=4.0 for reference. Bottom Panel : The $(NUV–V)_{rest}$ colors of the ETGs. I plot photometric and systematic (associated with the transformation function, see §4.4) uncertainties for all detected ETGs. I plot ETGs detected in Radio and/or X-ray surveys of the GOODS-S field with an "asterisk" ($*$). Photometric upper limits, defined by the recovery limits discussed in §4.2.2, are overplotted as downward-pointing arrows. I plot the colors of three, stellar evolution models derived from BC03, assuming a fixed redshift of formation ($z_f = 4.0$), and a star-formation history defined by Equation 5.1 with $\log(\tau[\mathrm{Gyr}]) \simeq 1.1$ (Blue), -0.3 (Green) and -2.0 (Red). Note that the low redshift evolution of the $(NUV–V)_{rest}$ colors of these models is an empirical fit to the UVX in quiescent ETGs at this redshift, and is not motivated by a physical theory of the stellar sources of the UVX.

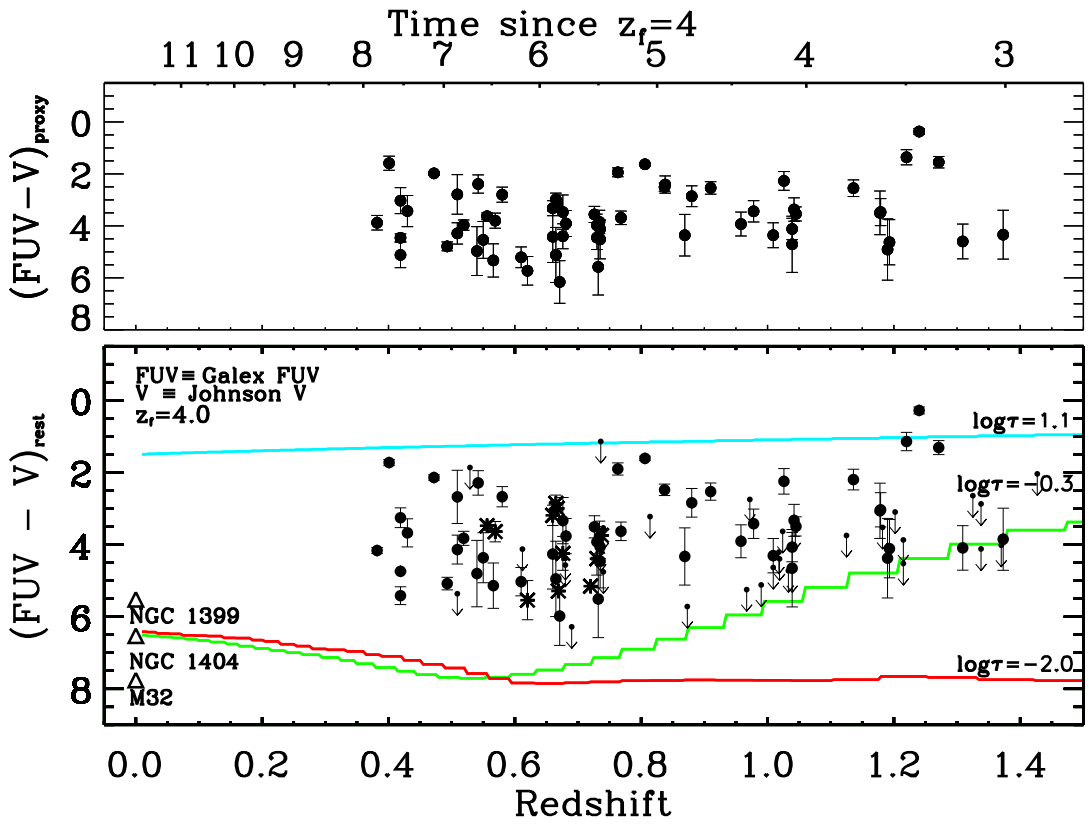

Figure 4.6: The same as for Figure 4.5, but here the (FUV–V) colors are plotted.

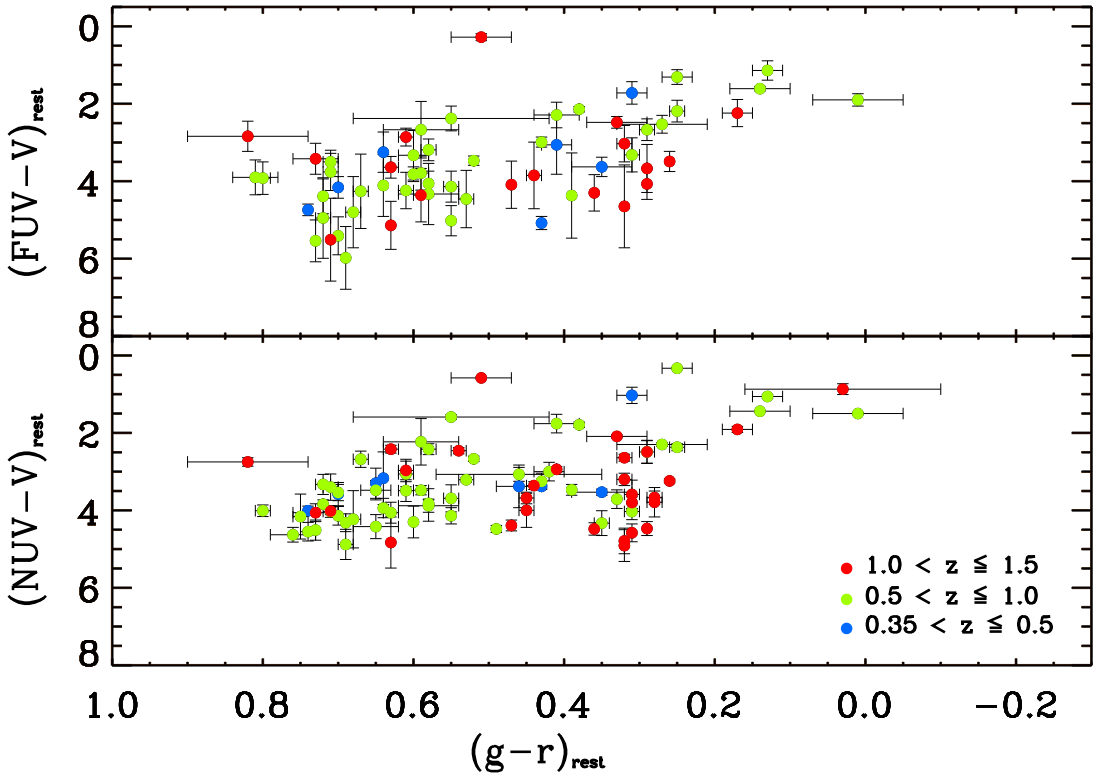

Figure 4.7: Upper Panel : The (NUV–V)$_{rest}$ and (g′–r′)$_{rest}$ colors of the ETGs are plotted. Bottom Panel : The (FUV–V)$_{rest}$ and (g′–r′)$_{rest}$ colors of the catalog ETGs are plotted. The conversion between the observed and rest-frame colors is outlined in §4.4. All data are color-coded according the the redshift-color scheme defined int he bottom panel. The span of rest-frame colors in these panels likely indicates recent star-formation in many ETGs (cf. Kaviraj et al. , 2007b).

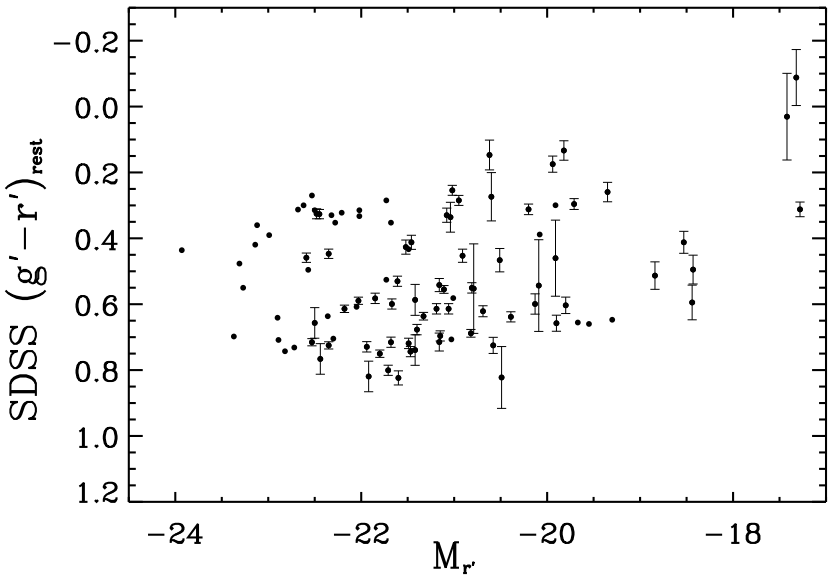

Figure 4.8: The $(g'–r')_{rest}$ colors of the ETGs. For clarity, error bars are overplotted only for ETGs with measured (photometric and systematic) uncertainties greater than 0.01 mag. The broadband SED-fitting method for determining the absolute magnitudes is outlined in §4.2.3. See §4.4 for full details of the color transformation that I use to calculate the colors and photometric completeness limits plotted.

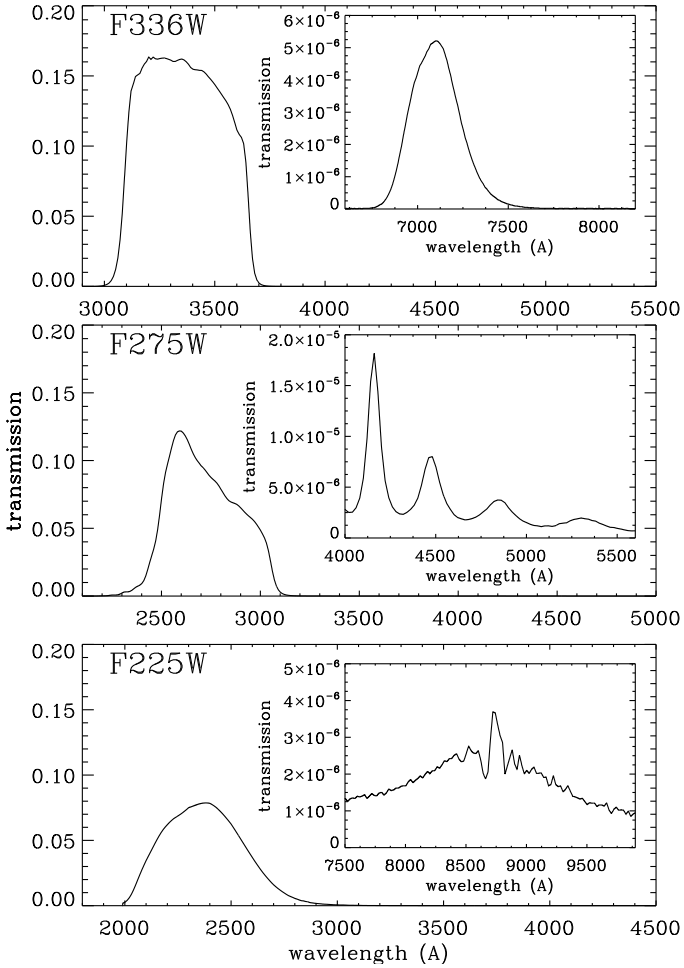

Figure 4.9: The total throughput for the F225W, F275W, and F336W filters are shown here. The inset in each panel illustrates the transmission of each filter at the wavelengths where the red-leak is most severe. N.B. the range differs between each panel. Using the BC03 and CWW template spectra, I estimate that for a typical ETG at $0.35 < z < 1.5$ the red-leak, $\mathcal{R} < 3\%$. For more details, see Addendum A2 and Table 4.6.

Chapter 5

EARLY-TYPE GALAXIES AT INTERMEDIATE REDSHIFT OBSERVED WITH HST WFC3: NEW PERSPECTIVES ON RECENT STAR FORMATION

A fundamental question of modern observational astrophysics concerns the assembly and evolution of massive early-type galaxies, which dominate the stellar mass budget of the local to intermediate redshift universe (z$\lesssim$1; see e.g., Bell et al. , 2004). Ground-based optical-near IR observations red optical colors (Bower, Lucey,& Ellis , 1992), a tight correlation on the fundamental plane (Bender et al. , 1992) and the measurement of chemical enrichment (Trager et al. 1998, 2000; Thomas et al. 2005) all agree on a theoretical formation paradigm (Larson , 1974; Pipino & Matteucci , 2004; Chiosi & Carraro , 2002) of massive ETGs in which these galaxies are passively evolving and formed the majority of their stellar mass in a burst of star-formation at relatively high redshift ($z > 1$). Space-based rest-frame Ultraviolet (UV) observations of ETGs (a wavelength regime that is uniquely sensitive to recent star-formation) have provided a very different portrait of these galaxies assembly and evolution. Many ($\sim$30%) ETGs have been identified at low redshift ($z < 0.3$) to also possess a minority population (typically $\ll 5-10\%$ of the total stellar mass of the ETG) of stellar objects that emit strongly at UV wavelengths (Ferreras & Silk , 2000; Yi et al. , 2005; Kaviraj et al. , 2007b). Combining these insights with studies of the rest-frame optical characteristics of galaxies at low redshift from SDSS and other surveys, the community has revised the picture of galaxy mass assembly and evolution whereby galaxies may "move" away from their (temporary) residence red or blue sequence of galaxies, transitioning towards or through a "green valley"(Wyder et al. , 2007; Schimonivich et al. , 2007) Galaxies residing in the blue sequence (i.e., late-type, star-forming galaxies, $(\mathrm{NUV}-r')_{rest} \simeq 2$ and specific star-formation rates,

sSFR$\gtrsim$8-9 (e.g., Villar et al. , 2011), may migrate away from the sequence for myriad reasons: suppression of star-formation by AGN (Schawinski et al. , 2009) and/or gas quenching and stripping (Hughes & Cortese , 2009) which removes the fuel available for production of future young stellar populations (YSP). Though the transition of these galaxies to the green valley occurs relatively quickly ($t < 1$Gyr), the transition to the red sequence may take many Gyr (Cortese & Hughes , 2009). In contrast, ETGs on the red sequence (which have largely exhausted their "in-situ" cold reservoirs) can appear significantly bluer at UV-optical wavelengths by forming YSPs. The fuel for this low-level star-formation is supplied via cold-gas accretion from mergers, which are ubiquitous in the ΛCDM paradigm of hierarchical galaxy assembly (Eliche-Moral et al. , 2010; Khochfar and Burkert , 2003).

Surveys with GALEX of ETGs have been technically limited to observing only ETGs at low redshift ($z \lesssim 0.1$) at rest-frame UV-optical wavelengths and at lower spatial resolution[1] than is possible with HST WFC3 (Schimonivich et al. , 2007; Kaviraj et al. , 2007b). At this spatial resolution, the morphological signatures of merger activity, for example, small-scale "disturbed" structure, small-scale and extended star-formation, or nearby low luminosity companions may be unresolved or undetected (cf. e.g., Salim et al. , 2012). The HST WFC3 UVIS provides nearly continuous coverage of the rest-frame UV SED of intermediate redshift ($0.35 < z < 1.5$) galaxies. Combined with the performance of the ACS and WFC3 IR, this instrument suite can provide novel insight into the stellar properties of intermediate redshift galaxies.

In Chapter 4, I observed $\sim$ 100 intermediate redshift ($0.35 < z < 1.5$) ETGs with the HST WFC3 as part of the Early Release Science program (Windhorst et al. , 2011). The rest-frame UV-optical colors (§5.1) calculated for these ETGs suggested that many of these ETGs had experienced a minor recent (t $\lesssim$ 1 Gyr), star-formation

[1]the FWHM of the GALEX PSF is approximately 5″

event. I extend this initial work by measuring the characteristics of the young and old stellar populations and investigate the pathways by which these ETGs approached the "green valley." In §5.1, I briefly describe the selection criteria which were used in Chapter 4 to define the sample I consider in this research. In §5.2, I present the results of an analysis of the ETG SEDs to constrain the age and mass of the young and old stellar populations. I measure the Sèrsic profile and the companion number for each ETG (§5.3 and §5.3.4), respectively, taking advantage of the HST UVIS/IR and ACS superior spatial resolution, stable PSF and low sky background at UV-optical-near IR wavelengths. I investigate correlations between these quantitative morphology parameters and the age and mass fraction of the best-fitted YSPs to constrain the mechanism(s) motivating the observed recent star-formation in these ETGs and discuss these results in §5.4.

Throughout this paper I assume a ΛCDM cosmology with Ω_m=0.27, Ω_Λ=0.73, and H_0=70 km s^1 Mpc^1 (Komatsu et al. , 2011). I use the following designations: F225W, F275W, F336W, F435W, F606W, F775W, F850LP, F098M, F125W, and F160W represent the HST filters throughout; FUV and NUV represent the GALEX 150 & 250 nm filters, respectively (Morrissey et al. , 2005). Throughout, I quote all fluxes on the AB-magnitude system (Oke and Gunn , 1983).

5.1 Observations and ETG Catalog

Near-UV and near-IR observations were acquired as part of the WFC3 ERS program (HST Program ID #11359, PI: R. W. O'Connell), a 104 orbit medium-depth survey using the HST UVIS and IR cameras. The ERS program observed approximately 50 square arcminutes in the Great Observatories Origins Deep Survey-South (GOODS-S) (see, Dickinson et al. , 2003; Giavalisco et al. , 2004, for more details) field with the HST WFC3 UVIS in three filters (F225W, F275W, & F336W) and approximately

40 square arcminutes in the same field with the WFC3 IR in three filters (F098M, F125W, & F160W). These images were prepared as a mosaicked image, produced for each of the UVIS and IR band tilings, and each image mosaic was drizzled to a matched pixel scale equal to $0.09''$ pixel^{-1}. We rebinned the existing ACS images (F435W, F606W, F775W, and F850LP) to match the pixel scale of the ERS mosaics. For more details regarding the ERS program, I refer the reader to Windhorst et al. (2011).

I will use the ETG catalog identified in Chapter 4 throughout the following analysis. For sample selection, I required ETGs to have:

- been imaged in all UV and IR bands, to uniform depth in the ERS field;
- a spectroscopically-confirmed redshift in the range $0.35 \lesssim z \lesssim 1.5$;
- an ETG morphology characterized by a centrally peaked light profile, which declines sharply with radius, a high degree of azimuthal symmetry, and a lack of visible internal structure.

Applying these selection criteria to the ERS field, I originally identified 102 ETGs. It is important to note at high redshift ($z > 1$), ground-based optical-IR spectrometers are not able to bracket the Balmer complex ($\sim$ 3600Å), thus it is unlikely that the spectroscopic redshift for these galaxies was measured using this absorption complex. Instead, an emission line (which likely is indicative of recent or ongoing star-formation activity in the host galaxy) may have been used to measure the redshift. Furthermore, the angular size scale decreases significantly ($\sim 2\times$) across the redshift range of the catalog, severely hindering the visual inspection of fine-scale structures in the ETG and its local environment.

In this analysis, I will use the panchromatic (10-filter) photometry for each galaxy measured in Chapter 4. This measured photometry for the ETGs was obtained with Source Extractor (SE Bertin & Arnouts , 1996) in dual-image mode, using the F160W image mosaic as the detection image. In Chapter 4, I determined 90% recovery limits for simulated bulge profiles with half-light radius of 1.0″ equal to F225W=26.5, F275W=26.6, F336W=26.4, and F435W=26.7 mag, respectively. I interpret ETGs with magnitudes fainter than these recovery limits as 1σ upper limits. I refer the reader to Chapter 4 for full details regarding the catalog selection and photometry.

5.2 Characterizing the Stellar Populations

5.2.1 Single-Component SED Analysis

Extending initial results presented in Chapter 4, I characterize the old (t$\gg$1 Gyr) stellar populations in the ETGs using a template library of single-component population synthesis models presented in Bruzual and Charlot (2003) (BC03). I fit the broad-band observed Optical-IR (F435W, F606W, F775W, F850LP, F098M, F125W, F160W) SEDs for each ETG in order to exclude most rest-frame UV emission from the minority (by mass) young stellar populations. The template library of models was generated assuming BC03 single burst stellar templates defined with a Salpeter stellar Initial Mass Function, solar metallicity, and with the star-formation history of the single burst defined by an exponentially declining function, weighted by time constant, τ, i.e.,:

$$\psi(t) \propto e^{-t/\tau} \tag{5.1}$$

These models were defined for a grid of time constants[2] ($-2.0 < \log(\tau[\mathrm{Gyr}]) < 2.0$) and ages ($1\times10^8 < t(\mathrm{yr}) < 13.7\times10^9$). In addition, I apply the Calzetti et

[2]We calculate models for N=15 values of τ defined with a stepsize of $\frac{max(\log(\tau))-min(\log(\tau))}{(N-1)}$=0.28.

al. (2000) prescription for dust extinction, assuming $0 \lesssim E(B-V) \lesssim 1$, a range known to well-fit low-redshift ETG and spheroidal galaxies (Kaviraj et al. , 2011). I minimize the goodness-of-fit χ^2 statistic[3] between this library of synthetic and observed fluxes to determine the optimal model (cf. Papovich et al. , 2001). For each ETG, I required the best-fitting age parameter to not be greater than the age of the universe at the redshift of the ETG. In Figure 5.1, I present the best-fitting mass-age profile for these ETGs to summarize the results of this analysis.

This analysis is strongly biased, by design, to the majority (by mass) old stellar populations extant in these ETGs. In Chapter 4, the rest-frame UV-optical colors of these galaxies suggest recent star-formation is non-negligible, thus to more completely assess the mass assembly and star-formation history of these ETGs I incorporate the rest-frame UV emission into the subsequent SED analysis. Salim et al. (2007) derived a prescription for the estimating the star-formation rate of ETGs from their analysis of thousands of low-redshift ($z \simeq 0.1$) galaxies observed in GALEX & SDSS surveys. This prescription relates the galaxy's rest-frame far-UV luminosity to the star-formation rate generally as follows:

$$SFR = 1.08 \times 10^{-28} L^0_{FUV} \tag{5.2}$$

where L^0_{FUV} is rest-frame far-UV luminosity, which I correct for dust attenuation using the prescription provided by the authors where:

$$A_{FUV} = \begin{cases} 3.32 \times (FUV - NUV)_{rest} + 0.22, & (FUV - NUV)_{rest} < 0.95 \\ 3.37, & (FUV - NUV)_{rest} \geq 0.95 \end{cases}$$

Using the best-fitting extinction co-efficient derived from previous analysis, I measure the mean star-formation rate ($\overline{\mathrm{SFR}}$=0.12; 1σ =0.19). Assuming the majority ($\gtrsim$90%)

[3] I assume 7 degrees of freedom when determining the reduced χ^2 statistic.

of stellar mass in these ETGs is captured in the one-component SED analysis above, I also estimate the specific star-formation rates ($\log(\overline{\mathrm{sSFR}})$=-12.02; 1σ=0.87) for the sample (Figure 5.2). The observed SFRs are in good agreement with similar studies of ETGs of this mass and redshift range (see recent work by Rowlands et al. , 2012, which used the Herschel Space Telescope to characterize a sample of dusty & non-dusty ETGs).

Implicit in this analysis is the assumption that the SFR measured from the UV luminosity represents primarily the formation of massive, young stellar populations that emit strongly at UV wavelengths. In massive ETGs, old stellar populations (e.g., Extreme Horizontal Branch, or EHB, stars, for a review see O'Connell , 1999) may produce a "UV Upturn" (UVX Burstein et al. , 1988; Donas et al. , 2007; Jeong et al. , 2009) and thus contribute a non-negligible flux to the UV SED. In low redshift ETGs, massive main-sequence stars are significantly brighter at UV wavelengths than are the old stellar populations ($(\mathrm{FUV\text{-}V})_{\mathrm{YSP}}/(\mathrm{FUV\text{-}V})_{\mathrm{UVX}} >$ 4-5 AB mags), but in ETGs that have not experienced a recent ($t < 1$ Gyr) star formation, the UVX may contribute significantly to the UV SED.

The evolution of EHB stars is not well-understood (cf. Yi et al. , 1999; Han et al. , 2007; Yi et al. , 2011), but if I assume that the UVX arises from metallicity-dependent mass-loss effect of the Horizontal Branch stars (Yi et al. , 1998) then the strength of this phenomenon is expected to decline with increasing look-back time. A priori, the UVX is detectable in, at most, $\sim$20% of the ETGs at the lowest redshift range of the survey, $0.3 < z < 0.6$ (Yi et al. , 1999), assuming a formation redshift of these galaxies at z =3-4 Kaviraj et al. (2013). Applying the UV-optical color-color criterion defined by Yi et al. (2011) to differentiate passively-evolving and possible UVX ETGs, we determine that the broadband UV-optical colors do not indicate the presence of a significant UVX component. Though it is a very minor effect in low

redshift ETGs ($\ll$1% of the total stellar mass, Yi et al. , 2011) and the majority of the ETGs have not aged sufficiently enough to develop a UVX (Ree et al. , 2007), old and young UV bright stellar populations may both be present. But, if a weak UVX is present the UV SED is likely to be dominated by emission from YSPs.

5.2.2 Two-Component SED Analysis

To estimate the age and mass fraction of the young stellar component I apply a synthesized, two-component model of the stellar populations extant in the ETGs. The templates I use are defined for a two-component star-formation history in which stars are formed instantaneously at two different epochs. The templates I use to model the initial, primary burst of star-formation (which I assume to occur at a high redshift, 12 Gyr prior to the age of the universe at the spectroscopic redshift of the ETG), during which the majority (by mass) of stars in these galaxies were formed, are derived from the Υ^2 models (Yi et al. , 2003). These model stellar populations are based on a metallicity-composite population (a short burst with chemical enrichment) with a mean metallicity equal to roughly solar. The stellar population templates I apply in this analysis include a model of the UVX stellar populations (Kodama & Arimoto , 1997). The second burst component, representing the YSP, in these models is again derived from the BC03 templates, has a fixed metallicity (solar), but I allow the age (t_{YC}) and mass fraction (f_{YC}) to vary for a wide range: $10^{-3} < t_{YC}[\mathrm{Gyr}] < 10$ and $10^{-6} < f_{YC}[\%] < 1$.

In Table 5.1, I present the best-fit parameters from the two-component SED analysis, with upper and lower uncertainties on the measurement of each free parameters representing the 68% confidence level. The χ^2 values of the best-fit models are generally small ($\chi^2 \lesssim 1-2$), I caution that this need not imply that the measurement uncertainties on t_{YC} & f_{YC} are correspondingly small. The large YSP parameter

uncertainties can be largely attributed to the photometric uncertainties associated with these data. The ERS program is a medium-depth survey and observed these UV-faint (AB(F225W)$\lesssim$ 23) ETGs to a signal-to-noise ratio, 1$\gtrsim$SNR$\gtrsim$20 (see Table 1 in Chapter 4). Note, these photometric uncertainties are markedly lower[4] than were measured in previous surveys of comparable galaxies at intermediate redshift (Ferreras & Silk , 2000).

I present the rest-frame UV-optical colors, (FUV-V)$_{rest}$ and (NUV-V)$_{rest}$, derived from this two-component analysis in Figure 5.4 as a function of redshift, where the plot symbols indicate f_{YC} of the YSP component. If I consider the maximal likelihood values derived from the two-component SED analysis, I measure at least $\sim 40\%$ of ETGs have YSP parameters measured within the range $0.05 < f_{YC}[Gyr] < 1.00$, $1 < f_{YC} < 10$, confirming that a significant fraction of ETGs have recently undergone a minor burst of star-formation[5]. The mean age and mass fraction of the best-fitting YSP component equals: $t_{YC} = 360\mathrm{Myr}(1\sigma = 160\mathrm{Myr})\& f_{YC} = 3.7\%(1\sigma{=}2\%)$. In the two-component SED analysis, there is no explicit correction for dust, which preferentially attenuates the SED at UV wavelengths, thus this fraction is a lower limit to total fraction of RSF ETGs in the ERS field. If I include the 68% confidence intervals in the measurement of the fraction of ETGs that have experienced RSF, the fraction declines to $\sim$10%. This lower limit can be attributed largely to degeneracy in the model fitting. The relatively large photometric uncertainties may introduce large uncertainties in the measurement of YSP age and mass fraction. Furthermore, there are degeneracies in these models with respect to $t_{YC}\&$ f_{YC} that are difficult to correct with broadband photometry alone. For example, distinguishing between a massive old stellar population and a very young (t$\lesssim$50Myr) starburst, whose UV

[4]This is a testament to the improved UVIS capabilities of the HST considering the time of exposure per ETG

[5]Of the 77 ETGs for which $\chi^2 < 2$ was measured for the two-component model template fit to the ETG SEDs, 32 ETGs are likely to have experienced recent star-formation.

light is strongly attenuated by the YSP dusty "birth cloud", is inherently difficult with broadband photometry (see e.g., Kaviraj et al. , 2007b, for which UV photometric uncertainties were much smaller, $\Delta \lesssim 0.1$ AB).

These results are consistent with studies of similar galaxies at lower to intermediate redshifts observed with GALEX. For example, at $z \lesssim 0.1$ Kaviraj et al. (2007b) found $\sim$30% of ETGs were measured to have UV colors consistent with recent star-formation with an average age of the young stellar component equal to 300-500 Myr. The estimate that $\sim$40% of ETGs have likely experienced minor RSF is also in general concordance with the expectation from that the fraction of ETGs undergoing star-formation should necessarily increase with redshift towards the broad peak of global star-formation at $z \simeq 2-3$ (Madau et al. , 1998) and the formation epoch of massive spheroidals (Kaviraj et al. , 2013).

5.3 Morphological Analysis of ETGs and local environment

For the first time, the high spatial resolution and continuous wavelength coverage of the HST WFC3 allows us to directly consider the mechanism(s) driving the RSF observed in §5.2.2. In the traditional formation and evolution scenario, these galaxies formed the majority of their stellar mass at an early epoch ($z > 3$ Kaviraj et al. , 2013). If the early burst of star-formation in ETGs largely exhausted the fuel necessary for subsequent bursts (see simulation results from Kaviraj et al. , 2007b), then the intermediate redshift ETGs must acquire new gas via mergers in order to develop the YSPs. An alternative scenario is that the observed RSF arises from S0/Lenticular-type ETGs that are transitioning towards the red sequence (Kannappan et al. , 2009). Here, the slow accretion of gas, originally present at surface densities too low to form YSPs, from the remaining disk component towards the core of the ETG may motivate the RSF I observe here(cf., Lucero and Young , 2007; Serra et al. , 2012).

In the following sections, I apply the `GalFit` software to measure the Sèrsic profile of the ETG (§5.3.1) to determine the fraction of ETGs which display a light profile indicating the presence of a disk component in addition to the observed bulge-dominated visual morphology. Secondly, in §5.3.2 & §5.3.4, I consider the frequency of companions for each ETG, applying a statistical likelihood formalism to measure the number of (AB(F850LP)$\lesssim$ 25) companions for each ETG. If the presence of YSPs and galaxy companion number are correlated, this could suggest that mergers and/or interactions are an important mechanism motivating the RSF observed for these ETGs.

5.3.1 Quantitative Morphology of ETGs

These ETGs were identified by visual selection based on their high degree of rotational symmetry and smoothly varying stellar light profile, i.e., the classical morphological signature of an ETG. Thus, we could expect that the light-profiles of these galaxies should be well fitted by a single Sèrsic profile. This versatile function is often used to characterize the stellar light-profile of galaxies on the Hubble sequence. The Sèrsic model of the intensity of a galaxy's light as a function of radius is defined as:

$$I(r) = I(0)exp[-b_n(r/r_e)^{1/n}] \tag{5.3}$$

where $I(0)$ is the intensity at radius $r = 0$, r_e is the half light radius, n is the Sèrsic index, and b_n is a normalization constant that is a function of the index and ensures the radius r_e encloses half of the total galaxy luminosity. It is often assumed that late-type galaxies are better-fitted by a Sèrsic profile with n=1 and bulge-dominated, spheroidal galaxies are best-fitted by Sèrsic profile with $n \simeq 4$. In practice, there is usually a significant spread in the best-fit Sèrsic index measured

for large samples of ETGs. In the local universe, Kormendy et al. (2009) measured the Sèrsic indices for 37 ETGs in the Virgo Cluster using observations obtained with both ground and space-based observatories. The mean Sèrsic index measured for these ETGs equaled $n \simeq 3.8$, but the spread in measured indices was quite large. Only 3 ETGs were measured with $4 < n < 5$, $> 35\%$ of the Virgo cluster ETGs were best fit with $n > 4$. Those galaxies with Sèrsic indices greater than 5, $> 60\%$ were measured with an index of $n > 7$. Similarly, at high redshift ($z > 1.5$), compact, quiescent galaxies have been measured to have low Sèrsic indices. For example, studies with WFC3 of massive ($\log(M[M_{\odot}])>11$), compact ($r_e < 1$ kpc) quiescent galaxies found 30-60% of these galaxies with Sèrsic indices less than $n \sim 2$ (see, e.g., van der Wel et al. , 2011; Ryan et al. , 2012). Thus, in this ETG sample, where galaxy selection was made exclusively based on visual morphology, it is likely that there will be significant scatter in their measured Sèrsic indices.

I use the popular two-dimensional profile fitting software `GALFIT` (Peng et al. , 2002) to measure the best-fit Sèrsic profile to each ETG in postage stamps extracted from the F160W mosaic, each with a uniform size of 200×200 kpc (i.e., $r \lesssim 100$ kpc). I implemented `GALFIT` via the IDL software "iGALFIT" (Ryan , 2011), which provides users a GUI to implement `GALFIT` with its full functionality, while also allowing users to select galaxies and mask extraneous sources (i.e, foreground and background galaxies, cosmic rays) "on-the-fly".

`GALFIT` calculates the brightness of the sky background locally and fits the light profile, assuming that all flux within the region of interest is associated with the ETG. Thus, identifying and removing the contamination from foreground/background objects is critical for accurate measurements. In the postage stamp images, I masked a large ($20 \lesssim N \lesssim 50$) number of galaxies and noise pixels (e.g., at chip and mosaic gaps), but in the large images it was never necessary to mask more than 5-10% of the

total image area.

The sample contains a number of galaxies which are intrinsically small, and even at the WFC3 high resolution they may be unresolved spatially. To ensure the light profile of each galaxy was well-sampled, ensuring accurate measurement of the Sèrsic profile, we fit each galaxy, individually with a single Sèrsic profile and also an empirical PSF defined using known stars in the ERS field. I then calculated the fractional difference, f, equal to :

$$F_{crit} = \frac{(\chi^2_{PSF} - \chi^2_{\text{Sèrsic}})}{\chi^2_{\text{Sèrsic}}} \tag{5.4}$$

where χ^2 equals the reduced chi-square of the model fit measured by `GALFIT`. Ryan et al. (2012) determined that for ERS ETGs, $F_{crit} \simeq 0.01$ can generally distinguish stars from poorly resolved ETGs in the F160W images. I excluded 16 ETGs from further consideration by applying this criterion. In Table 5.2, these galaxies are designated "Failed F_{crit}". A visual inspection of publicly-available spectra[6] confirms that $\sim$50% (7 of 13) those ETGs were identified with [OII]3727Å, or an unknown emission line, in their spectrum indicating the presence of a hard ionizing source(s), potentially young stars or an AGN. If the stellar disk/bulge in these ETGs were relatively faint in comparison to a bright, spatially unresolved point source, this would explain the poor Sèrsic profile fit. Furthermore, if the visual inspection was strongly biased by this compact profile, these galaxies should necessarily be excluded from subsequent analysis.

I have excluded an additional 4 ETGs because their light profiles were well-blended with close companions (on the plane of the sky). Masking these companions

[6] as PNG images, available online at `http://archive.eso.org/archive/adp/GOODS/FORS2_spectroscopy_v3.0/index.html`

could remove significant light from the ETG which would affect the best-fit parameters. These ETGs are indicated "Not Fit" in Table 5.2.

The average reduced χ^2 goodness of fit statistic measured for the Sèrsic profile fits to those galaxies that were not exluded by the previous criteria was small (χ^2_ν=0.54). I note that the half-light radii for a significant fraction ($\sim$20%) of the ETGs were not well-fit[7], thought the ETG may be small ($\chi^2 < 1$).

I inspected the residual map—produced by differencing the best-fit Sèrsic model profile from the original input image—for each ETG. These ETGs typically showed poor residuals, i.e., the model profile under-subtracted the galaxy light resulting in an irregular patchy or "toroidal"-morphology (a bright core bounded by an over-subtracted "ring") in the residual map. For comparison, I inspected all residual maps and found that the features present in the residual maps produced for "failed" results were sometimes also found in otherwise good (i.e., low χ^2_ν and all parameters well-determined) fits. Physically, this residual "toroid" may indicate a centrally-concentrated, nuclear star- forming region (as observed or implicated in "blue core" local ETGs Suh et al. , 2010), or a disk (as expected for an S0/Lenticular ETG morphology). For example, fitting a Sèrsic profile with a large index to account for a bright core results in an over-subtraction at larger radii (for ETGs with small effective radii), considering the Sèrsic function with large index profile relative to the flatter, truncated profile for a Sèrsic function with small index. Thus, the poor residual maps are most likely due to the use of insufficient number of components to model the ETG's light profile.

To better model the Sèrsic profile of each ETG, I re-measured all ETGs, this

[7]If `GALFIT` can not converge on a parameter solution after a finite number of iterations, it will designate the poorly constrained parameter with an asterisk, "*". The reduced χ^2 for the model fit may be small ($\lesssim 1$), but this solution should not be considered robust.

time applying a two-component model for the light profile composed of a combined Sèrsic (to account for the stellar light profile) and an empirically-defined PSF model (to better account for any core light). In Table 5.2, I indicate those galaxies for which this method produced better results in measuring the Sèrsic parameters with a star ($\star$). 47 ETGs were improved with this two-component spatial model (i.e., `GALFIT` parameter solution converged and/or lower reduced χ^2) . `GALFIT` could not determine an accurate solution[8] for 5 ETGs using either the one (Sèrsic only) or two (Sèrsic & empirical PSF) component model. I designate the row values for this minor fraction of the catalog "Fail to Converge" in Table 5.2. Of 102 ETGs, 77 were well-fit with either the one- or two-component Sèrsic model in total.

In Figure 5.5(a), I plot the best-fit measured half-light radii (converted to kpc at the distance to the ETG) against the Sèrsic index, with the symbol colors indicating YSP age. Note that the Sèrsic indices span a large range ($1 \lesssim n \lesssim 10$) range; the mean Sèrsic index for the sample equal to 3.7(1σ=2.1). In the top panel of Figure 5.5(a), I overplot a Gaussian function fitted to the distribution of n, the centroid (FWHM) of which I measured equal to 2.7 (2.3). Similarly, I measured a mean half-light radii, $\bar{r}_e$ =2.9 kpc (1σ=1.88kpc); I overplot in the right panel of Figure 5.5 a Gaussian fitted to the distribution of r_e, with a centroid equal to 2.1kpc (FWHM=1.9kpc). Note that ETGs with ages $0.1 \lesssim t_{YC}[\mathrm{Gyr}] \lesssim 0.3$ appear to be located in a morphological parameter space distinct from ETGs with older YSP ages. I do not believe that this represents a physical distinction when the measurement uncertainties for the YSP ages are taken into consideration. But, I do note that many (50%) ETGs with low Sèrsic index are likely to have experienced RSF ($1 < f_{YC}[\%] < 10; 0.05 < t_{YC}[\mathrm{Gyr}] < 1.00$).

[8] If `GALFIT` can not converge on a parameter solution after a finite number of iterations, it will designate the poorly constrained parameter with an asterisk, "*". The reduced χ^2 for the model fit may be small ($\lesssim 1$), but this solution should not be considered robust.

5.3.2 Statistical Likelihood Analysis of Local Environment

By design, I have selected a population of ETGs that lack any readily identifiable morphological scenarios of a recent, gas-rich majors merger[9], I consider the possibility here that the observed RSF can be induced by minor mergers and interactions between the ETG and local companions.

I consider a galaxy to be a companion if it is in close physical association with the ETG, i.e., within a three dimensional spatial region defined by $\{X, Y, Z\} \propto \{X_{ETG} \pm 1000\text{kpc}, Y_{ETG} \pm 1000\text{kpc}, v_{spec,ETG} \pm 500\,\text{km s}^{-1}\}$, as opposed to a two dimensional search (cf., Rutkowski et al. , 2013). This "search radius" is comparable to the radius over which "close pairs" of galaxies at intermediate redshifts are identified, $\{X, Y\} = 0 - 1000\text{kpc}$ and $z \simeq 500 - 750\text{km s}^{-1}$ in the literature, (López-Sanjuan et al. , 2010; Tal et al. , 2013). Physically, this region contains galaxies which may have, if physically associated with the ETG, interacted (via merger or close passage), in the previous ~ 200 Myr (i.e., 1 kms$^{-1} \simeq 1$pc Myr-1).

If the $\{X, Y, Z\}$ spatial positions of all galaxies in a field are known, calculating the number of companions is a trivial counting exercise. In practice, counting the number of companions is difficult as both high-resolution imaging and spectroscopic data are not generally available for all galaxies in the field. In the ERS field, extensive galaxy redshift catalogs obtained with ground-based spectrographs alleviate this issue (Cimatti et al. , 2002; Vanzella et al., 2008). In Chapter 4, I estimated the spectroscopic redshift deficit for visually-classifiable (i.e., as early or late-type morphologies) for the ERS field and in for a catalog of morphological ETGs, the frac-

[9]The catalog does include one galaxy which exhibits two bright cores. This system, J033210.7-274234.6, does likely represent a major merger, but likely represents a merger of two "dry" (gas-poor) ETGs in which the orbits of only intermediate to old stellar populations—in contrast to a significant gas transfer—are modified by the merger.

tion of galaxies without measured photometric redshifts may be as a large as ∼75%. This spectroscopic in-completeness arises from two technical limitations. First, spectroscopic redshift campaigns are limited by the apparent brightness of the observed galaxies; thus, fainter sources may not be detected. Spectroscopic redshift surveys of the ERS/GOODS-S are likely only to be ∼10-20% complete (see, e.g., Vanzella et al., 2008) to faint (AB(F850LP) < 25) galaxies. As the strenght of the broadband near-IR emission is correlated with the stellar mass of the galaxies, this spectroscopic incompleteness implies an mass incompleteness for the catalog of possible companions. Secondly, quiescent ETGs may (as they lack significant line emission) only be detected by the strength of their Balmer (∼3600Å) complex, which beyond $z \sim 1$ may can not be well-constrained using ground-based optical-near IR spectrographs. Thus, the passively evolving stellar continuum alone may be used to measure the spectroscopic redshift.

To gain a more accurate measure of the number of galaxies that are physically associated with these ETGs lacking spectroscopic redshifts, I apply the statistical likelihood analysis adapted from López-Sanjuan et al. (2010). In the following section I briefly outline the methodology (§5.3.3) and the measurements and discussion of the companion number for the sample (§5.3.4)

5.3.3 Principles of Statistical Likelihood Test of Companion Number

Lacking spectroscopic redshifts for all galaxies in close physical proximity (i.e, in $\{X, Y, Z\}$), I first assume that the probability distribution function (PDF) of a galaxy in redshift space is defined as either,

$$P_i(z_i|\eta_i) = P_G(z_i|z_{phot,i}, \sigma_{phot,i}) = \frac{1}{\sqrt{2\pi}\sigma_{z_{phot,i}}} exp\left\{-\frac{(z_i - z_{phot,i})^2}{2\sigma^2_{zphot,i}}\right\}, \qquad (5.5)$$

if a galaxy in a system, j, composed of one primary galaxy and oen secondary galaxy that may be a companion (if its physical position meets the conditions for $\{X, Y, Z\}$ defined in §5.3.2), has a measured photometric redshift with uncertainty $\sigma_{z_{phot,2}}$.

Or, if a galaxy has a spectroscopic redshift, then its PDF is defined as

$$P_i(z_i|\eta_i) = P_D(z_i|z_{spec,i}, \sigma_{z_{phot,i}}) = \delta(z_i - z_{ETG}) \tag{5.6}$$

where $\delta(x)$ is the Dirac delta-function and z_{ETG} is the spectroscopic redshift of the primary or "host ETG."

The total number, N_c, of companions contributed from j unique systems of galaxies within a redshift range $z \in [z_k, z_{k+1}]$ centered on the "host ETG" can then be calculated using:

$$N_c = \frac{\Sigma_c \int_{z_-}^{z_+} v_j(z_1) dz_1}{\Sigma_i \int_{z_k}^{z_{k+1}} P_i(z_i|\eta_i) dz_i}. \tag{5.7}$$

Here, the limits on the integration $[z^-, z^+] \equiv [z_{ETG} \times (1 - \Delta v^{max}/c) - \Delta v^{max}/c, z_{ETG} \times (1 + \Delta v^{max}/c) + \Delta v^{max}/c]$, where I fix $\Delta v^{max} = 500 \text{km s}^{-1}$ when calculating N_c as discussied in §5.3.2.

In Equation 5.7, the distribution of the probability of the galaxies in the system within this redshift range is defined as $v_j(z_1)$, with respect to the ETG. If the primary and secondary galaxies in a system have measured spectroscopic redshifts (Case 1),

$$v_j(z_1) = 2 \times P_D(z_1|z_{ETG}). \tag{5.8}$$

For systems where the primary galaxy has a measured spectroscopic redshift and secondary galaxy has a photometric redshift, then (Case 2)

$$v_j(z_1) = C_j \delta(z_1 - z_{ETG}) \int_{z_-}^{z_+} P_G(z_2|z_{phot,2}, \sigma_{phot,2}) \tag{5.9}$$

where C_j is a constant that normalizes the function to the number of galaxies in each system. Similarly, when a system contains a primary galaxy with a measured photometric redshift and the secondary galaxy (by the definition of limits in Equation 5.7, this galaxy may only be the host ETG) has a spectroscopic redshift,

$$v_j(z_1) = C_j \times P_G(z_1|z_{phot,1}, \sigma_{phot,1}) \tag{5.10}$$

Note that $v_j(z_1)$ is only non-zero in the velocity range of interest, which I define with respect to the "host ETG." In Case 1,$\delta = 1$ only at $z = z_{ETG}$. In Case 2, the probability of detecting the primary galaxy as a companion is only non-zero within the velocity range $z \in [z^+, z_-]$. Throughout this analysis, I only consider possible companions for which the PDF of the photometric companion intersects this velocity range at $2\times$ the Gaussian (photometric uncertainty) width, σ.

5.3.4 ETG Companion Number from Statistical Likelihood Method

I first measured photometry for all objects within a 200kpc×200kpc square region, centered on each of the host ETG, using all ten filters (F225W-F160W). I applied SE in dual-image mode (the F160W was the detection image), and applied the detection criteria outlined in Chapter 4. Next, I fit the measured SED for all objects in this region using the software, EAZY (Brammer, van Dokkum, & Coppi , 2008) to measure the photometric redshift of each companion. The observed SEDs were fitted against a spectral template library defined by combinations of five SED templates provided with the software by the authors which they derived from the PÈGASE model SEDs. The full library of spectral templates was defined by all combinations of the five model SEDs. I refer the readers to the Users' Manual[10] for additional details regarding the construction of the spectral template library. No redshift priors were used.

[10]available online at http://www.astro.yale.edu/eazy/eazy_manual.pdf

To produce a catalog for each ETG of possible companions, I matched a catalog of galaxies with spectroscopic redshifts with the results of the EAZY photometric catalog. Members of both catalogs were assigned the spectroscopic redshift, which is measured with higher precision.

For each catalog of possible companions, I then applied the statistical formalism outlined in §5.3.3. The measurement of the photometric redshift has an implicit uncertainty (I can anticipate an uncertainty of at least a few percent, cf. Brammer, van Dokkum, & Coppi , 2008), thus I calculated the companion number within a Monte Carlo (MC) simulation run 1000s of times and allow the Gaussian σ associated with the PDF of the galaxies with photometric redshifts to vary for a large range (0.01-0.1). The companion number calculated for each iteration is then folded into the calculation of the uncertainty in the companion number.

In Table 5.3, I present the number of likely companions, N_c, for each ETG in Column 2. I also include the mean contribution to N_c from companions with measured photometric (Col. 3) and spectroscopic (Col. 4) redshifts. I note that in this table, because measurement uncertainties only apply to possible companions with measured photometric redshifts, the uncertainty in N_c for the full system is motivated only by the photometric redshift companions, which could minimally contribute $\sim$0 companions to N_c. The velocity width over which the search for possible companions was made was fixed (see §5.3.3), thus the number of spec-z companions was fixed throughout the MC simulation.

I have identified more than one companion for $\sim$ 10% (9/102) of the ETGs. In Figure 5.7, I present the measured companion number for each ETGs as a function of there YSP age & mass fraction. Here, I note that the distribution of galaxies with more than one likely companion appear well distributed, and do not appear to reside

in any particular regime in this parameter. The mean age and mass fraction of YSPs measured for ETGs with more than one companions differ from those ETGs without companions — $\bar{t}_{YC} \simeq 260$ (660)Myr & $\bar{f}_{YC} \simeq 2\%$ (9%) for ETGs with (without) companions, respectively. I discuss the implications of this result in the following section.

5.4 Discussion of the Mechanism of Recent Star-Formation

In §5.2.2, I confirmed recent star-formation in a large fraction (40%) of the catalog ETGs from the results of the two-component SED fitting. In part due to the photometric uncertainties ($\Delta m \gtrsim 0.1$ AB mag) associated with measurements of the UV SED of these ETGs, this fraction represents a lower limit to the number of ETGs that have experienced minor, recent star-formation.

The high spatial resolution of the data allow us to consider the frequency of RSF in ETGs as a function of environment and galaxy morphology. From visual inspection alone, I can confirm that major mergers do not motivate the measured RSF. This conclusion may not extend generally to the complete class of field ETGs at intermediate redshift as the selection criteria for ETGs has excluded galaxies in which major mergers are ongoing or are likely to have occurred recently.

I measure two trends that may provide new insight into the mechanism by which RSF is initiated in intermediate redshift ETGs. First, in §5.3.1, I measured a wide range of Sèrsic profiles of the ETGs' observed F160W morphology. ETGs at these redshifts are known to be well-fit by a similar range of Sèrsic profiles. With this unique ERS data, I am able to correlate the YSP parameters with the measured Sèrsic profile parameters, and find that many (15%) ETGs are well-fit by Sèrsic profiles with low index and half-light radii and have likely experienced a minor burst of RSF. There are multiple pathways observed in the local universe which galaxies can

approach the "green valley" in which many of the catalog ETGs "reside." Specifically, disk-dominated galaxies on the "blue cloud" can be removed to the green valley via gas consumption and other more "secular' gas processing. Though the ETGs do not show a significant disk component in their visual morphologies, the large dispersion in measured Sèrsic indices may indicate that a significant fraction of ETGs are experiencing this "in-situ" recent star-formation as relatively gas-rich ETGs (potentially S0s) in their "death throes" evolve away from blue sequence.

Secondly, in §5.3.4, I find that approximately 10% of ETGs have companions. For ETGs whose young stellar age and mass fraction could be well-constrained (i.e., $\chi^2 \sim 2$), I measured a large difference in the best-fit ages and mass fractions of the young stellar component for those galaxies with & without companions. Specifically, ETGs with companions were likely to be better fit in the two-component analysis with much younger aged stellar ($t_{YC} = 700 - 800$Myr) population which comprised a smaller fraction of the total stellar mass of the galaxy.

Based on theory and observations of massive galaxies, I can expect a high fraction (40-60%) of these companions to merge with the more massive ETG by z∼0(Tal et al. , 2013). If I increase the velocity range of the companion search (maintaining $\{X, Y\}$ as defined in §5.3.2) to $v^{max} = 1000$km s^{-1} the likelihood of the companion merger increases to more than 80%. The number of ETGs with companions approximately doubles (14/102) if we increase the velocity range. For this larger velocity case, we identify the same trend as in §5.3.4: ETGs with companions are more likely to host a small fraction of their stellar mass in relatively younger stars than is observed for ETGs without companions. Though I am limited by small number statistics, this correlation would appear to support the hierarchical picture of galaxy assembly identified at lower redshifts whereby ETGs are formed at high redshift, but periodically experience minor punctuated bursts of star formation due

to the consumption of cold gas reservoirs introduced by minor mergers (Kaviraj et al. , 2007b; Naab, Johanssen,& Ostriker , 2009). At the redshift of the catalog, the spatial resolution is insufficient to identify the signatures of this merger activity (cf. Peirani et al. , 2010). Galaxies without companions have generally older ages, but these galaxies are not generally "red and dead" and have likely experienced a burst of recent star-formation at higher ($t > 1$ Gyr) redshift. Thus, an estimate to the fraction of ETGs that have undergone a minor merger event is likely to be only constrained at a minimum by this analysis. Repeating a similar analysis in HST deep fields where HST rest-frame UV data (e.g., the Hubble Ultra Deep Field, for which deep data is available to AB(FUV=27-28)) or for a larger sample size, would significantly improve the picture of massive galaxy assembly at these redshifts.

In summary, there are likely to be multiple mechanisms motivating the observed RSF in intermediate redshift ETGs. From the quantitative analysis of the F160W band morphologies of these ETGs, a significant fraction of the sample appear to have "diskier" morphologies. These galaxies may have approached the green valley from a previous residence in the blue cloud and are experiencing low level star formation as they transition to a residence on the "red and dead" sequence. In addition, the frequency of companions appears to be correlated with the age and mass fraction of the young stellar population measured for the ETG. Thus, as is observed or implicated in both the local (Crockett et al. , 2011) and high redshift (López-Sanjuan et al. , 2012) universe, minor mergers—which are ubiquitous in the hierarchical paradigm of massive galaxy assembly—are also likely to motivate minor star-formation in ETGs at intermediate redshift.

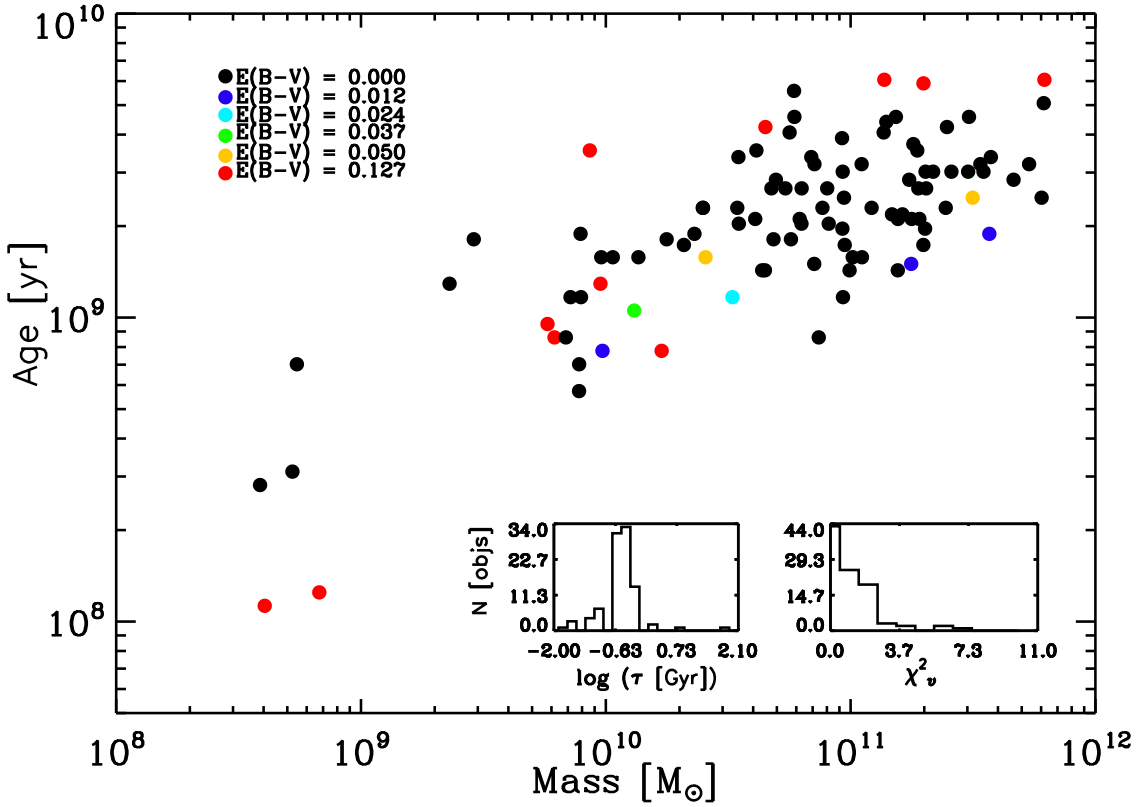

Figure 5.1: The mass ($M_\odot$) and age (yr) of the old stellar populations of the ETGs, measured from best-fit stellar template (§5.2.1). Stellar templates were fit only to the Optical+IR SED (F435W, F606W, F775W, F850LP, F098M, F125W, F160W). In the primary panel, I plot the measured mass-age distribution of ETGs, coded by the best-fitting dust extinction. Inset in this panel are the distributions of the best-fitting τ (see §5.2.1) parameter (left) derived from the SED fitting, and reduced χ^2 values of each fit.

Table 5.1: ETG Young Stellar Population

GOODS ID	t_{YC}[Gyr]	$f_{YC}/100\%$	χ^2
J033202.71-274310.8	$0.641^{0.078}_{0.000}$	$0.580^{0.4200}_{0.2400}$	7.84
J033203.29-274511.4	$0.143^{0.059}_{0.053}$	$0.050^{0.0300}_{0.0240}$	1.08
J033205.09-274514.0	$0.114^{0.047}_{0.023}$	$0.058^{0.0820}_{0.0220}$	0.96
J033205.13-274351.0	$0.114^{0.029}_{0.023}$	$0.094^{0.1860}_{0.0380}$	1.21
J033206.27-274536.7	$0.571^{1.929}_{0.443}$	$0.009^{0.2904}_{0.0089}$	1.10
J033206.48-274403.6	$0.047^{0.208}_{0.047}$	$0.000^{0.0067}_{0.0006}$	0.83
J033206.81-274524.3	$0.003^{0.014}_{0.002}$	$0.000^{0.0002}_{0.0000}$	2.35
J033207.55-274356.6	$0.404^{0.402}_{0.349}$	$0.030^{0.9700}_{0.0291}$	0.88
J033207.95-274212.1	$0.181^{0.141}_{0.109}$	$0.009^{0.0202}_{0.0066}$	0.56
J033208.41-274231.3	$0.404^{0.236}_{0.177}$	$0.016^{0.0220}_{0.0102}$	0.34
J033208.45-274145.9	$0.003^{0.042}_{0.002}$	$0.000^{0.0006}_{0.0000}$	1.04

Continued on next page ...

Table 4.1:Y oung Stellar Populations, cont.

GOODS ID	t_{YC}[Gyr]	$f_{YC}/100\%$	χ^2
J033208.53-274217.7	$0.072^{0.089}_{0.050}$	$0.001^{0.0034}_{0.0012}$	1.95
J033208.55-274231.1	$0.003^{0.078}_{0.002}$	$0.000^{0.0023}_{0.0000}$	1.08
J033208.65-274501.8	$1.015^{0.419}_{0.110}$	$0.260^{0.7400}_{0.1200}$	1.19
J033208.90-274344.3	$0.286^{0.074}_{0.031}$	$0.340^{0.6600}_{0.1800}$	1.09
J033209.09-274510.8	$0.114^{0.047}_{0.033}$	$0.072^{0.0680}_{0.0240}$	1.31
J033209.19-274225.6	$0.571^{1.329}_{0.368}$	$0.022^{0.3380}_{0.0184}$	1.02
J033210.04-274333.1	$0.001^{0.089}_{0.000}$	$0.000^{0.0005}_{0.0000}$	0.86
J033210.12-274333.3	$0.227^{1.573}_{0.226}$	$0.002^{0.2776}_{0.0023}$	1.42
J033210.16-274334.3	$0.001^{1.699}_{0.000}$	$0.000^{0.0899}_{0.0000}$	0.82
J033210.76-274234.6	$0.360^{0.044}_{0.105}$	$0.012^{0.0060}_{0.0076}$	0.59
J033210.86-274441.2	$0.143^{0.143}_{0.112}$	$0.007^{0.0126}_{0.0058}$	0.24
J033211.21-274533.4	$0.052^{0.108}_{0.048}$	$0.000^{0.0021}_{0.0005}$	3.67
J033211.61-274554.1	$0.023^{0.158}_{0.022}$	$0.000^{0.0026}_{0.0001}$	1.77
J033212.20-274530.1	$0.360^{0.093}_{0.074}$	$0.024^{0.0180}_{0.0100}$	1.06
J033212.31-274527.4	$0.360^{0.149}_{0.133}$	$0.026^{0.0260}_{0.0140}$	1.28
J033212.47-274224.2	$0.453^{0.451}_{0.167}$	$0.032^{0.0880}_{0.0160}$	0.75
J033214.26-274254.2	$0.181^{0.074}_{0.090}$	$0.028^{0.0380}_{0.0184}$	2.37
J033214.45-274456.6	$0.005^{0.250}_{0.004}$	$0.000^{0.0138}_{0.0000}$	1.30
J033214.65-274136.6	$0.001^{0.019}_{0.000}$	$0.000^{0.0001}_{0.0000}$	0.97
J033214.68-274337.1	$0.161^{0.066}_{0.047}$	$0.054^{0.0860}_{0.0300}$	2.84
J033214.73-274153.3	$0.404^{0.236}_{0.118}$	$0.042^{0.0580}_{0.0180}$	0.31
J033214.78-274433.1	$0.025^{0.296}_{0.024}$	$0.000^{0.0112}_{0.0006}$	1.21
J033214.83-274157.1	$0.404^{0.167}_{0.118}$	$0.046^{0.0540}_{0.0220}$	0.21
J033215.98-274422.9	$0.404^{0.049}_{0.083}$	$0.078^{0.0620}_{0.0360}$	1.06
J033216.19-274423.1	$0.286^{0.118}_{0.106}$	$0.024^{0.0220}_{0.0120}$	0.39
J033217.11-274220.9	$0.020^{0.006}_{0.016}$	$1.000^{0.0000}_{0.9964}$	3.78
J033217.12-274407.7	$0.453^{0.562}_{0.251}$	$0.024^{0.1160}_{0.0178}$	0.25
J033217.14-274303.3	$0.286^{0.035}_{0.031}$	$0.040^{0.0180}_{0.0140}$	0.59
J033217.49-274436.7	$0.360^{0.093}_{0.133}$	$0.044^{0.0320}_{0.0260}$	1.09
J033217.91-274122.7	$0.013^{0.077}_{0.012}$	$0.000^{0.0009}_{0.0000}$	1.51
J033218.31-274233.5	$0.255^{0.066}_{0.074}$	$0.009^{0.0086}_{0.0048}$	3.84
J033218.64-274144.4	$0.001^{0.003}_{0.000}$	$0.000^{0.0000}_{0.0000}$	1.51
J033218.74-274415.8	$0.321^{0.132}_{0.094}$	$0.014^{0.0140}_{0.0070}$	0.67
J033219.02-274242.7	$0.072^{0.214}_{0.070}$	$0.001^{0.0106}_{0.0013}$	1.50
J033219.48-274216.8	$0.321^{0.132}_{0.118}$	$0.016^{0.0120}_{0.0094}$	0.65
J033219.59-274303.8	$0.404^{0.105}_{0.083}$	$0.036^{0.0280}_{0.0160}$	1.23
J033219.77-274204.0	$0.509^{0.925}_{0.505}$	$0.034^{0.9660}_{0.0339}$	0.50
J033220.02-274104.2	$0.005^{0.198}_{0.004}$	$0.000^{0.0035}_{0.0000}$	1.30
J033220.09-274106.7	$0.001^{0.056}_{0.000}$	$0.000^{0.0000}_{0.0000}$	2.64
J033220.67-274446.4	$0.102^{0.079}_{0.063}$	$0.003^{0.0046}_{0.0022}$	3.62
J033221.28-274435.6	$0.509^{0.132}_{0.105}$	$0.022^{0.0240}_{0.0100}$	1.76
J033222.33-274226.5	$5.000^{1.000}_{4.999}$	$0.030^{0.9700}_{0.0300}$	1.14
J033222.58-274141.2	$0.571^{1.129}_{0.250}$	$0.036^{0.4440}_{0.0220}$	0.20
J033222.58-274152.1	$0.255^{0.031}_{0.052}$	$0.740^{0.2600}_{0.5200}$	0.84
J033223.01-274331.5	$0.806^{1.094}_{0.520}$	$0.076^{0.9240}_{0.0640}$	0.97
J033224.36-274315.2	$0.019^{0.003}_{0.014}$	$1.000^{0.0000}_{0.9880}$	9.69
J033224.98-274101.5	$0.102^{0.042}_{0.044}$	$0.006^{0.0034}_{0.0034}$	1.80
J033225.11-274425.6	$0.031^{0.016}_{0.026}$	$0.009^{0.0122}_{0.0091}$	2.11
J033225.29-274224.2	$0.404^{0.049}_{0.044}$	$0.920^{0.0800}_{0.4800}$	2.71
J033225.47-274327.6	$0.404^{0.167}_{0.202}$	$0.009^{0.0146}_{0.0072}$	3.52
J033225.85-274246.1	$0.014^{0.041}_{0.013}$	$0.000^{0.0016}_{0.0003}$	1.40
J033225.97-274312.5	$0.453^{2.297}_{0.452}$	$0.009^{0.9902}_{0.0097}$	0.36
J033225.98-274318.9	$0.006^{0.058}_{0.005}$	$0.000^{0.0006}_{0.0000}$	1.48
J033226.05-274236.5	$5.000^{0.000}_{0.750}$	$1.000^{0.0000}_{0.4000}$	2.76

Continued on next page ...

Table 4.1:Y oung Stellar Populations, cont.

GOODS ID	t_{YC}[Gyr]	$f_{YC}/100\%$	χ^2
J033226.71-274340.2	$0.321^{0.132}_{0.118}$	$0.012^{0.0120}_{0.0066}$	0.36
J033227.18-274416.5	$0.571^{0.000}_{0.062}$	$0.120^{0.0400}_{0.0540}$	3.69
J033227.62-274144.9	$0.203^{0.052}_{0.042}$	$0.018^{0.0140}_{0.0060}$	2.75
J033227.70-274043.7	$1.015^{0.885}_{0.375}$	$0.120^{0.8800}_{0.0840}$	1.34
J033227.84-274136.8	$0.050^{0.153}_{0.047}$	$0.001^{0.0070}_{0.0009}$	1.83
J033227.86-274313.6	$0.019^{0.062}_{0.016}$	$0.000^{0.0056}_{0.0009}$	1.43
J033228.88-274129.3	$0.203^{0.202}_{0.164}$	$0.003^{0.0102}_{0.0033}$	0.64
J033229.04-274432.2	$5.000^{0.000}_{4.999}$	$1.000^{0.0000}_{1.0000}$	0.58
J033229.30-274244.8	$0.072^{0.089}_{0.052}$	$0.004^{0.0096}_{0.0034}$	0.89
J033229.64-274030.3	$0.102^{0.101}_{0.062}$	$0.009^{0.0268}_{0.0066}$	2.08
J033230.56-274145.7	$0.143^{0.059}_{0.042}$	$0.042^{0.0460}_{0.0200}$	1.82
J033231.84-274329.4	$0.002^{0.225}_{0.001}$	$0.000^{0.0099}_{0.0000}$	0.58
J033232.34-274345.8	$0.114^{0.029}_{0.050}$	$0.040^{0.0560}_{0.0240}$	1.58
J033232.57-274133.8	$0.001^{0.001}_{0.000}$	$0.002^{0.0004}_{0.0002}$	2.37
J033232.96-274106.8	$0.143^{0.037}_{0.016}$	$0.048^{0.0260}_{0.0140}$	0.57
J033233.28-274236.0	$5.000^{0.000}_{4.999}$	$0.180^{0.8200}_{0.1800}$	0.10
J033233.40-274138.9	$0.203^{0.084}_{0.089}$	$0.016^{0.0260}_{0.0104}$	2.20
J033233.87-274357.6	$0.005^{0.250}_{0.004}$	$0.000^{0.0077}_{0.0000}$	1.48
J033234.34-274350.1	$0.161^{0.094}_{0.059}$	$0.009^{0.0108}_{0.0044}$	3.56
J033235.10-274410.7	$0.052^{0.028}_{0.026}$	$0.012^{0.0100}_{0.0068}$	8.73
J033235.63-274310.2	$0.001^{0.025}_{0.000}$	$0.000^{0.0001}_{0.0000}$	1.16
J033236.72-274406.4	$0.143^{0.059}_{0.063}$	$0.009^{0.0064}_{0.0052}$	0.67
J033237.32-274334.3	$0.114^{0.113}_{0.079}$	$0.004^{0.0058}_{0.0030}$	1.15
J033237.38-274126.2	$0.404^{0.167}_{0.149}$	$0.007^{0.0124}_{0.0052}$	1.72
J033238.06-274128.4	$0.128^{0.232}_{0.127}$	$0.001^{0.0060}_{0.0013}$	2.32
J033238.36-274128.4	$0.286^{0.223}_{0.125}$	$0.050^{0.2900}_{0.0340}$	6.48
J033238.44-274019.6	$0.026^{0.117}_{0.025}$	$0.000^{0.0021}_{0.0002}$	1.14
J033238.48-274313.8	$0.255^{0.066}_{0.052}$	$0.160^{0.3600}_{0.0780}$	1.66
J033239.17-274026.5	$0.321^{0.083}_{0.066}$	$0.032^{0.0300}_{0.0140}$	1.02
J033239.17-274257.7	$0.571^{0.236}_{0.211}$	$0.032^{0.0400}_{0.0180}$	0.54
J033239.18-274329.0	$0.003^{0.224}_{0.002}$	$0.000^{0.0069}_{0.0000}$	0.44
J033239.52-274117.4	$0.052^{0.203}_{0.052}$	$0.000^{0.0051}_{0.0004}$	1.42
J033240.38-274338.3	$0.025^{0.047}_{0.022}$	$0.000^{0.0018}_{0.0006}$	0.65
J033241.63-274151.5	$0.038^{0.052}_{0.034}$	$0.000^{0.0017}_{0.0007}$	4.30
J033242.36-274238.0	$0.509^{0.132}_{0.149}$	$0.018^{0.0180}_{0.0104}$	1.51
J033243.93-274232.4	$0.001^{0.063}_{0.000}$	$0.000^{0.0003}_{0.0000}$	3.03
J033244.97-274309.1	$0.009^{0.171}_{0.008}$	$0.000^{0.0029}_{0.0002}$	4.93

Notes- Uncertainties provided for each parameter were derived from the 68% confidence interval.

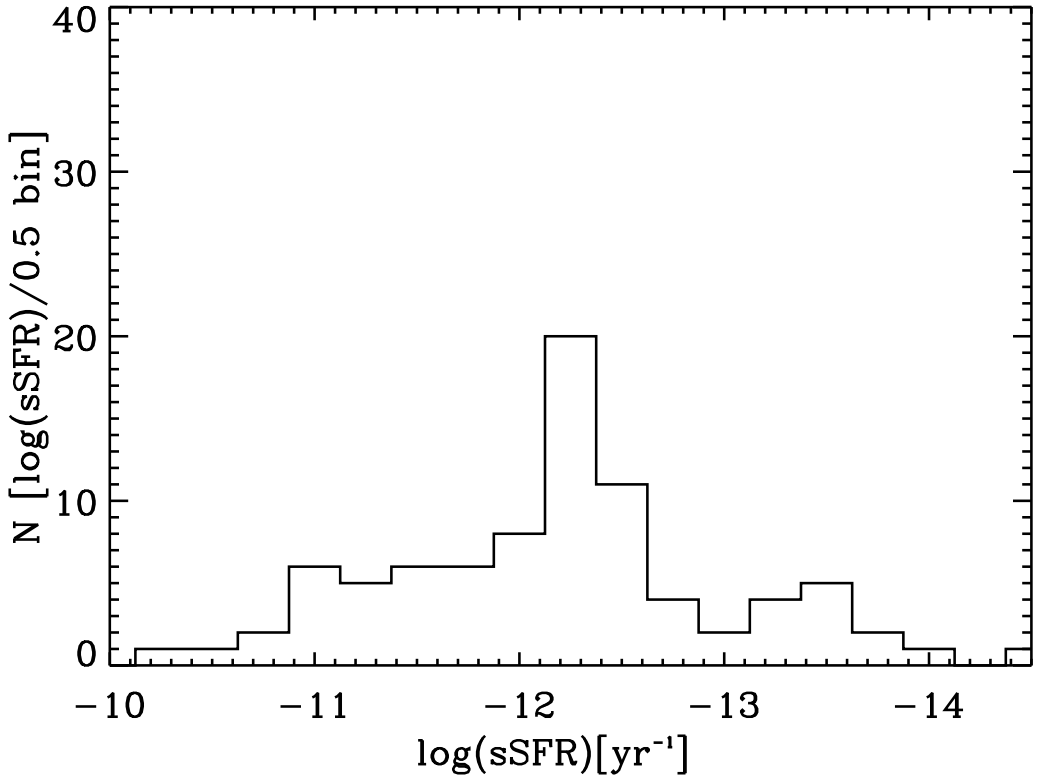

Figure 5.2: In §5.2.1, I measured the mass-weighted star-formations rates for the ETGs (i.e., specific SFR, or sSFR) applying the conversion provided by Salim et al. (2012) measured for low-redshift ETGs using GALEX. These sSFRs are in good agreement with comparable ETGs observed at these redshifts (see Rowlands et al. , 2012).

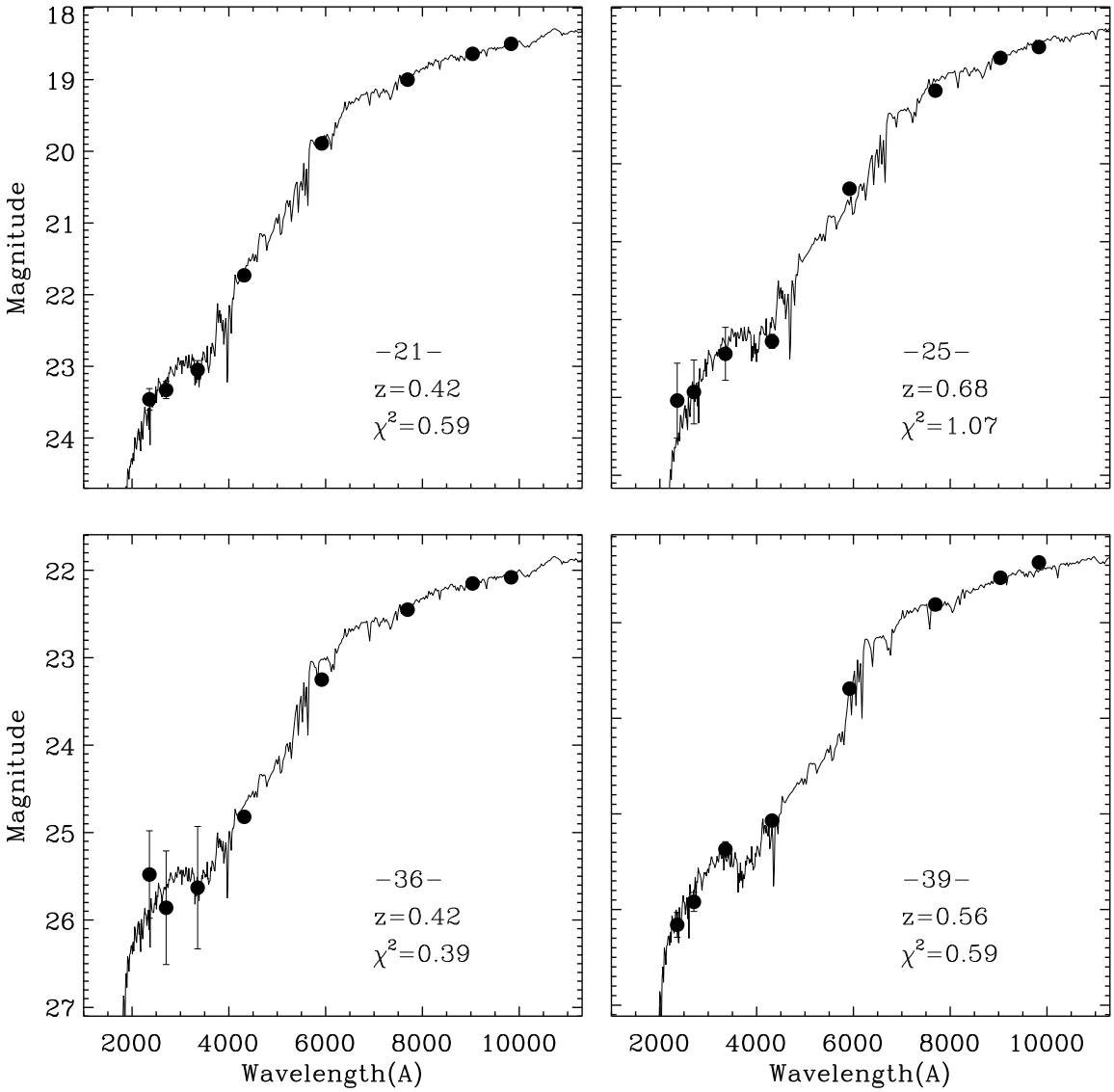

Figure 5.3: Representative fits of the two-component stellar models to the complete (UV-optical-near IR) SED of the catalog. For more details regarding the fitting technique, see Jeong et al. (2009) and §5.2.2.

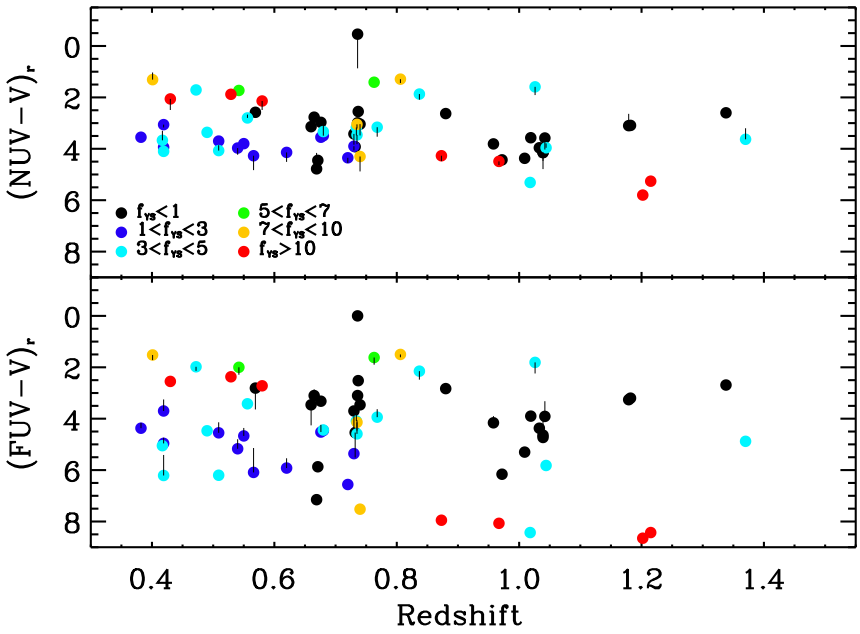

Figure 5.4: The rest-frame UV-optical colors of the ETGs from the best-fit two-component stellar population model (see §5.2.2). In Panels (a) and (b) I plot the rest-frame UV-optical colors, shaded according to the color scheme provided in the panel. Overplotted on these data are vertical lines representing the offset in magnitude between colors measured in Chapter 4 and those presented here. These offsets are typically small ($\Delta \ll 0.3$), confirming the transformation applied in Chapter 4 to measure rest-frame UV-optical colors from the observed photometry is generally valid.

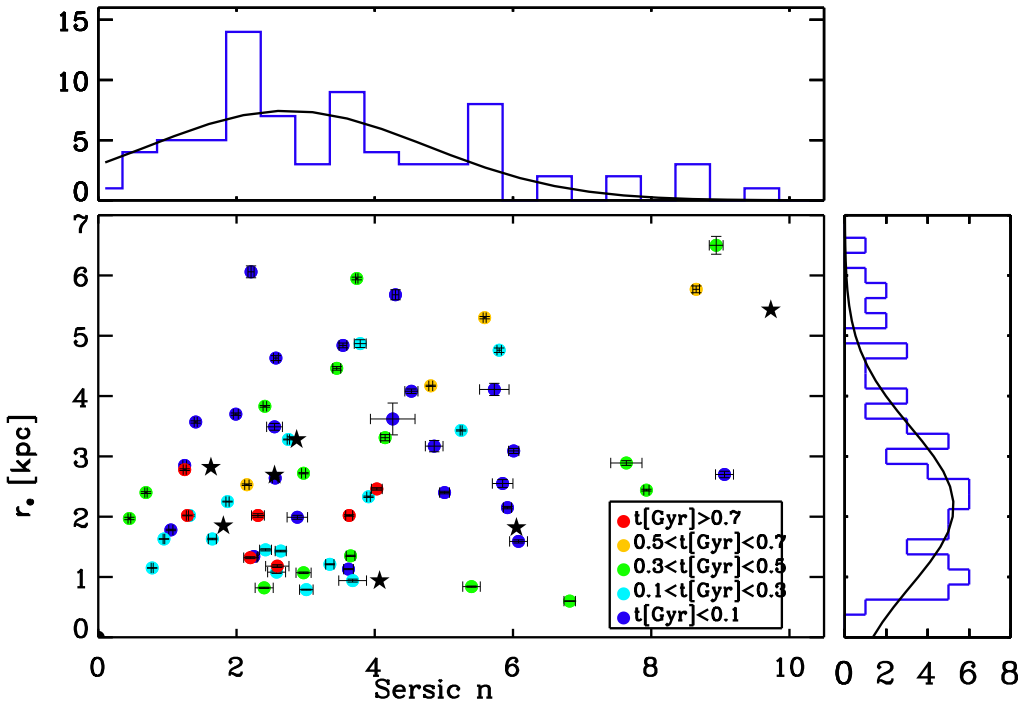

Figure 5.5: In §5.3.1, I measured the best-fit Sèrsic function, effective radius and ellipticity for the two-dimensional F160W light profile of each ETG. The distribution of these parameters is provided here, with respect to the YSP mass fraction. ETGs identified in Chapter 3 as AGN are designated with a filled star symbol.

Table 5.2: Early-Type Galaxies, Measured Spatial Parameters: F160W

Object	R_e	n	B/A	θ	m_{F160W}	χ^2_ν
000	5.78±0.007	10.24±0.023	0.79±0.000	-69.3±0.07	17.18±0.001	1.020
001				Failed F_{crit}		
002	2.42±0.086	1.45±0.018	0.92±0.011	27.8±5.62	22.48±0.009	0.441
003⋆	2.58±0.130	1.08±0.021	0.86±0.007	34.9±2.83	23.61±0.033	0.355
004⋆	2.55±0.023	2.69±0.008	0.29±0.000	-89.1±0.05	21.95±0.009	0.443
005⋆	1.25±0.027	2.85±0.017	0.81±0.004	27.6±0.88	21.94±0.005	0.468
006⋆	2.88±0.148	1.99±0.033	0.34±0.004	-34.0±0.27	22.98±0.034	0.401
007	4.15±0.064	3.31±0.051	0.85±0.005	-72.6±1.35	21.31±0.008	0.400
008	3.01±0.098	0.79±0.008	0.55±0.007	68.5±0.67	22.29±0.004	0.526
009	6.82±0.083	0.60±0.002	0.91±0.003	-17.0±1.33	20.42±0.003	0.721
010	5.92±0.059	2.15±0.020	0.86±0.003	74.3±0.75	20.21±0.004	0.596
011⋆	2.87±0.029	3.28±0.012	0.66±0.001	-87.3±0.16	22.03±0.010	0.817
012⋆	4.26±0.323	3.62±0.264	0.90±0.016	43.8±7.56	24.60±0.052	0.671
013⋆	1.29±0.016	2.02±0.006	0.63±0.001	-55.7±0.18	21.35±0.005	0.603
014⋆	1.65±0.058	1.63±0.012	0.62±0.006	-23.8±0.74	24.70±0.065	0.377
015				Fail To Converge		
016⋆	1.63±0.018	2.82±0.009	0.62±0.001	-34.4±0.18	22.46±0.008	0.551
017				Not Fit		
018				Not Fit		
019				Not Fit		
020⋆	1.76±0.002	4.11±0.005	0.73±0.000	77.8±0.10	20.85±0.002	3.786
021⋆	3.68±0.201	0.94±0.024	0.47±0.007	-73.0±0.69	23.86±0.057	0.442
022⋆	2.25±0.060	1.34±0.021	0.46±0.002	-30.6±0.15	24.93±0.456	0.439
023⋆	5.01±0.071	2.40±0.021	0.37±0.002	-55.1±0.15	24.11±0.047	0.407
024				Fail To Converge		
025				Fail To Converge		
026⋆	0.45±0.019	5 1.97±0.020	0.85±0.007	-14.4±2.16	21.78±0.002	0.637
027				Failed F_{crit}		
028				Failed F_{crit}		
029⋆	5.73±0.213	4.11±0.101	0.88±0.006	-32.2±2.24	23.00±0.017	0.449
030	2.64±0.080	1.43±0.013	0.40±0.007	-29.2±0.43	22.31±0.005	0.401
031	5.40±0.127	0.84±0.010	0.56±0.006	83.2±0.54	21.44±0.004	0.647
032⋆	1.05±0.030	1.78±0.012	0.70±0.002	-82.2±0.53	23.168±0.022	0.425

Continued on next page ...

Spatial Parameters, cont.

Object	R_e	n	B/A	θ	m_{F160W}	χ^2_ν
033⋆	0.69±0.017	2.40±0.015	0.88±0.005	-27.2±1.70	22.055±0.002	0.531
034⋆	3.45±0.057	4.46±0.030	0.55±0.002	64.0±0.19	23.704±0.028	0.413
035⋆	4.43±0.757	4.11±0.535	0.81±0.033	48.6±6.00	22.920±0.050	4.375
036				Failed F_{crit}		
037⋆	2.97±0.109	1.07±0.013	0.31±0.005	-2.6±0.37	23.43±0.028	0.386
038	4.07±0.019	0.94±0.001	0.87±0.001	-49.8±0.40	19.72±0.001	0.533
039	8.94±0.100	6.50±0.148	0.99±0.003	-31.1±113.40	20.14±0.009	0.387
040⋆	2.56±0.041	2.64±0.016	0.93±0.002	-59.3±1.72	22.82±0.014	0.439
041	5.25±0.014	3.43±0.010	0.48±0.000	-10.9±0.04	19.09±0.001	0.665
042				Failed F_{crit}		
043⋆	2.97±0.029	2.72±0.010	0.58±0.001	61.4±0.12	22.59±0.013	0.450
044⋆	2.21±0.044	6.06±0.099	0.59±0.005	17.5±0.55	22.87±0.008	0.930
045	7.93±0.038	2.44±0.015	0.71±0.001	-82.7±0.14	19.29±0.002	0.560
046⋆	7.64±0.226	2.89±0.039	0.92±0.003	-36.4±1.33	22.05±0.027	0.681
047				Failed F_{crit}		
048⋆	9.06±0.130	2.70±0.053	0.89±0.003	-31.4±1.09	20.11±0.007	0.612
049⋆	2.57±0.035	4.63±0.041	0.67±0.003	-62.2±0.42	22.05±0.006	0.678
050	3.91±0.026	2.33±0.011	0.60±0.001	-87.8±0.17	20.39±0.002	0.670
051⋆	0.64±0.004	6.31±0.014	0.49±0.001	-35.1±0.12	20.36±0.002	13.968
052	3.63±0.050	2.02±0.013	0.43±0.003	60.8±0.20	21.28±0.003	0.421
053⋆	2.15±0.032	2.53±0.013	0.88±0.003	-85.5±0.93	21.49±0.004	0.666
054				Failed F_{crit}		
055⋆	1.25±0.022	2.78±0.014	0.84±0.003	-71.5±0.94	22.45±0.006	0.425
056				Failed F_{crit}		
057	6.05±0.035	1.82±0.009	0.82±0.001	44.6±0.32	20.03±0.002	0.506
058				Failed F_{crit}		
059				Failed F_{crit}		
060⋆	3.74±0.017	5.95±0.022	0.87±0.001	71.2±0.30	21.49±0.004	0.538
061				Failed F_{crit}		
062	2.40±0.131	0.82±0.011	0.57±0.011	-33.9±1.22	22.77±0.005	0.443
063	6.08±0.129	1.59±0.026	0.44±0.005	-45.2±0.34	21.46±0.005	0.518
064⋆	2.31±0.093	2.02±0.029	0.24±0.002	-9.1±0.19	23.05±0.032	0.445
065⋆	3.65±0.063	1.35±0.011	0.58±0.002	42.9±0.27	22.65±0.014	0.467
066⋆	4.81±0.028	4.17±0.010	0.56±0.000	29.0±0.05	21.16±0.009	1.034
067⋆	1.81±0.028	1.85±0.008	0.68±0.002	-44.8±0.28	21.66±0.007	0.640
068⋆	4.03±0.078	2.46±0.020	0.33±0.001	-77.0±0.10	22.17±0.017	0.478

Continued on next page ...

Spatial Parameters, cont.

Object	R_e	n	B/A	θ	m_{F160W}	χ^2_ν
069	6.75±0.075	10.16±0.21	60.61±0.002	52.7±0.27	20.30±0.009	0.492
070				Failed F_{crit}		
071⋆	2.75±0.017	3.28±0.007	0.91±0.001	-56.4±0.59	21.88±0.005	0.542
072	2.20±0.096	1.32±0.016	0.20±0.010	-51.3±0.42	22.34±0.004	0.922
073				Failed F_{crit}		
074	1.32±0.036	2.02±0.013	0.43±0.005	87.3±0.40	22.39±0.004	0.449
075	0.95±0.012	1.63±0.005	0.58±0.002	78.4±0.26	21.64±0.001	0.361
076⋆	2.55±0.114	3.49±0.056	0.86±0.009	-70.5±2.83	23.68±0.020	0.391
077				Failed F_{crit}		
078				Not Fit		
079⋆	0.78±0.015	1.15±0.005	0.89±0.002	69.8±1.37	23.30±0.019	0.480
080	2.59±0.169	1.18±0.023	0.39±0.014	38.6±0.92	23.03±0.008	0.464
081⋆	1.87±0.023	2.25±0.007	0.82±0.002	-21.0±0.48	23.37±0.029	0.388
082	3.62±0.070	1.13±0.008	0.91±0.005	53.1±2.57	21.53±0.004	0.458
083	9.73±0.086	5.43±0.093	0.84±0.002	28.7±0.51	19.77±0.006	0.430
084	4.86±0.128	3.17±0.094	0.83±0.009	35.9±1.91	21.44±0.014	0.392
085⋆	4.53±0.095	4.08±0.037	0.54±0.002	-24.8±0.22	22.43±0.013	0.439
086⋆	3.79±0.086	4.87±0.065	0.54±0.003	23.9±0.28	22.96±0.022	0.403
087				Fail To Converge		
088				Fail To Converge		
089	5.80±0.032	4.76±0.037	0.58±0.001	40.0±0.12	19.67±0.003	0.535
090⋆	3.35±0.060	1.21±0.008	0.90±0.004	46.2±2.49	24.37±0.046	0.475
091	6.01±0.074	3.09±0.042	0.72±0.003	-80.6±0.45	20.71±0.006	0.442
092				Failed F_{crit}		
093⋆	2.41±0.026	3.83±0.014	0.65±0.001	-28.7±0.21	22.85±0.010	0.448
094⋆	5.59±0.022	5.30±0.019	0.89±0.000	20.8±0.24	20.47±0.002	0.562
095	5.85±0.149	2.55±0.065	0.87±0.008	25.1±2.21	21.81±0.012	0.360
096⋆	1.41±0.022	3.57±0.019	0.63±0.003	4.7±0.33	22.26±0.006	0.457
097	4.30±0.048	5.68±0.083	0.64±0.003	26.2±0.37	20.90±0.007	0.376
098⋆	1.99±0.036	3.70±0.020	0.94±0.004	9.3±2.85	22.70±0.008	0.474
099	8.65±0.048	5.77±0.056	0.46±0.000	74.4±0.06	18.79±0.004	0.977
100⋆	3.54±0.056	4.84±0.039	0.59±0.001	28.6±0.25	22.49±0.010	0.478
101				Failed F_{crit}		

Continued on next page ...

Spatial Parameters, cont.

Object	R_e	n	B/A	θ	m_{F160W}	χ^2_ν

Notes-Row values are defined as follows:"Failed F_{crit}"=Galaxies that failed the Ryan et al. (2012) critierion for identifying well-resolved glaxies were not fitted (see §5.3.1; "Not Fit"=Galaxies were not fit because the light profiles of the ETG were strongly blended with bright; neighbors; "Fail to Converge"=One (or more) parameters could not be well-fitted by `GALFIT`. Galaxies designated "$\star$" were best-fit by a two-component model, see §5.3.1.

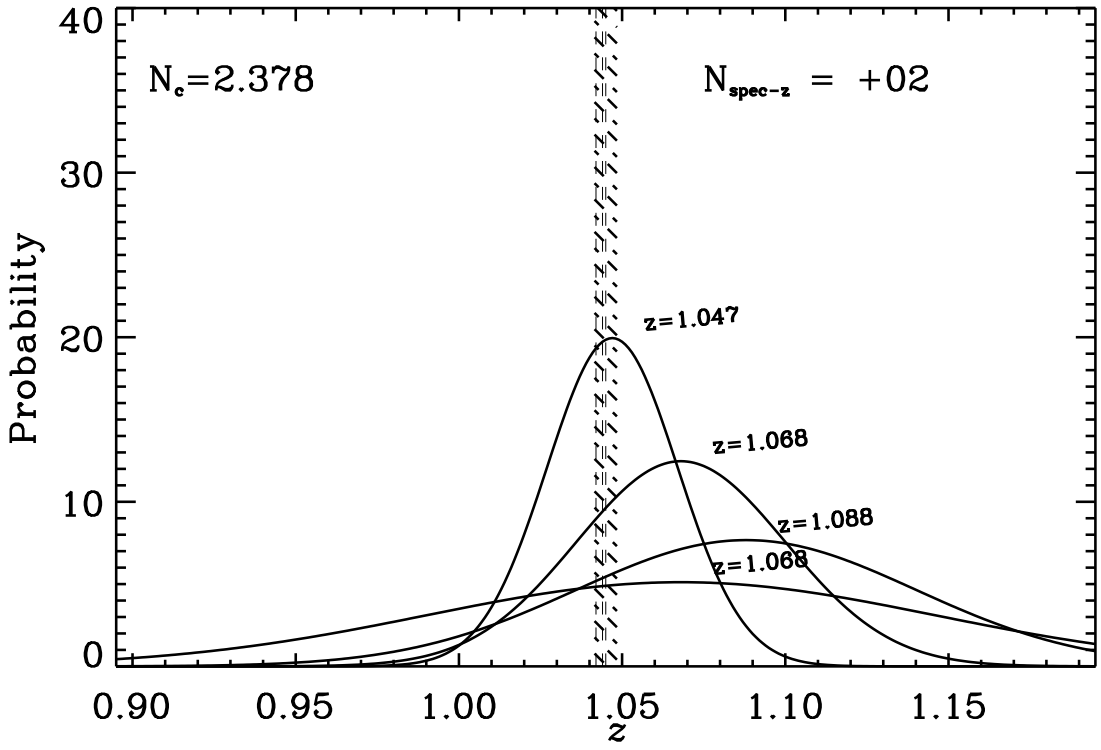

Figure 5.6: One realization of a Monte Carlo simulation to measure the companion number for J033233.40-274138.9, an ETG identified with greater than one companion in the simulation ($\bar{N}_c \simeq 2.4$, see Table 5.3). In this analyis, I required that all galaxies be identified within 1000kpc, on the plane of the sky, and that their velocities lie with $v_{comp} = v_{ETG} \pm 500$km s^{-1} (hatched region; $1.04 < z < 1.05$), minimally, 2σ from the mean of the galaxies' PDF. In this simulation, the ETG was identified with both photometric (indicated by Gaussian functions, with area normalized to one) and spectroscopic (vertical dashed lines) companions within this range. For clarity, I have extended the probability range of possible companions with spectroscopic redshifts to $+\infty$. In practice, the PDF of these galaxies is defined by the Dirac-delta function.

Table 5.3: ETG Statistical Companion Number

GOODS ID	$\tilde{N}_c^a$	$\tilde{N}_{spec-z}^b$	$\tilde{N}_{phot-z}^c$
J033202.71-274310.8	$0.00^{+0.00}_{-0.00}$	0	0.00
J033203.29-274511.4	$0.09^{+0.11}_{-0.09}$	0	1.93
J033205.09-274514.0	$3.10^{+0.07}_{-0.10}$	3	1.47
J033205.13-274351.0	$0.14^{+0.11}_{-0.14}$	0	1.56
J033206.27-274536.7	$1.00^{+0.00}_{-0.00}$	1	0.00
J033206.48-274403.6	$0.10^{+0.09}_{-0.10}$	0	1.31
J033206.81-274524.3	$0.03^{+0.09}_{-0.03}$	0	0.59
J033207.55-274356.6	$1.10^{+0.07}_{-0.10}$	1	0.85
J033207.95-274212.1	$0.19^{+0.24}_{-0.14}$	0	2.22
J033208.41-274231.3	$0.02^{+0.03}_{-0.02}$	0	0.52
J033208.45-274145.9	$0.01^{+0.09}_{-0.01}$	0	0.55
J033208.53-274217.7	$0.16^{+0.10}_{-0.16}$	0	2.45
J033208.55-274231.1	$0.03^{+0.03}_{-0.03}$	0	0.61
J033208.65-274501.8	$0.27^{+0.16}_{-0.20}$	0	3.04
J033208.90-274344.3	$0.15^{+0.13}_{-0.10}$	0	2.04
J033209.09-274510.8	$0.00^{+0.00}_{-0.00}$	0	0.00
J033209.19-274225.6	$0.02^{+0.06}_{-0.02}$	0	0.70
J033210.04-274333.1	$1.15^{+0.17}_{-0.09}$	1	1.71
J033210.12-274333.3	$1.14^{+0.19}_{-0.08}$	1	1.21
J033210.16-274334.3	$0.24^{+0.14}_{-0.18}$	0	2.72
J033210.76-274234.6	$0.14^{+0.10}_{-0.14}$	0	2.15
J033210.86-274441.2	$0.03^{+0.04}_{-0.03}$	0	0.64
J033211.21-274533.4	$1.00^{+0.00}_{-0.00}$	1	0.00
J033211.61-274554.1	$1.23^{+0.15}_{-0.23}$	1	2.60
J033212.20-274530.1	$0.12^{+0.10}_{-0.12}$	0	2.08
J033212.31-274527.4	$0.16^{+0.13}_{-0.16}$	0	2.25
J033212.47-274224.2	$0.25^{+0.24}_{-0.18}$	0	3.26
J033214.26-274254.2	$0.42^{+0.31}_{-0.30}$	0	4.96
J033214.45-274456.6	$1.14^{+0.09}_{-0.14}$	1	2.12
J033214.65-274136.6	$0.00^{+0.00}_{-0.00}$	0	0.00
J033214.68-274337.1	$0.16^{+0.16}_{-0.10}$	0	1.57
J033214.73-274153.3	$0.00^{+0.00}_{-0.00}$	0	0.00
J033214.78-274433.1	$0.00^{+0.03}_{-0.00}$	0	0.03
J033214.83-274157.1	$0.21^{+0.12}_{-0.16}$	0	3.06
J033215.98-274422.9	$0.15^{+0.10}_{-0.15}$	0	2.06
J033216.19-274423.1	$0.01^{+0.03}_{-0.01}$	0	0.27
J033217.11-274220.9	$0.02^{+0.05}_{-0.02}$	0	0.42
J033217.12-274407.7	$0.18^{+0.15}_{-0.18}$	0	3.12
J033217.14-274303.3	$0.02^{+0.09}_{-0.02}$	0	0.61
J033217.49-274436.7	$0.15^{+0.12}_{-0.10}$	0	1.97
J033217.91-274122.7	$0.31^{+0.24}_{-0.31}$	0	4.04
J033218.31-274233.5	$0.01^{+0.03}_{-0.01}$	0	0.26
J033218.64-274144.4	$0.14^{+0.19}_{-0.07}$	0	1.00
J033218.74-274415.8	$0.00^{+0.00}_{-0.00}$	0	0.00
J033219.02-274242.7	$1.75^{+0.40}_{-0.49}$	1	8.81
J033219.48-274216.8	$0.00^{+0.00}_{-0.00}$	0	0.00
J033219.59-274303.8	$0.21^{+0.16}_{-0.21}$	0	3.41
J033219.77-274204.0	$0.56^{+0.55}_{-0.37}$	0	5.03
J033220.02-274104.2	$0.23^{+0.14}_{-0.17}$	0	3.29
J033220.09-274106.7	$0.21^{+0.20}_{-0.14}$	0	1.76
J033220.67-274446.4	$0.00^{+0.03}_{-0.00}$	0	0.16

Continued on next page ...

Table 4.3: ETG Catalog, Measured Phot. (Continued)

GOODS ID	$\bar{N}_c^a$	$\bar{N}_{spec-z}^b$	N_{phot-z}^c
J033221.28-274435.6	$0.05^{+0.66}_{-0.05}$	0	1.04
J033222.33-274226.5	$0.26^{+0.25}_{-0.26}$	0	3.93
J033222.58-274141.2	$0.10^{+0.15}_{-0.05}$	0	1.00
J033222.58-274152.1	$0.00^{+0.00}_{-0.00}$	0	0.00
J033223.01-274331.5	$0.00^{+0.00}_{-0.00}$	0	0.00
J033224.36-274315.2	$0.01^{+0.04}_{-0.01}$	0	0.34
J033224.98-274101.5	$0.02^{+0.03}_{-0.02}$	0	0.47
J033225.11-274425.6	$0.00^{+0.00}_{-0.00}$	0	0.00
J033225.29-274224.2	$0.18^{+0.19}_{-0.14}$	0	2.28
J033225.47-274327.6	$0.10^{+0.06}_{-0.10}$	0	1.56
J033225.85-274246.1	$0.05^{+0.05}_{-0.05}$	0	0.66
J033225.97-274312.5	$0.33^{+0.20}_{-0.27}$	0	3.72
J033225.98-274318.9	$0.00^{+0.00}_{-0.00}$	0	0.00
J033226.05-274236.5	$0.01^{+0.04}_{-0.01}$	0	0.25
J033226.71-274340.2	$1.02^{+0.09}_{-0.02}$	1	0.81
J033227.18-274416.5	$0.33^{+0.36}_{-0.24}$	0	3.78
J033227.62-274144.9	$0.29^{+0.21}_{-0.29}$	0	3.64
J033227.70-274043.7	$0.52^{+0.35}_{-0.34}$	0	5.40
J033227.84-274136.8	$0.40^{+0.32}_{-0.36}$	0	4.82
J033227.86-274313.6	$0.22^{+0.15}_{-0.22}$	0	2.18
J033228.88-274129.3	$0.32^{+0.21}_{-0.32}$	0	4.79
J033229.04-274432.2	$0.03^{+0.05}_{-0.03}$	0	0.53
J033229.30-274244.8	$0.06^{+0.08}_{-0.06}$	0	1.06
J033229.64-274030.3	$0.10^{+0.07}_{-0.10}$	0	1.09
J033230.56-274145.7	$0.24^{+0.14}_{-0.17}$	0	2.62
J033231.84-274329.4	$1.17^{+0.19}_{-0.17}$	1	2.65
J033232.34-274345.8	$0.29^{+0.18}_{-0.23}$	0	3.45
J033232.57-274133.8	$0.07^{+0.09}_{-0.07}$	0	1.45
J033232.96-274106.8	$0.08^{+0.08}_{-0.08}$	0	0.91
J033233.28-274236.0	$0.13^{+0.21}_{-0.07}$	0	1.00
J033233.40-274138.9	$2.41^{+0.29}_{-0.29}$	2	4.38
J033233.87-274357.6	$0.05^{+0.05}_{-0.05}$	0	0.64
J033234.34-274350.1	$0.20^{+0.13}_{-0.15}$	0	2.84
J033235.10-274410.7	$1.16^{+0.15}_{-0.10}$	1	1.82
J033235.63-274310.2	$0.05^{+0.12}_{-0.05}$	0	0.96
J033236.72-274406.4	$0.07^{+0.07}_{-0.07}$	0	1.26
J033237.32-274334.3	$0.04^{+0.07}_{-0.04}$	0	0.99
J033237.38-274126.2	$0.14^{+0.10}_{-0.09}$	0	2.32
J033238.06-274128.4	$0.21^{+0.20}_{-0.16}$	0	2.47
J033238.36-274128.4	$0.04^{+0.04}_{-0.04}$	0	0.61
J033238.44-274019.6	$0.42^{+0.31}_{-0.36}$	0	5.35
J033238.48-274313.8	$0.11^{+0.07}_{-0.11}$	0	1.66
J033239.17-274026.5	$0.01^{+0.03}_{-0.01}$	0	0.40
J033239.17-274257.7	$0.04^{+0.04}_{-0.04}$	0	0.71
J033239.18-274329.0	$0.02^{+0.04}_{-0.02}$	0	0.39
J033239.52-274117.4	$0.29^{+0.21}_{-0.27}$	0	3.66
J033240.38-274338.3	$0.00^{+0.00}_{-0.00}$	0	0.00
J033241.63-274151.5	$0.16^{+0.14}_{-0.16}$	0	1.51
J033242.36-274238.0	$0.00^{+0.00}_{-0.00}$	0	0.00
J033243.93-274232.4	$0.00^{+0.00}_{-0.00}$	0	0.00
J033244.97-274309.1	$0.14^{+0.13}_{-0.09}$	0	1.73

Notes- Col. 2 and 4 are average values from simulation. Associated uncertainties for N_c are derived from Monte-Carlo simulation (§5.3.4)

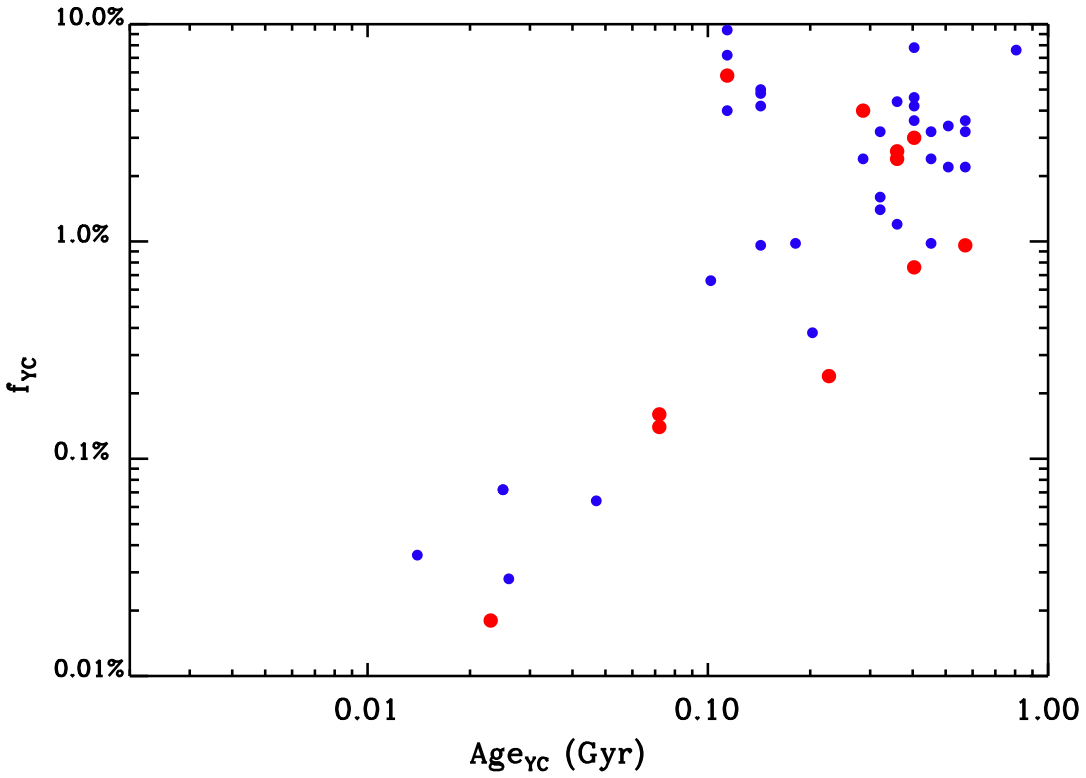

Figure 5.7: In §5.3.4 I measured the companion number for each ETG using the statistical likelihood formalism presented in López-Sanjuan et al. (2010). Here, I represent ETGs measured with more (fewer) than one companion with large red (blue) filled circles, plotting each as function of the best-fit age and mass fraction of the young stellar component (§5.2.2). The distribution of ETGs with more than one companion appears similar to the broader distribution, but the mean age and mass fraction measured for those ETGs with companions is significantly smaller ($\bar{t}_{YC} \simeq$ 260Myr; $\bar{f}_{YC} \simeq$2%) than is observed for ETGs without companions ($\bar{t}_{YC} \simeq$ 660Myr; $\bar{f}_{YC} \simeq 9\%$).

Chapter 6

CONCLUSION

6.1 Summary and conclusions on the nature of Seyfert core morphologies

I have investigated the dust-morphology–AGN class relationship for highly spatially-resolved galaxies in the local universe by visually inspecting a catalog of archival WFPC2 F606W images of the cores of 85 local ($z < 0.015$) Seyfert galaxies. I have classified the presence and distribution of dust features the cores (r<1kpc) of these galaxies and determined that Sy2 galaxies were more likely to be associated with galaxies whose core dust morphology is more irregular and of "later– type" morphology. This visual classification confirms the qualitative morphological relationship established by MGT98. We concur with the conclusion of MGT98 that—if this morphological relationship is indicative of a fundamental distinction between the subclasses of AGN—this result weakens the central postulate of the Unified Model of AGN.

I have extended the study of this qualitative morphological relationship by re–analyzing the images using quantitative morphological tools. First, I developed and measured the C^*, A^*, S^* and G^*–M_{20}^* parameters for use in assessing the morphology of the galaxy cores. The distribution of these parameters, as measured for Sy1 and Sy2 AGN, did not strongly distinguish between the Seyfert class and morphology of the host galaxy. I determined that the parameter distributions for Sy1 and Sy2 AGN are likely drawn from the same parent distribution using a two–sample K–S test, with the exception of the concentration C^* parameter. In principle, C^* is the least effective method for measuring galaxy morphology, though. I conclude from this analysis that no strong morphological distinction exist between the cores of the Sy1 and Sy2 AGN host galaxies. This conclusion conflicts with the established MGT98 relationship. I

developed an alternative, new method to quantify the core dust morphologies of the AGN galaxies. This method combines `SE` with the inverse unsharp mask-technique to directly detect dust features. I found that the distributions of the average number of detected dust features in Sy1 and Sy2 AGN may in fact be unique to AGN class. But, there was no concordance between this result and others derived from this new quantitative method (i.e., the radial distribution, size and covering fraction of dust features). I therefore cannot strongly distinguish between Sy1 and Sy2 AGN on the basis of their core morphologies using this quantitative method.

Combining the results from the analysis of dust morphology using new and existing methods, I conclude that the Unified Model of AGN is still sufficient to explain the observed diversity of AGN and need not be significantly modified to accommodate the results of this analysis. Though no conclusive trend was identified using all of the 10 parameterized measurements of the dust distribution, in the analyses using both the adapted and novel parameters we identified one parameter for which the Seyfert distributions were statistically distinguishable by the results of the two-sample Kolmogorov-Smirnov test. We can rule out the null hypothesis—that the distributions sampled were likely to be drawn from the same parent distribution—with high certainty for the adapted Concentration (C^*) and the number of dust features (N_t) parameters.

The concentration parameter is not, by first principles, the most-sensitive measure of galaxy morphology, in comparison to the other adapted parameters that were considered. But, the results of the analysis presented in Addendum A1 of Chapter 3 demonstrated that C^* was most robust to the changes in spatial resolution amongst $C^*A^*S^*$. These results present an interesting prospect for future research. Though I have considered a large sample of AGN in this study, if this study could be extended to a larger sample (N$\gg$100), the statistical uncertainty associated with each of the

measurements could be significantly reduced. One way the sample size could be increased is to extend a similar study to a larger survey of AGN, such as the SDSS. Though the spatial resolution of the dust features in such a survey would be reduced considerably in comparison with the HST data we have used, ifthe concentration parameter is in fact sensitive to the dust morphology, increasing the sample size to include all SDSS Seyfert galaxies in the local Universe ($z < 0.1$) would provide a more statistically robust study of the Malkan relation.. I will extend this work here to consider this larger sample in the future.

In the future, better and more internally consistent quantitative methods should also be developed in order to assess larger, complete samples of local AGN. Developing these techniques in the next few (<2) years is critical. The the launch of the JWST and the deployment of wide-field ground-based surveys by the end of the decade will soon provide large, panchromatic imaging and spectroscopy which will better reveal the dust and the nature of the AGN embedded in the cores of these galaxies.

6.2 Summary and conclusions on the evolution of massive early-type galaxies

I have extended the study of formation and evolution of ETGs to include the study of the morphology and star-formation history of these galaxies at intermediate ($0.35<z<1.5$) redshift. Combining high-spatial resolution rest-frame UV and near IR HST ERS medium-depth data with existing rest-frame optical ACS data, I produced a catalog of $\sim$100 morphologically-selected ETGs. A one-component SED analysis confirms these galaxies have relatively large stellar masses ($M \gtrsim 10^{10} M_{\odot}$) and their UV-optical colors suggest that a significant fraction of them have recently experienced a minor burst of recent star-formation.

Simultaneous fitting of the ETG SEDs to measure both young and old stellar populations confirms that at least 30-40% of these ETGs are likely host to a young (t<1 Gyr) minority (by mass, $\ll$10%) young stellar component. The potential mechanisms driving this recent star-formation were investigated morphologically. First, using the `GalFit` software, I measured the Sèrsic profiles for each ETG, and found many to have low Sèrsic indices (n$\lesssim$2). As many of these galaxies were also identified with young stellar populations, these galaxies may represent a population of formerly disky galaxies (S0s/Lenticulars). Lacking companions in their local environments which could potentially replenish these gas reservoirs, these galaxies will likely transition to their eventual residence on the red sequence of galaxies, as is observed in the local universe. Extending this and similar analysis of the stellar light profiles is a top priority in the future, as the distribution of stellar objects provides one of the few observable constraints on the underlying dark matter distributions in these galaxies. With the high spatial resolution of the HST WFC3/IR, it may be possible to measure the core (d$\sim$100 pc) light distribution in these galaxies. For a large sample of ETGs, I can correlate "cuspy-core" and "flat-core" ETGs with the observed young stellar populations. This provides an alternative method of measuring the characteristics of the merger that may have generated the young, massive stars. Cuspy core profiles are believed to occur, based on observations of local ETGs and simulations, from relatively gas-rich mergers which interact in different ways with the dark matter distribution than do gas-poor mergers. This extended study would provide constraints on the fraction of gas introduced into the old ETG system to refresh star formation, as well as constrain the halo distributions of dark matter.

Applying a statistical likelihood analysis to measure the frequency of companions, I identify $\sim$10% of the ETGs with close, faint (M(F850LP)$\gtrsim$25, thus, low-mass) companions. The characteristics of the young stellar populations measured for these

galaxies are notably younger and constitute a smaller fraction of the total stellar mass in these galaxies than is observed for galaxies without companions. It is interesting to note that mean age of the young stellar populations of ETGs with companions identified by this statistical analysis are significantly younger (t$\sim$400 Myr) than the mean identified by ETGs without companions. The mean age is also equivalent to the dynamical scale over which companions are expected to interact with the ETG, assuming their relative velocities and positions in the search volume. Thus, non-destructive interactions between the ETG and these local companions could be considered as a plausible mechanism for the production of the observed young stellar populations. I conclude that these galaxies have, due to their location in small groups or pairs, likely undergone a recent minor merger event which initiated the low-level observed star-formation, as is identified for galaxies of similar morphologies in the local and high redshift universe.

With these broadband, continuous observations of the UV-optical-near IR SEDs of intermediate redshift ETGs, I have demonstrated that HST can be effective in measuring recent star-formation in this class of galaxies which have been traditionally considered to be "red and dead." Combined with the high spatial resolution, medium-depth HST surveys of field ETGs can also be used to constrain the mechanism for star-formation. This survey provides strong observational constraints on theoretical models of galaxy formation and evolution in the hierarchical assembly paradigm.

Abraham, R. G., van den Bergh, S., & Nair, P. 2003, ApJ, 588, 218

Antonucci, R. 1993, ARA&A, 31, 473

Atlee, D., Assef, R. J., & Kochanek, C. 2009, ApJ, 694, 1539

Barkana, R., & Loeb, A. 2001, Phys. Rep., 349, 125

Bartel, P. D., Miley, G. K., Schilizzi, R. T., & Preuss, E., 1984, A&A, 140, 399

Bell, E., et al. 2004, ApJ, 608, 752

Bertin, E., & Arnouts, S. 1996, A&A, 117, 393

Bender, R., Burstein, D., & Faber, S. M. 1992, ApJ, 399, 462

Bezanson, R., et al. 2009, ApJ, 697, 1290

Bower, R. G., Lucey, J. R., & Ellis, R. S. 1992, MNRAS, 254,589

Brammer, G. B., van Dokkum, P. G.,& Coppi, P. 2008, ApJ, 686, 1503

Brown, T. M., Bowers, C. W., Kimble, R. A., & Ferguson, H. C. 2000, ApJ, 529, L89

Brown, T. M., Ferguson, H. C., Smith, E., Bowers, C. W., Kimble, R. A., Renzini, & Rich, R. M. 2003, ApJ, 584, L69

Bruzual, A. G., & Charlot, S. 2003, MNRAS, 344, 1000

Burstein, D.,Bertola, F., Buson, L. M., Faber, S. M., Lauer, T. R. 1988, ApJ, 328, 440

Calzetti, D., et al. 2000, ApJ, 533, 682

Casoli, F., Combes, F., & Gerin, M. 1984, A&A, 133, 99

Chiosi, C. & Carraro, G. 2002, MNRAS, 335, 335

Cimatti, A., et al. 2002, A&A, 392, 395

Clemens, M. S., Bressan, A., Nikolic, B., & Rampazzo, R. 2009, MNRAS 392, 35

Colbert, J. W., Mulchaey, J. S., & Zabludoff, A. I. 2001, AJ, 121,808

Coleman, G. D., Wu, C. C., Weedman, D. W. 1980, ApJS, 43, 393

Conselice, C. J., Bershady, M.A., & Jangren, A. 2000, ApJ, 529, 886

Conselice, C. J. 2003, ApJS, 147, 1

Conselice, C. J., et al. 2004, ApJ, 600,L139

Conselice, C. J., Rajgor, S., & Myers, R. 2008, MNRAS, 386, 909

Cooke, A. J., Baldwin, J. A., Ferland, G. J., Netzer, H.,& Wilson, A. S. 2000, ApJS, 129, 517C

Cortese,L. & Hughes, T. M. 2009, MNRAS, 400, 1225

Crockett, R. M., et al. 2011, ApJ, 727, 115

Daddi, E., et al. 2005, ApJ, 626, 680

Davis, M., et al. 2007, ApJ, 660, L1

Dickinson, M., Giavalisco, M., & the GOODS Team, 2003 The Great Observatories Origins Deep Survey in "The Mass of Galaxies at Low and High Redshift," eds. R. Bender & A. Renzini, 324

Donas, J., et al. 2007, ApJs, 173, 597

Dorman, B., Rood, R., & O'Connell, R. W. 1993, ApJ, 419, 596

Dorman, B., O'Connell, R. W., & Rood, R. T. 1995, ApJ, 442, 105

Eggen, O., Lynden-Bell, D., & Sandage, A. 1962, ApJ, 136, 748

Eliche-Moral, M.C., et al. 2010, A&A, 519, A55

Ferreras, I, & Silk, J. 2000, ApJ, 541, 37

Ferreras, I., et al. 2009, ApJ, 706, 158

Frei, Z., Guhathakurta, P., Gunn, J., & Tyson, J. A. 1996, AJ, 111, 174

Fukugita, M. 1996, AJ, 111, 174

Fukui, Y. & Kawamuro, A. 2010, ARA&A, 48, 547

Giacconi, R., et al. 2002, ApJS, 139, 369

Giavalisco, M., et al. 2004, ApJ, 600, L93

Gil de Paz, A., et al. 2007, ApJS, 173, 185

Gilli, R., et al. 2003, ApJ, 592, 791

Graves, G. J., Faber, S. M., & Schiavon, R. P. 2009, ApJ, 698, 1590

Greggio, L., & Renzini, A. 1990, ApJ, 364, 35

Guainazzi, M., Bianchi, S., de La Calle Pérez, I., Dovčiak, M.,& Longinotti, A. L. 2011, A&A, 531, A131

Han, Z., Podsiadlowski, P., & Lynas-Gray, A. E. 2007, MNRAS, 380, 1098

Hambleton, K.M. et al. 2011, MNRAS, 418, 801

Hernández-Toledo, H. M., Avila-Reese, V., Salazar-Contreras, J. R., & Conselice, C. J. 2006, AJ, 132, 71

Hernández-Toledo, H. M., et al. 2008, AJ, 136, 2115

Ho, L. C., Filipenko, A. V., & Sargent, W. 1997, 487,568

Ho, L. C. & Peng, C. 2001, ApJ, 555, 650

Holwerda, B. W., Pirzkal, N., de Blok, W. J. G, & van Driel, W., 2011, MNRAS, 416, 2447

Holwerda, B. W., et al. 2012, ApJ, 753, 25

Hughes, T. M., & Cortese, L., 2009, MNRAS, 396, L41

Jeong, H., et al. 2009, MNRAS, 398, 2028

Kacprzak, G. G., Churchill, C. W, & Nielsen, N. M., 2012, arXiv:1205.0245K

Kalirai, J. S., et al. 2009a, Instrument Science Report WFC3, 2009-21

Kalirai, J. S., MacKenty, J., Bohlin, R., Brown, T., Deustua, S., Kimble, R. A., & Riess, A. 2009b, Instrument Science Report WFC3, 2009-30

Kannappan et al., 2009, AJ, 138, 579

Kaviraj, S., et al. 2007a, ApJS, 173, 619

Kaviraj, S., Rey, S.-C., Rich, R. M., Yoon, S. J., & Yi, S. K., 2007b, MNRAS, 381, L74

Kaviraj, S., et al. 2008, MNRAS, 388, 67

Kaviraj, S., Peirani, S., Khochfar, S., Silk, J., & Kay, S., 2009, MNRAS, 394, 1713

Kaviraj, S. 2010, MNRAS, 406, 382

Kaviraj, S., et al. 2011, MNRAS, 411, 2148

Kaviraj, S., et al. 2013, MNRAS, 428, 925

Khochfar, S., & Burkert, A., 2003, ApJ,597, L117

Kodama T., & Arimoto N., 1997, A&A, 320, 41

Komatsu, E., et al. 2011, ApJS, 192, 18

Kondo, Y. 1987, Exploring the universe with the IUE satellite. Dordrecht : Reidel. 787 pp.

Kormendy, J., Fisher, D. B., Cornell, M. E., & Bender, R. 2009, ApJS, 182, 216

Kron, R. G., Koo, D. C., Windhorst, R. A. 1985 A&A, 146, 38

Larson, R. B. 1974, MNRAS, 166, 585

Lee, Y.-W., et al. 2005, ApJl, 619, L103

Le Fèvre, O., et al. 2004, A&A, 428, 1043

Lisker, T. 2008, ApJS, 179, 319

López-Sanjuan et al. 2010, A&A, 518, A20

López-Sanjuan et al. 2012, A&A, 548, A7

Lotz, J. M., Primack, J., & Madau, P. 2004, AJ, 128, 163

Lotz, J. M., et al. 2008, ApJ, 672, 177

Lucero, D. M., & Young, L. M. 2007, AJ, 134, 2148

Luo, B., et al. 2010, ApJS, 187, 560

Madau, P., Pozzetti, L. & Dickinson, M. 1998, ApJ, 498, 106

Malkan, M. A., Gorjian, V., & Tam, R. 1998, ApJ, 117, 25

Martin, C., et al. 1997, Bull. Amer. Astron. Soc. 191:#63.04

Baggett, S., et al. 2008, in HST WFPC2 Data Handbook, v. 10.0, ed. M. McMaster & J. Biretta, Baltimore, STScI

Marchesini, D., et al. 2009, ApJ,701, 1765

Mignoli, M. et al. 2005, A&A, 437, 883

Miller, N., et al. 2008, ApJS, 179, 114

Morganti, R., et al. 2006, MNRAS, 371, 157

Morrissey, P., et al. 2005, ApJS, 619, L7

Naab, T., Johansson, P. H.,& Ostriker, J. P., ApJ, 699, L178

Nenkova, M., et al. 2008, ApJ, 685,160

O'Connell, R. W. 1980, ApJ, 236, 430

O'Connell, R. W. 1999, ARA&A, 37, 603

Ohl, R. G., et al. 1998, ApJ, 505, L11

Odewahn, S. C., Windhorst, R. A., Driver, S. P., & Keel, W. C. 1996, ApJ, 472, L13

Oke, J. B., & Gunn, J. E. 1983, ApJ, 266, 713

Panessa, F. & Bassani, L. 2002, A&A, 394, 435

Park, J.-H., & Lee, Y.-W. 1997, ApJ, 476, 28

Papovich, C., Dickinson, M., & Ferguson, H. C. 2001, ApJ, 559, 620

Pasquali, A., et al. 2006, ApJ, 636, 115

Patton, D. R., et al. 2002, ApJ, 565, 208

Peirani, S., et al. 2010, MNRAS, 405, 2327

Pipino, A. & Matteucci, F. 2004, MNRAS, 347, 968

Peng, C., Ho, L. C., Impey, C. D., & Rix, H.-W. 2002, AJ, 124, 266

Popesso, P., et al. 2009, A&A, 494, 443

Postman, M., et al. 2005, ApJ, 623, 721

Ravikumar, C. D., et al. 2007, A&A, 465, 1099

Ree, C., et al. 2007, ApJS, 173, 607

Ricci, C., Walter, R., Courvoisier, T.J.– L., & Paltani, S., 2011, A&A, 532,A102

Rose, J. A. 1985, AJ, 90, 1927

Rowlands, K., Dunne, L., Maddox, S., et al. 2012, MNRAS, 419, 2545

Rutkowski, M. J., et al. 2012, ApJS, 199, 4

Rutkowski, M. J., et al. 2013, IAU Pro., "Highlights of Astronomy", submitted

Ryan, R. E. 2011, arXiv:1110.1090

Ryan, R. E. et al. 2012, ApJ, 749, 53

Salim, S., et al., 2007, ApJS, 173, 267

Salim, S., & Rich, R. M. 2010, ApJ, 714, 290

Salim, S. et al., 2012, ApJ, 755, 105

Schawinski, K., et al. 2007, ApJS, 173, 512

Schawinski, K., et al., 2009, ApJ, 619, L19

Schimonivich, D.A., et al., 2007, ApJS, 173, 315

Schweizer, F., Seitzer, P., Faber, S. M., Burstein, D., Dalle Ore, C. M., & González, J. J. 1990, ApJ, 364, L33

Scott, N., et al. 2009, MNRAS, 398, 1835

Serra et al. 2012, MNRAS, 414, 940

Strolger, L.-G. et al. 2004, ApJ, 613, 200

Suh, H., Jeong, H., Oh, K., Yi, S. K., Ferreras, I., & Schawinski, K. 2010, ApJ, 187, 374

Szokoly, G., et al. 2004, ApJS, 155, 271

Tal, T., et al. 2013, subm. ApJ, arXiv:1302.2912

Tamura, K. et al. 2010, JNM, 185, 325

Tantalo, R., Chiosi, C., Bressan, A., & Fagotto, F. 1996, A&A, 311, 361

Taylor-Mager, V. A., Conselice, C. J., Windhorst, R. A., & Jansen, R. A. 2007, ApJ, 659, 162

Tinsley, B. M. 1980 Fund. of Cosmic Physics, 5, 287

Toomre, A., & Toomre, J. 1972, ApJ, 178, 623

Trager, S. C., Worthey, G., Faber, S. M., Burstein, D., Gonalez, J. J. 1998, ApJS, 116, 1

Trager, S. C., Faber, S. M., Worthey, G., & González, J. J. 2000, AJ, 119,1645

Tran, H. D. 2001, ApJ, 554, L19

Tran, H. D. 2003, ApJ, 583, 632

Urry, M. & Padovani, P. 1995 PASP, 107, 803

vanden Berk, D.E., et al. 2001, AJ, 122, 549

van der Wel, A., et al. 2011, ApJ, 730, 38

van Dokkum, P. G., 2001, PASP 113, 1420

van Dokkum, P. G. 2005, AJ, 130, 2647

van Dokkum, P. G., et al. 2010, ApJ, 709, 1018

Vanzella, E., et al. 2008, A&A, 478, 83

Villar, V., et al 2011, ApJ, 740, 47

Weiner, B. J., et al. 2005,ApJ, 620, 595

Willmer, C. N. A., et al. 2006, ApJ, 647, 85

Windhorst, R. A., et al. 2011, ApJS, 193, 27

Worthey, G., Faber, S. M., González, J. J., & Burstein, D. 1994, ApJS, 94, 687

Wyder, K., et al., 2007, ApJS, 173, 293

Yi, S. K., Afshari, E., Demarque, P., & Oemler, A., Jr. 1995, ApJL, 453, L69

Yi, S. K, Demarque, P., & Oemler, A., Jr. 1998, ApJ, 492, 480

Yi, S. K, Lee, Y.-W., Woo, J.-H., Park, J.-H., Demarque, P., & Oemler, A. 1999, ApJ, 513, 128

Yi, S. K., Kim, Y, Demarque, P. 2003, ApJS, 144, 259

Yi, S. K. & Yoon,S-J. 2004, Ap&SS, 291, 205

Yi, S. K., et al. 2005, ApJS, 619, L111

Yi, S. K., et al. 2011, ApJS, 195, 22

Appendix A

Additional Figures for Chapter Two

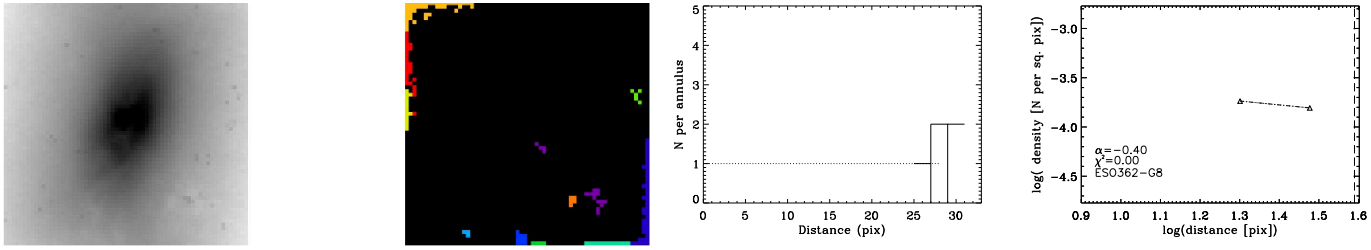

e.ESO362-G8

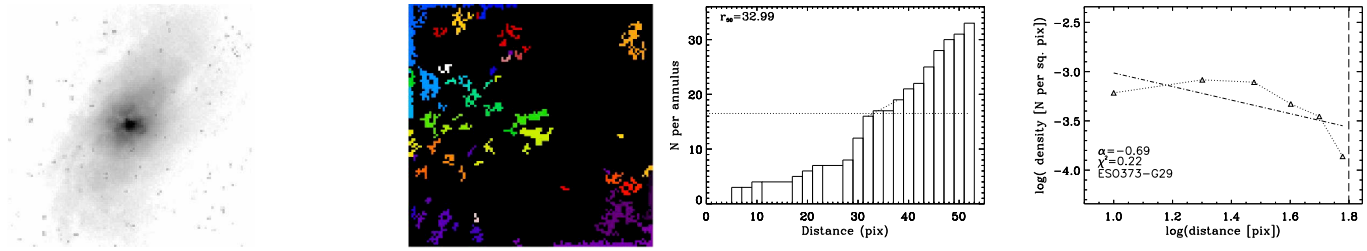

f.ESO373-G29

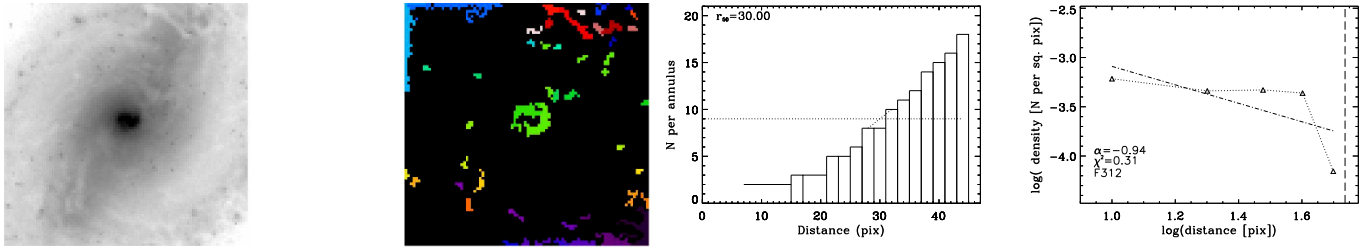

g.FRL312

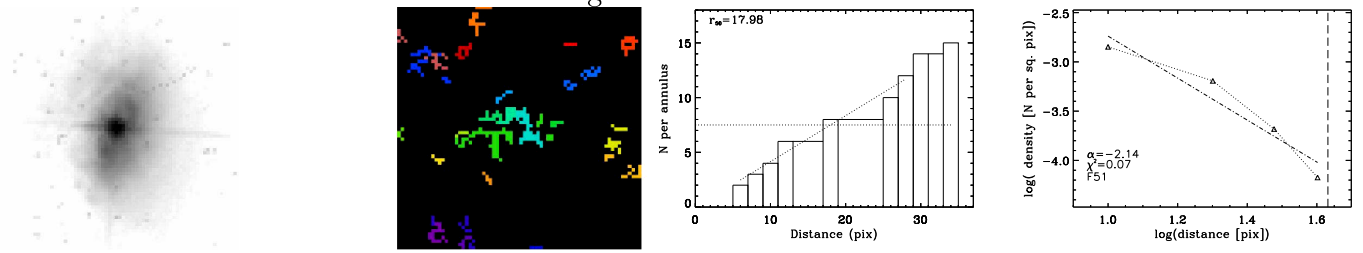

h.FRL51

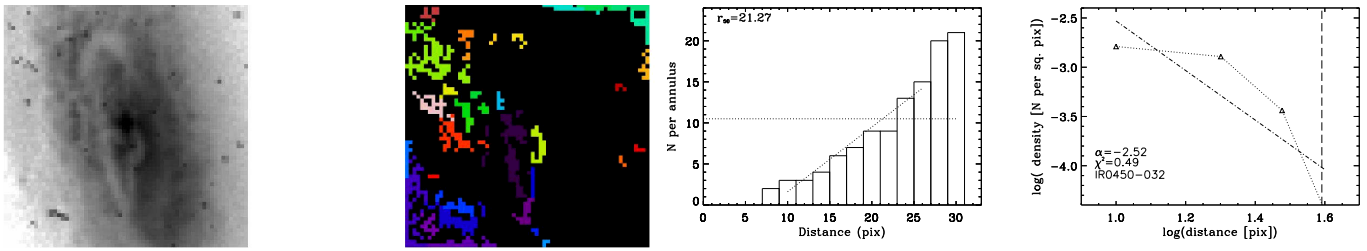

i.IR0450-032

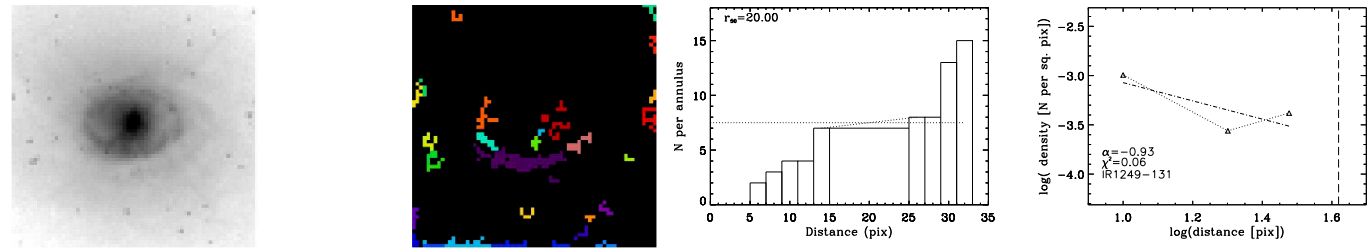

j.IR1249-131

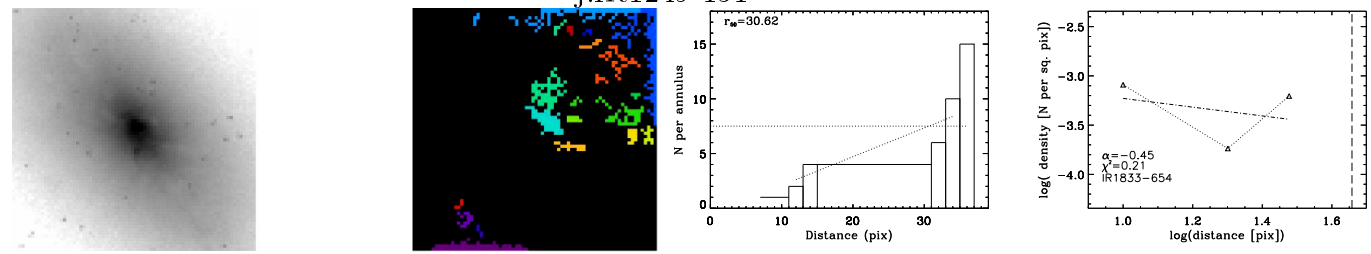

k.IR1833-654

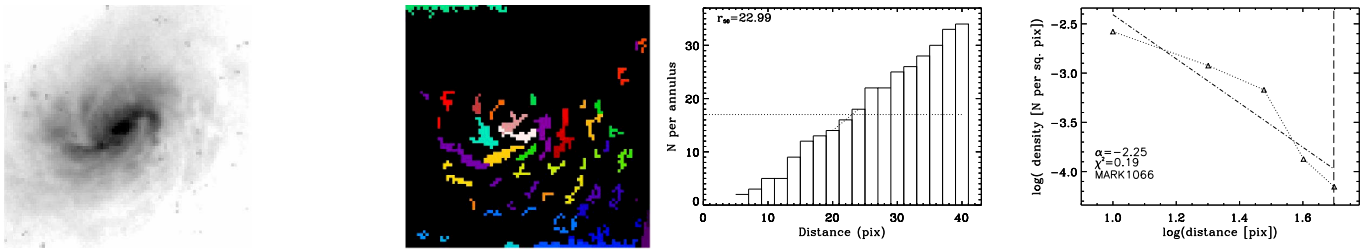

l.MARK1066

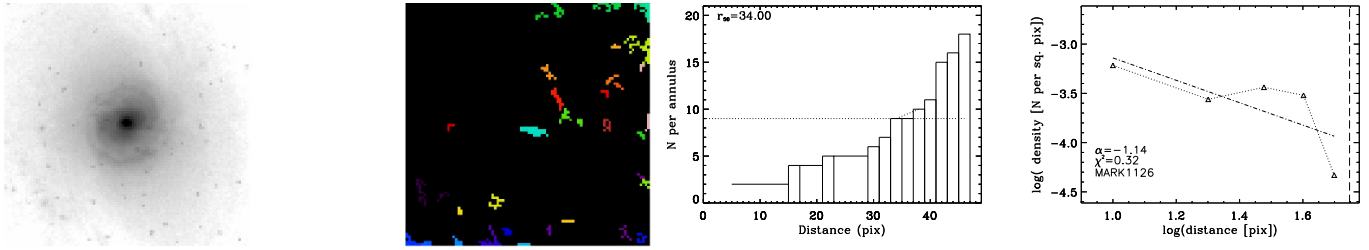

m.MARK1126

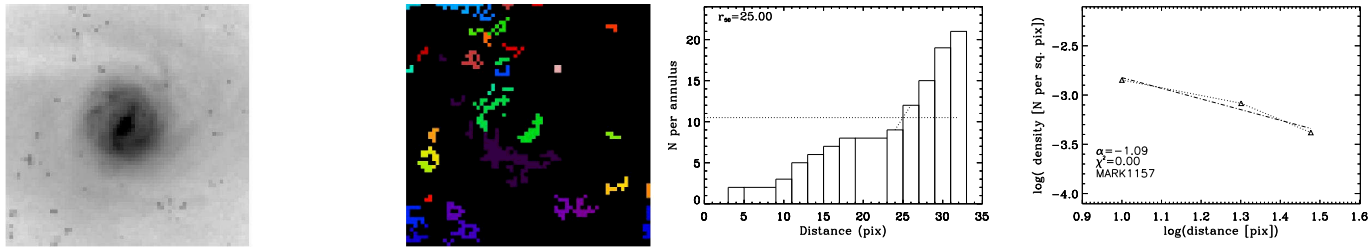

n.MARK1157

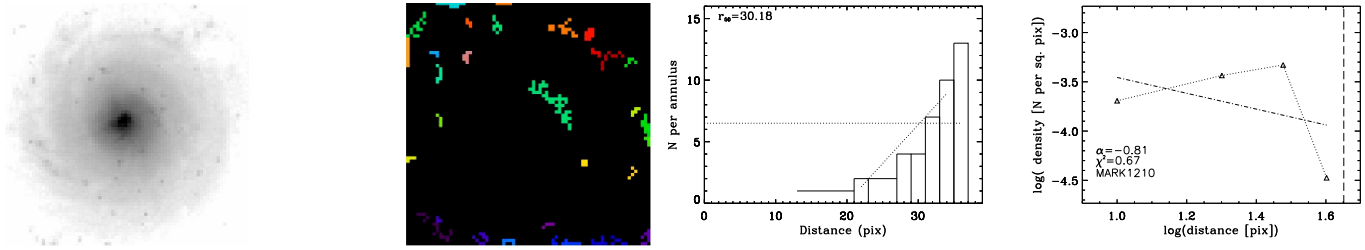

o. MARK1210

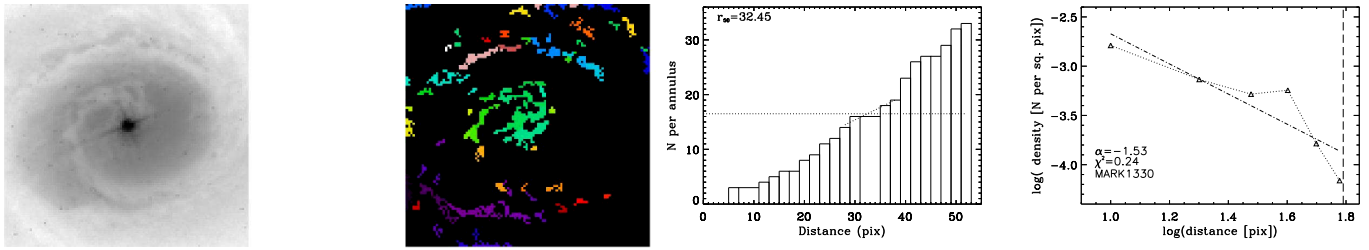

p.MARK1330

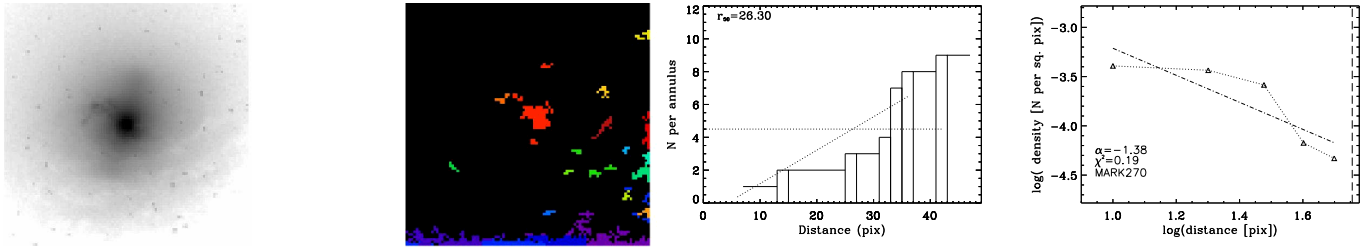

q.MARK270

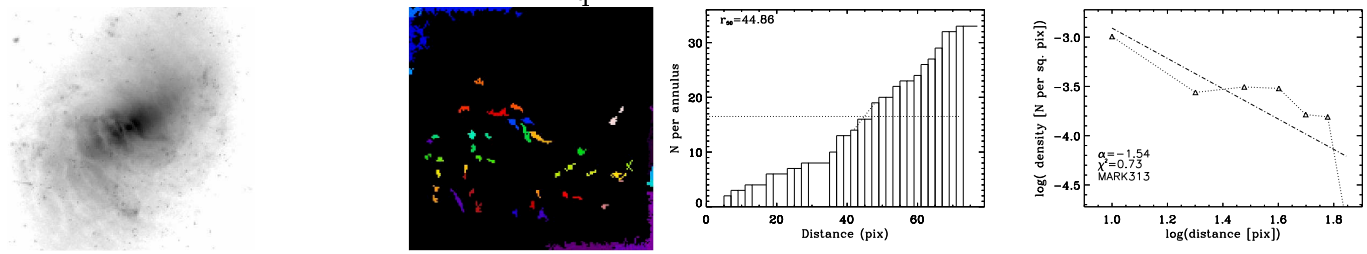

r.MARK313

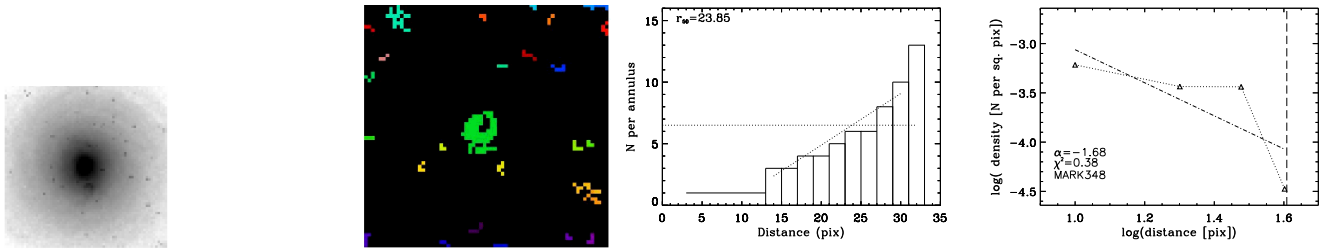

s.MARK348

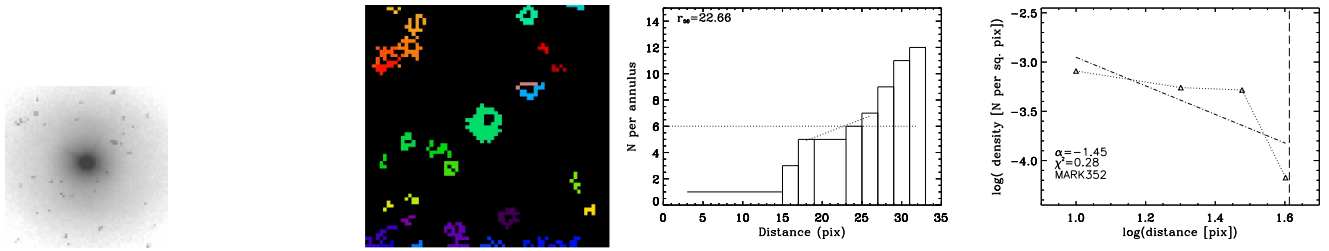

t.MARK352

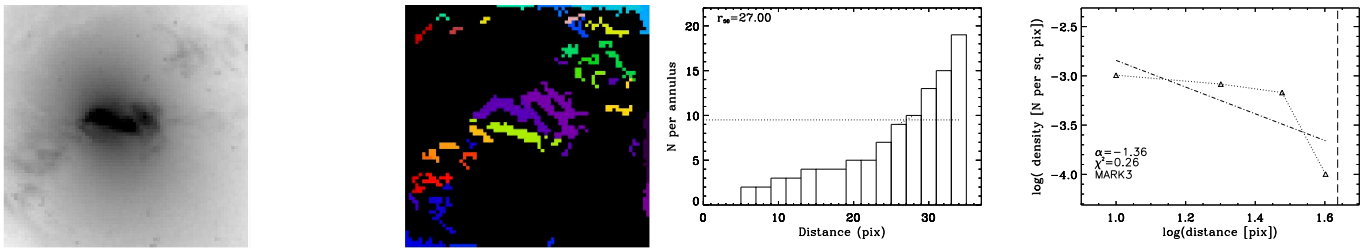

u.MARK3

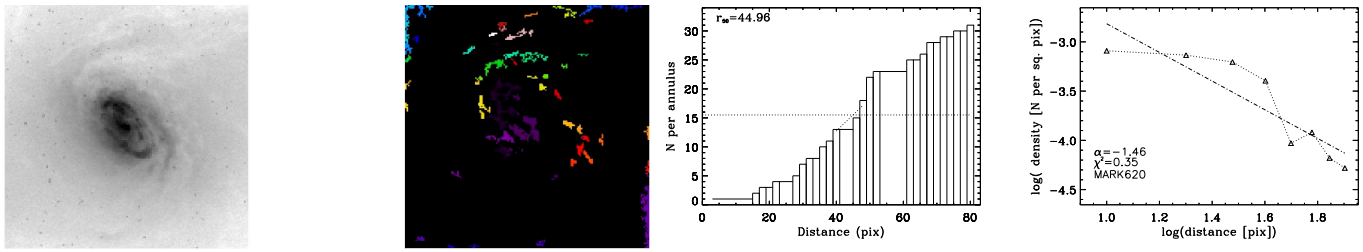

v.MARK620

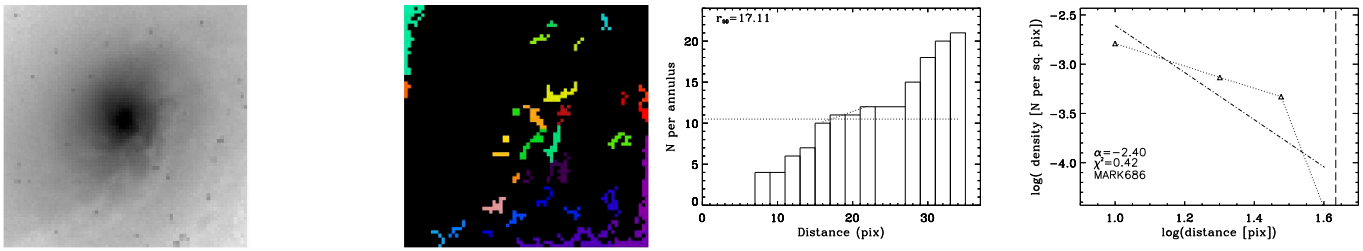

w.MARK686

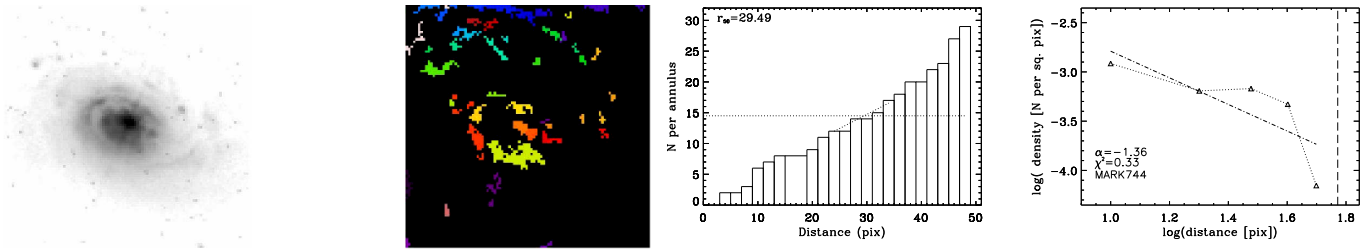

x.MARK744

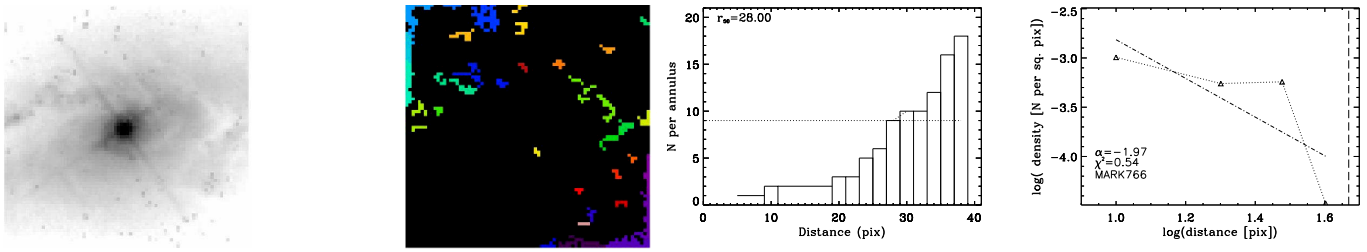

y.MARK766

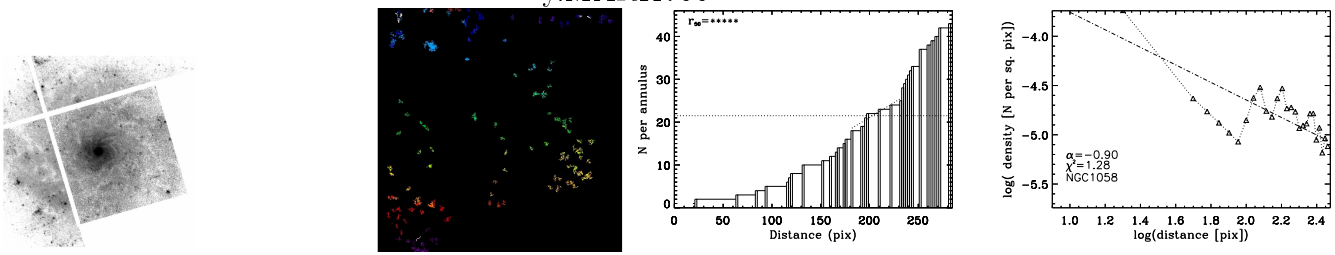

z.NGC1058

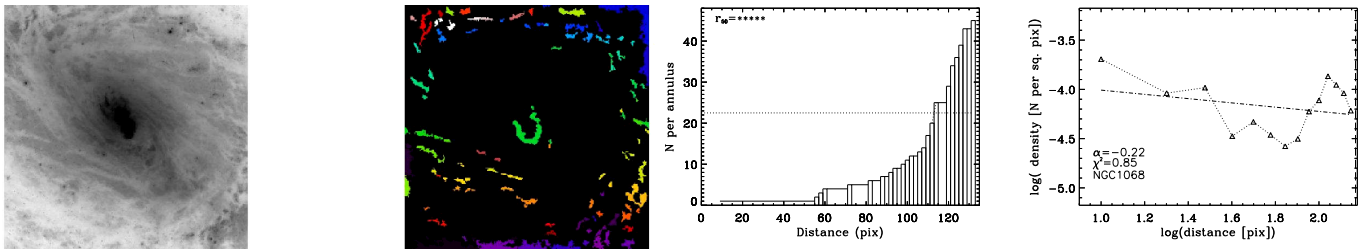

aa.NGC1068

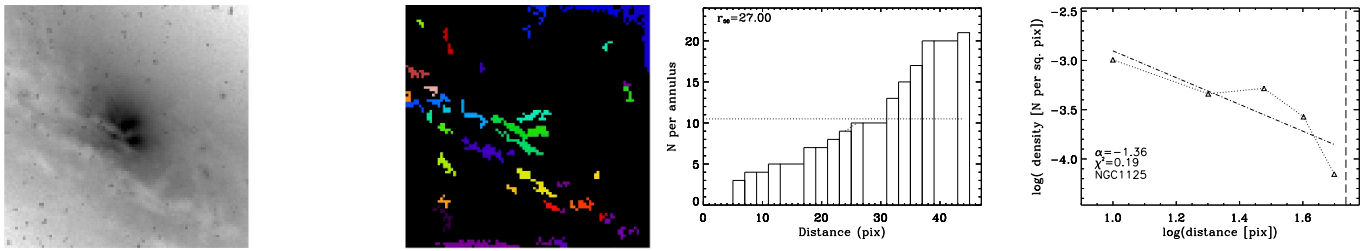

ab.NGC1125

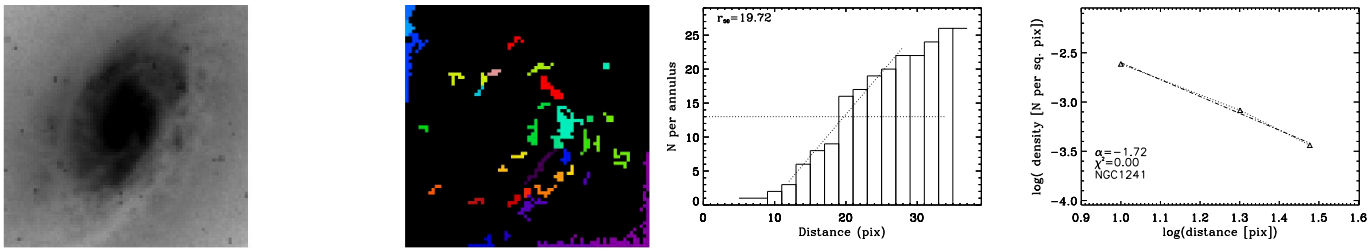

ac.NGC1241

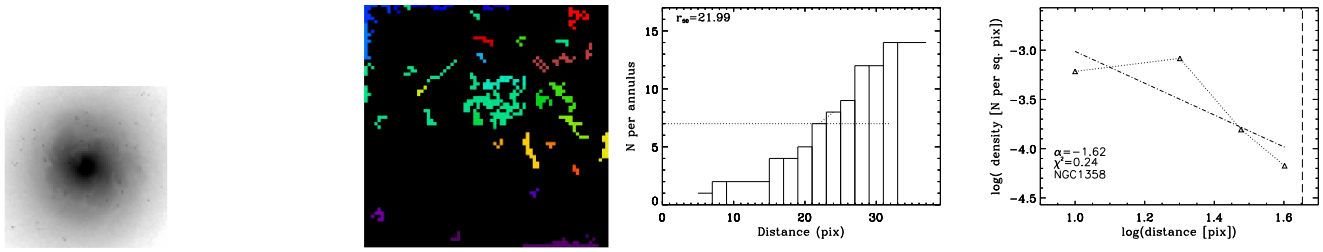

ad.NGC1358

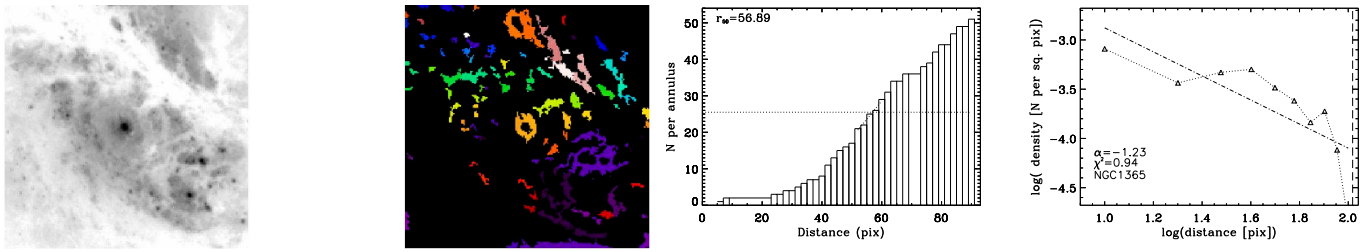

ae.NGC1365

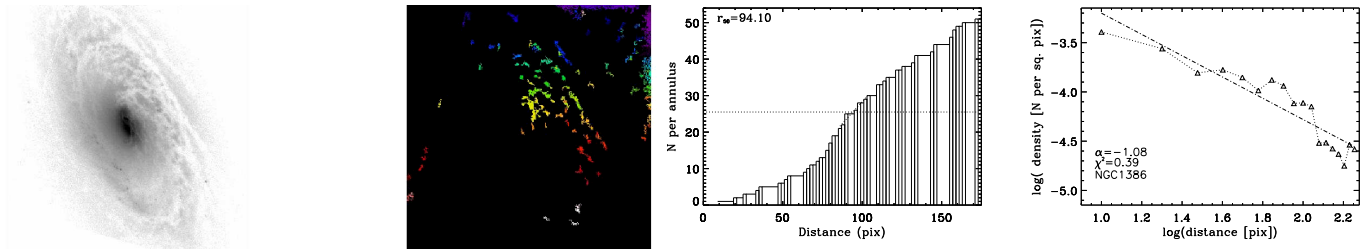

af.NGC1386

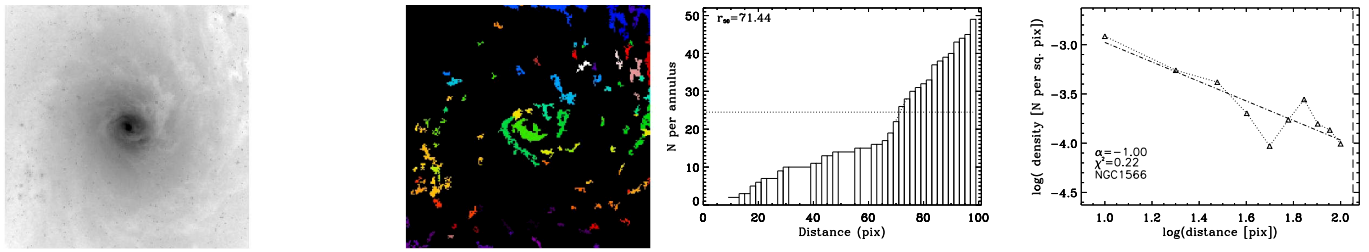

ag.NGC1566

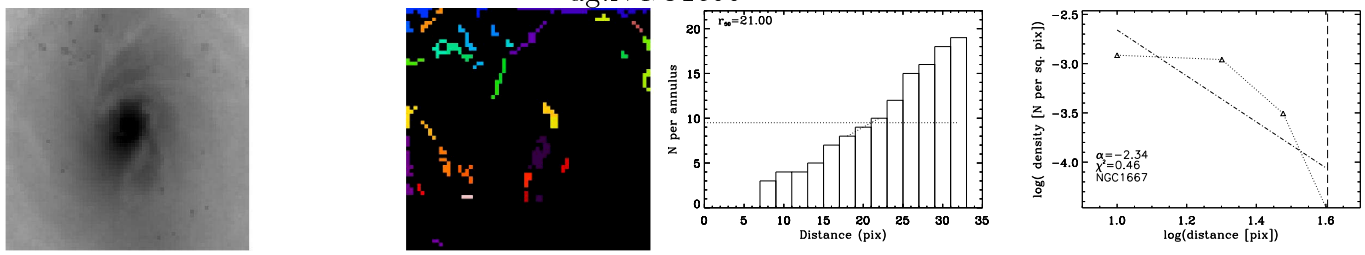

ah.NGC1667

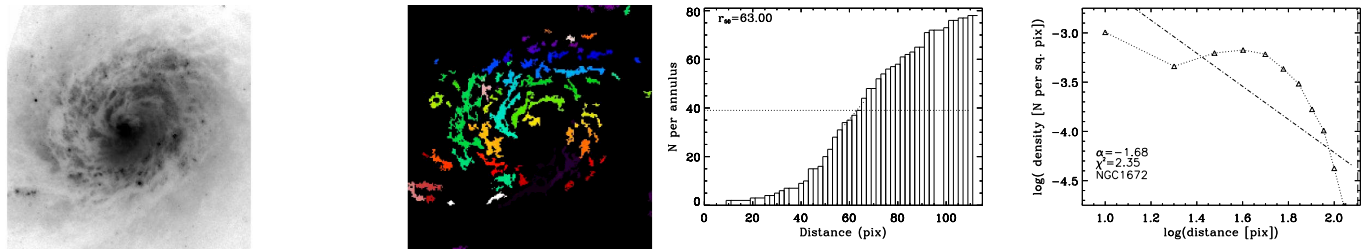

ai.NGC1672

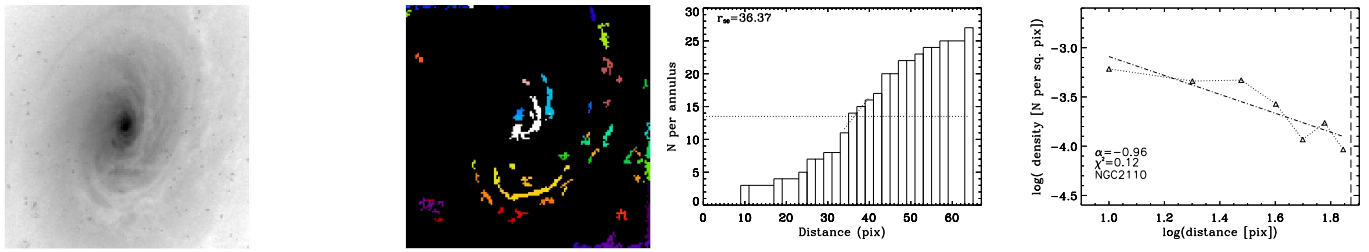

aj.NGC2110

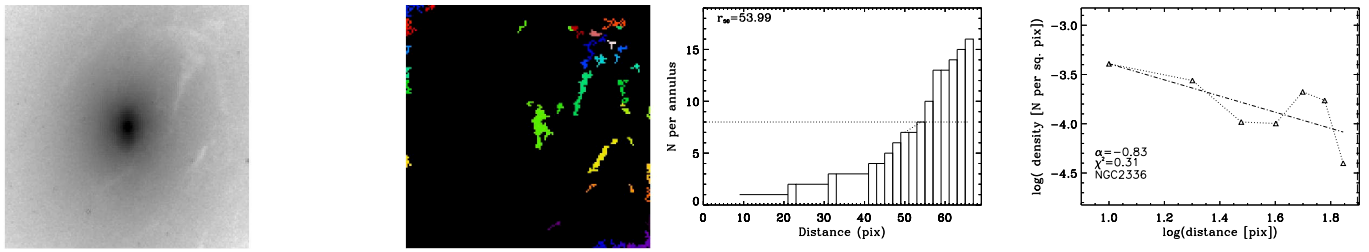

ak.NGC2336

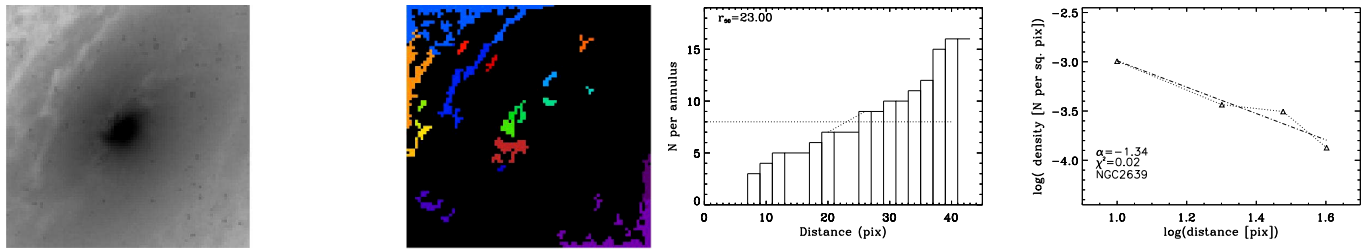

al.NGC2639

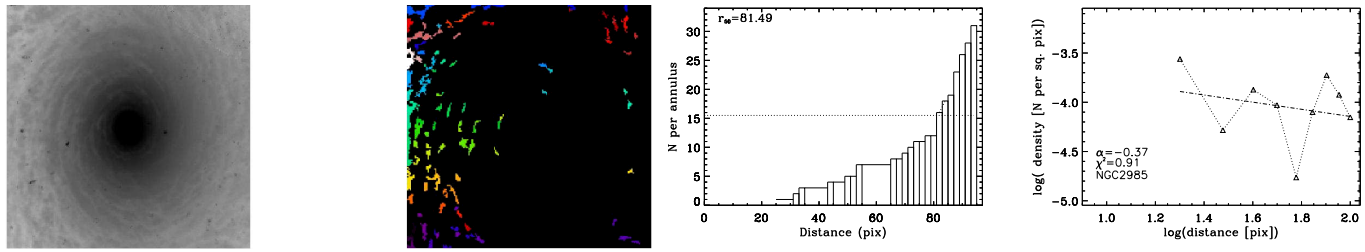

am.NGC2985

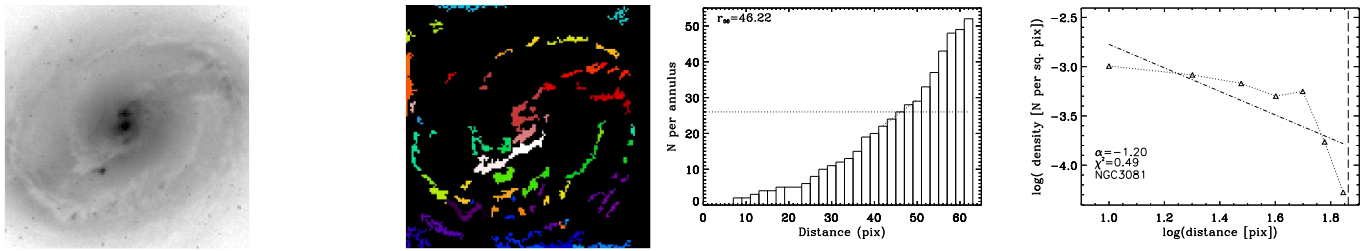

an.NGC3081

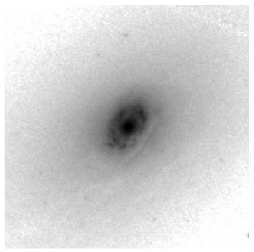

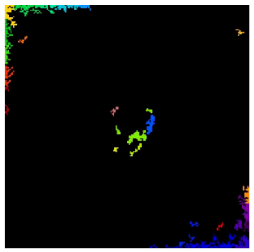

ao.NGC3185

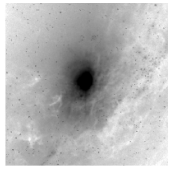

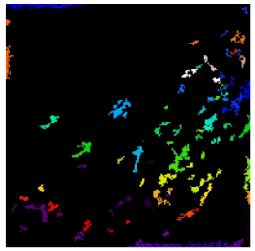

ap.NGC3227

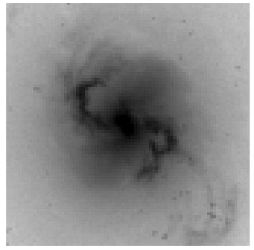

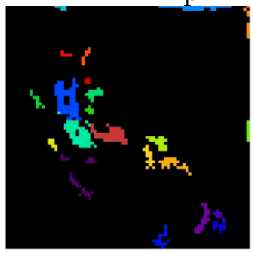

aq.NGC3393

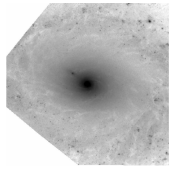

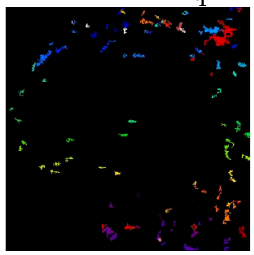

ar.NGC3486

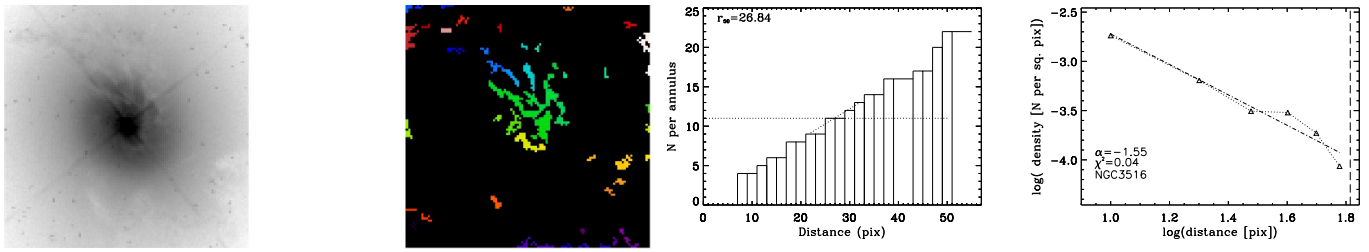

as.NGC3516

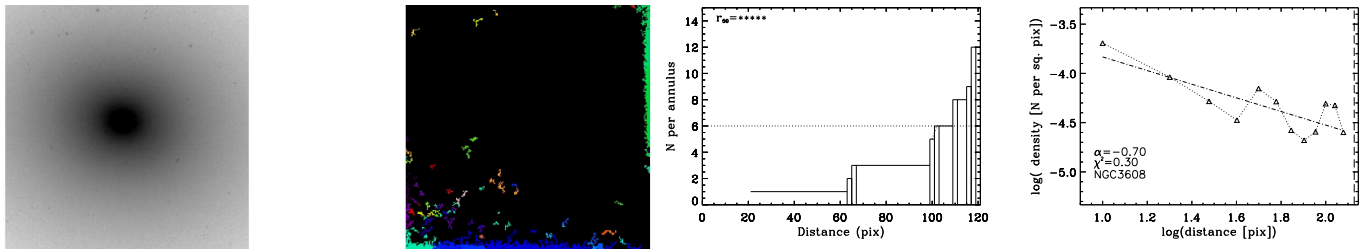

at.NGC3608

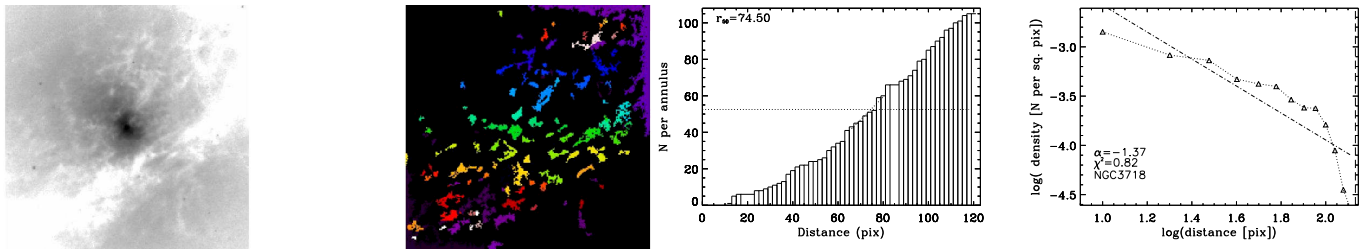

au.NGC3718

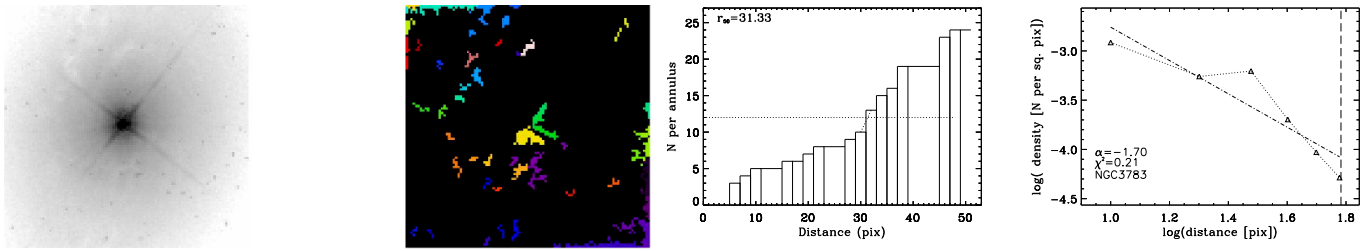

av.NGC3783

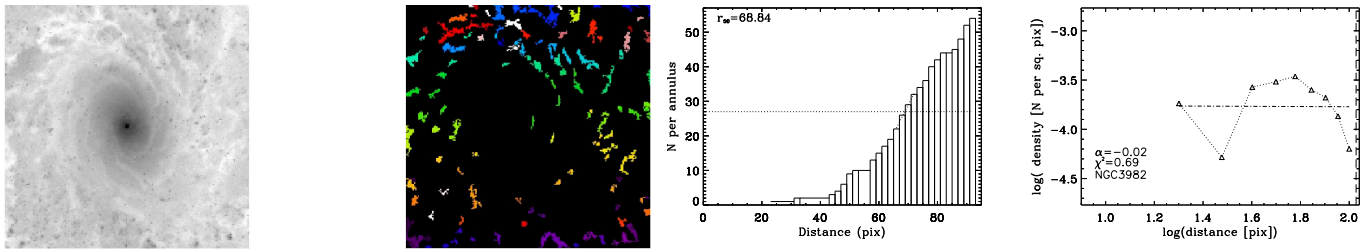

aw.NGC3982

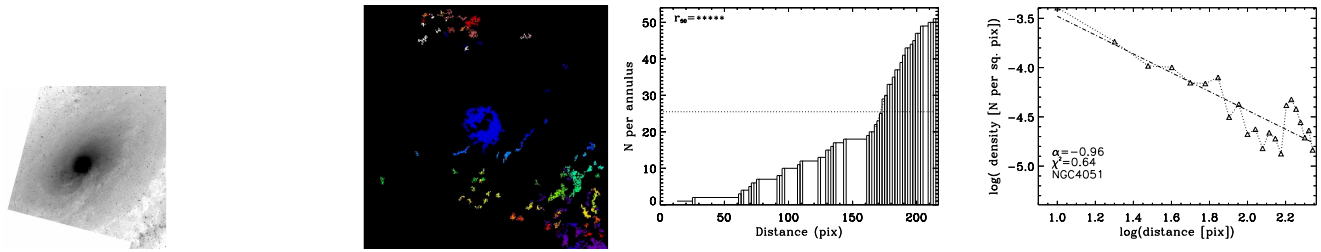

ax.NGC4051

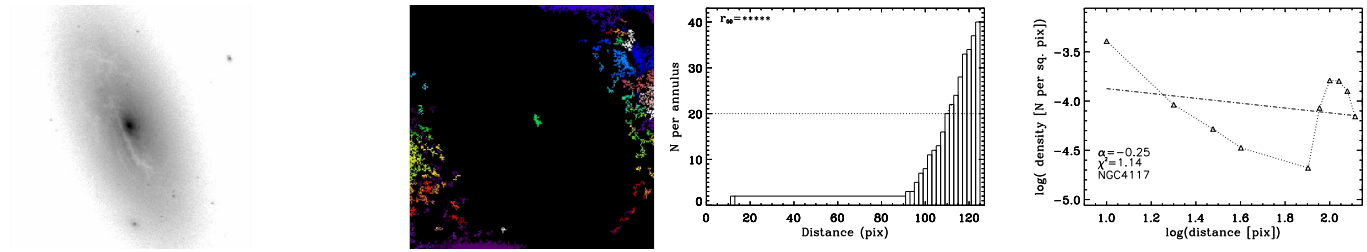

ay.NGC4117

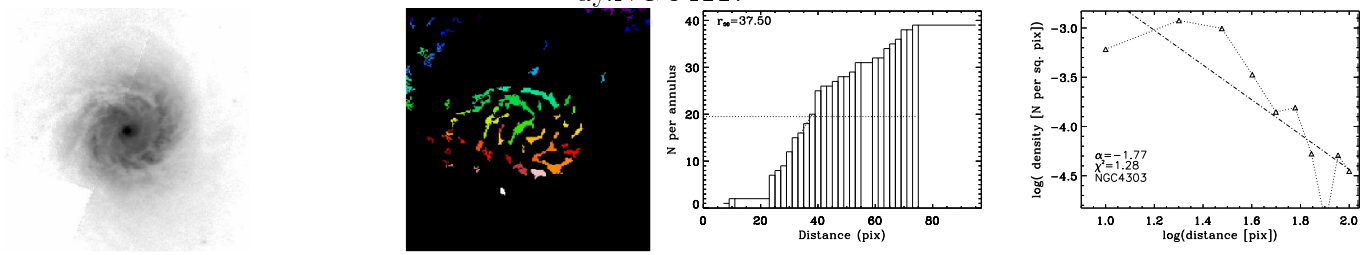

az.NGC4303

ba.NGC4378

bb.NGC4395

bc.NGC4477

bd.NGC4507

be.NGC4639

bf.NGC4698

bg.NGC4725

bh.NGC4939

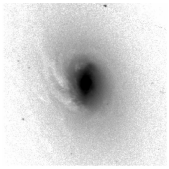
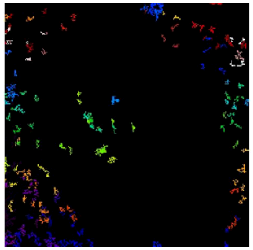
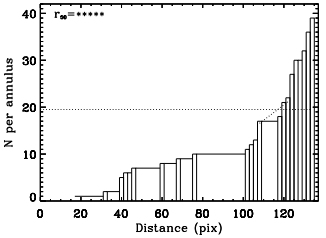

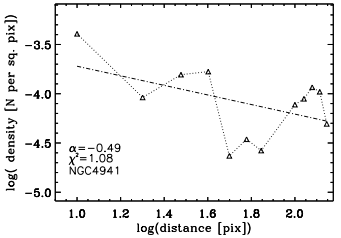

bi.NGC4941

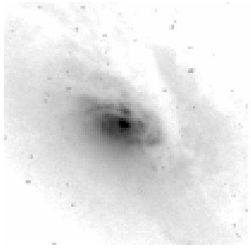
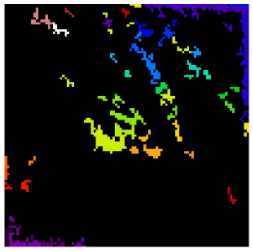
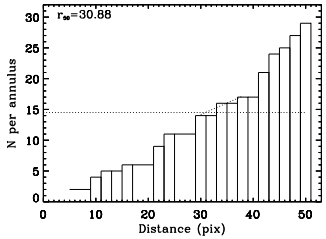

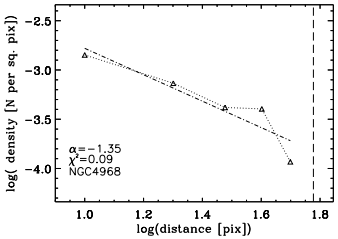

bj.NGC4968

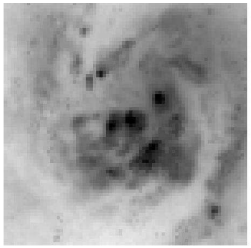
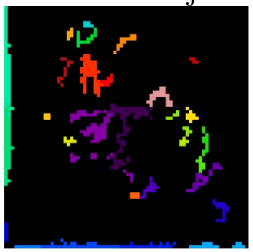
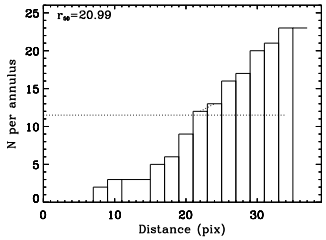

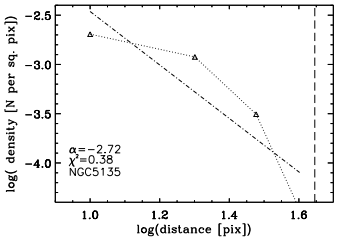

bk.NGC5135

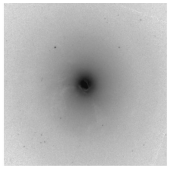
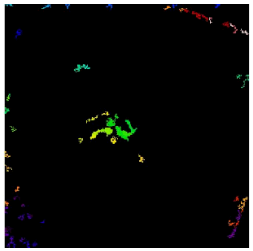
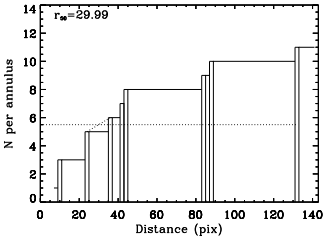

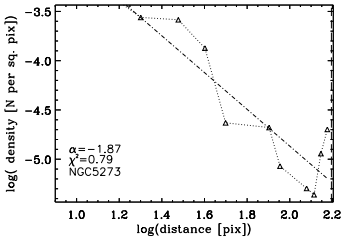

bl.NGC5273

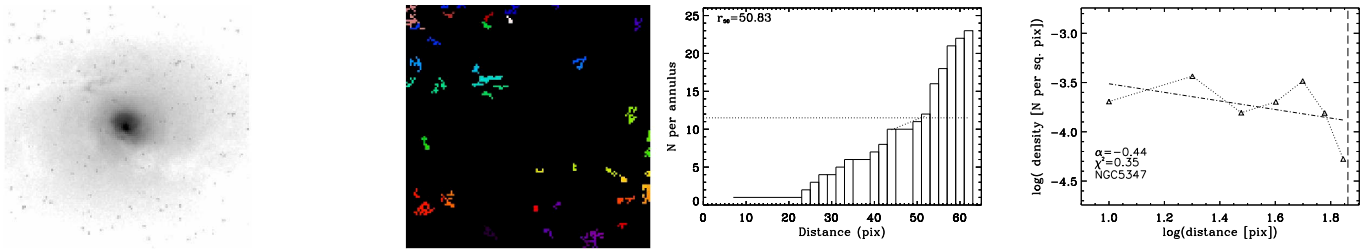

bm.NGC5347

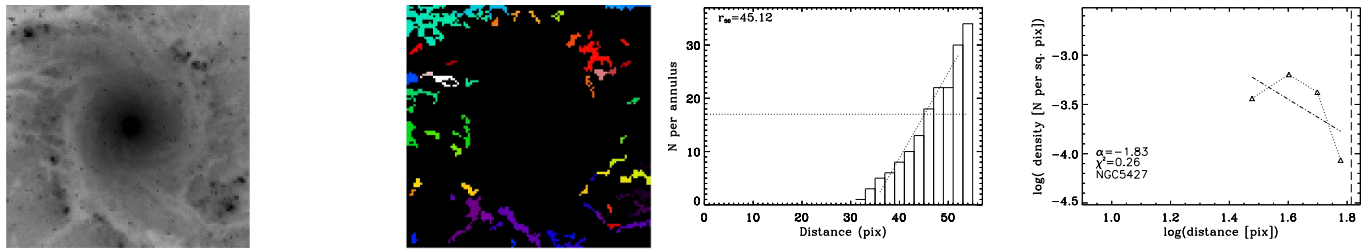

bn.NGC5427

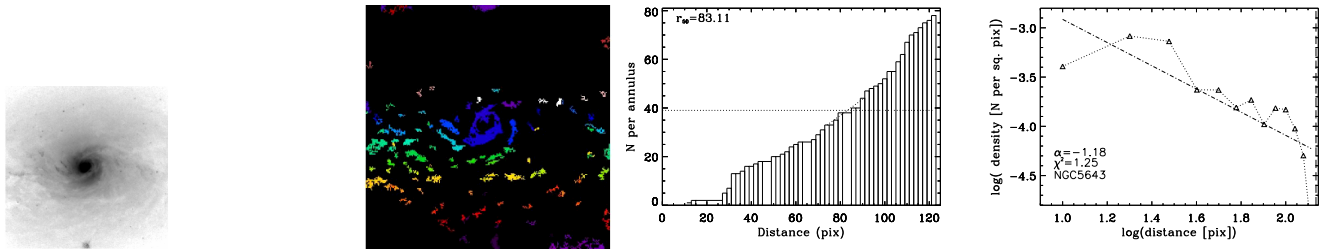

bo.NGC5643

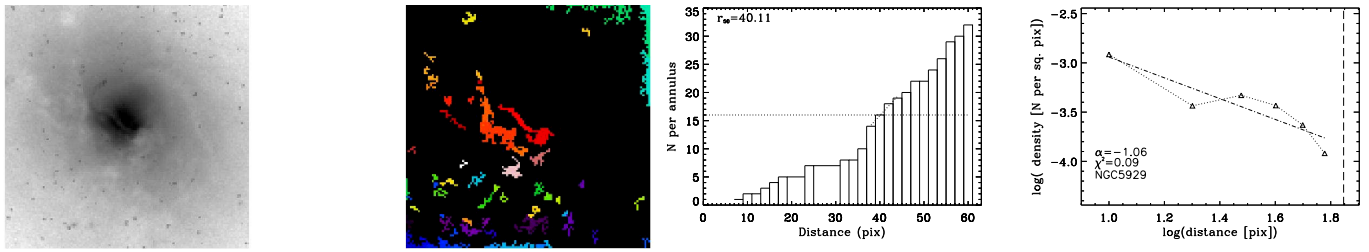

bp.NGC5929

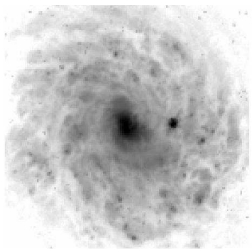
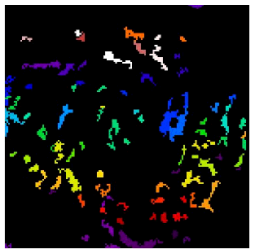
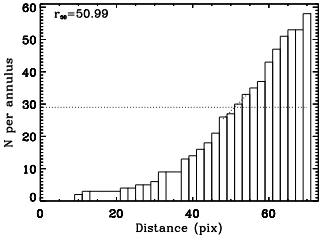

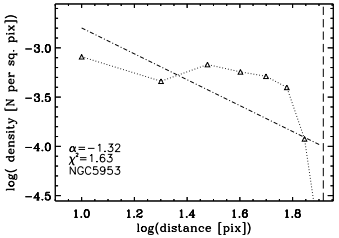

bq.NGC5953

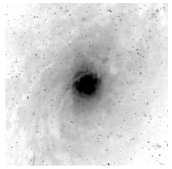
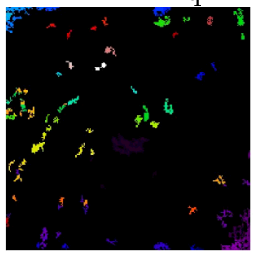
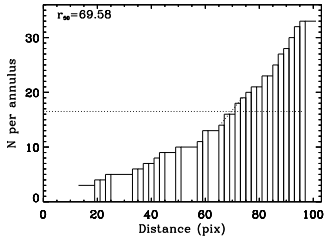

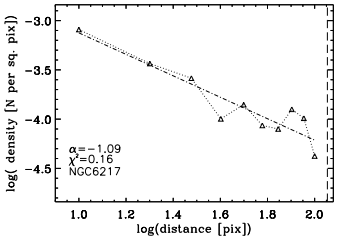

br.NGC6217

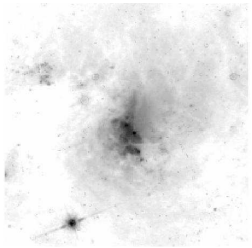
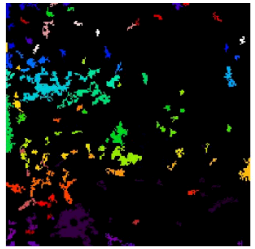
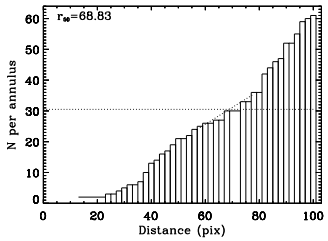

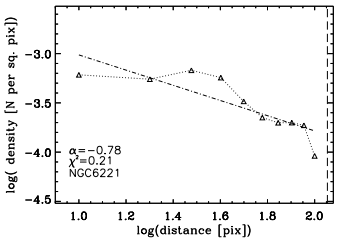

bs.NGC6221

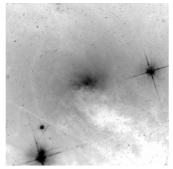
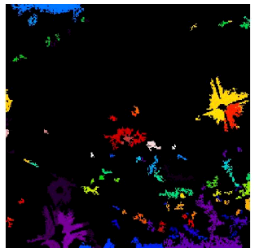
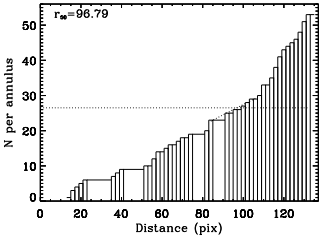

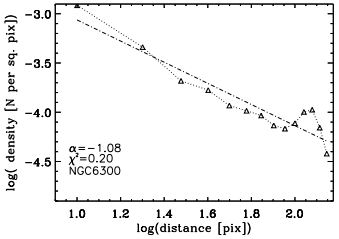

bt.NGC6300

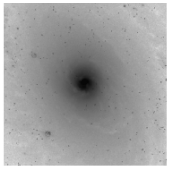

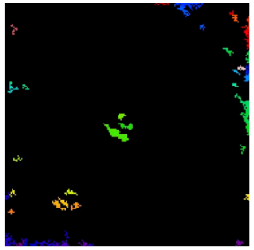

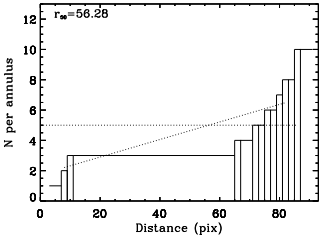

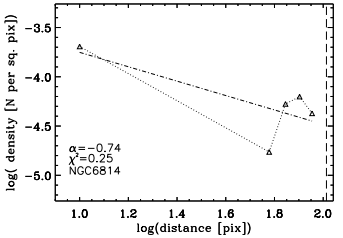

bu.NGC6814

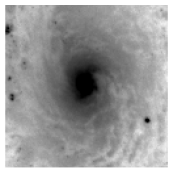

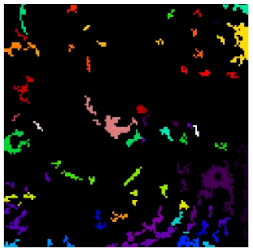

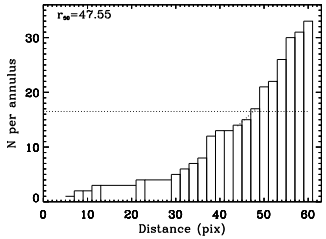

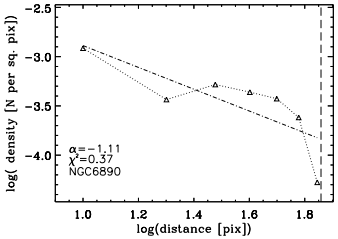

bv.NGC6890

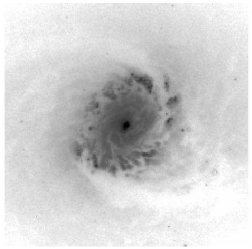

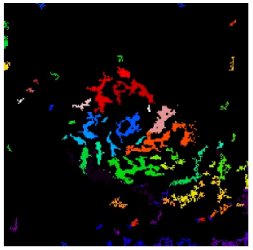

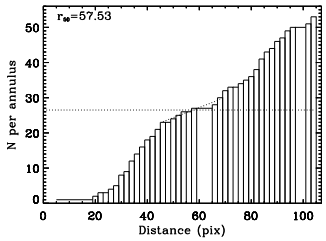

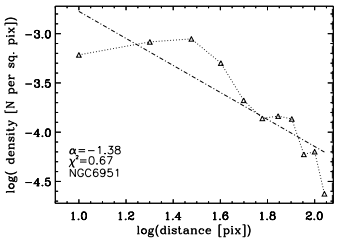

bw.NGC6951

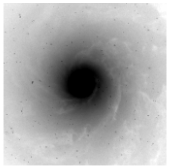

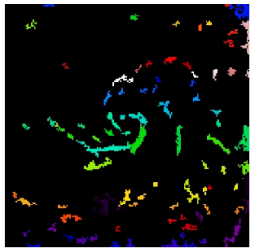

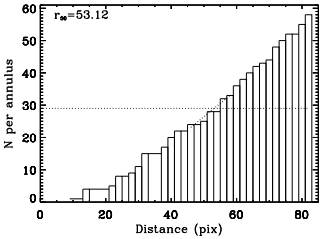

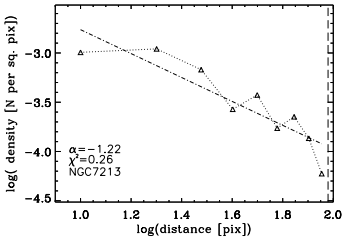

bx.NGC7213

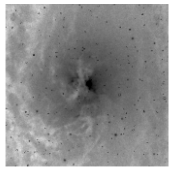
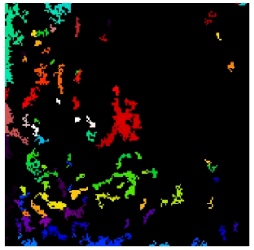
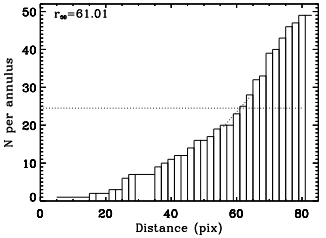

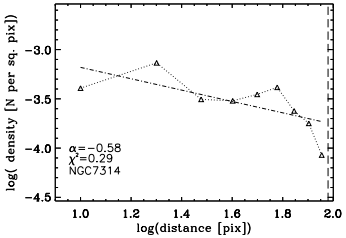

by.NGC7314

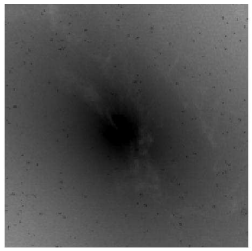
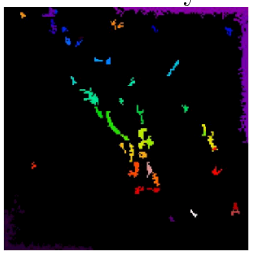
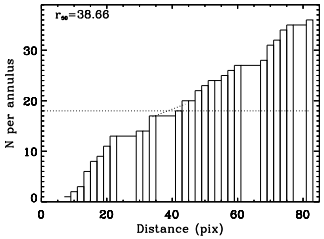

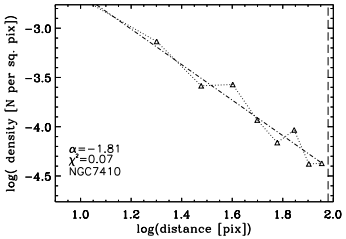

bz.NGC7410

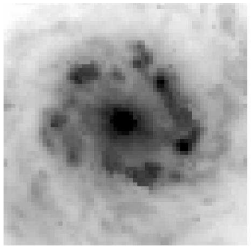
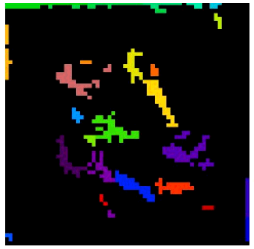
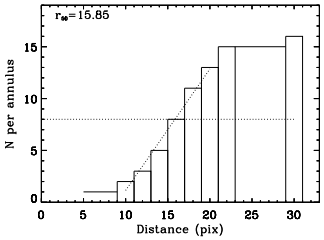

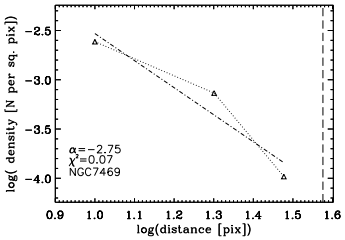

ca.NGC7469

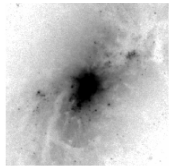
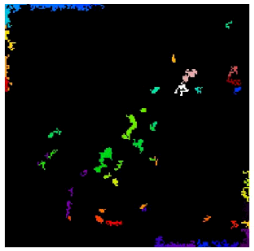
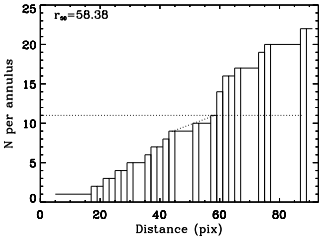

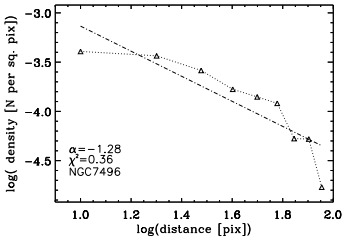

cb.NGC7496

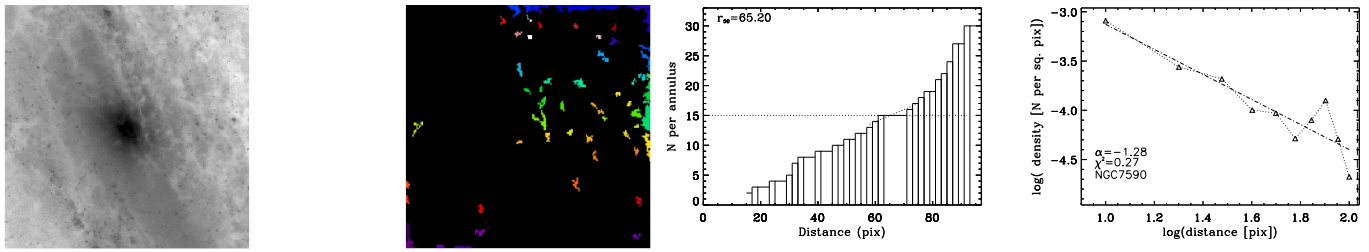

cc.NGC7590

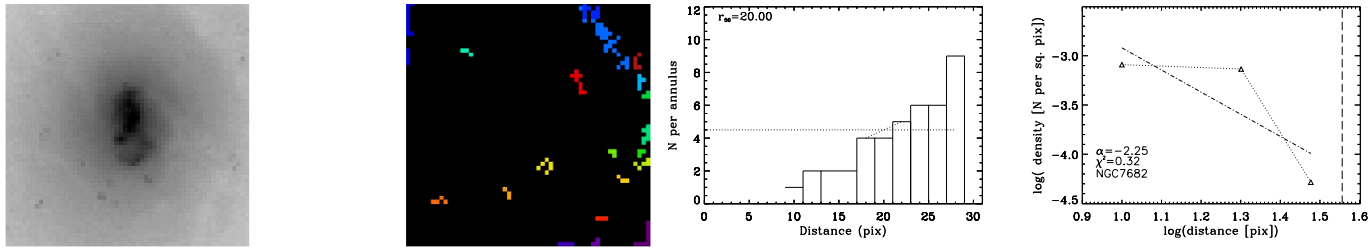

cd.NGC7682

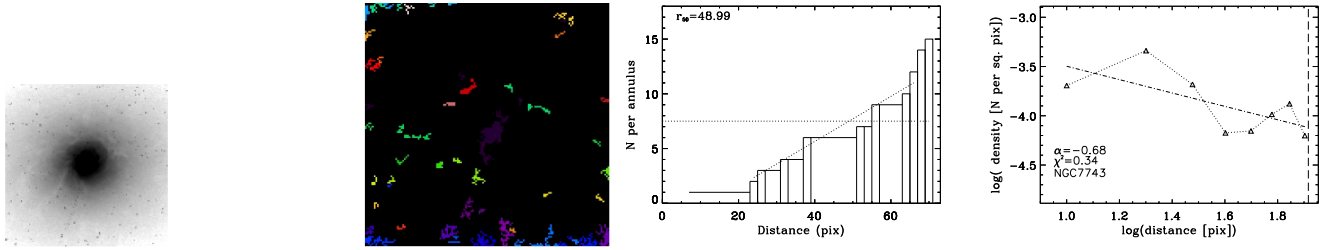

ce.NGC7743

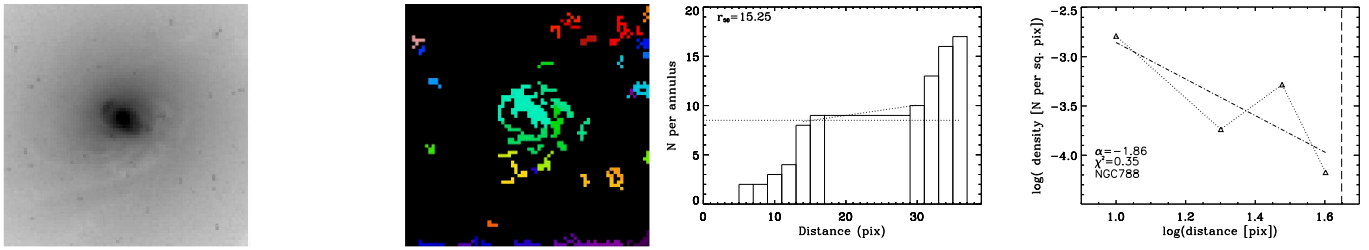

cf.NGC788

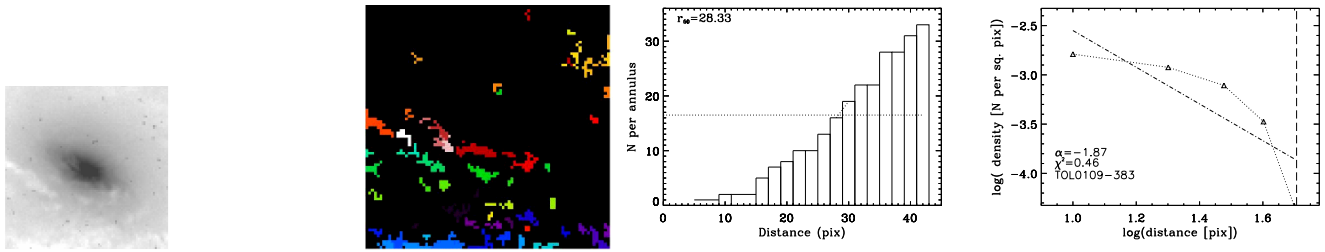

cg.TOL0109

Fig 3(a.-cg.): From left to right, I provide the WFPC2 F606W postage–stamp image of the catalog galaxy that was used to classify galaxy morphology qualitatively (§3.2) and quantitatively (§3.3 and §3.4). I have re-scaled the sizes of these images only for publication; full scale fits images are available on request from the corresponding author. Next, I provide the segmentations maps that were generated using the inverse unsharp–mask method defined in §3.4.1 are provided. Finally, I provide the cumulative number function of objects measured for radii less than 1 kpc and the half— object radius as well as the object surface density, defined as the number of objects per annulus and the best–fit slope α. I discuss each of these data products at length in §3.4.2.

Appendix B

Additional Figures for Chapter Three

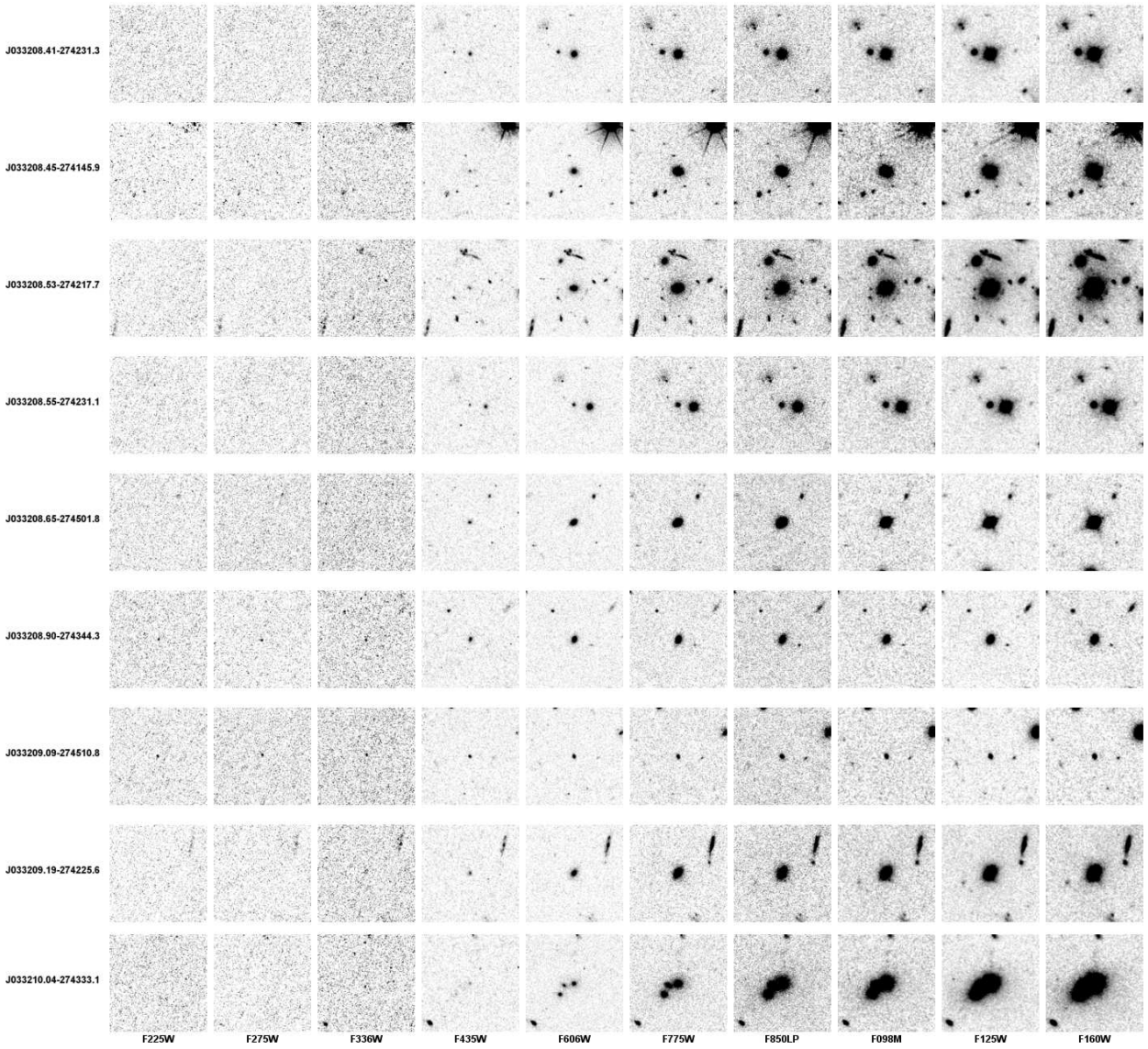
J033208.41-274231.3
J033208.45-274145.9
J033208.53-274217.7
J033208.55-274231.1
J033208.65-274501.8
J033208.90-274344.3
J033209.09-274510.8
J033209.19-274225.6
J033210.04-274333.1
F225W
F275W
F336W
F435W
F606W
F775W
F850LP
F098M
F125W
F160W

Fig. 1b

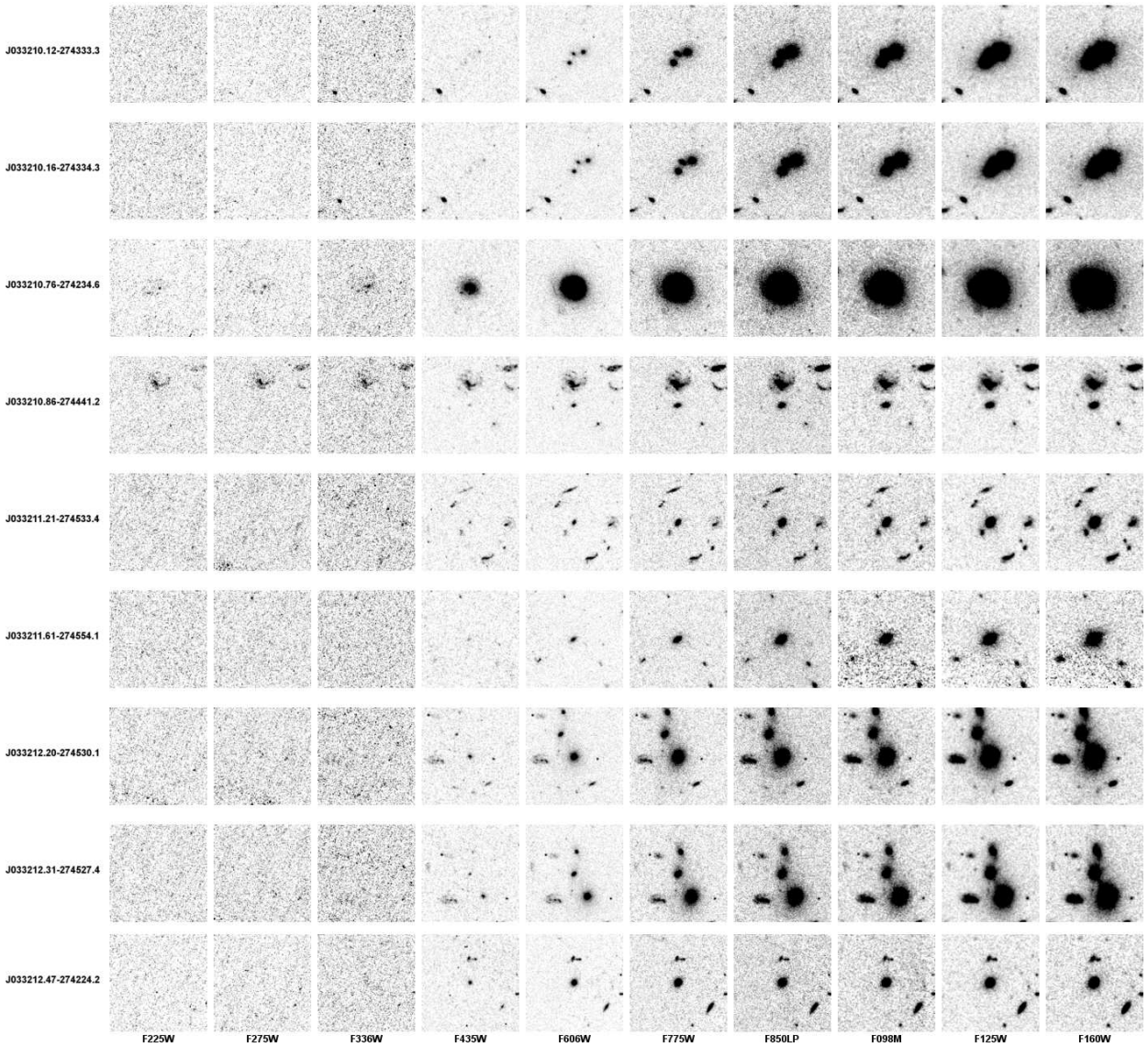
J033210.12-274333.3
J033210.16-274334.3
J033210.76-274234.6
J033210.86-274441.2
J033211.21-274533.4
J033211.61-274554.1
J033212.20-274530.1
J033212.31-274527.4
J033212.47-274224.2
F225W
F275W
F336W
F435W
F606W
F775W
F850LP
F098M
F125W
F160W

Fig. 1c

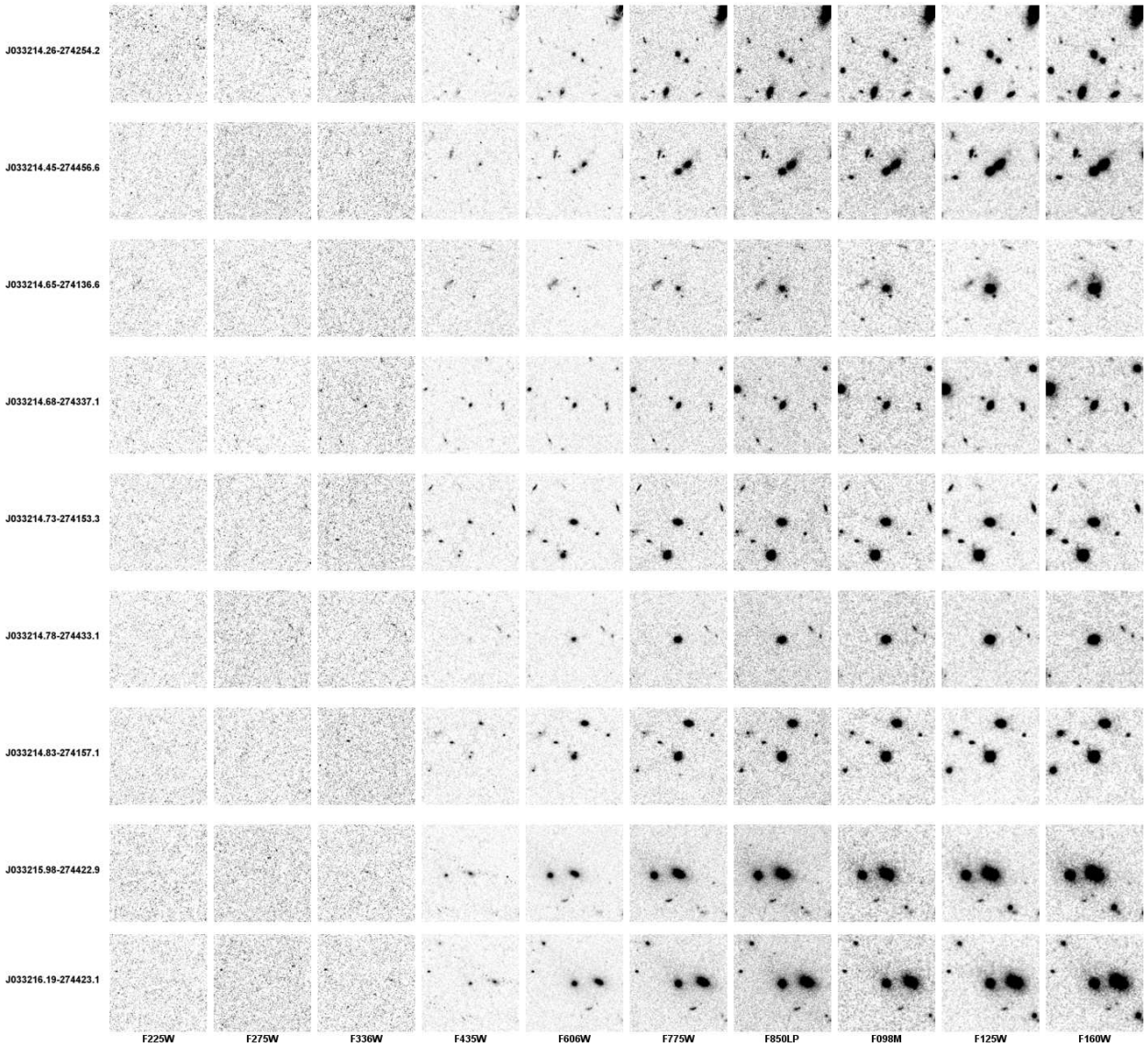
J033214.26-274254.2
J033214.45-274456.6
J033214.65-274136.6
J033214.68-274337.1
J033214.73-274153.3
J033214.78-274433.1
J033214.83-274157.1
J033215.98-274422.9
J033216.19-274423.1
F225W
F275W
F336W
F435W
F606W
F775W
F850LP
F098M
F125W
F160W

Fig. 1d

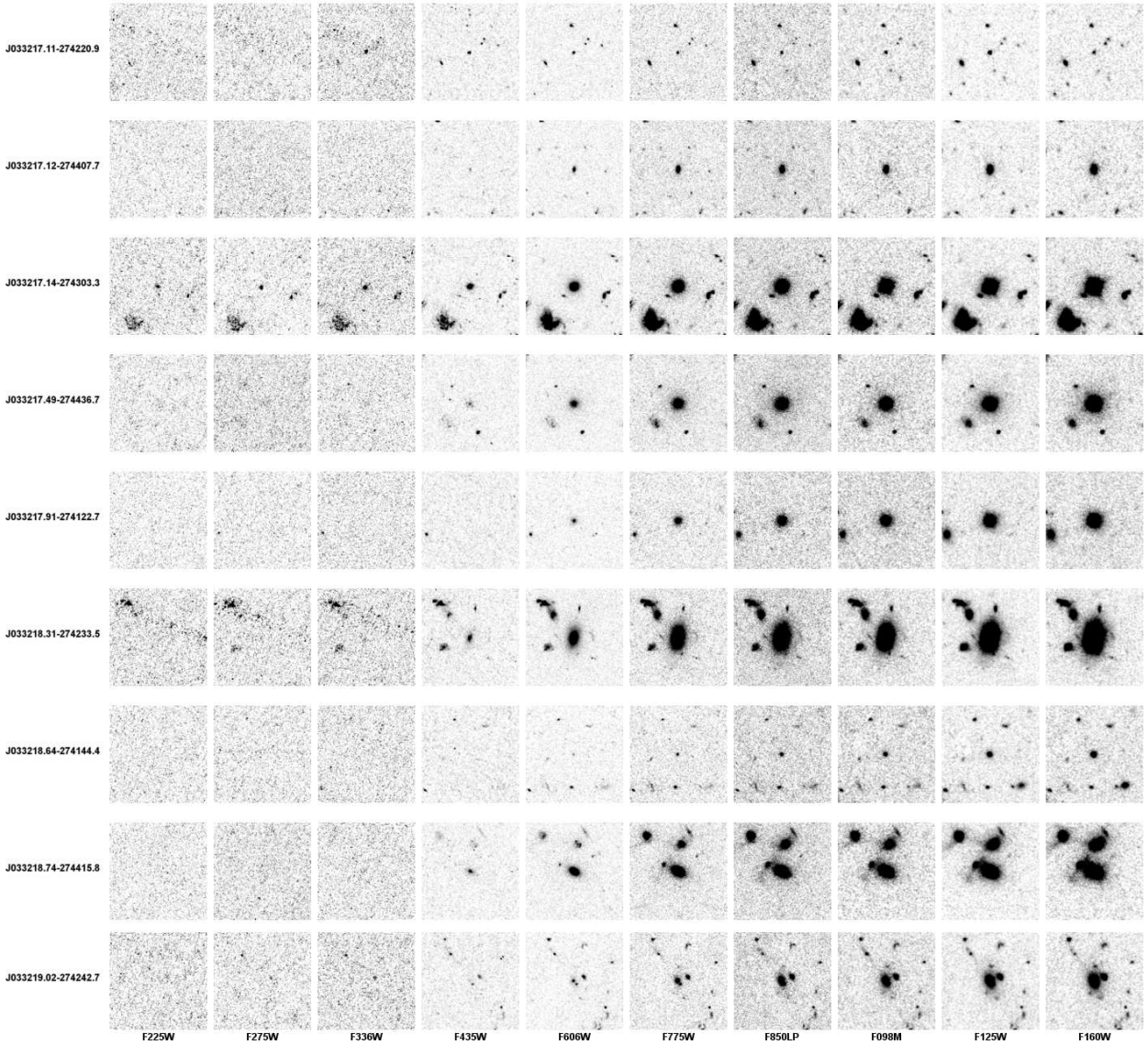
J033217.11-274220.9
J033217.12-274407.7
J033217.14-274303.3
J033217.49-274436.7
J033217.91-274122.7
J033218.31-274233.5
J033218.64-274144.4
J033218.74-274415.8
J033219.02-274242.7
F225W
F275W
F336W
F435W
F606W
F775W
F850LP
F098M
F125W
F160W

Fig. 1e

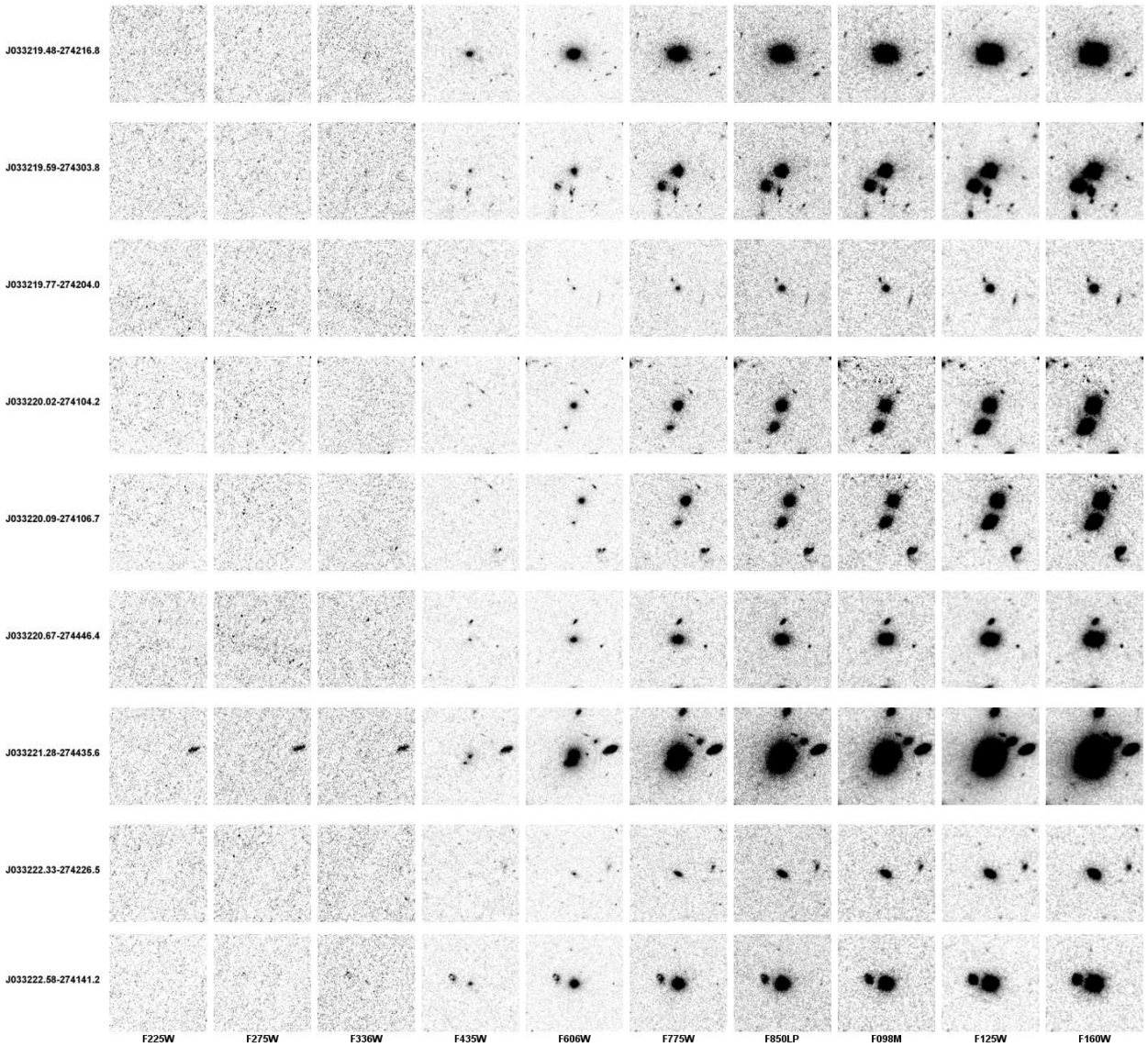
J033219.48-274216.8
J033219.59-274303.8
J033219.77-274204.0
J033220.02-274104.2
J033220.09-274106.7
J033220.67-274446.4
J033221.28-274435.6
J033222.33-274226.5
J033222.58-274141.2
F225W
F275W
F336W
F435W
F606W
F775W
F850LP
F098M
F125W
F160W

Fig. 1f

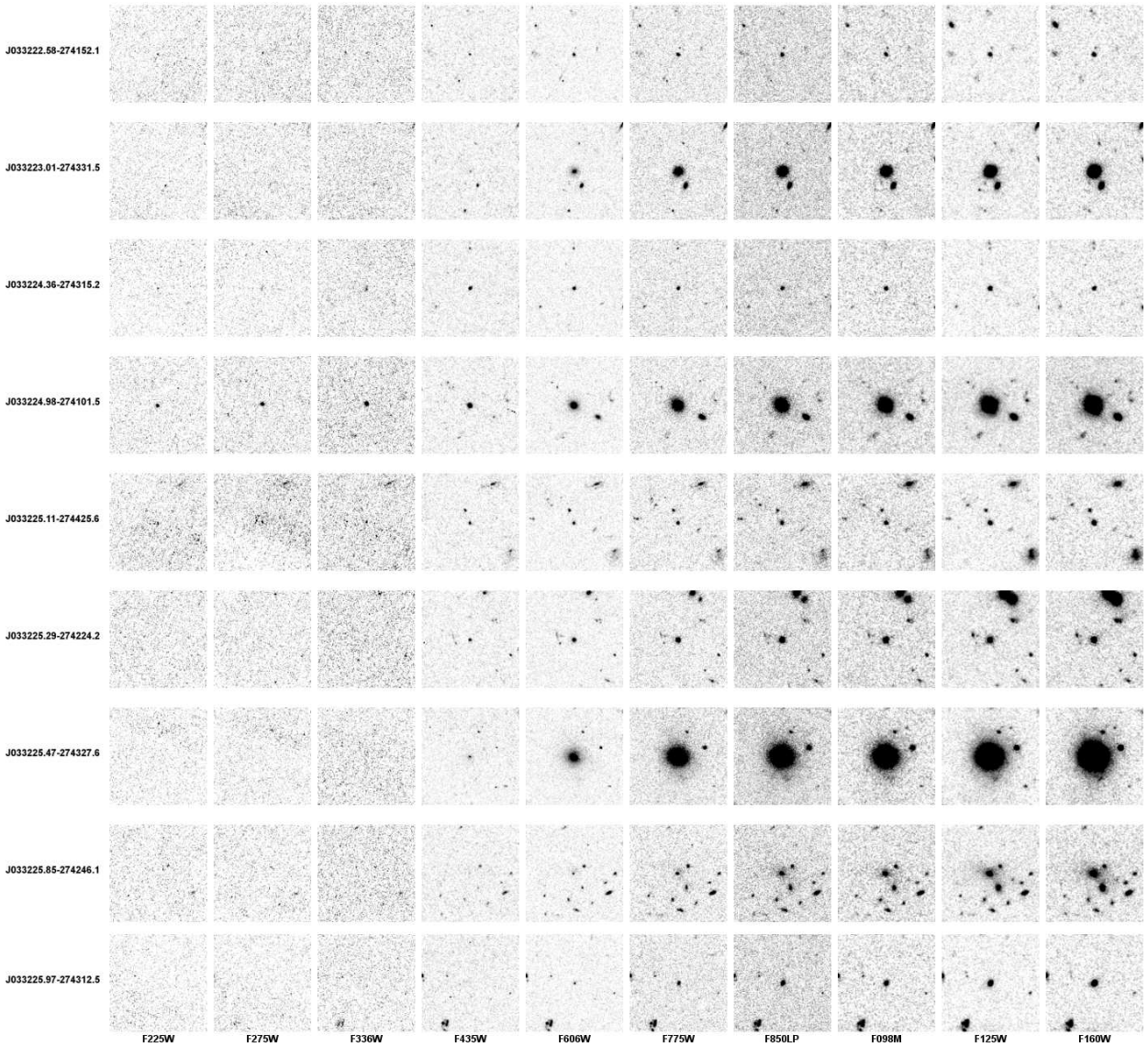
J033222.58-274152.1
J033223.01-274331.5
J033224.36-274315.2
J033224.98-274101.5
J033225.11-274425.6
J033225.29-274224.2
J033225.47-274327.6
J033225.85-274246.1
J033225.97-274312.5
F225W
F275W
F336W
F435W
F606W
F775W
F850LP
F098M
F125W
F160W

Fig. 1g

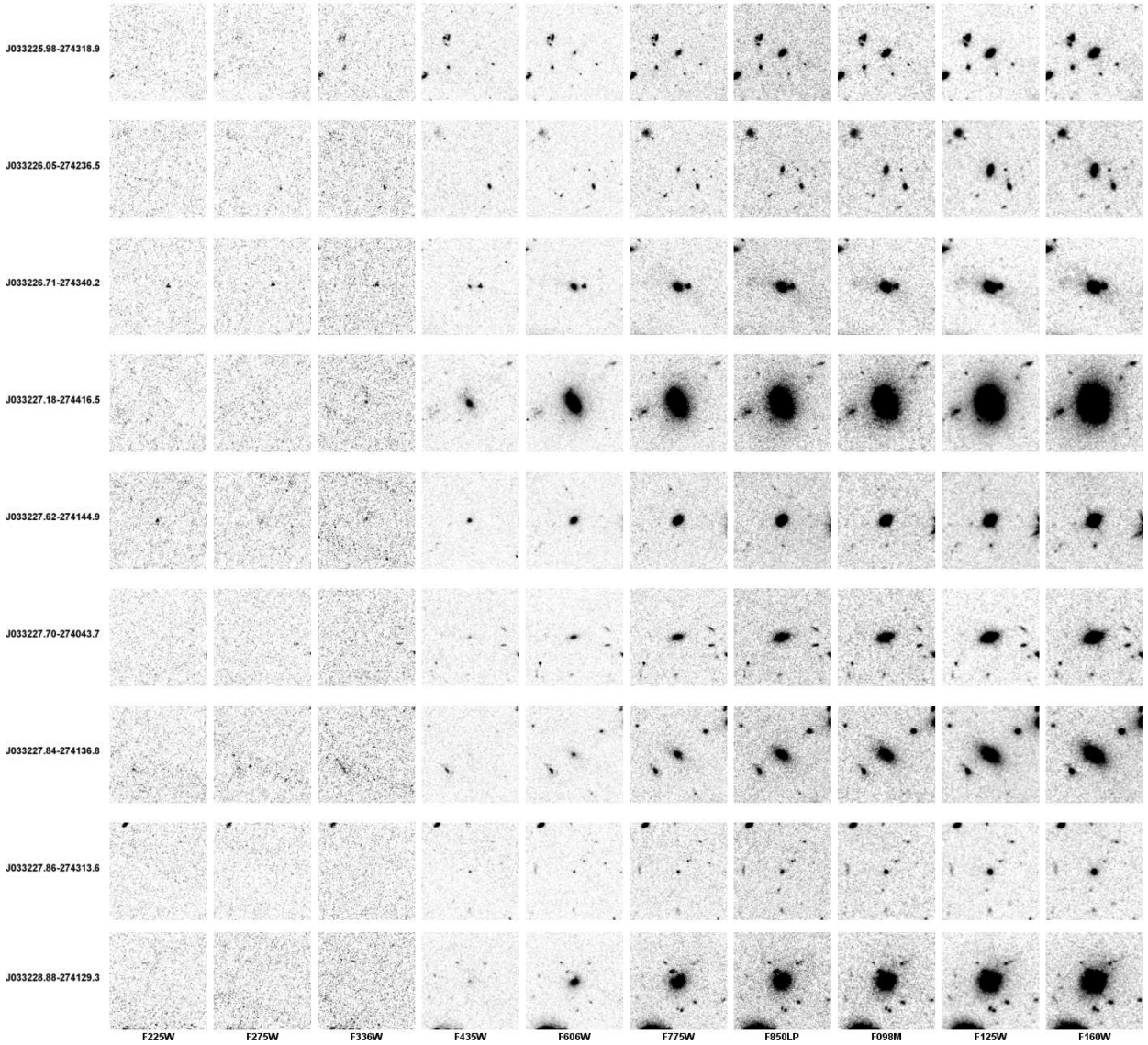
J033225.98-274318.9
J033226.05-274236.5
J033226.71-274340.2
J033227.18-274416.5
J033227.62-274144.9
J033227.70-274043.7
J033227.84-274136.8
J033227.86-274313.6
J033228.88-274129.3
F225W
F275W
F336W
F435W
F606W
F775W
F850LP
F098M
F125W
F160W

Fig. 1h

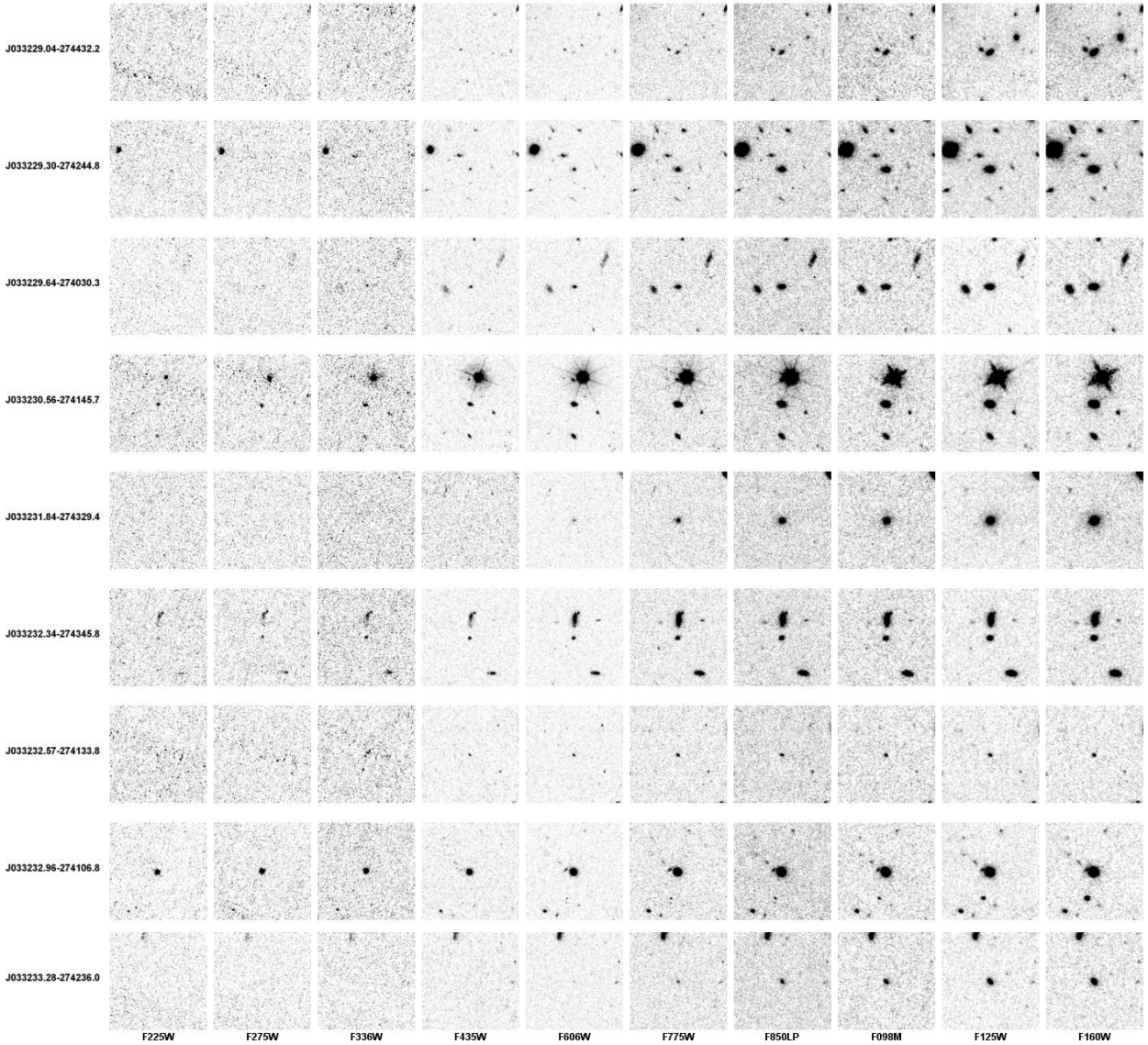
J033229.04-274432.2
J033229.30-274244.8
J033229.64-274030.3
J033230.56-274145.7
J033231.84-274329.4
J033232.34-274345.8
J033232.57-274133.8
J033232.96-274106.8
J033233.28-274236.0
F225W
F275W
F336W
F435W
F606W
F775W
F850LP
F098M
F125W
F160W

Fig. 1i

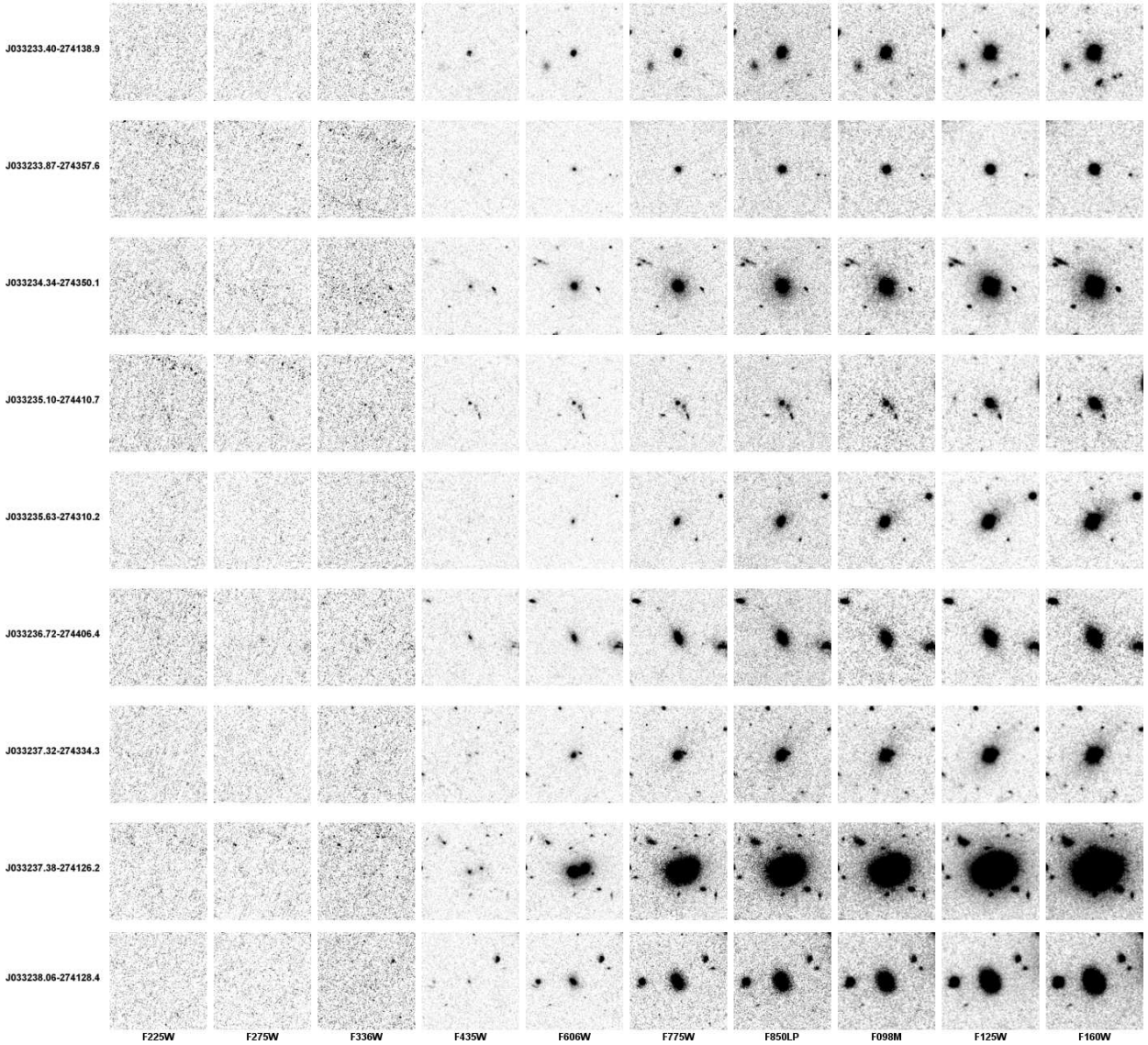
J033233.40-274138.9
J033233.87-274357.6
J033234.34-274350.1
J033235.10-274410.7
J033235.63-274310.2
J033236.72-274406.4
J033237.32-274334.3
J033237.38-274126.2
J033238.06-274128.4
F225W
F275W
F336W
F435W
F606W
F775W
F850LP
F098M
F125W
F160W

Fig. 1j

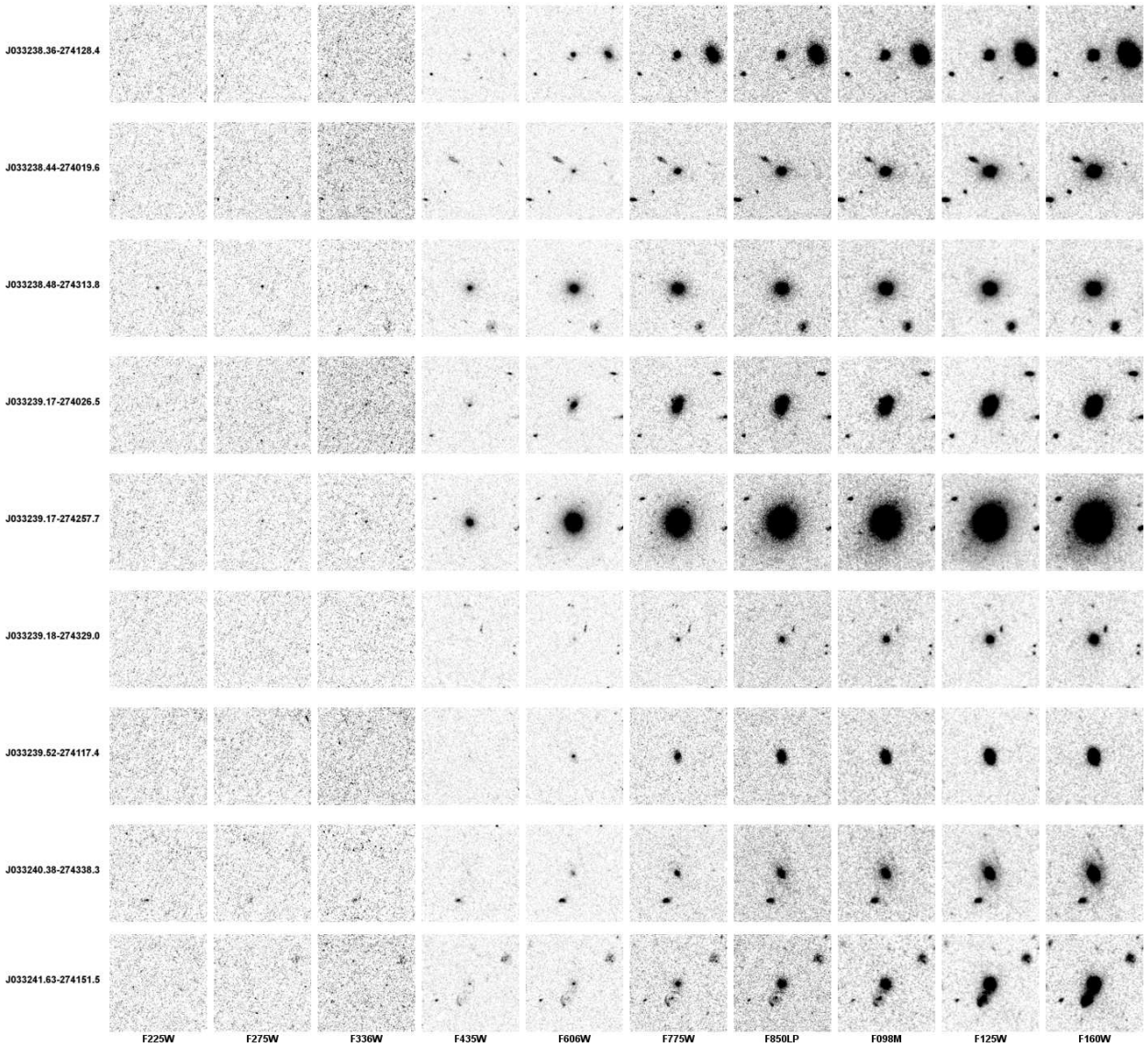
J033238.36-274128.4
J033238.44-274019.6
J033238.48-274313.8
J033239.17-274026.5
J033239.17-274257.7
J033239.18-274329.0
J033239.52-274117.4
J033240.38-274338.3
J033241.63-274151.5
F225W
F275W
F336W
F435W
F606W
F775W
F850LP
F098M
F125W
F160W

Fig. 1k

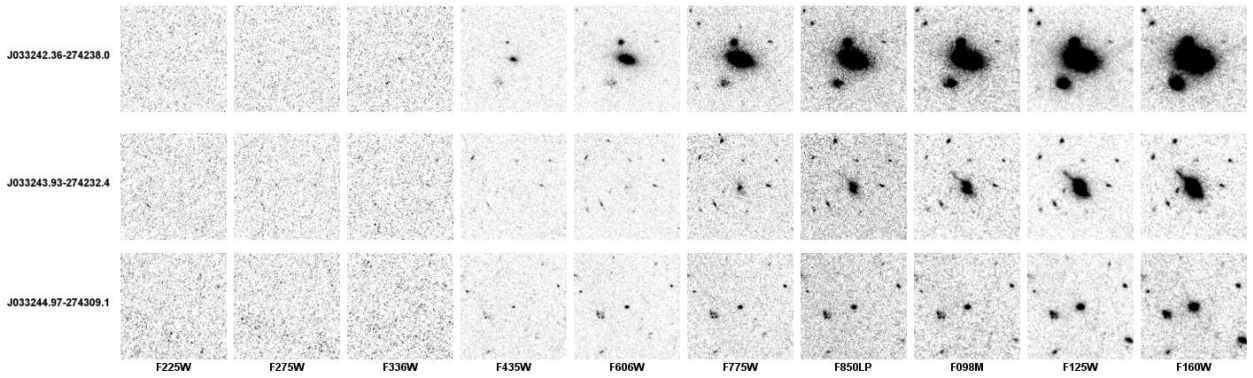
J033242.36-274238.0
J033243.93-274232.4
J033244.97-274309.1
F225W
F275W
F336W
F435W
F606W
F775W
F850LP
F098M
F125W
F160W

Fig. 11